Very large zenith angle observations of VHE gamma-ray sources by IACT telescopes and development of the system for their precision pointing

Zarić, Darko

University of Zagreb

FACULTY OF SCIENCE

DEPARTMENT OF PHYSICS

Darko Zarić

Very large zenith angle observations of VHE gamma-ray sources by IACT telescopes and development of the system for their precision pointing

DOCTORAL DISSERTATION

Zagreb, 2022.

University of Zagreb

FACULTY OF SCIENCE

DEPARTMENT OF PHYSICS

Darko Zarić

Very large zenith angle observations of VHE gamma-ray sources by IACT telescopes and development of the system for their precision pointing

DOCTORAL DISSERTATION

Supervisor:

prof. dr. sc. Nikola Godinović

Zagreb, 2022.

Sveučilište u Zagrebu

PRIRODOSLOVNO–MATEMATIČKI FAKULTET

FIZIČKI ODSJEK

Darko Zarić

Opažanja izvora gama zraka vrlo visokih energija IACT teleskopima pri velikim zenitnim kutovima i razvoj sustava za njihovo precizno usmjeravanje

DOKTORSKI RAD

Mentor:

prof. dr. sc. Nikola Godinović

Zagreb, 2022.

SUPERVISOR

At the beginning of his career Nikola Godinović was working on the commissioning of the 500 keV Van de Graaf accelerator at the University of Split, FESB. Since 1994 he is a member of the CMS Collaboration and has significantly contributed to the design and development of the electromagnetic calorimeter, performing detailed analyses of the test beam data for different prototypes of the CMS electromagnetic calorimeter. He also had a significant contribution in the CMS Higgs physics, as he was the first one in evaluating the CMS potential to measure the spin and CP of the Higgs boson in the decay channel H>ZZ>4l, as a part of his PhD thesis. He continued this study and had contributed to the development of the software tool for more precise calculation of the Higgs boson angular correlation in this decay channel. In 2008 he was initiator, together with a group of colleagues with background in particle physics and astrophysics, of a new research activity in Croatia, very high energy gamma-ray astronomy. Nikola Godinović has been leading this Croatian pioneering activity since the very beginning, which is a part of an internationally recognised group making significant contributions to the advance of very high energy gamma-ray astronomy. He had duties and responsibilities in the MAGIC and CTA Collaborations, and has contributed to the improvement of the performance of the MAGIC telescopes by leading the group responsible for the development of the software tools for data quality checks and also contributed to the Crab pulsar analysis. Nikola Godinović initiated and is currently coordinating Croatian contribution to the CTA LST working group to develop, design and commission the LST pointing system.

Nikola Godinović co-supervised one PhD student and supervised one postdoc and is currently supervising two PhD students. In addition, he was a mentor of 7 diploma students and 10 bachelor students. In the last five years he had 6 invited talks at international conferences and has given lectures at high energy physics schools.

ACKNOWLEDGEMENTS

Here I would like to express my gratitude to everyone supporting me during the time I was working on this thesis.

First of all, I want to thank my supervisor Dr. Nikola Godinović for introducing me to the field of gamma-ray astronomy and giving me the opportunity to conduct my research in this area. I would like to thank Nikola not only for his professional guidance during the years but also his constant support and words of encouragement.

Furthermore, I want to thank all my colleagues here at FESB, Split. You made this a great environment to work in and I could always count on your support.

I would like to thank Dr. Razmik Mirzoyan for providing me the opportunity to conduct research at the Max Planck Institute in Munich. The work I did there laid the foundations of this thesis.

Without the help of Dr. Ievgen Vovk I don't know if I would have been able to make it this far. I would like to thank Ievgen for his endless patience and valuable time spent in discussions with me. Your help meant more than you know.

Thanks to everyone in Munich, there are simply too many to name here. During my stay I always felt like a part of the group, it's been a blast to get to know all of you.

I would also like to thank everyone in MAGIC and LST Collaborations. They are a great examples of friendly and motivating working atmospheres.

There are many more to whom I owe my gratitude, sorry for not mentioning your names here.

Last but not least I would like to express my gratitude to my family for always supporting me and my decisions. This goes to Branko, Tanja and especially to my parents Dušanka and Milan for their unconditional love and support.

TECHNICAL ACKNOWLEDGMENTS

The MAGIC and LST Collaborations are acknowledged for allowing the use of proprietary observational data. MAGIC and LST results presented in this thesis have not undergone the internal review procedure of MAGIC and LST publications.

SUMMARY

The search for cosmic particle accelerators capable of reaching the PeV (10^{15} eV) range, PeVatrons, is a key science objective for the very-high-energy (VHE) community (gamma-ray domain around TeV = 10^{12} eV). As the PeV particles are accelerated, gamma rays in the $\sim$100 TeV range should be produced. Thus, investigations into this energy domain are necessary in the search for PeVatrons.

For the purpose of identifying PeVatrons with the MAGIC telescopes a novel observational method of performing observations at very large zenith angles ($\gtrsim 70^{\circ}$) is introduced in the first part of the thesis. The goals and technical characteristics are explained, together with the benefits and drawbacks of the method. The performance of this observational method has been performed on the "standard candle" of the VHE gamma-ray astronomy, the Crab Nebula.

After the Very Large Zenith Angle (VLZA) method was validated it was applied on two extended sources of VHE gamma-rays, MGRO J2019+37 and HESS J1809-193 which covers the second part of the thesis. Since the sources are extended a spatial likelihood analysis was performed on these sources.

In the last part of the thesis a technical contribution to the (Large Size Telescope) LST-1 is presented called Camera Displacement Monitor (CDM). It is a system for monitoring the displacement of the LST-1 camera which I was in charge of implementing and testing. The software implementation is explained together with the tests performed in the laboratory and on site. From the technical observations the CDM performance was evaluated and the results show that the requirements are fullfilled and the CDM is capable of measuring the oscillations of LST-1 photomultiplier tube camera.

Keywords: gamma ray, Imaging Atmospheric Cherenkov Telescope, Crab Nebula, MGRO J2019+37, HESS J1809-193, Camera Displacement Monitor

SAŽETAK

Potraga za izvorima kozmičkih zraka koji mogu ubrzati čestice do PeV (10^{15} eV), tzv. PeVatroni, jedan je od ključnih ciljeva visokoenergijske astronomije gama zraka. Čestice ubrzane do energija $\sim$PeV bi trebale proizvesti gama zrake energija $\sim$100 TeV. Stoga istraživanja su nužna u ovom energetskom rasponu pri potrazi za PeVatronima.

U svrhu identificiranje PeVatrona s MAGIC teleskopima nova metoda opservacije pri velikim zenitnim kutovima ($\simeq 70^{\circ}$) je predstavljena u prvom dijelu disertacije. Cilj i tehničke karakteristike su objašnjene, zajedno s prednostima i manama metode. Učinak ove metode opservacije je odrađen na "standardnoj svijeći" visokoenergijske astronomije, Maglici Rakovici.

VLZA metoda je primjenjena i na 2 proširena izvora visokoenergijskih gama zraka, MGRO J2019+37 i HESS J1809-193 koji su obrađeni u drugom dijelu disertacije. Kako su izvori prošireni za njihovu analizu upotrijebljena je metoda prostorne maksimizacije vjerojatnosti.

U zadnjem dijelu disertacije predstavljen je tehnički doprinos za LST-1 (Large Size Telescope) naziva Camera Displacement Monitor (CDM). To je sustav za nadziranje pomaka LST-1 kamere za koju sam bio zadužen za implementaciju i testiranje. Objašnjena je softverska implementacija zajedno s testovima izvršenim u laboratoriju i na mjestu instalacije. Iz tehniških opservacija performanse CDM-a su procijenjene i rezultati pokazuju da su zahtjevi ispunjeni i CDM može mjeriti oscilacije LST-1 detektorske kamere.

CONTENTS

1. Introduction to Cosmic and Gamma Rays

1.1. Cosmic rays

1.1.1. Background

Victor Hess conducted a series of groundbreaking balloon flights in 1912, measuring ionizing radiation levels as high as 5 km above the Earth's surface [1]. His observation of enhanced radiation at high altitude demonstrated that ionizing particles are impinging from above. Protons are now known to make up the majority of cosmic-ray (CR) particles. Energy and isotropy measurements firmly revealed that the Sun is not the primary source of these particles. The Sun dominates the observed proton flux only below a kinetic energy of around 100 MeV due to the solar wind shielding the protons from beyond the Solar System. Far beyond the Earth's atmosphere and magnetosphere, spacecraft missions reveal that abundances of $\sim$1 GeV are strikingly similar to those found in typical Solar System material.

The rate of CR primaries drops to less than one particle per square metre per year above $\sim 10^5$ GeV. This makes the direct observation in the upper layers of the atmosphere (with balloon or aircraft), or even above (with spacecrafts) inefficient. Only ground-based experiments equipped with sufficiently big apertures and lengthy exposure durations have a reasonable likelihood of obtaining a considerable number of events. These experiments use the atmosphere as a massive calorimeter. Cosmic radiation collides with the atomic

For this section [2, 3] were used as main references.

nuclei of air molecules, resulting in the formation of air showers that spread over enormous areas. Based on the size of air showers Pierre Auger concluded in 1938, that the spectrum of cosmic rays extends up to and maybe above 10^6 GeV [4, 5]. Significant progress has been achieved in recent years in measuring the extremely low flux at the high end of the spectrum.

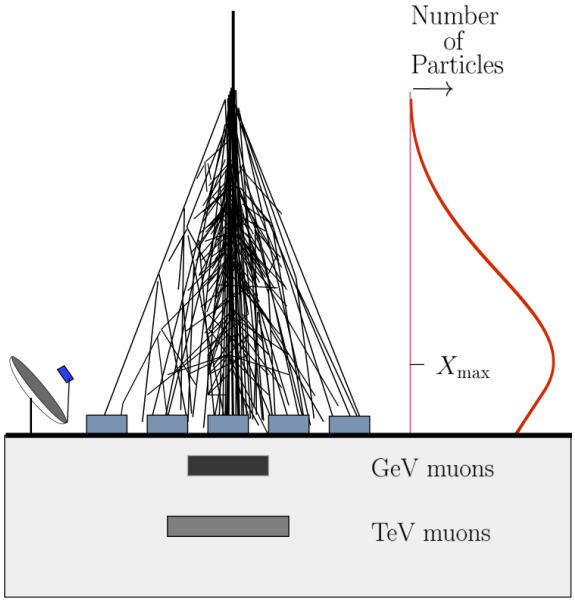

Figure 1.1: When particles imping the top of the atmosphere, an electromagnetic and hadronic cascade is started. On the right the profile of such cascade is shown. Mirrors gather Cherenkov and nitrogen fluorescent light, arrays of detectors sample the shower as it approaches the ground, and subsurface detectors identify the shower's muon component. Adopted from [6].

At sea level, the extent of an extended air shower (EAS) is determined by the energy of the incoming particle and the direction of arrival. The cascade for ultra-high-energy cosmic ray (UHECR) showers is typically several hundreds of meters wide and contains millions of secondary particles. Secondary electrons and muons created during the decay of pions can be detected using scintillation counters or the Cherenkov light released in the watertanks. The distances between these detectors can range between 10 m and 1 km, depending on the CR energy and the detection array's optimal cost effectiveness. The shower core and thus the direction of arrival can be determined from the relative arrival time and density of particles in the detector grid. The primary energy can be calibrated us-

ing the lateral particle density of the showers. Another well-established way of detection is to monitor the longitudinal development of the shower (number of particles against atmospheric depth, as schematically depicted in Figure 1.1) by measuring the fluorescence light produced by charged particle interactions in the atmosphere. The emitted light is typically in the 300-400 nm ultraviolet (UV) region, which is completely transparent to the atmosphere. EASs can be observed at distances of up to 20 kilometers (approximately two attenuation lengths in a standard desert atmosphere at ground level) under favorable atmospheric conditions.

1.1.2. Cosmic ray energy spectrum

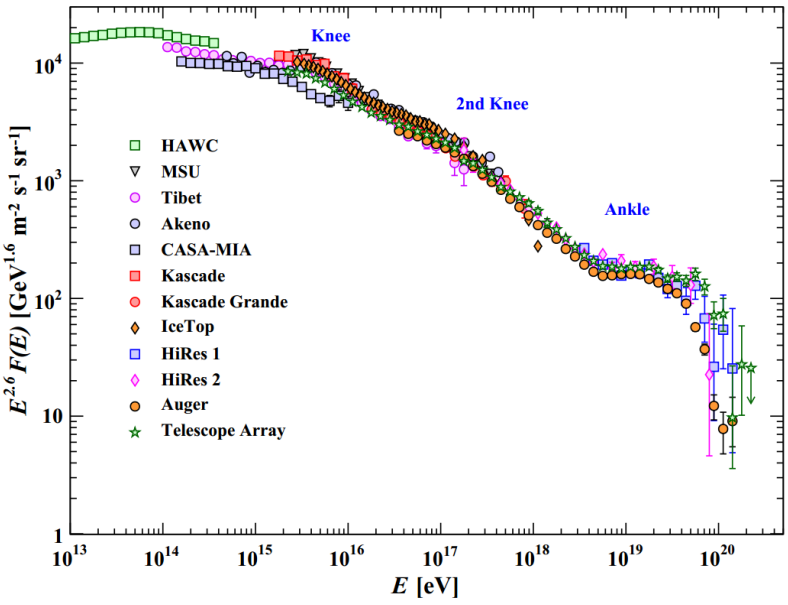

Figure 1.2: The all-particle spectrum as a function of E (energy per nucleus) from air shower measurements. Adopted from [7].

The CR spectrum spans over approximately 11 orders of magnitude in energy with the flux decreasing from $10^4\,\mathrm{m}^{-2}\,\mathrm{s}^{-1}$ at ~ 1 GeV to $10^{-2}\,\mathrm{km}^{-2}\,\mathrm{yr}^{-1}$ at $\sim 10^{11}$ GeV.

The differential energy spectrum of cosmic rays is defined as the number of particles crossing a unit area dA per unit time dt and unit solid angle $d\Omega$, with energy within E and $E + dE$:

$$F(E) = \frac{dN}{dA\,dt\,d\Omega\,dE}. \tag{1.1}$$

Its shape is notable for its lack of features, with little variation from a constant power law ($F \propto E^{-\Gamma}$, with $\Gamma \simeq 3$) over this broad energy range. The minor variations in the power index, Γ, can be viewed by multiplying the flux by a power of the energy. In such situation, the spectrum reveals a structure like a leg, as illustrated in Figure 1.2. The changes in slope, mass composition, and arrival direction of this structure reflect the many facets of CR propagation, generation, and distribution.

The cosmic-ray knee is a steepening of the CR spectrum ($\Gamma \simeq 2.7 \rightarrow 3.1$) at an energy of around $10^{6.5}$ GeV. Composition studies in cosmic-ray observatories show that this characteristic of the spectrum is composed of the subsequent fall-off of Galactic nuclear components with maximal energy E/Z [8–10]. This scaling with atomic number Z is consistent with particle acceleration in a magnetically confined environment, which is effective only if the particle's Larmor radius is smaller than the accelerator's size. If this interpretation is correct, the Galactic contribution to CRs cannot exceed 10^8 GeV [11], assuming the largest component is iron ($Z = 26$). However, the experimental evidence at these energies are not conclusive.

The start of extragalactic contribution may be indicated by the second knee - a further steepening ($\Gamma \simeq 3.1 \rightarrow 3.2$) of the spectrum at around $10^{8.7}$ GeV [12]. It is worth noting that extragalactic CRs are prone to interactions with the interstellar medium throughout their propagation and these particle-specific interactions affect the spectrum observed on Earth, depending on the initial chemical composition. It has been suggested [13, 14] that an extragalactic proton population with a simple power-law injection spectrum may be capable of reproducing the spectrum above the second knee. According to these models, the flattening ($\Gamma \simeq 3.2 \rightarrow 2.7$) of the spectrum at roughly $10^{9.5}$ GeV - the ankle - can be attributed to a "dip" in the spectrum caused by e^+e^- pair creation and a "pile-up" of protons caused by pion photoproduction. However, this feature is dependent on a proton dominance in extragalactic cosmic rays, as heavier nuclei such as oxygen or iron have significantly different energy-loss properties in the cosmic microwave background (CMB), and mixed compositions will not reproduce the spectral features in general [15].

A crossover is also possible at higher energy: above the ankle, the Larmor radius of a proton in the Galactic magnetic field surpasses the size of the Galaxy, and it is commonly considered that the spectrum at these energies is dominated by an extragalactic

component [16]. Additionally, the Galactic-extragalactic crossover should be followed by the emergence of spectral features; for example, two power-law contributions would naturally result in a flattening of the spectrum at lower energies if the harder component dominates. As a result, the ankle appears to be an obvious candidate for this crossover.

Around $\sim 4.2 \times 10^{19}$ eV, a considerable suppression of the flux has been reported [17, 18], and has recently reached a statistical significance of more than 20σ. This suppression can be attributed to energy losses during propagation (the Greisen-Zatsepin-Kuzmin (GZK) effect [19, 20]) or to an intrinsic limit of sources, which are incapable of accelerating particles beyond a certain energy [21].

1.1.3. Acceleration mechanism

There are two different kinds of processes capable of accelerating charged particles to ultra-high energies and simultanously producing a power law spectrum. One is the direct acceleration of particles to very high energies using an extended electric field [21], as in the case of unipolar inductors in relativistic magnetic rotators (e.g. neutron stars, [22]) or black holes with magnetized disks that lose rotational energy in jets. They have the advantage of being fast, but suffer from the fact that the acceleration happens in extremely dense astrophysical regions, creating new opportunities for energy loss. Additionally, a harsh injection spectrum is expected which is incompatible with the observed slope. In 1949 Fermi developed the statistical acceleration mechanism [23]. There he studied the scattering of cosmic particles on moving magnetized clouds, which resulted in a fractional energy gain $\xi = \langle \Delta E \rangle / E \propto \beta^2$, where β is the average velocity of the scattering centers in units of c. Although there is a net transfer of macroscopic kinetic energy from the moving cloud to the particle, the average gain in energy is rather low. This mechanism is now referred to as "second order Fermi acceleration." The first truly successful theory of high-energy cosmic ray acceleration was established as the Fermi acceleration in nonrelativistic shock waves in supernova remnants in [24]. The diffusion of cosmic rays in moving magnetized plasmas upstream and downstream of shocks forces particles to repeatedly cross the shock front, accumulating energy as a result of multiple interactions. This results in $\xi \propto \beta$, where β is the shock fluid's speed in units of c when measured in the stationary upstream frame. This process is referred to as "first order Fermi acceleration."

Gamma Ray Burst (GRB) shocks, jets and hot spots of Active Galactic Nuclei (AGN), and gravitational accretion shocks all serve as shock sources for UHECR acceleration.

An attractive feature of Fermi acceleration is its prediction of a power-law flux of CRs, like in [25]. One can consider a test particle with momentum p in the rest frame of the upstream fluid as in Figure 1.3. Then the energy E_n of a cosmic particle after n acceleration cycles is:

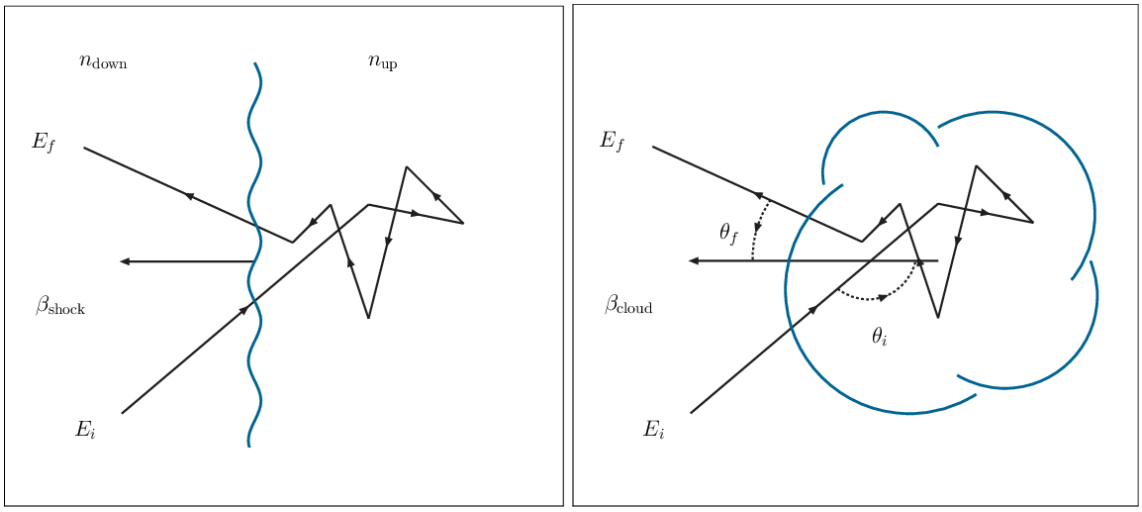

Figure 1.3: A sketch of first and second-order Fermi acceleration by scattering off (left) plasma shocks and (right) magnetic clouds. Adopted from [2].

$$E_n = E_0(1+\xi)^n \tag{1.2}$$

and the number of cycles to reach E results from Equation 1.2 is:

$$n = \ln\left(\frac{E}{E_0}\right) / \ln(1+\xi), \tag{1.3}$$

where E_0 is the energy at injection into the acceleration site. If the escape probability P_{esc} per encounter is constant, then the probability to stay in the acceleration region after n cycles is $(1-P_{\text{esc}})^n$. The fraction of particles accelerated to energies $> E$, the integral spectrum, is:

$$N(>E) \propto \frac{(1-P_{esc})^n}{P_{esc}} \propto \frac{1}{P_{esc}}\left(\frac{E}{E_0}\right)^{-\Gamma} \tag{1.4}$$

with $\Gamma \propto P_{\rm esc}\,/\xi$ for $\xi \ll 1$ and $P_{\rm esc} \ll 1$. Both first and second order Fermi acceleration produce a power law energy spectrum.

For the case of shock accelerations the spectral index can also be estimated to be $\Gamma \propto 1$. This injection spectrum is in good agreement with the observed flux of cosmic rays, $dN/dE \propto E^{-2}$, although additional effects like energy losses or an energy dependence of the escape probability, could have an important impact on the shape of the injection spectrum.

The requirements for astrophysical objects to be sources of UHECR are stringent. The Larmor radius of a particle with charge Ze increases with its energy E according to

$$r_L = \frac{1.1}{Z}\left(\frac{E}{10^{18}\ \mathrm{eV}}\right)\left(\frac{B}{\mu\mathrm{G}}\right)^{-1}\mathrm{kpc} \tag{1.5}$$

The search for UHECR extralagalactic sources was motivated by the fact that r_L in the galactic magnetic field is significantly bigger than the thickness of the galactic disk, implying that UHECR cannot be contained within the galaxy. According to the well-known Hillas criterion [21], the Larmor radius of accelerated particles cannot exceed the size of the source ($R_{\rm source}$), hence establishing a natural limit on the particle's energy.

$$E_{\rm max} \simeq Z\left(\frac{B}{\mu\mathrm{G}}\right)\left(\frac{R_{\rm source}}{\mathrm{kpc}}\right)\times 10^{18}\ \mathrm{eV}. \tag{1.6}$$

This energy constraint is represented in the Hillas plot [21] shown in Figure 1.4, in which potential sources are plotted with their characteristic magnetic field B and size R. For UHECR protons, the only possible sources appear to be radio galaxy lobes and galaxy clusters. Exceptions may exist for sources that move relativistically in the host-galaxy frame, most notably AGN and GRB jets. In this situation, the maximal energy may be amplified by a factor of ~ 30 or ~ 1000 due to a Doppler boost.

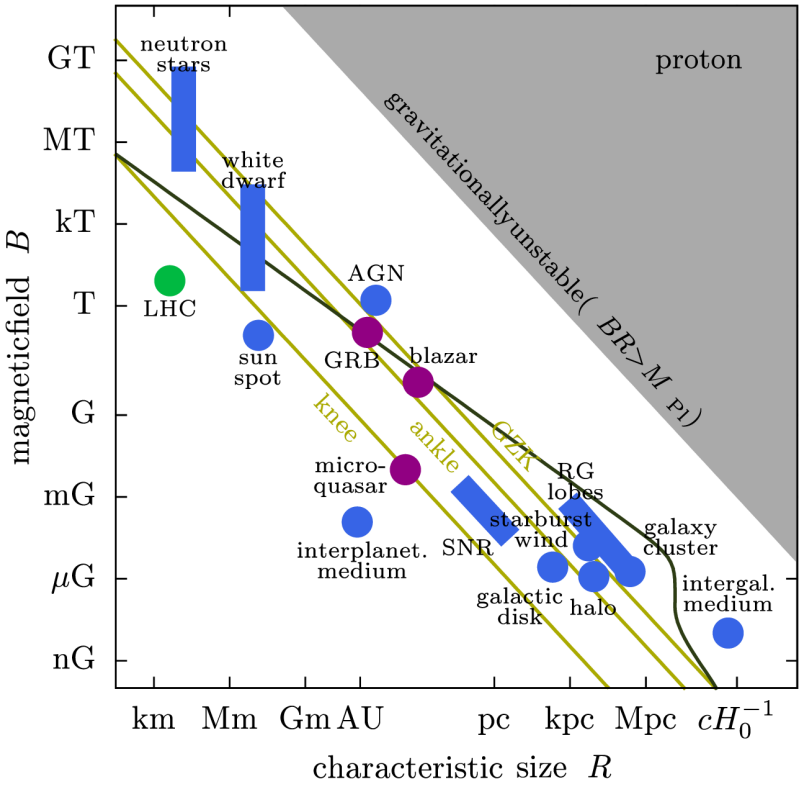

Figure 1.4: The "Hillas plot" for various CR source candidates (blue areas). Also shown are jet-frame parameters for blazars, gamma-ray bursts and microquasars (purple areas). The corresponding point for the Large Hadron Collider (LHC) beam is also shown. The red dashed lines show the lower limit for accelerators of protons at the CR knee $\left(\sim 10^{6.5}\ \text{GeV}\right)$, CR ankle $\left(\sim 10^{9.5}\ \text{GeV}\right)$ and the GZK suppression $\left(\sim 10^{10.6}\ \text{GeV}\right)$. The dotted grey line is the upper limit from synchrotron losses and proton interactions in the cosmic photon background ($R \gg 1$ Mpc). The grey area corresponds to astrophysical environments with extremely large magnetic field energy that would be gravitationally unstable. Adopted from [2].

1.2. GAMMA-RAY ASTRONOMY

Photons are the standard messengers for astrophysical studies, providing insight into physical processes in the Universe. Typically, the term gamma refers to electromagnetic radiation $\gtrsim$ 100 keV, with high energy (HE) gamma rays ranging from a few MeV to $\sim$ 30 GeV and very high energy (VHE) gamma rays ranging beyond $\gtrsim$ 30 GeV. Gamma rays are particularly fascinating since they are closely linked to all of the Universe's messengers: cosmic rays, neutrinos, and gravitational waves. Additionally, they serve as an indirect probe for fundamental physics challenges such as the nature of dark matter and searches for Lorenz invariance violation.

Gamma-ray astronomy provides a unique insight on the non-thermal Universe and enables studying the most extreme processes. Numerous pulsars, pulsar wind nebulae (PWNe), supernova remnants (SNRs), and microquasars have been identified in our galaxy that produce this type of intense radiation. Outside of the Milky Way, gamma rays have been observed in galaxies with a high rate of star formation and in ultra-relativistic jets of particles escaping from supermassive black holes (SMBHs) in the centers of some galaxies. Furthermore, the gamma-ray sky is populated by extremely energetic transient outbursts known as GRBs. Lastly, gamma-ray emission is observed not just from point-line sources but also from diffuse regions within and beyond our galaxy. Indeed, the Universe is observed not only through the various electromagnetic spectrum windows, but also by other cosmic messengers, such as cosmic rays, neutrinos, and gravitational waves (GWs). Gamma rays, in general, make ideal companions for multi-messenger astronomy.

The study of CRs above 1 PeV is extremely difficult for a variety of reasons: on one hand, their flux decreases with increasing energies, making direct observations with space-based instruments impossible; on the other hand, CRs suffer magnetic deflection as they traverse the Galactic and/or intergalactic medium as depicted in Figure 1.5. Gamma rays, on the other hand, point to their sources and are virtually transparent to them up to about 100 GeV. Gamma rays can thus be utilized as probes to identify the locations of CR acceleration.

Various source populations have been explored as potential CR accelerators in order

For this section [26] was used as main references.

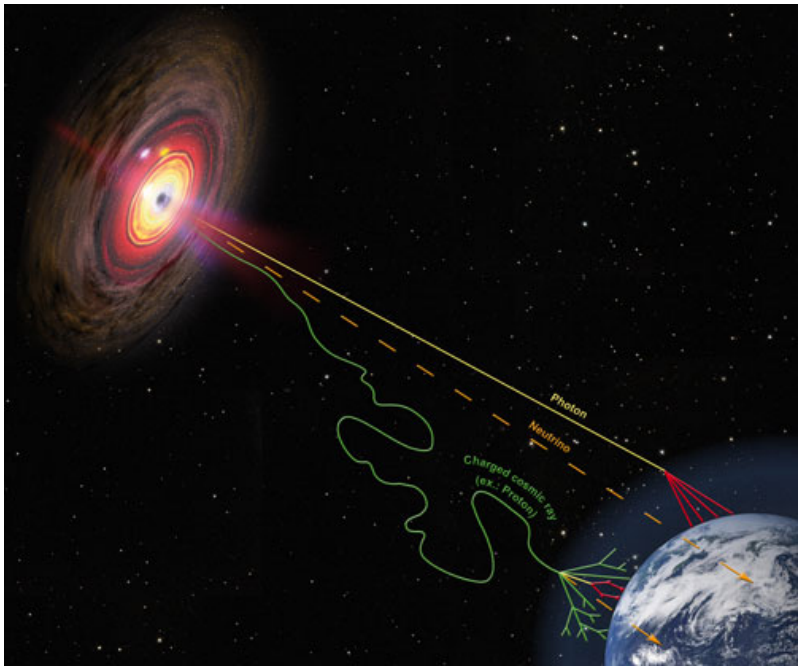

Figure 1.5: Image depicts path of photon, neutrino and charged nucleus (proton) through space. The path of proton is deflected due to interstellar magnetic fields.
Credit: Helmholtz Alliance for Astroparticle Physics/Astrid Chantelauze.

to determine the relationship between gamma rays and charged particles. Gamma-ray emission from pulsars and PWNe is believed to arise from CR electrons in our galaxy. As a result, leptonic models typically account for the measured spectrum. SNRs, on the other hand, have been assumed to be accelerators of CR ions since the theory proposed by Baade and Zwicky in 1934 [27]. These populations have the potential to accelerate CRs to PeV energies, making them candidate "PeVatrons." This theory is justified in two ways. On the one hand, SNRs are natural environments in which powerful shocks form and they can have the required energies to produce the energy density of CRs. Additionally, the SNR environment provides targets for CR interaction, such as molecular clouds and photon fields. As a general statement, there is no doubt that SNR accelerate (parts of the) Galactic CR. The open questions are which type of SNR accelerate particles and whether the maximum energy of these accelerated particles can exceed $\sim$ 1 PeV. The answers to these questions should shed light on the nature, energy, and composition of the knee CR spectrum.

H.E.S.S. presented a study of the Galactic Center [28] where the gamma-ray emission

has been found to be compatible with a stable source accelerating CRs to PeV energies within the Galaxy's core 10 pc region. The SMBH Sgr A* may be connected to this hypothetical PeVatron.

Gamma rays can be produced by the radiation from charged particles in a magnetic field in the bottom-up scenario (i.e. CRs accelerated by astrophysical sources). Neutrinos are neither absorbed nor radiated along their transit from the source to the observer, but still the extreme difficulty of detection is present. Identifying neutrino sources and their link with their gamma ray counterparts provides valuable insights into the long-standing puzzle of the CR formation.

Finally, the study of gamma rays can address a variety of fundamental physics questions, including the violation of Lorentz invariance and the existence of exotic particles and objects such as axion-like particles [29] and primordial black holes [30]. Furthermore, it may shed light on the matter-antimatter discrepancy and, not least, on properties of Dark Matter (DM) particles.

1.2.1. Production of gamma rays

The spectrum of photons is typically expressed in terms of the energy flux F_ν in erg (or eV) per unit area per unit time per unit frequency ν (in Hz). Properties of a spectrum can be determined by its spectral index. Another essential quantity is the spectral energy distribution (SED): νF_ν in erg cm^{-2} s^{-1}, which can also be written as:

$$\nu F_\nu = E^2 \frac{dN}{dE}, \tag{1.7}$$

where E is the energy and dN/dE is the differential energy spectrum.

The major hypotheses on the origin of astrophysical gamma rays can be classified into two categories:

- bottom-up models: according to this scenario, gamma rays are produced due to the acceleration of charged particles from astrophysical sources;
- top-down models: in this case, the observed radiation is the decay product of exotic particles.

1.2.2. Bottom-up scenario

It is essential to understand the electromagnetic emission at the source in order to comprehend the observed gamma-rays and their connection to other cosmic messengers. Due to the fact that photons cannot be accelerated directly, a population of charged particles in a specific environment is typically used as a starting point. Thus, observations of gamma rays are connected to problems about the astrophysical sources of cosmic rays. According to the current theories the latter are accelerated via the first-order Fermi mechanism, which involves a shockwave traveling at relativistic speeds [31]. The maximum energy to which a particle can be accelerated, $E_{CR,\max}$, and is defined as:

$$E_{CR,\max} \propto Z\beta \left(\frac{B}{1\mu\mathrm{G}}\right)\left(\frac{L}{1\mathrm{pc}}\right)\mathrm{PeV}, \tag{1.8}$$

where Z is the charge of the particle, L is the size of the accelerating region, B the magnetic field permeating it, and β is the speed of the shock in unit of light speed [32]. According to this simplified relationship (simplified since it ignores radiative losses), there are astrophysical objects with the appropriate size and magnetic field combination. Thus, the latter are capable of accelerating particles to ultra-high energy, above $\sim 10^{18}$ eV (1 EeV).

If the parent population generating gamma rays is composed of leptons or hadrons, we speak about leptonic or hadronic emission. In particular, the flux of gamma rays of leptonic origin is traced by the electron density and by the radiation fields; the flux of gamma rays of hadronic origin depends on the CR density and the target gas density.

1.2.2.1 Leptonic emission

Gamma rays are emitted from a population of e^-/e^+ when the astrophysical environment is permeated by a magnetic field and/or the population of leptons is relativistic. Leptonic emission is considered to originate from both galactic (e.g. pulsars) and extragalactic sources. Synchrotron photons are produced when relativistic particles are propagated in a magnetic field. The power loss of a charged particle with mass M and charge Ze in the presence of an intense magnetic field B can be described [26] as follows:

$$-\frac{dE_{CR}}{dt} \simeq 2.6 \frac{\text{keV}}{\text{s}} \left(\frac{Zm_e}{M}\right)^4 \left(\frac{E_{CR}}{1\ \text{keV}}\right)^2 \left(\frac{B}{1\ \mu\text{G}}\right)^2. \tag{1.9}$$

It is evident from this equation that this type of process is more critical for electrons than for protons. As a result, the synchrotron is frequently credited with the acceleration of leptons. Given an isotropic distribution of energy E_e and the angle of velocity with respect to the magnetic field, the synchrotron photons will have an energy [33]:

$$E_{sync} = 0.2 \frac{B}{10\ \mu\text{G}} \left(\frac{E_e}{1\ \text{TeV}}\right)^2 \text{eV}. \tag{1.10}$$

Thus, assuming normal magnetic fields of 10 μG and an TeV energy electron population, synchrotron photons will have an energy of roughly 0.2 eV (i.e. visible light). This mechanism is also crucial for the emission of gamma rays.

The Inverse Compton (IC) scattering is another mechanism using photons and relativistic electrons. In this scenario, electrons scatter low-energy photons, gaining energy at the expense of the electrons' kinetic energy. This process can occur in two different extreme regimes, depending on the photon's energy (E_γ):

- the Thomson regime: $E_\gamma \ll m_e c^2$
- the Klein-Nishina regime: $E_\gamma \gg m_e c^2$.

Both synchrotron and IC can occur in astrophysical sources, such as AGN or in the region of SNRs. In particular, electrons with a Lorenz factor of $\gamma_e \sim 10^4 - 10^5$ are accelerated in a magnetic field and radiate photons up to the infrared/X-ray range. These photons then interact with their parent electron population via Compton scattering; because electrons are ultra-relativistic, the photon energy can be amplified significantly. This is referred to as Synchrotron Self Compton (SSC).

Given a population of electrons with a spectral index of α and a blackbody population of photons with a temperature of T and an energy of ε, the mean energy of gamma rays and the accompanying energy distribution can be determined as:

$$\begin{aligned} E_\gamma &\simeq \tfrac{4}{3}\gamma_e^2\langle\varepsilon\rangle && \text{(Thomson regime)} \\ E_\gamma &\simeq \tfrac{1}{2}\langle E_e\rangle && \text{(Klein-Nishina regime)} \\ \tfrac{dN_\gamma}{dE_\gamma} &\propto E_\gamma^{-\frac{\alpha+1}{2}} && \text{(Thomson regime)} \\ \tfrac{dN_\gamma}{dE_\gamma} &\propto E_\gamma^{-(\alpha+1)}\ln E_\gamma && \text{(Klein-Nishina regime)} \end{aligned} \tag{1.11}$$

A helpful expression for the relationship between the electron and photon energies is [30]:

$$E_\gamma \simeq 6.5\left(\frac{E_e}{1\ \text{TeV}}\right)^2\left(\frac{\varepsilon}{\text{meV}}\right)\text{GeV}. \tag{1.12}$$

The Compton component usually peaks at GeV − TeV energies.

1.2.2.2 Hadronic emission

Gamma rays can be the product of the interaction between accelerated protons (and/or heavier nuclei) and the astrophysical environment. In general, a hadron can collide with a target of nucleons (for example, a molecular cloud), initiating a hadronic cascade. Almost the same number of π^+, π^-, π^0 are produced, due to isospin simmetry. Given to the short lifetime, π^0 immediately decay into two gamma rays, having approximately half the energy of π^0. This is referred to as hadron-nucleon collision, or simply $p-p$ interaction in the simple case of a collision between protons. Gamma rays can originate also from the interaction between protons and a sea of photons, coming for example from synchrotron radiation or from bremsstrahlung of accelerated electrons. This kind of interaction is called photoproduction. It has a small cross section (fraction of mb) and it is therefore important in environments where the target photon density is much higher than the matter density. In particular, photoproduction occurs mainly via the Δ^+ resonance:

$$\begin{aligned} p+\gamma &\to \Delta^+ \to \pi^+ + n \\ p+\gamma &\to \Delta^+ \to \pi^0 + p \end{aligned} \tag{1.13}$$

Due to isospin balance, the cross sections of these two processes at the *Delta* resonance are roughly 1 : 2. Once again, a π^0 decays into two photons. Their energy is proportional to the average momentum fraction carried by secondary pions relative to

the primary particle and the average energy fraction carried by the photon. The relation $E_\gamma \sim E_p/10$ is approximately valid [30].

A feature of hadronic production of gamma rays is a peak in the spectral energy distribution at $\simeq m_\pi c^2/2 \simeq 67.5$ MeV that can be attributed to a component of π^0 decay. This feature, which is almost completely independent of the energy distribution of π^0 mesons and therefore of the parent protons, is referred to as the "pion bump." Both photons have the same energy and opposite momentum in the neutral pion's rest frame, $E_\gamma \simeq 67.5$ MeV. Once boosted for the emitting π^0 energy E, the probability of emitting a photon with energy E_γ is constant over the range of kinematically permitted energies (the range between $E(1-v/c)/2$ and $E(1+v/c)/2$). The spectrum of gamma rays for an arbitrary distribution of neutral pions is thus a superposition of rectangles for which only one point at $m_\pi c^2/2$ is always present. This should result in a spectral maximum that is independent of the parent pions' energy distribution. The "pion bump" is assumed to be a spectral feature of active hadronic processes.

It's worth noting that hadron generated gamma rays are always accompanied by neutrinos. If the π^0 instantly decays into two gamma rays, the charged pions decay into $\pi^+ \to \mu^+ + \nu_\mu$ and $\pi^- \to \mu^- + \bar{\nu}_\mu$, while muons decay into $\mu^+ \to e^+ + \nu_e + \bar{\nu}_\mu$ and $\mu^- \to e^- + \bar{\nu}_e + \nu_\mu$. At emission, an approximate relation exists between the spectral production rates of neutrinos and gamma rays [30]:

$$E_\nu^2 \frac{dN_\nu(E_\nu)}{dE_\nu} \sim \frac{3K}{4} E_\gamma^2 \frac{dN_\gamma(E_\gamma)}{dE_\gamma}, \tag{1.14}$$

for photo-hadronic (or hadronuclear) processes with $K = 1/2$ (or $= 2$). Gamma rays may escape or cascade further depending on the optical depth of the source, distorting the temporal and energy correlation between neutrinos and their electromagnetic counterparts. Simultaneous discovery of gamma rays and neutrinos, on the other hand, would be a significant indicator of hadro-production, and thus of CR acceleration. So far a correlation has been observed, but still not above 3σ level [34].

1.2.3. Top-down scenario: dark matter

Gamma rays could be produced by exotic particles, specifically by their decay or annihilation, in a top-down scenario. Gamma rays, in particular, are thought to originate from DM. The weakly interacting massive particles (WIMPs), with masses and coupling strengths on the electroweak scale, are one of the most prominent DM candidates. The predicted flux of gamma rays produced by annihilation can be represented as follows:

$$\phi_\gamma = \frac{1}{4\pi} \underbrace{\frac{\langle \sigma_{ann} v \rangle}{2m_{DM}^2} \frac{dN_\gamma}{dE}}_{\text{Particle Physics}} \underbrace{\int_{\Delta\Omega - l.o.s} dl(\Omega) \rho_{DM}^2}_{\text{Astrophysics}} , \tag{1.15}$$

where the first factor is determined by the DM's particle physics properties: $\langle \sigma_{ann} v \rangle$ is the velocity-weighted annihilation cross section (also known as annihilation rate) of DM particles with mass m_{DM} and dN_γ/dE is the gamma-ray spectrum per annihilation event. The second factor is the integral of the squared DM density along the line of sight, and hence is related to its astrophysical distribution. It is referred to as the boost factor. Gamma rays produced by DM may also have distinct spectral characteristics, such as $\gamma\gamma$ or $Z\gamma$ annihilation lines, with energies directly linked to the WIMP mass. Due to the electrical neutrality of WIMPs, these activities are loop suppressed and so should be unlikely. Thus, it is assumed that WIMP-induced gamma rays will be dominated by a generally featureless continuum of by-products of cascades and decays (mainly from π^0) following quark or lepton annihilation.

As shown in Equation 1.15, the flux of produced gamma rays is quadratically related to the DM density along the observer's line of sight. This encourages searches for targets with expected increases in DM density. Among these targets are the Galactic center (GC), galaxy clusters, and nearby dwarf spheroidal galaxies

1.2.4. Gamma-ray propagation

Gamma rays propagate through intergalactic/galactic space after they are created. Although magnetic fields do not deflect them, they can interact with photon fields. The highest photon background density corresponds to the Cosmic Microwave Background (CMB), which has an average energy of ~ 0.6 meV and a photon density of ~ 410

photons/cm^3. This is the electromagnetic energy that persists after the Big Bang. The Extragalactic Background Light (EBL) is another photon background. This radiation was mostly radiated during star formation; its spectrum contains a peak at around 8 meV (far infrared) and another at approximately 1 eV (near infrared).

The primary mechanism of gamma ray absorption is pair creation:

$$\gamma + \gamma_{\text{background}} \rightarrow e^+ + e^-. \tag{1.16}$$

Given ε, the energy of the target (background) photon, the process is kinematically permitted for:

$$\varepsilon > \varepsilon_{\text{thr}}(E, \varphi) \equiv \frac{2m_e^2 c^4}{E(1-\cos\varphi)}, \tag{1.17}$$

where φ denotes the scattering angle, m_e is the electron mass, E is the energy of the incident photon. The corresponding cross section [35] is:

$$\sigma_{\gamma\gamma}(E, \varepsilon, \varphi) \simeq 1.25 \cdot 10^{-25} W(\beta) \text{cm}^2, \tag{1.18}$$

where $W(\beta)$ depends on electron speed β:

$$W(\beta) = \left(1-\beta^2\right)\left[2\beta\left(\beta^2-2\right) + \left(3-\beta^4\right)\ln\left(\frac{1+\beta}{1-\beta}\right)\right]. \tag{1.19}$$

According to [35] , for an isotropic background of photons, the cross section is maximized for:

$$\varepsilon(E) \simeq \left(\frac{900 \text{ GeV}}{E}\right) \text{eV}. \tag{1.20}$$

This means that the EBL plays the leading role in the absorption for gamma rays of energies 10 GeV $\leq E < 10^5$ GeV. For 10^5 GeV $\leq E < 10^{10}$ GeV the interaction with the CMB becomes dominant. At energies $E \geq 10^{10}$ GeV the main source of opacity of the Universe is the radio background [36].

The interaction with photon backgrounds causes a horizon beyond at which gamma rays are strongly absorbed. This horizon gets closer as the energy increases. At PeV energies, the horizon is close to the distance of our own Galactic Center.

1.2.5. Gamma-ray detectors

Quantity	*Fermi*-LAT	IACTs	Particle detector arrays
Energy range	20 MeV – 200 GeV	100 GeV – 50 TeV	400 GeV – 100 TeV
Energy res.	5 – 10%	15 – 20%	$\sim 50\%$
Duty cycle	80%	15%	$> 90\%$
FoV	$4\pi/5$	5deg $\times$ 5deg	$4\pi/6$
PSF (deg)	0.1	0.07	0.5
Sensitivity	1% Crab (1 GeV)	1% Crab (0.5 TeV)	0.5 Crab (5 TeV)

Table 1.1: A comparison of the *Fermi*-LAT, IACT, and EAS particle detector arrays' properties. Sensitivity values calculated over a one year for *Fermi*-LAT and the particle detector arrays, and over a 50 hour for the IACTs. Adopted from [26]

There are two main types of gamma-ray instruments: space-based detectors and ground-based detectors. The spectrum of gamma rays spans over seven decades in energy and around 14 in flux. Thus, the higher the energy, the larger the effective area should be which is defined as the product of the geometrical area and the detector efficiency. However, because to the large price of space technology, the geometrical area cannot surpass ~ 1 m^2. This property makes space-based detectors more suitable for studying gamma rays in the MeV-mid-GeV energy range. At higher energies, larger detection areas are required, which can be placed mainly on the ground, taking advantage of the fact that, at energies greater than 30 GeV, electromagnetic air showers become measurable (whereas if the energy is too low, the shower cannot be detected). When a gamma ray reaches the atmosphere, it produces a cascade of secondary particles: the photon converts to pairs of e^+e^- at high altitude, and each high-energy $e^\pm$ radiates secondary gamma rays primarily via bremsstrahlung, which then convert to lower-energy e^+e^- pairs.

The main properties of the current detectors are shown in Table 1.1. Figure 1.6 shows the sensitivity for past, current and future gamma-ray detectors.

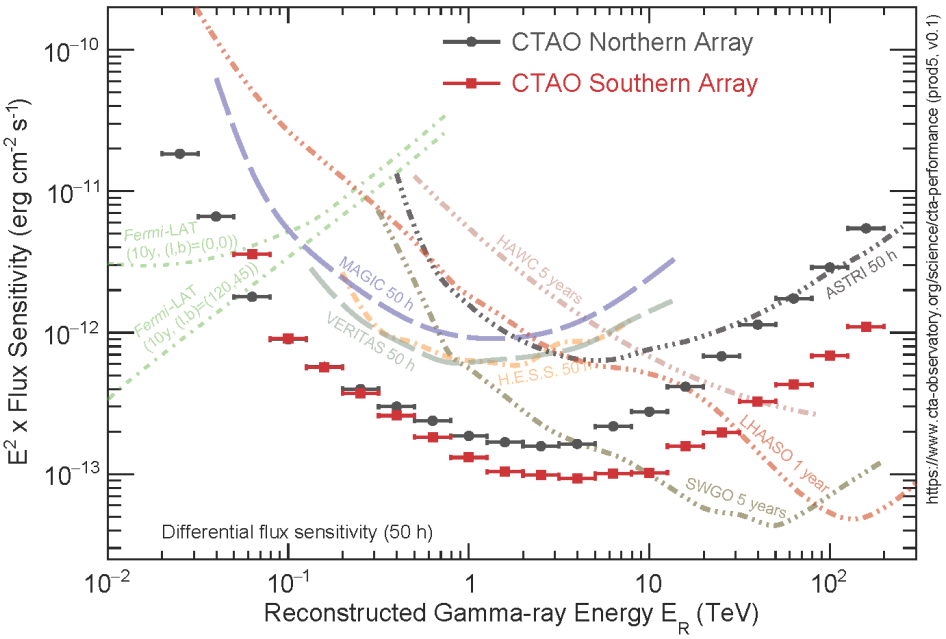

Figure 1.6: The differential sensitivity shown is defined as the minimum flux needed to obtain a 5-standard-deviation detection of a point-like source, calculated in non-overlapping logarithmic energy bins (five per decade). Besides the significant detection, at least ten detected gamma rays per energy bin are required, and a signal/background ratio of at least 1/20. The curves shown allow only a rough comparison of the sensitivity of the different instruments, as the method of calculation and the criteria applied are not identical. In particular, the definition of the differential sensitivity for HAWC is rather different due to the lack of an accurate energy reconstruction for individual photons in the HAWC analysis. Adopted from [37]

1.2.6. Space-based detectors

Space-based telescopes can detect gamma ray sources between ~ 300 keV and ~ 300 GeV, depending on their flux. In comparison to soft X-ray astronomy, space-based gamma-ray astronomy has additional difficulties. One of these is that gamma rays with energies more than a few MeV cannot be focused and must be detected via their interaction products. As a result, two sub-detectors are required to determine the direction and energy of incoming gamma rays: a tracker and a calorimeter. Additionally, an anti-coincidence detector (ACD) is critical for eliminating background noise caused by CRs.

Compton scattering and pair production are the two processes by which cosmic photons can interact in the detector, with the transition energy being roughly $E_\gamma \sim 10 - 20\,\text{MeV}$. Thus, the tracker is composed of some active material that detects interaction products and, if necessary, some passive material that increases the probability of interaction. The effective area is proportional to the amount of material. Below $\sim 10\,\text{GeV}$, the angular resolution is limited by multiple scattering, which rises with the converter's mass. Thus, a trade-off must be made between increasing the effective area and sacrificing angular resolution. In general, the effective area of these detectors cannot exceed $\sim 1\ \text{m}^2$, due to the high cost of launch and the stringent specifications for the equipment that must be sent into space.

In 2008, the *Fermi*-LAT gamma-ray telescope was launched. It is currently operational and is the world's largest gamma-ray space-based detector to date. *Fermi*-LAT [38] is composed of a spacecraft and two instruments: the Large Area Telescope (LAT) and the Fermi Gamma Burst Monitor (GBM). The LAT has an energy range of approximately 20 MeV to approximately 300 GeV and higher. The GBM supplements LAT observations of transient sources.

1.2.7. Ground-based detectors

One of the major distinctions between space- and ground-based detectors is that the latter can observe gamma rays at very high energies, between GeV and TeV. Above a certain energy level, $\gtrsim$ GeV, a gamma ray entering the atmosphere generates a detectable electromagnetic cascade:

- Either by detecting the Cherenkov radiation emitted by charged particles in the air (Cherenkov technique). The majority of secondary charged particles travel faster than the speed of light in air and hence emit Cherenkov radiation, which can be observed with specialized telescopes. The effective detection area is comparable to that of a light pool reaching the ground, i.e. a few $10^4\ \text{m}^2$.

- Or by directly detecting the charged particles reaching ground (EAS technique).

1.2.7.1 Imaging Air Cherenkov Telescopes

CR induced Cherenkov light emission in the atmosphere was detected for the first time in 1952 by W. Galbraith and J.V. Jelley [39].
In 1985 the Hillas parameters methodology, proposed by A.M. Hillas [40], significantly enhanced Imaging Atmoshpheric Cherenkov Telescope (IACT) background rejection. This method uses the events camera image intensity and area to provide an estimate of the shower's energy, while the orientation of the image corresponds to the shower's direction. The shape of the image is used to determine the type of the event and thus used to reduce the background. This was critical in achieving the first confirmed localization of a gamma ray emitter when the Whipple collaboration detected the Crab Nebula above 0.7 TeV in 1989 [41].

A primary photon of 100 GeV will cause approximately ten Cherenkov photons per square meter to arrive at heights of around 2000 m above sea level (a.s.l.). A 100 m^2 collection area is therefore sufficient to detect gamma ray showers. Due to the dim nature of the Cherenkov light, observations require clear and dark nights. As a result, these instruments have a relatively low duty cycle of roughly 15%. Additionally, they have a limited field of view ($\lesssim 5^\circ$), but high sensitivity and a low energy threshold.

HEGRA [42] on the Canary Islands and CANGAROO [43] in Australia were the second generation of IACTs. The current generation of instruments is mostly composed by H.E.S.S. in Namibia [44], MAGIC [45] and FACT [46] in the Canary Islands and VERITAS in Arizona [47]. The next generation of telescopes has already started with the observations, namely Large Size Telescope (LST) [48] as a part of upcoming Cherenkov Telescope Array (CTA) [49].

1.2.7.2 Particle Detector Arrays

This technique tracks the arrival of secondary particles reaching ground from gamma-ray-induced air showers. Particle detector array detectors feature a high duty cycle and a big field of view, but their sensitivity is rather low. The energy threshold is quite high - a shower initiated by a 1 TeV photon typically reaches its maximum at roughly 8 km above sea level. The technique of operation is same to that employed to identify CRs

with energies greater than 1 PeV. The density of secondary particles and their arrival timings enable reconstruction of the shower geometry. The gamma-hadron discrimination is possible via the geometry and also the muon content of the showers.

HAWC (High Altitude Water Cherenkov) detector is one of the currently operational [50] particle detector arrays. It consists of a network of 300 water Cherenkov detectors that spans an area of approximately 22000 m^2. Each detector is comprised of a tank with a diameter of 7.3 m and a depth of 4.5 m, filled with purified water and housing three photomultiplier tubes (PMTs) with a diameter of 20 cm. Photons passing through water create electrons and positrons, resulting in the emission of Cherenkov light. The HAWC observatory is located in Mexico at an elevation of 4100 m above sea level and the array constructions was finished in 2015. HAWC monitors a $2/3$ of the sky with an instantaneous field of view of ~ 2 sr and a duty cycle of 90%.

Another notable detector array is LHASSO which consists of three sub-arrays: the Square Kilometre Array (KM2A), the Water Cherenkov Detector Array (WCDA), and the Wide-Field Air Cherenkov Telescope Array (WFCTA). KM2A contains 5195 electromagnetic particle detectors and 1188 muon detectors, covering an area of 1.3 km^2. The electromagnetic particle detectors detect the electromagnetic particles in the shower, which are used to reconstruct the primary direction, core location and energy. The muon detectors are used to detect the muon component of showers, which is used to discriminate between gamma-ray and hadron induced showers. Half of the KM2A array including 2365 electromagnetic particle detectors and 578 muon detectors has been put into operation since December 2019.

2. GROUND BASED VERY-HIGH-ENERGY GAMMA-RAY DETECTORS

2.1. INTRODUCTION

Although the first attempts to detect Cherenkov light from charged particles passing through the atmosphere date all the way back to 1953 [39], it took several decades for ground-based very high-energy gamma-ray astronomy to develop. Prior to attempting to differentiate gamma rays from charged cosmic rays, the primary hurdle to overcome at the time was just detecting a Cherenkov signal. The detection challenges were caused by the flashes' extremely short duration, the signal's low strength, and the very large background coming from the night sky (light from stars and scattered light, which required the use of sensitive detectors and fast electronics).

The Whipple collaboration detected the first source of VHE gamma rays in 1989 [41]. This breakthrough discovery opened up a new era in gamma-ray astronomy and sparked a thriving study field in an energy range that is largely accessible only to ground-based detectors.

Around 240 VHE γ-ray sources have been detected up to now [51, 52] with the sky locations shown in Figure 2.1. These include a variety of source classes (pulsars and their associated nebulae, supernova remnants, and active galactic nuclei, to mention a few), and most of them were detected using IACTs.

Due to the fact that Earth's atmosphere is opaque to high-energy photons, the most direct method of studying the gamma-ray sky is to launch detectors into space. How-

For this chapter [53, 54] were used as main references.

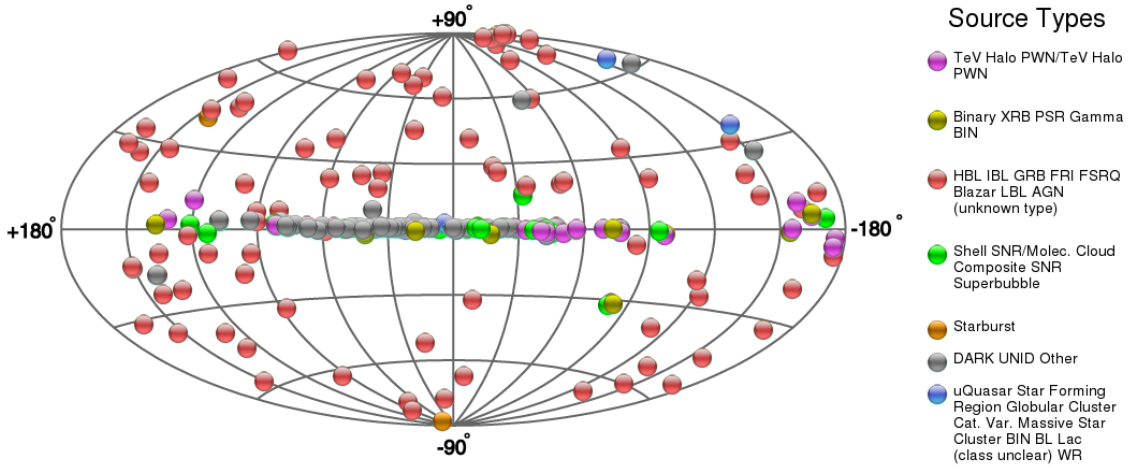

Figure 2.1: The locations, in Galactic coordinates, of all known astrophysical sources of TeV gamma-ray emission as of 2021. Adopted from [52].

ever, most astrophysical gamma-ray emission processes yield steeply dropping power-law spectra, resulting in extremely low photon flux at high energies.

For example, the Crab Nebula - one of the brightest astrophysical gamma-ray sources - yields a flux of ~ 6 photons m^{-2} year^{-1} at energies greater than 1 TeV. For studying the physical processes at these energies, a detector with a huge collection area is required, much exceeding the feasible maximum size of a satellite-borne instrument (which is ~ 1 m^2). IACTs accomplish this by detecting the Cherenkov light produced in the atmosphere by gamma-ray induced particle cascades (or air showers). Thus, by using the Earth's atmosphere as an intrisic part of the detection technique, effective collection areas can easily exceed 10^5 m^2.

Jelley and Galbraith originally examined the possibility of this approach for gamma-ray astronomy in 1950 [55], but attempts to use it were impeded by the strong background of charged cosmic rays. The first significant discovery of an astronomical TeV gamma-ray source did not occur until 1989, when the Crab Nebula was detected using the Whipple 10-meter telescope [41]. This achievement was made possible by the development of efficient ways for capturing an image of the Cherenkov emission produced by air showers.

The major IACT facilities currently operating are MAGIC (Figure 2.2), H.E.S.S., VERITAS, FACT and LST-1 (part of CTA).

Figure 2.2: In this picture MAGIC I and II can be seen, together with the Counting House. Credit: Alicia Lopez-Oramas.

2.2. ATMOSPHERIC SHOWERS

2.2.1. Shower development

When a high-energy particle (such as a gamma ray or nucleus) reaches the atmosphere, it can interact with the atmospheric nuclei in a variety of ways, resulting in the formation of a extended air shower of particles. Electromagnetic showers are primarily governed by two primary processes:

- e^+e^- pair production by conversion of high energy photons in the Coulomb field of the nuclei;
- e^+e^- Bremsstrahlung emission in the same Coulomb field, leading the production of further high-energy photons.

As the shower develops in the atmosphere, the incoming particle's energy is redistributed over a large number of secondary particles. Pair production and bremsstrahlung emission have approximately the same characteristic length (X_0), referred to as the "electromagnetic radiation length."

The radiation length in the atmosphere is ≈ 36.7 g cm^{-2}, which is $7/9$ of the mean free path for pair production. This relationship enables a straightforward analytical approximation for the shower development (first established by Heitler [56]), in which the total number of electrons, positrons, and photons doubles every $\ln(2)X_0$. The original gamma-ray energy, E_0, is equally distributed throughout the secondary products. The shower continues to form until the average electron energy reaches $E_c = 84$ MeV, the critical energy below which ionization losses dominate. The cascade's maximum number of particles is given by E_0/E_c. The Heitler shower model scheme is depicted in Figure 2.3.

The atmosphere is a very inhomogeneous calorimeter due to its changing density. At sea level, one radiation length amounts to ~ 300 m for an atmospheric density of ~ 1.2 kg m^{-3}. At an altitude of 10 km (about the height of the showers' maximum development), the radiation length corresponds to a threefold increase in distance (~ 1 km). This has a significant effect: as a shower penetrates deeper into the atmosphere, it develops more rapidly because of the increased abundance of target matter. In a homogeneous

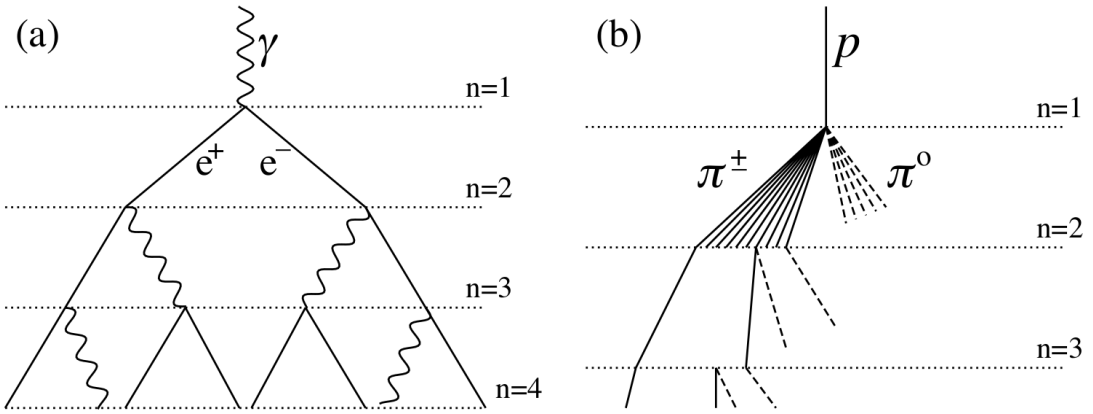

Figure 2.3: Schematic views of (a) an electromagnetic cascade and (b) a hadronic shower. In the hadron shower, dashed lines indicate neutral pions, which do not re-interact, but quickly decay, yielding electromagnetic subshowers (not shown). Not all pion lines are shown after the n = 2 level. Neither diagram is to scale. Adopted from [57].

calorimeter, the depth of the shower maximum is logarithimically proportional to the originating particle's energy. In the atmosphere, the evolution of the shower maximum's altitude is significantly slower.

Additional mechanisms, primarily at low energies, contribute significantly to the shower's development:

- charged particle multiple scattering, resulting in shower broadening;
- e^+e^- energy losses due to ionization and atomic excitation result in the shower fast extinction when the energy of the charged particles in the shower falls below the "critical energy" ($E_c = 83$ MeV in the air);
- electron scattering and positron annihilation result in an excess of electrons relative to positrons of $\sim 10\%$ ("charge excess"), which might result in a strong radio emission signal ("Askaryan effect");
- the Earth's magnetic field, which broadens the shower in the East-West direction.

Photo- or electro-production of hadrons can produce a hadronic component in electromagnetic showers at very high energies. The associated cross-sections, on the other hand, are almost a factor of 10^{-3} less than those for pair production.

Cosmic rays - charged, relativistic protons and nuclei - also generate atmospheric air showers. In this scenario, the cascade development is more complicated, with hadronic interactions occurring via a number of channels, resulting in the formation of secondary nucleons as well as charged and neutral pions with substantial transverse moments. The pions do not survive to sea level: neutral pions decay quickly into two gamma-rays, whereas charged pions generate muons and neutrinos:

$$\begin{aligned} \pi^{o} &\longrightarrow \gamma + \gamma \\ \pi^{+} &\longrightarrow \mu^{+} + \nu_{\mu} \\ \pi^{-} &\longrightarrow \mu^{-} + \bar{\nu}_{\mu} \end{aligned} \tag{2.1}$$

The gamma-ray secondaries generated in this way can create electromagnetic sub-showers, while the long-lived muons form the cascade's most penetrating component, usually reaching the ground.

Hadronic showers are more difficult to characterize since they are dependent on a variety of different characteristic lengths (nuclear interaction length, decay lengths for unstable particles, and radiation length), making universal scaling unfeasible. They are made up of various components:

- hadronic components: nuclear fragments resulting from collision with atmospheric nuclei, isolated nucleons, π and K mesons, etc.
- an electromagnetic component resulting in particular from the decay of neutral pions into γ rays,
- high-energy muons resulting from the decay of charged mesons ($\pi^{\pm}$ and $K^{\pm}$ mainly),
- atmospheric neutrinos resulting from the decay of mesons and muons ($\pi^{\pm}, K^{\pm}$, and $\mu^{\pm}$).

As a result, cosmic ray induced air showers develop far less regularly than gamma-ray induced cascades, as shown in Figure 2.4. These variations in shower shape, together with the reconstruction of the incoming primary's arrival direction, enable IACTs to discriminate efficiently between gamma-ray photons and the generally overpowering isotropic cosmic ray background.

2.2.2. Cherenkov radiation

In air showers, relativistic charged particles travel faster than the speed of light($v > c/n_{air}$, where n_{air} is the refractive index) and so generate Cherenkov radiation. Cherenkov light is produced throughout the cascade's development, with the maximum emission being at an altitude of $\sim$ 10 km for primary gamma-ray energies ranging from 100 GeV to 1 TeV. Each particle creates Cherenkov light at a fixed angle to the direction of motion, defined by (θ_C).

$$\cos\theta_C = \frac{c}{v n_{air}}. \tag{2.2}$$

At sea level, the Cherenkov angle is $\sim 1.3^\circ$. Additionally, electromagnetic cascade particles are prone to repeated Coulomb scattering, which spreads their orientations over a limited angular range and contributes $\sim$ 100 photons m^{-2} for a 1 TeV gamma-ray primary and a radial extent of $\sim$ 130 m.

The yield of Cherenkov photons is proportional to $1/\lambda^2$ (where λ is the wavelength). As a result, the spectrum is dominated by blue/UV emission, with a peak about 340 nm. The emission of shorter wavelengths is absorbed by the atmosphere (especially ozone), and hence does not reach the ground unless it is created extremely deep in the atmosphere (for example by penetrating muons). Each shower produces a short pulse of Cherenkov radiation lasting a few nanoseconds. While the total photon emission from all air showers is just $\sim 1/10000$ of the visible background night sky light, the brightness from a single shower can rival the brightest objects in the night sky for the duration of the pulse.

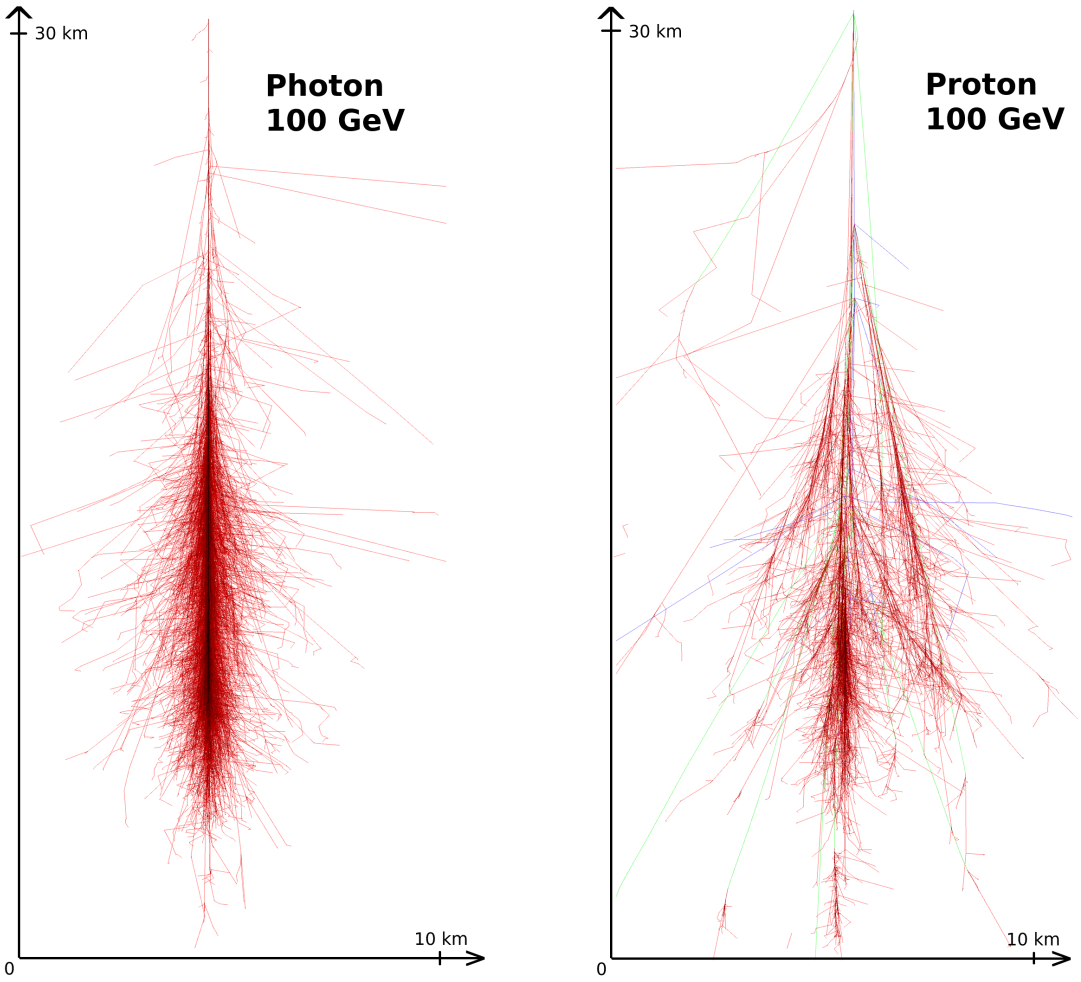

Figure 2.4: Monte Carlo simulations if the tracks of particles in photon and proton initiated air showers made with CORSIKA package. The first interaction height is fixed at 30 km. The vertical axis range is 0 - 30 km and the horizontal axis range is ± 5 km around the shower core. Adopted from [58]

2.3. IMAGING ATMOSPHERIC CHERENKOV TELESCOPE

2.3.1. Principle of operation

Cherenkov detectors are used to observe showers that dissipate before reaching the ground by detecting the Cherenkov light generated in the atmosphere. This approach utilizes the atmosphere as a calorimeter. The most successful way is to acquire an "image" of the showers using optical telescopes by recording the blueish Cherenkov radiation released by them, as illustrated in Figure 2.5. The experimental difficulties derive from the signal's extremely low intensity and short duration (which necessitates extremely rapid and sensitive acquisition methods), and from the massive background, which comes from both the night sky's illumination and the air showers produced by charged cosmic rays.

While detection is quite straightforward, gamma-ray discrimination and reconstruction are considerably more difficult. The stereoscopic imaging technique is by far the most successful strategy, being employed by all of the main facilities in operation today. This is demonstrated in Figure 2.9. The Cherenkov light from air showers is focused onto a camera made of photo-detector pixels using large convex reflectors. The camera captures an image of the shower, and the image's parameters (its shape, intensity, and orientation) allow for the estimation of the shower's primary properties (type of particle, energy and direction). By combining this with an array of telescopes ("stereoscopy"), the same shower can be viewed from a variety of various perspectives, enhancing the geometrical shower reconstruction. A critical component of this technique is a requirement for precise Monte Carlo simulations of both the shower evolution and detector response.

IACTs have a small field of view (a few degrees of angular diameter), a low duty cycle ($\sim 10\%$, corresponding to moonless, clear nights), but a very large effective area (equal to the size of the light-pool illuminated by the showers $\left(\sim 10^5\ \mathrm{m}^2\right)$. The optimal altitude $(\sim 1500\ \mathrm{m})$ for this technique is determined by a trade-off between the atmosphere's transparency to Cherenkov light (which favors higher altitude) and the development of the shower (which results in larger effective areas, improved shower containment, and

enhanced calorimetric capabilities). To perform a calorimetric measurement, the shower must die before it reaches the ground, so that the Cherenkov emission accurately reflects the amount of charged particles in the shower.

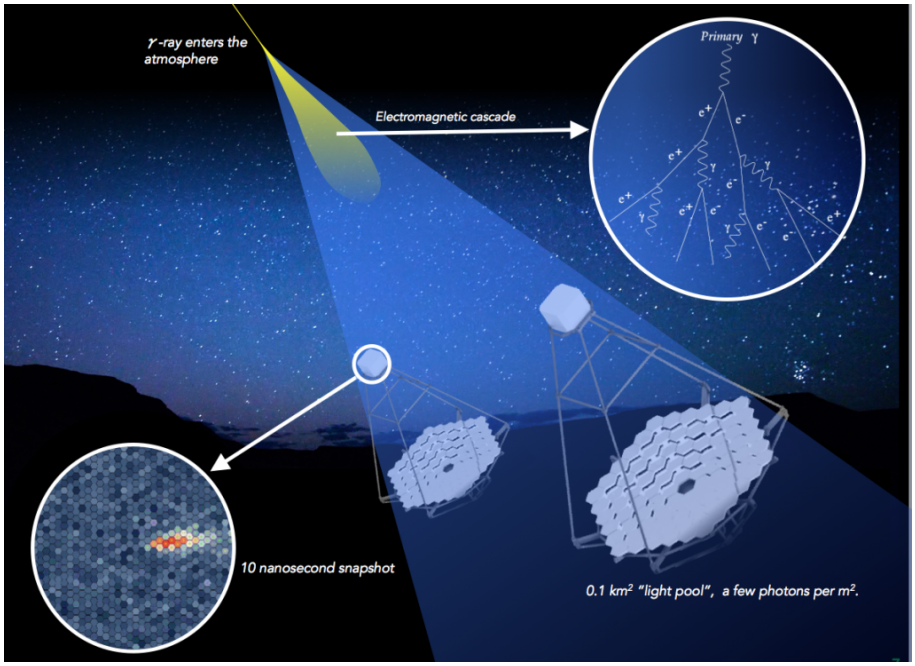

Figure 2.5: Cherenkov light emitted by the charged particles in the shower is collected by the dish of the telescope. Adopted from [59].

2.3.2. Optical systems

The optical design of IACTs is guided by two requirements. The first is for a large aperture and, thus, a large mirror area. This enables the collection of as many Cherenkov photons as possible from each shower, so limiting lowest gamma-ray energy threshold of a telescope. Fortunately, the comparatively primitive cameras of IACTs and the absence of precise structure in the Cherenkov images mean that mirror shape and surface quality are far less critical than they are for optical telescopes. Typically, an optical point-spread function of a few arcminutes is sufficient. This degree of performance is possible due to the use of tessellated reflectors, which are comprised of hundreds of separate mirror facets.

The second criterion is a wide field of view. Cherenkov event images from air showers have an elliptical structure and an angular extent of up to a few degrees. The images are

offset from the shower primary's arrival direction; in the case of gamma-ray initiated showers, this implies that the image is offset from the position of the gamma-ray source in the field of view. The offset angle is related to the shower impact parameter (distance between the shower core projected onto the ground and the telescope) Thus, gamma-rays require a field of vision of a few degrees in diameter. In reality, a number of known sources of gamma-ray emission (most notably supernova remnants and pulsar wind nebulae) have a huge angular extent. Additionally, IACT data analysis often employs a section of the field of view devoid of known gamma-ray sources to infer the background of residual cosmic ray showers. Arrays currently in operation have fields of view of $3^\circ - 5^\circ$, but future instruments will have fields of view of $8^\circ - 10^\circ$.

2.3.3. Telescope structure

Mechanical design of IACTs is additionally difficult due to the extraordinarily large apertures and the requirement to sustain a huge, delicate, and massive camera at the distance of a focal length. Considerations of weight and simplicity have resulted in the adoption of altazimuth mounts for all current IACTs. The rigidity requirements of the optical system and camera support structures have been met in two ways: either by using a steel space frame to construct the telescope superstructure (as was done with the H.E.S.S. and VERITAS telescopes), or by using a lightweight carbon fiber frame coupled with an active mirror adjustment system (as it is done with MAGIC and LST - see Figure 2.6).

Additionally, the telescope must track precisely. Encoders are used to determine the telescope's position (usually optical, with arcsecond resolution). To convert these values to a place on the sky, a software model of the telescope's pointing is utilized that has been calibrated using star observations. Online tracking is aided by CCD pointing monitors, which are attached to the telescope structure and track both star positions and the precise location of the gamma-ray camera. Offline corrections based on these CCD readings enable systematic telescope pointing errors to be reduced to tens of arcseconds.

Additionally, some IACTs are capable of swiftly slewing to new targets. For example, the 40 tonne, 17 m diameter MAGIC telescopes can move within 40 seconds to examine any point in the sky. This necessity stems from the transient aspect of the gamma-ray sky, which contains numerous sources known to flare spectacularly over short timescales.

Figure 2.6: Image of the LST-1 telescope of the upcoming CTA.
Credit: Tomohiro Inada.

2.3.4. Camera

To cover a suitably large field of view with big aperture, single-reflector IACTs have physically large cameras (≥ 1 m). To acquire an image, the photosensitive area are divided into hundreds or thousands of pixels, each sampling $\lesssim 0.1°$. The photodetector pixel of choice for IACTs has been the photomultiplier tube in the majority of detectors. These devices have a reasonable photon detection efficiency of ($\sim 20\%$), nanosecond reaction times, a big detection area, and exceptionally clean signal amplification (factors of ~ 100000), which enables them to resolve single photon signals easily. By arranging closely packed light-concentrating Winston cones on the camera front, dead space between the photosensitive regions of individual pixels is minimized. While the size of IACTs prevents the construction of domes around the entire telescope, the expensive and sensitive PMT cameras are kept in light-tight boxes that permit testing and calibration throughout the day.

2.3.5. Trigger and data acquisition systems

Atmospheric Cherenkov flashes reach the telescope at random and unpredictable times. Additionally, the flashes last only a few nanoseconds and exhibit temporal structure on much shorter timeframes. Continuous monitoring of the sky at GHz sampling rates on hundreds or thousands of channels is impractical; instead, the data acquisition system of IACTs must be triggered in such a way that the photodetector outputs are recorded for a brief time window surrounding the arrival time of the Cherenkov flash. Due to the fact that the trigger decision time is longer than the duration of the flash, the photodetector output signals is delayed (e.g., via long analog cables) or constantly sampled and stored in digital memory buffers. The appropriate data time window can be accessed and saved to disk as digital samples upon receipt of a valid trigger.

Typically, trigger systems operate on multiple levels, with the goal of triggering on the faintest possible Cherenkov flashes while avoiding an excessively high rate of false triggers caused by the varying night sky background. Individual pixels have discriminators that generate a digital output. Each camera's output is sent to a logic circuit that checks for spatial coincidences (e.g. 3 neighbouring pixels must have triggered within a few nanoseconds). The final trigger selection is made at the array level - generally, at least two telescope cameras must have triggered simultaneously, after adjusting for the Cherenkov light's varying path lengths to each telescope. Figure 2.7 displays a "bias curve" for MAGIC showing the changing event rate as a function of the discriminator threshold for each pixel, for both the telescope individually and the stereo trigger.

To summarize, trigger systems operate on a three-tiered concept:

- a minimal response is required at the pixel level, which is typically accomplished with a basic threshold discriminator (or a constant fraction discriminator),
- the second-level trigger is a pattern trigger: either groups of adjacent pixels or a certain number of pixels inside a predefined area must satisfy the first-level trigger requirement.
- the third level is an array trigger that requires at least two IACTs to coincide events within a specified time range.

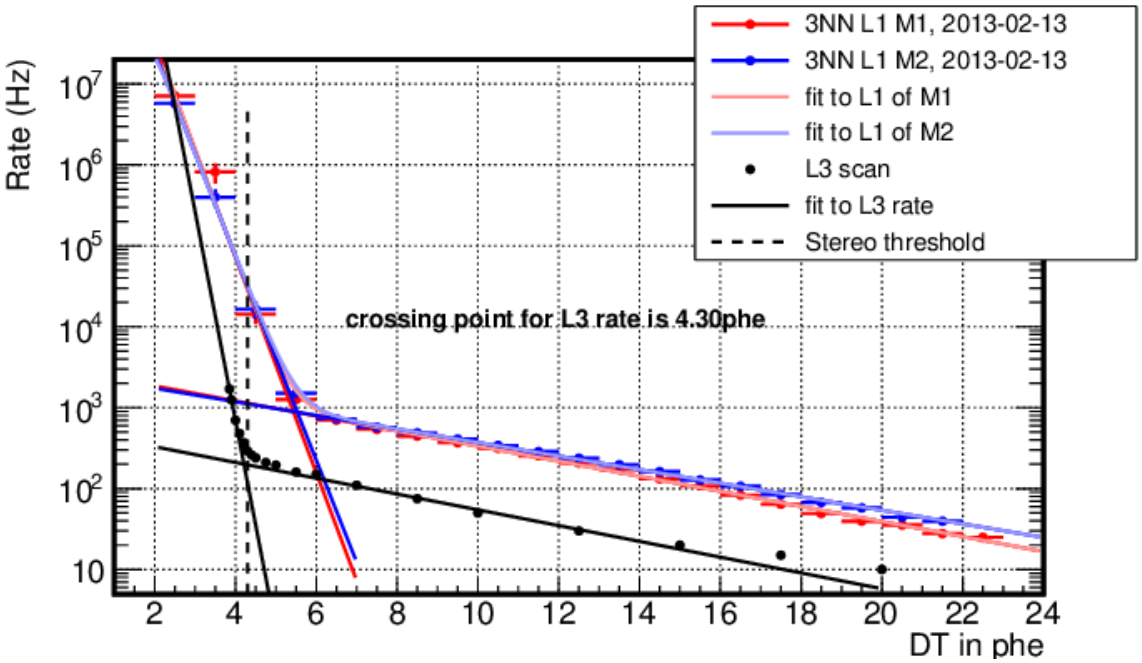

Figure 2.7: Rate scans taken changing discriminator thresholds (DTs) to optimize the operating point of the MAGIC telescopes. Red (blue) points are "Level 1 - 3 next neighbour" trigger rate scans taken with MAGIC-I (MAGIC-II) telescopes and the lines are analytical fits to them. The black points correspond to the measured stereoscopic rate of the system, and the black lines are fitted functions. Adopted from [60]

2.3.6. Peripheral and environmental systems

Along with the telescopes themselves, a number of peripheral systems are typically deployed to perform calibration and monitoring operations on both the telescopes and the surrounding atmosphere. Nanosecond light pulsers are required for telescope calibration, since they are utilized to flat-field photodetector gains and assess their single photon response. Monitoring the atmosphere can be accomplished using both local weather stations and LIDARs [61], and pyrometer, which can detect the presence of clouds by measuring the night sky's radiative temperature.

2.3.7. Array design

The combination of multiple telescopes substantially boosts the technique's sensitivity, as well as its angular and spectral resolution. Numerous studies on the optimal configuration

and spacing of IACT arrays have been conducted, including [62–64]. The conclusions can be put in broad terms as follows: (1) more telescopes are preferable, with array sensitivity typically proportional to the square root of the number of telescopes, and (2) the ideal spacing is dependent on the energy range to be covered: The greater the distance, the greater the sensitivity to higher energies. Additionally, when the array is much larger than the Cherenkov light pool, the performance of the array changes [65]. Multiple telescopes always sample the central region of the Cherenkov light pool in this regime (unlike smaller arrays, where the shower core often lies outside of the area enclosed by the array). As a result, telescopes of relatively modest size have significantly improved sensitivity at low energies.

2.4. IACT DATA ANALYSIS

The analysis of IACT data is sophisticated, and the software reconstruction steps have a similar influence on the array's sensitivity and performance as many parts of the hardware do. To summarize, the objective of the analysis is to identify the primary particle and reconstruct its arrival direction and energy. This data is then used to determine the statistical significance of every gamma-ray signal, map its distribution across the sky, and recreate the gamma-ray flux and energy spectrum.

2.4.1. Hillas parameterization

Since the inception of ground-based gamma-ray astronomy, data analysis techniques have relied heavily on the "Hillas parameterization" [40] of shower images, based on the fact that gamma-ray images in the focal plane are, to a good approximation, elliptical in shape and intrinsically narrower than hadronic images. A.M. Hillas suggested in 1985, based on pioneering Monte Carlo simulations, that recorded images could be reduced to a few parameters generated from the first and second moments of the camera's light distribution and corresponding to the image being modelled by a two-dimensional ellipse.

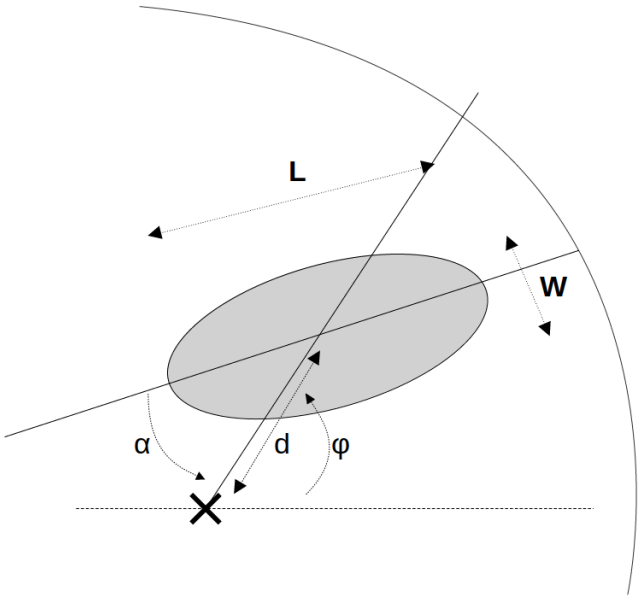

Figure 2.8: Geometrical definition of the Hillas Parameters.

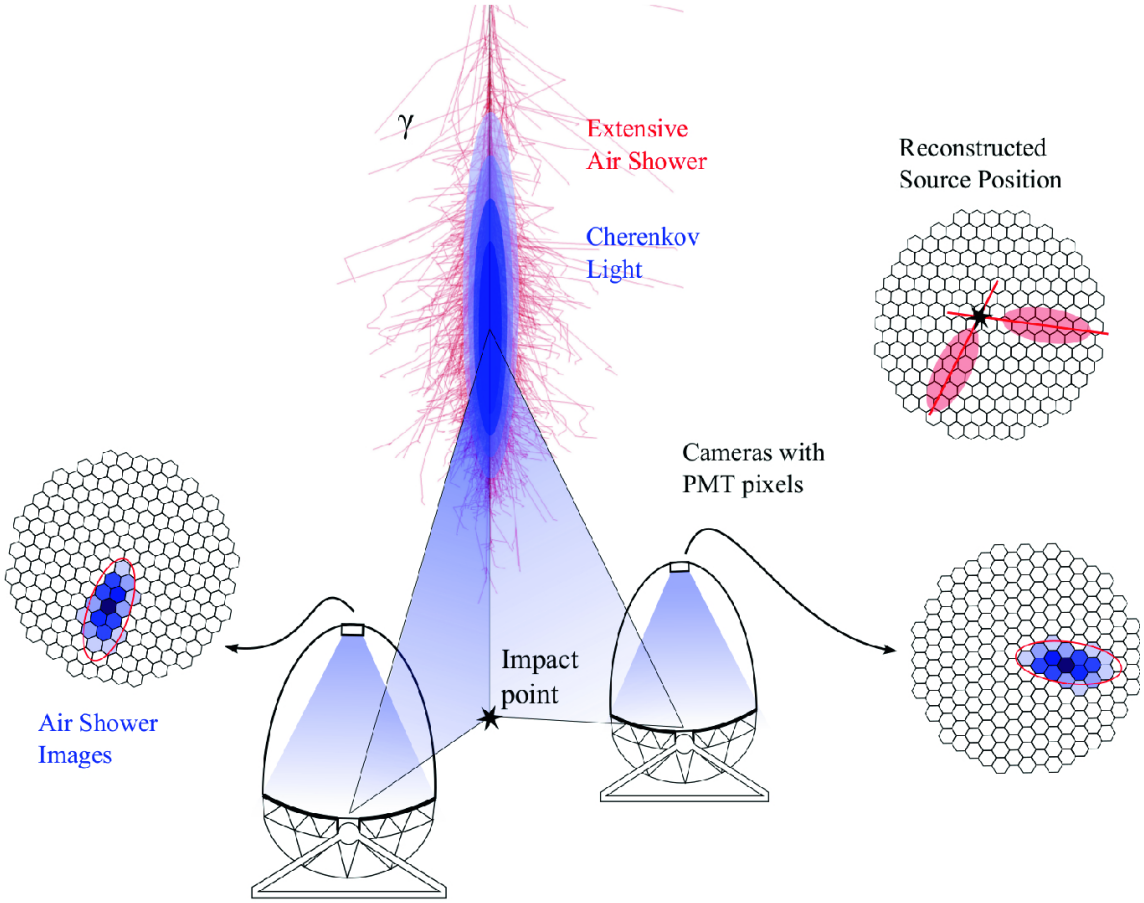

Figure 2.9: Multiple telescopes use PMTs to record the Cherenkov light from the air shower. The telescopes' shower images can be combined to obtain immensely effective stereo parameters. One can reconstruct the shower axis using the impact point and the gamma ray's reconstructed origin in the sky (also referred to as the reconstructed source position). Adopted from [66].

These parameters, shown in Figure 2.8, are the following:

- image center of gravity (first moments)
- length L and width w of the ellipse (second moments)
- size (total charge of photo-electrons in the image)
- nominal distance d (angular distance between the center of the camera and the image center of gravity)
- azimuthal angle of the image main axis ϕ (second moments)

- orientation angle α .

The stereoscopic imaging technique, which was first advocated in 1977 [67] and successfully developed by HEGRA in 1997 [68], enabled a simple geometric reconstruction of the shower direction and impact parameter, resulting in a significant improvement in angular resolution and background rejection. The source direction is determined by intersecting the primary axes of the shower images in the camera (as seen in Figure 2.9), and the shower impact point is determined similarly, by intersecting the planes containing the telescopes and the shower axes geometrically. Not only do the Hillas parameters allow for the reconstruction of shower properties, but they also allow discriminating between γ-ray candidates and the far more prevalent hadrons, based on the extension (width and length) of the recorded images.

2.4.2. Flat-fielding and image cleaning

For IACTs, the raw data outputs consist of a digitally sampled signal trace for each of the cameras' photosensors, roughly centered on the arrival time of the Cherenkov pulse. The initial stage of data processing involves measuring and subtracting the signal pedestal value. The following step is to determine which pixels contain a Cherenkov signal that exceeds a predefined threshold. After that, the signals are corrected for differences in the photodetector gain values, which are determined with the use of a calibration light pulse. This pre-processing produces a cleaned, calibrated image that is typically elliptical in shape as shown in Figure 2.10).

2.4.3. Particle classification

Even for a moderately bright gamma-ray source, cosmic ray shower outnumber gamma-ray shower by a factor of $\sim 10^4$. Classifying the gamma-ray events effectively is therefore critical. While the arrival direction of the primary is by far the most effective tool for discrimination in the case of a point source of gamma rays, many TeV sources have a substantial angular extent, up to a few degrees in diameter. Fortunately, significant differences in the Cherenkov image shape caused by differences in the air shower development allow for discrimination [40].

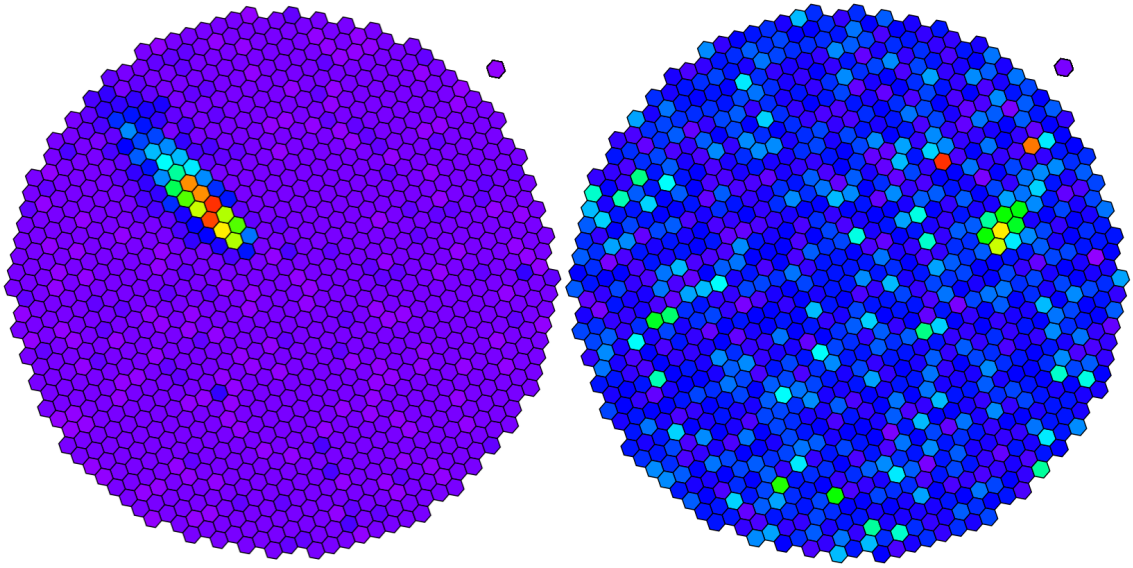

Figure 2.10: Simulated MAGIC events in displayed in camera frame. Left: gamma-like; Right: background-like. The event on the left is more easily fit with an ellipse than the event on the right. Adopted from [69].

The gamma/hadron separation is based on the image parameter distributions which reflect the varying development features of the hadronic cascades in comparison to gamma-induced ones. After selecting a set of parameters with high discriminating power, the cuts separating gamma-ray from hadronic candidates are optimized and this leads to the definition of a global parameter, called *hadronness*. Most common strategy is to utilize advanced pattern recognition or multivariate analysis techniques to improve the discrimination between gamma-ray and cosmic ray events. While numerous approaches have been developed (neural networks etc.), the most effective tend to be multi-dimensional classification system based on the construction of decisional trees, such as random forests (RF) which are used in MAGIC. [70].

The RF is first trained with events of known nature, i.e. Monte Carlo (MC) simulated gamma-ray events and hadron events extracted randomly from "off" data. In order to avoid artifacts in the training, events in the hadron sample are selected in such a way that the shape of their size and zenith angle distributions matches with those of the MC sample. After the RF tree has been produced it is applied to the data. Images produced by gamma rays tend to produce a hadronnness close to zero, whereas hadrons have a hadronness that spans the entire range from 0 to 1.

2.4.3.1 Gamma-ray analysis cut efficiency

The gamma-ray analysis cut efficiency is defined as the ratio between the simulated gamma-ray events surviving the analysis cuts, and the total number of produced MC events:

$$\varepsilon = \frac{N_{\gamma}^{MC}(\text{ after cuts })}{N_{\gamma}^{MC}(\text{ simulated })}. \tag{2.3}$$

A harder cut corresponds to lower gamma-ray efficiency and provides better background rejection. Typically gamma-ray efficiency cuts of 80% to 95% are used in the analysis. Cuts lower than $\sim 80\%$ are not used as they can cause MC to data mismatch and thus bias the results.

2.4.4. Arrival direction reconstruction

The reconstruction of the shower primary's arrival direction serves two purposes: it allows efficient discrimination between gamma-ray photons from the source and the isotropic charged cosmic ray background, and it enables analysis and mapping of the shower's gamma-ray emission. Accurate location of the gamma-ray emission source is commonly employed for gamma-ray source identification, and gamma-ray mapping of extended astrophysical sources provides insight into the particle acceleration processes at work in these objects.

The major axes of the image ellipses intersect in the field of view of the telescopes at the position corresponding to the primary particle's arrival direction, as schematically represented in Figure 2.9. This fact is utilized to estimate the direction of arrival, typically using a weighting technique that adds additional weight to the axis of the brightest images [71]. The distance between the source and the reconstructed photon direction is denoted as θ.

The technique's resulting angular resolution is energy dependant, with around 68% of the gamma rays from a point source being reconstructed to within 0.1° of the source position at energies around 1 TeV. This is the parameter of the Point Spread Function (PSF) which is the response of an imaging system to a point source. For a point-like source the PSF is the expected θ^2 distribution.

2.4.5. Detection significance

After estimating the arrival directions, each location in the field of view can be tested for evidence of gamma-ray emission by selecting events that occur within a predefined radius of the test point. This approach is complicated by the fact that each point's gamma-ray emission is superimposed on the residual background of misidentified cosmic ray events. To determine the gamma-ray excess and its statistical significance, it is important to obtain an independent estimate of the residual background at each point. This is performed by determining the background rate in parts of the sky with little or no predicted gamma-ray emission. These "OFF-source" locations can be picked in a variety of methods, including through dedicated observations of neighbouring fields of view, or (more typically) through selection of regions within the same field of view but offset from the test location.

The reliability of a source detection can be expressed by quoting the probability that the measured number of excess events is due to a spurious background fluctuation. The lower this probability, the more likely the observed excess is produced by a real source. This probability is usually expressed in terms of Gaussian standard deviation (σ) equivalents. To compute this probability a likelihood ratio test can be used.

One can define:

- N_{on}: Number of events measured in the signal (On) region
- N_{off}: Number of events measured in the background control (Off) region
- α: The ratio of On to Off exposure

then the exact formula used for significance computation [72] is:

$$S = \sqrt{2}\left\{N_{\mathrm{on}} \ln\left[\frac{1+\alpha}{\alpha}\left(\frac{N_{\mathrm{on}}}{N_{\mathrm{on}}+N_{\mathrm{off}}}\right)\right] + N_{\mathrm{off}} \ln\left[(1+\alpha)\left(\frac{N_{\mathrm{off}}}{N_{\mathrm{on}}+N_{\mathrm{off}}}\right)\right]\right\}^{1/2} \quad (2.4)$$

2.4.6. Energy estimation

Calculating the energy of an incident gamma-ray is based on the fact that the number of particles in the shower, and hence the Cherenkov photon yield, is proportional to the energy of the primary particle. Measuring the intensity of the Cherenkov radiation and

combining it with the distance to the shower enables an estimate of the gamma-ray energy to be made [73]. Multiple telescopes significantly increase this energy estimate by providing multiple measurements of the shower light yield and a better estimate of the shower core location [74].

In practice, the energy is estimated using look-up tables (LUT) that contain the expected gamma-ray energy as a function of the impact parameter and Cherenkov intensity. The table contents are generated from MC simulations of the shower's growth and instrument response of the telescope. The Earth's atmosphere is the most crucial component in reproducing the Cherenkov yield at telescope mirrors. This is difficult to monitor and account for, and hence introduces systematic errors of at least 10%. Numerous tables are created to adapt to various observation conditions (elevation angle, background night-sky brightness, source offset in the field-of-view). The technique's energy resolution is dependent on the primary's energy, often reaching $\sim 15\%$ above 1 TeV and degrading below this.

The Random Forest method can also be as a regression mode to estimate the energy from a set of parameters and is commonly used nowadays.

2.4.7. Collection area

Converting the energy distribution of gamma-rays measured from a source to an usable flux estimate, or energy spectrum, necessitates information about the detector's effective area. In the case of IACTs, the maximum effective area is defined by the size of the Cherenkov light pool rather than the size of the telescopes or the array's area, and can exceed $> 10^5$ m^2 at high energies. At lower energies, the array's trigger effectiveness (and thus its effective area) rapidly decreases until it reaches zero. The energy-dependent effective area is estimated by simulating gamma-ray showers using a wide variety of impact parameters and a typical energy distribution (e.g. a power law with an index of -2.0). The effective area is calculated by multiplying the number of triggered events by the number of simulated events and by the region over which the events were simulated as in Equation 2.5.

$$A_{\text{eff}} = \left(N_{\gamma,\text{ final}} / N_{\gamma,\text{ simulated}}\right) \cdot A_{MC} \tag{2.5}$$

where $N_{\gamma,\text{simulated}}$ is the number of simulated gamma rays, $N_{\gamma,\text{final}}$ is the number of gamma rays that trigger the telescope and A_{MC} is the area over which the impact points of gamma rays are simulated. The calculations have to be done in bins of parameters affecting the value of A_{eff}, like energy and zenith angle and they must accurately match the data observing conditions.

2.4.8. Flux calculations

A gamma-ray flux is defined as a rate of gamma rays per unit area:

$$\Phi = \frac{d^2N}{dS\,dt} \quad \text{, units:} \quad \left[L^{-2}\right]\left[t^{-1}\right]\text{, e.g. cm}^{-2}\text{ s}^{-1} \tag{2.6}$$

Needed ingredients for its calculation are:

- number of detected gamma rays
- effective observation time (in general, smaller than the elapsed time, since all instruments have some dead time)
- effective gamma-ray collection area of the instrument

Related concepts to the gamma-ray flux are:

- Differential energy spectrum: energy flux per interval in gamma-ray energy, i.e.

$$\frac{d\Phi}{dE} = \frac{d^3N}{dS\,dt\,dE} \quad \left(\text{cm}^{-2}\text{ s}^{-1}\text{ TeV}^{-1}\right) \tag{2.7}$$

- Integral flux: total flux in a given energy range. For instance, $100-1000$ GeV. Very often it is just the flux above a given energy, e.g. >100 GeV

$$\Phi_{E>100\text{ GeV}} = \int_{100\text{ GeV}}^{\infty} \frac{d\Phi}{dE} dE \left(\text{cm}^{-2}\text{ s}^{-1}\right) \tag{2.8}$$

- Spectral Energy Distribution : energy flux per logarithmic energy range

$$E^2 \cdot \frac{d\Phi}{dE}\left(\text{TeV cm}^{-2}\text{ s}^{-1}\right) = E \cdot \frac{d\Phi}{d(\log E)} \tag{2.9}$$

2.4.9. Unfolding

True energy spectrum of the source can be reconstructed from the estimated energy distribution of gamma-ray events in which the systematic biases can arise due to the fact that the effective area estimate depends upon the simulated gamma-ray spectrum (due to the finite energy resolution of the instrument).

The problem can be described as:

$$\vec{g} = \mathbf{M} \cdot \vec{f} + \vec{b} \tag{2.10}$$

where:

- $\vec{g}$ is the distribution of the measured parameter, e.g. estimated energy of a photon (E_{est})
- $\vec{f}$ is the distribution of the sought parameter, e.g. true energy of a photon (E_{true})
- $\mathbf{M}$ is the migration matrix or response function determined by Monte Carlo simulations
- $\vec{b}$ is the possible background distribution occurred in the measurement process

The migration matrix element M_{ij} represents the probability that an event in bin j of E_{true} is reconstructed in bin i of E_{est} .

To find a solution for $\vec{f}$ different approaches are possible and such methods are called "unfolding" and are used to account for the finite resolution of the technique [75].

2.4.10. Main systematics effects

The primary systematic effects are caused by uncertainty in the absolute energy scale and in our understanding of atmospheric conditions. The former is due to the absence of a VHE gamma ray calibration beam device. The latter is related to variations in the temperature, pressure, and humidity profiles in the atmosphere, as well as the amount of aerosols or thin clouds: these factors affect the density of Cherenkov light arriving at the observatory level, thereby affecting energy reconstruction and trigger efficiency (effective

collection area). The best current estimates on the energy scale are within an accuracy of $10-15\%$, while the absolute flux level is uncertain within a precision of $10-15\%$.

The Earth's magnetic field tends to separate positively and negatively charged particles in the shower, resulting in its broadening in the direction orthogonal to the magnetic field's direction. This introduces an asymmetry into the system's response, resulting in decreased performance in areas of the sky perpendicular to the observing direction. This effect, which is especially pronounced at low energies, is appropriately accounted for in Monte Carlo simulations and hence does not account for a significant portion of the systematic uncertainty.

2.5. CHERENKOV TELESCOPE ARRAY

The current generation of detectors, both in space and on the ground, provide a wealth of information about the nonthermal Universe in the GeV-TeV energy band. For what concerns ground-based observatories at the TeV scale, the Cherenkov Telescope Array (CTA) [76] represents the future for IACTs, with an order of magnitude improvement in sensitivity over existing instruments. An array of tens of telescopes will detect gamma-ray-induced showers over a large area on the ground, increasing the efficiency and the sensitivity, while providing multiple views of each cascade. This will result in both improved angular resolution and better suppression of CR background events. In particular, three types of telescopes are foreseen:

- The low energy (the goal is to detect showers starting from an energy of 20 GeV) instrumentation will consist of 23 m large-size telescopes (LST) with a FoV of about $4-5$ degrees.
- The medium energy range, from around 100 GeV - 1 TeV, will be covered by medium-size telescopes (MST) of the 12 m class with a FoV of $6-8$ degrees.
- The high-energy instruments, dominating the performance above 10 TeV, will be small size (SST, 4 m in diameter) telescopes with a FoV of around 10 degrees.

CTA will be deployed in two sites. The Southern site is less than 10 km southeast of the European Southern Observatory's (ESO's) existing Paranal Observatory in the Atacama Desert in Chile; it will cover about three square kilometers of land with telescopes that will monitor all the energy ranges in the center of the our Galaxy. It will consist of all three types of telescopes with different mirror sizes (14 MSTs and 37 SSTs in the present design) arranged in so called "Alpha Configuration". The Northern hemisphere site is located on the existing Roque de los Muchachos Observatory on the Canary island of La Palma, close to MAGIC; only the two larger telescope types (4 LSTs and 9 MSTs in the present design) would be deployed, on a surface of about one square kilometer. These telescopes will be mostly targeted at extragalactic astronomy. The telescopes of different sizes will be arranged in concentric circles, the largest in the center. Different modes of

operation will be possible for CTA: deep field observation, pointing mode, scanning mode - also pointing to different targets. PeVatrons and the nature of the emitters in the Galaxy will be studied in detail. CTA will generally improve sensitivity by an order of magnitude over the current generation IACTs. The sensitivity of CTA is shown in Figure 1.6 and compared to present detectors. Additionally, it will expand the accesible energy range accessible from about 20 GeV (greatest overlap with gamma-ray satellites) to about 300 TeV (crucial for Pevatron searches).

3. VLZA OBSERVATIONS

3.1. SEARCH FOR PEVATRONS

Galactic PeVatrons are a class (or maybe classes) of the Galactic objects, which accelerate protons up to the PeV energies, roughly corresponding to the knee in the measured CR spectrum. The presence of the knee is often attributed to the high-energy cut-off of the Galactic CR population, which makes PeVatrons the most powerful accelerators of CR in the Milky Way.

The gamma-ray energy domain above several tens of TeVs was not very well studied until recently. An attempt to detect the sources of the γ-ray radiation up to 100 TeV was performed by MILAGRO experiment [77], which resulted in detection of only a couple of sources, such as Crab Nebula, Mrk 421, Galactic plane and Cygnus region emission, at the energies of a few tens of TeV [78].

At the same time, the observations of astrophysical sources in the energy band of ~ 100 TeV are of great importance. This energy band corresponds to the emission of relativistic particles (presumably protons) with energies of $\sim 10^{15}$ eV, corresponding to the knee in the observed spectrum of CR. The most plausible explanation is that the CR below the knee are of a galactic origin, however a direct detection of a source population hosting the 10^{15} eV protons (particles, which constitute the majority of CR) is yet to come. The source population, responsible for the acceleration of CR up to the knee energies, should be in accord with the total power of CR contained in the Galaxy. In the absence of the direct detection of the sources of CR, several different possible parent populations are considered as PeVatron candidates: supernovae remnants (e.g. [79–81]), pulsars and pulsar wind nebulae [82] and OB-associations (young star clusters containing $\sim 10-100$

massive stars of spectral class O and B, e.g. [83]).

A direct detection of astrophysical objects at $\sim$ 100 TeV and measurement of their spectra in this band can clarify the nature of the sources of the CR and shed the light onto numerous questions related to the CR acceleration and propagation. A clear detection of cut-offs in the source spectra would clearly to which extent a given source class can be responsible for the production of CR in the knee region.

Nowadays the interest to the PeVatron observations is significantly increased by the reported detections of the likely PeVatrons in the Galactic Centre ([28]) and in the Galactic Plane in general ([84, 85]). While several PeVatron candidates are now reported to emit gamma rays $>$ 100 TeV [86], due to the curvature of their spectra the emission from these sources likely originates from leptonic emission processes as opposed to the coveted hadronic emission processes.

It is critical to keep in mind that ultra-high-energy (UHE) gamma-rays ($\gtrsim$ 100 TeV) represent a necessary but not sufficient condition for PeVatron identification. Hadronic cosmic rays can be detected via their association with molecular clouds or through the smoking gun of a coincident neutrino signal. A cloud illuminated by hadronic cosmic rays, on the other hand, is evidence of PeVatron activity, but not a PeVatron in and of itself (accelerator). Thus, a PeVatron ceases to be a candidate when an unambiguous accelerator with gamma-ray emission at energies greater than $\sim$ 100 TeV is detected [87].

Many sources of TeV gamma-rays remain unidentified (e.g., [88, 89]) and their multiwavelength studies could help reveal the nature of some of them and contribute to solve the puzzle of the CR origin. The detection of such objects with the high angular resolution instruments would allow to not only to confirm their nature, but also to establish the properties of the CR diffusion in their surroundings. Such observations could provide a missing link between the sources of the CR and their spectrum, as measured in the Solar System.

3.1.1. Case for Crab Nebula obsevations

It has long been known that pulsars can drive powerful winds of highly relativistic particles [90]. Confinement of these winds leads to the formation of strong shocks, which may accelerate particles to $\sim$PeV energies. This generates luminous nebulae seen across the

entire electromagnetic spectrum: in the synchrotron emission from radio to hard X-rays, and through the inverse Compton process and potentially π^0 decay from $p-p$ interactions [91] from the surrounding medium, in the VHE domain. Measurements of high-energy gamma-ray radiation resulting from IC scattering provide a direct view of the parent particle population if the target photon fields are spatially uniform and have a well-known density e.g where the dominant target is the CMB radiation or possibly the dense interstellar radiation fields present in the inner Galaxy. Hence, VHE gamma-ray observations are also important in understanding the origin and acceleration of cosmic rays. The best studied example of a PWN is the Crab nebula, which exhibits strong non-thermal emission across most of the electromagnetic spectrum from radio to $>$ 50 TeV gamma rays [74, 92, 93].

Crab Nebula commonly serves as a calibration target for IACT observations as it is a "standard candle" in the field of VHE astrophysics. Apart from the technical, but important role, observations of Crab Nebula in the 10-100 TeV energy range are interesting since it may allow to differentiate between several emission mechanisms (IC on CMB, SSC, bremsstrahlung) that could be contributing to the TeV flux. This is possible due to the different energy scaling of their relative fluxes and can be done with sufficiently accurate observations in the $>$ 10 TeV energy range.

Crab Nebula observation at $\sim$100 TeV itself is of a great interest. Though the high-energy spectrum of this source is likely of a leptonic origin, the definite proof of this can be obtained with the detection of the Klein-Nishina cut-off, which should happen in the 100-300 TeV energy range.

The very-high energy spectrum of the Crab Nebula was reported to have a signature of a cut-off around $\sim 15-30$ TeV [94, 95], though other measurements suggest that the spectrum continues up to $\sim$ 80 TeV without it [74]. This discrepancy can be further investigated with $>$ 30 TeV observations.

Alternative measurements of the Nebula signal at the same energies were also reported by HAWC and TIBET [96, 97], making its $>$ 100 TeV emission one of the current hot topics.

Additionally, the Crab Nebula has demonstrated several bright flares at GeV energies in the past [98, 99], whose nature has been actively debated. There is a general con-

sensus that the detected GeV emission is produced by the synchrotron emission of the highest energy electrons in the Nebula. However, determination of the other properties of this emission (e.g. magnetic field and electron energy) requires measurements of the corresponding SSC emission, expected at $\sim$ 100 TeV energies.

3.2. VLZA TECHNIQUE

Due to the extremely low count rates at energies of tens of TeV, the detection of even the brightest sources requires either very deep (e.g. > 100 hr) observations or extremely large, $\sim$ km^2 detector arrays (such as the future CTA). At the same time, there is an observational strategy, that allows current IACTs to reach $\sim$ km^2 collection areas without using large size telescope arrays - observations at Very Large Zenith Angles (VLZA) beyond 70° [100].

The collection area A_{eff} of IACTs is determined by the size of the Cherenkov light cone produced by gamma-ray extended air showers. A single telescope's collection area for vertical observations is ~ 0.05 km^2. The collection area can be increased by increasing the number of telescopes, such as the upcoming CTA. Alternatively, a comparable effect can be obtained by observing at larger zenith angles (ZA) [101–103]. Due to the increased distances to the shower maximum, this observation mode results in an increase in the size of the Cherenkov pool. Simultaneously, the decreased photon density on the ground increases the telescope's low energy threshold to much higher energies. The VLZA observation approach is described in more detail in [100] and the principle of VLZA observational scheme is depicted in Figure 3.2.

Till now only a few measurements or attempts of observations with IACTs were carried out at large zenith angle till 70°. The primary reason for it is the rapidly increasing atmosphere thickness with zenith angle (shown in Figure 3.1), which leads to a significant absorption of Cherenkov light from air showers. Despite the rapidly increasing thickness of the atmosphere with zenith angle, the increase of A_{eff} compensates the reduced count rates at higher energies and enables the source detection at very high energies in a significantly shorter time.

There are some factors which are particularly important for VLZA observations that are not so relevant in case of lower zenith observations, such as:

- *Reduced stereo baseline of the telescopes.*

  MAGIC can observe the Crab Nebula in two configurations: while the sources rises and while it sets above the horizon. Due to the variable projected inter-telescope

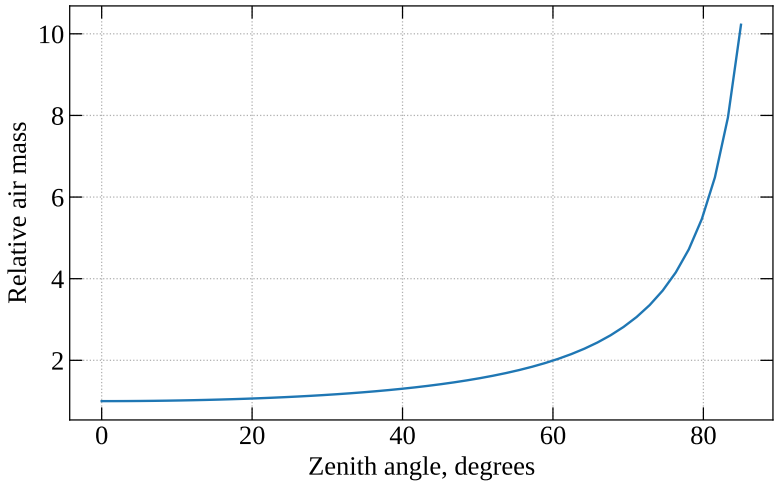

Figure 3.1: Relative air mass versus zenith angle. Adopted from [100].

distances in relation to the direction of the source, these configurations result in slightly differing sensitivities of the MAGIC stereoscopic system to the incoming gamma-ray flux (stereo baseline). The two MAGIC telescopes are positioned north-east and south-west of the system's center, offering a bigger baseline in the north-northwest and south-southeast directions, respectively. With a declination of around 22 degrees, the Crab Nebula rises at approximately 77 degrees and sets at approximately 283 degrees azimuth, respectively northnortheast and northnorthwest. The situation is depicted in Figure 3.3.

- *The transparency of the atmosphere at large zenith angles at the MAGIC site.*

  The VLZA regime observations correspond to the shower maximum distances of $\gtrsim 50 - 100$ km from the telescopes, compared to ~ 10 km at lower zenith angles $\lesssim 30°$. As a consequence, these results are susceptible to increased light attenuation caused by atmospheric scattering and absorption. The standard MAGIC method for accounting for this effect (by using the dedicated LIDAR system [61]) allows estimations of air absorption at distances of $\lesssim 20$ km. Using the auxiliary optical cameras at the MAGIC telescopes the data with the estimated bad weather conditions can be discarded based on the number of stars seen in the field of view of the telescopes.

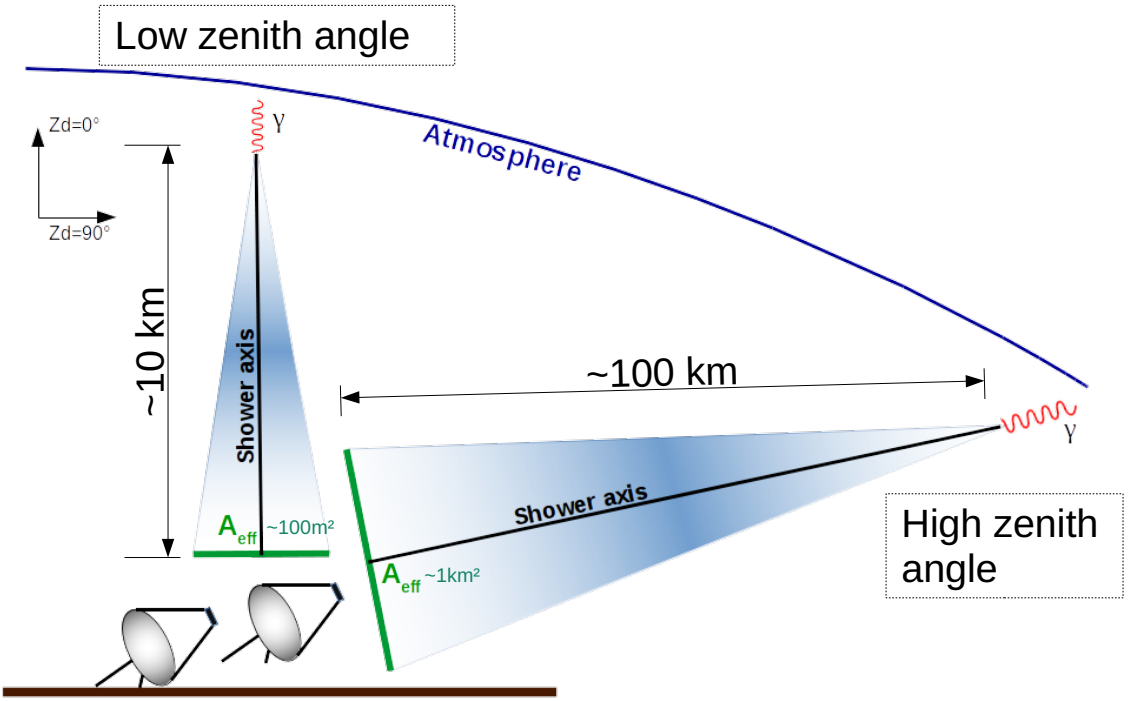

Figure 3.2: Illustration showing the effect of zenith angle on the Cherenkov light pool and the collection area.

- *Shower development at high zenith angles.*

  At these zenith angles the distance to the gamma-ray induced air showers is of the order of $\sim$ 100 km). The Monte Carlo study shows that the gamma-ray induced showers at high zenith angles appear relatively small in the MAGIC cameras with the typical lengths around 30 mm and length to width ratio around 2. An example can be seen in Figure 3.4. This results in the reduced ability to reconstruct the initial shower direction.

  Monte Carlo studies also show that the low energy threshold of MAGIC in this observational regime is relatively low ($\sim 1 - 10$ TeV in the $70° - 75°$ zenith range).

- *Gamma hadron separation.*

  VLZA Monte Carlo simulation of gamma-rays and protons suggest a relatively low gamma-hadron separation power, which causes an increased amount of the background that survives the selection cuts. This is in part due to the smaller event image size in the camera.

Figure 3.3: Photo showing the configuration in which the source can be observed. In this case the rise and set direction of the Crab Nebula are shown. Better stereo performance is obtained in the set direction as the telescope baseline is greater in such case as opposed to observing in the rise direction case.

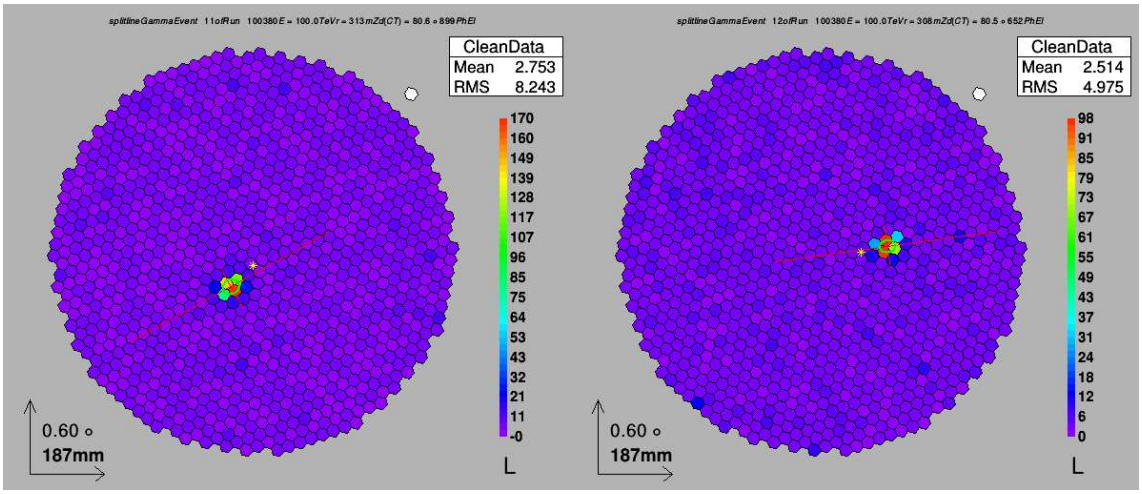

Figure 3.4: Results of a Monte Carlo simulation: example images of the showers from 100 TeV photons at zenith angle of 80°, triggered and detected by the telescope. Images are small, featuring a bright core and a small weaker mantle.

3.3. DATA ANALYSIS

The data was reduced using the standard MAGIC Analysis and Reconstruction Software (MARS) [104].

Two different methods were used to reconstruct the energy of the incident γ-ray : (a) the usual MARS procedure based on LUTs [105] generated from MAGIC MC simulations, and (b) RF multivariate analysis. The cosmic-ray background suppression used in this study was based on a classification technique constructed using RF [70, 105]. Both of these energy estimation methods produce similar results. The results presented below were obtained using LUT energy estimation and RF event identification algorithms.

3.3.1. Data taking

Crab Nebula coordinates (Right ascension: 5h 34m 32s, Declination: +22°0′ 52″) were tracked with both telescopes in stereoscopic mode where only events simultaneously triggering both telescopes are recorded. Data were taken during dark nights without moon, environment humidity below 90%, no rain, with wind speeds below 50 km/h and average PMT current below 30 μA. The optical focusing of the telescopes was set to 10 km. The principle of operation of IACT telescope during data taking was previously described in section 2.3 and section 2.4.

Results presented here are produced from two data samples. Both datasets were taken in the zenith angle range $70^\circ - 80^\circ$ in wobble mode [106] with the wobble offset of 0.4° and rotation angles of 35° and 215°. The first (old) data sample was accumulated from December 2014 to April 2018 and comprises $\approx$ 54 hr of data after the quality selection cuts. 20 hr of data were taken while the source was rising and 37 h were taken while the source was setting. This dataset was published in [107].

The second (new) data sample was accumulated from August 2018 to April 2021 and comprises $\approx$ 46 hr of good-quality data. 28 h of data were taken while the source was rising and 19 h were taken while the source was setting.

3.3.2. Data selection

Events taken during periods of bad weather need to be removed. Due to the nature of VLZA observations, conventional data-quality estimation techniques are inefficient, such as LIDAR and pyrometer. Alternative way of estimating the data quality need to be used. These include the number of stars identified by the MAGIC starguider cameras.

Since the number of stars seen in the telescope field of view depends on the individual pointing position the data was divided into datasets by wobble pointing position. Furthermore, since the number of stars identified by the starguider cameras depends on the atmosphere thickness, the datasets were also divided by zenith angle range: 70°-75°and 75°-80°. This is especially important in VLZA case as the atmosphere thickness changes rapidly for large zenith angles (Figure 3.1).

Figure 3.5 shows the data quality plot used for determining the data selection cuts. It contains the information about the number of correlated stars seen by a telescope, the zenith corrected trigger rate and the current in the camera. In the subplot containing the number of stars an approximately Gaussian distribution can be seen together with long tails containing low number of stars. The tails with low number of stars correspond to the periods of bad weather. From this plot a best cut can be determined that keeps the bulk of good data, but doesn't keep the tails. In this particular case the cut was chosen to be 15. This can also be seen in the plot containing the trigger rate distribution. There the data that was affected by this cut is colored black, while the rest of the data is colored gray. It can be seen from that plot that the same data having low number of stars also has low trigger rates. This further proves the validity of the used cut, as it points to the same cause, such a the presence of the clouds. The same procedure was applied to the off data, which are provided for the training the classifiers and estimators.

3.3.3. Monte Carlo data for VLZA

Until recently the MC energies in the 70°-80° zenith range were produced with the maximum energy of 150 TeV. Since the energy range of interest is higher than the usual energy range observed by IACTs, additional MC production was made in order to be used for VLZA analyses. So, additional MC were produced in the range of 150 TeV - 500 TeV.

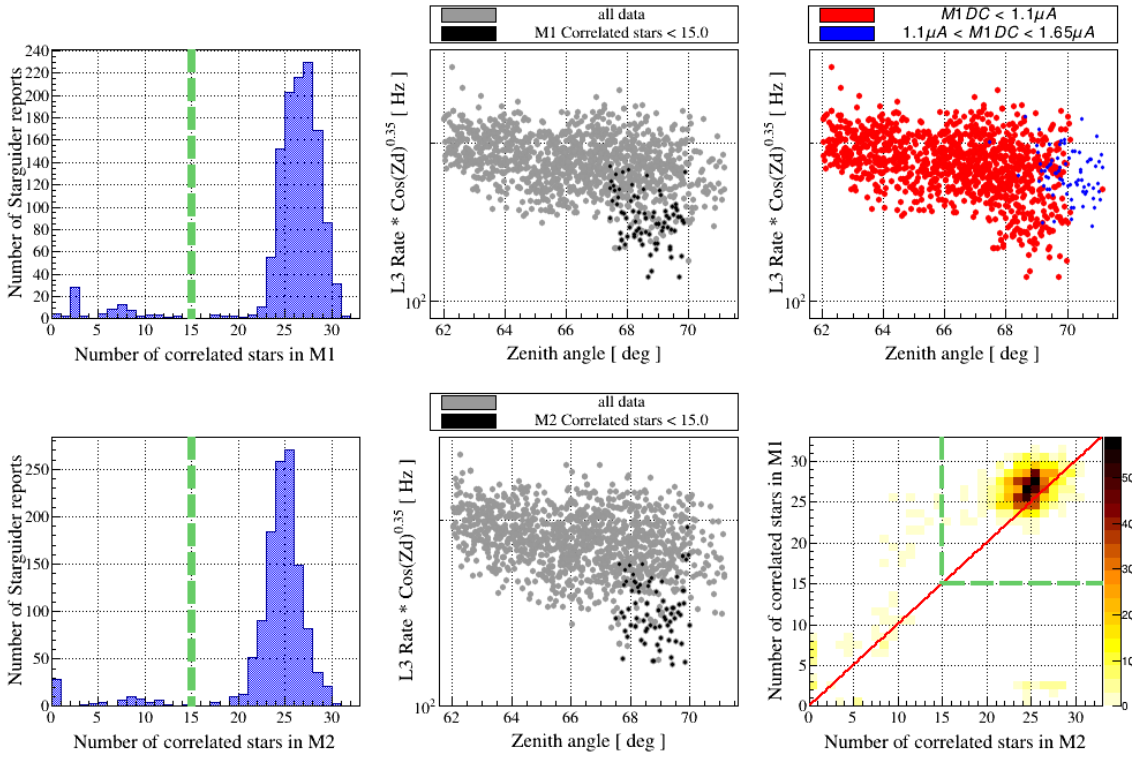

Figure 3.5: Data quality plot used for determining the best quality cuts for data selection. It contains the plots for number of correlated stars seen by the starguider camera, zenith corrected trigger rate and the DC current for both of the MAGIC telescopes.

The >150 TeV MC events are important due to the limitation of the RF energy estimation method. In particular, if the training set doesn't have events above 150 TeV the testing dataset will never contain events above 150 TeV, although the real data could contain those events. The effect is also relevant below 150 TeV due to the intrinsic energy resolution of the method ($\sim 15\% - 20\%$). Because of all this, MCs above 150 TeV are needed. Figure 3.6 shows the joined lower and higher energy MC productions for $70° - 75°$ zenith range. The distribution of events matches nicely the expected slope of -1.6 which can also be seen in the bottom plot which is around 1. Only at the highest energies ($> 10^5$ GeV) there are some fluctuations due to lower statistics, but the mean is still around 1.

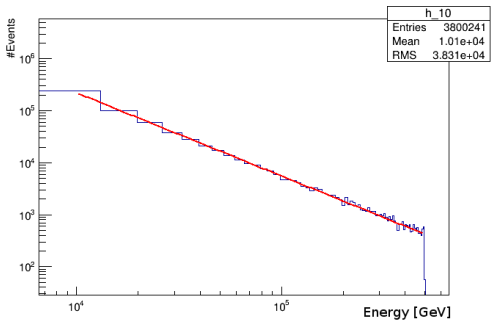

(a) Red line represents a power law with the slope of -1.6 with which the MCs were generated with.

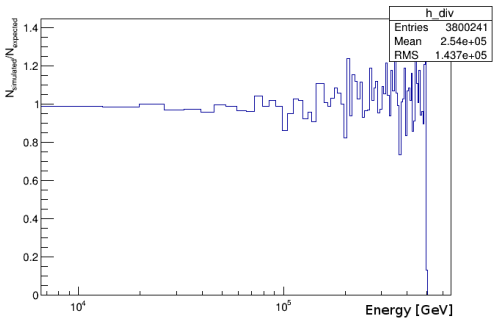

(b) This plot shows the ratio of the simulated and expected number of events from the power law with -1.6 slope.

Figure 3.6: Distribution of merged lower energy (up to 150 TeV) MC events and higher (150-500 TeV) energy events for $70^\circ - 75^\circ$ zenith range in log-log plot.

The situation is different for the $75^\circ - 80^\circ$ zenith range as shown in Figure 3.7. A clear shift in the normalization can be seen in the top plot. Similarly, in the bottom (ratio) plot a shift in the ratio can be seen at 150 TeV. Not only that the normalization of the distribution is different, but also the slopes of the two distribution is different which can be seen in Figure 3.8.

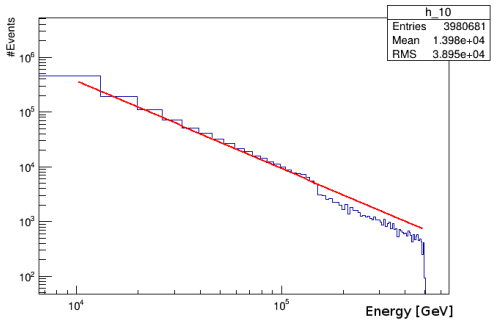

(a) Red line represents a power law with the slope of -1.6 with which the MCs were generated with.

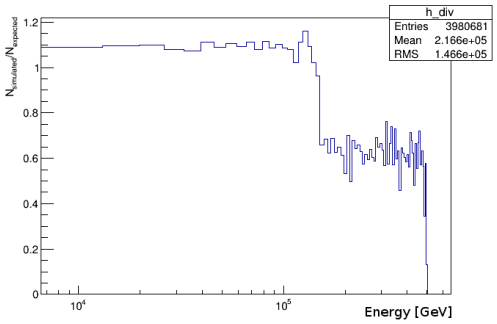

(b) This plot shows the ratio of the simulated and expected number of events from the power law with -1.6 slope.

Figure 3.7: Distribution of merged lower energy (up to 150 TeV) MC events and higher (150-500 TeV) energy events for $75^\circ - 80^\circ$ zenith range in log-log plot.

Both the normalization and slope differences can lead to biases during training of

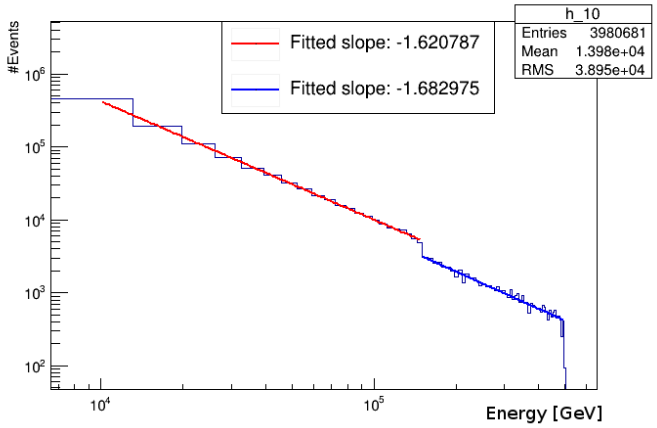

Figure 3.8: Distribution of merged lower energy (up to 150 TeV) MC events and higher (150-500 TeV) energy events for $75° - 80°$ zenith range in log-log plot. Both slopes were fitted with power law distributions.

the energy estimator, so it needs to be corrected for. This was done by discarding a number of higher energy events (>150 TeV) until the slope and the distribution of the two distributions matched. The fraction of higher energy events that need to be discarded in order achieve that was 55%. The resulting distribution is shown in Figure 3.9.

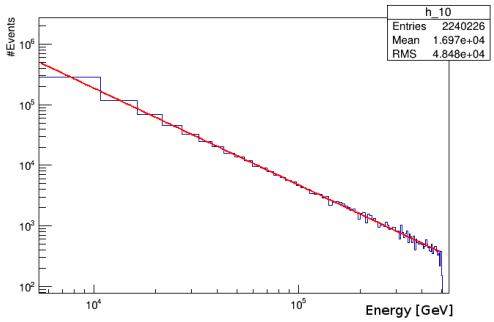

(a) Red line represents a power law with the slope of -1.6 with which the MCs were generated with.

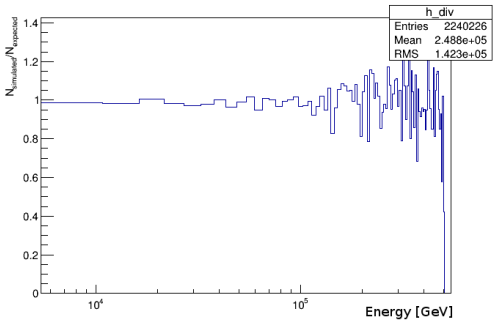

(b) This plot shows the ratio of the simulated and expected number of events from the power law with -1.6 slope.

Figure 3.9: Distribution of merged lower energy (up to 150 TeV) MC events and higher (150-500 TeV) energy events for $75° - 80°$ zenith range in log-log plot after a part of higher energy events has been discarded.

Using this data MC simulation were performed based on MAGIC observations of

gamma-ray produced air showers in the $70^\circ - 80^\circ$ zenith angle range to estimate the performance in case of VLZA observations. The simulations were run using the Corsika code [108] which incorporates the curvature of the Earth's atmosphere to adequately describe the growing air column density observed near the horizon. The remaining parts of the simulation study was identical to that used for the observations at lower zenith angles [109].

3.4. VLZA RESULTS

3.4.1. Collection area

The estimated collection area as a result of the data selection cuts is depicted in Figure 3.10. At energies greater than 70 TeV, the collection area reaches 2 km^2 (compared to ~ 0.1 km^2 for low zenith angle observations, [109]), resulting in an increase by a factor of ~ 10. In Figure 3.10 the first dataset was dubbed "VLZA paper" while the second dataset was further subdivided by individual MC periods (in MAGIC dubbed internaly ST.03.10-14) which account for different response of the telescope with respect to time. At the higher energies (>20 TeV) the collection areas are the same for all MC periods. The difference in the lower energy collection areas comes from different settings of the MC simulations to match the telescope conditions at the time of data taking, mostly mirrors focusing quality and reflectivity.

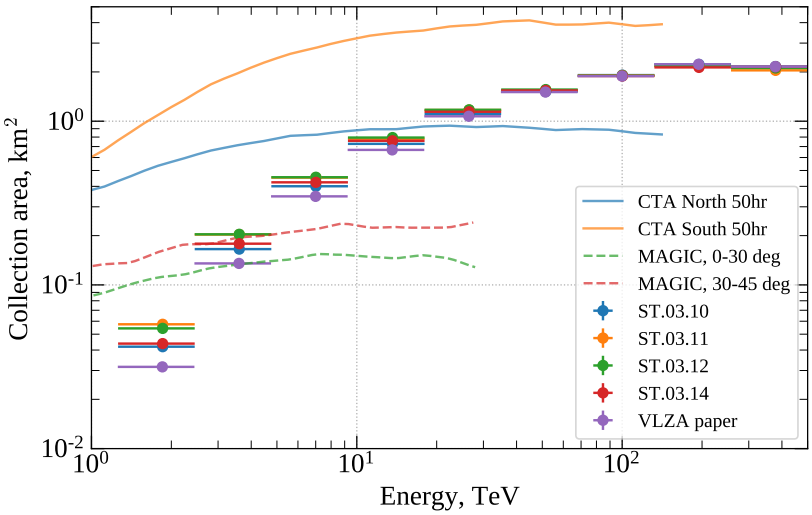

Figure 3.10: MAGIC collection area from [107], estimated for an observational sample in the zenith angle range $70^\circ - 80^\circ$ with Monte Carlo simulations [100]. The "VLZA paper" dataset is shown compared to the new dataset that is further divided into individual MC periods. For comparison the collection area (for 20° zenith angle observations in Production 3 layout) of the future CTA [37] array. Also shown is the MAGIC collection area at lower zenith angles from [109].

3.4.2. Gamma-hadron separation

Gamma-hadron separation performance was checked to see if there was any difference in the newerdataset compared to the old one. For both datasets a gamma efficiency cut of 80% was applied. Although the old (Figure 3.11a) and the new (Figure 3.11b) dataset have different corresponding hadronness values (0.225 and 0.285) for that applied efficiency cut, that does not matter as the hadronness values depend on the individual classifier. Since each dataset has it's own trained classifier, the hadronness values cannot be compared directly. But looking at the number of background events that are kept with the same efficiency cut, one can see that both old and new classifiers perform the same as both keep 4.72% of background for set 80% gamma efficiency cut.

3.4.3. Pointing accuracy

Increased gravity loads caused by the telescopes almost horizontal orientation result in bending of the telescope structure and camera support arch during the VLZA observations. This influence is minimized to a large extent by an active mirror control mechanism and contemporaneous observations of the locations of a number of reference stars adjacent to the MAGIC field of view (with a so called starguider camera) [60, 109]. To further correct for the mechanical imperfections and deformations a pointing model is applied to the drive subsystem of the MAGIC telescopes [110]. To calibrate the pointing model the mispointing measurements of a collection of bright stars is periodically taken with so-called TPoints [111]. Traditionally the zenith angle of the stars was taken up to 70° as this was the usual range of the telescope operation. But since April 2017 the stars up to 85° zenith were also taken into account when making the pointing model in order to increase the validity of the model even in the highest zenith regime.

To assess the influence of the residual telescope mispointing, the approach described in [109] was done. The nominal sky position of the Crab Nebula was compared to that obtained from data from different observational epochs. Due to the lower count rates observed during the VLZA observations, a nightly comparison is not practicable. Thus, the data sets spanning one or more months were integrated in order to accurately estimate the fitted source coordinates in the skymaps. The mispointing was defined as the difference

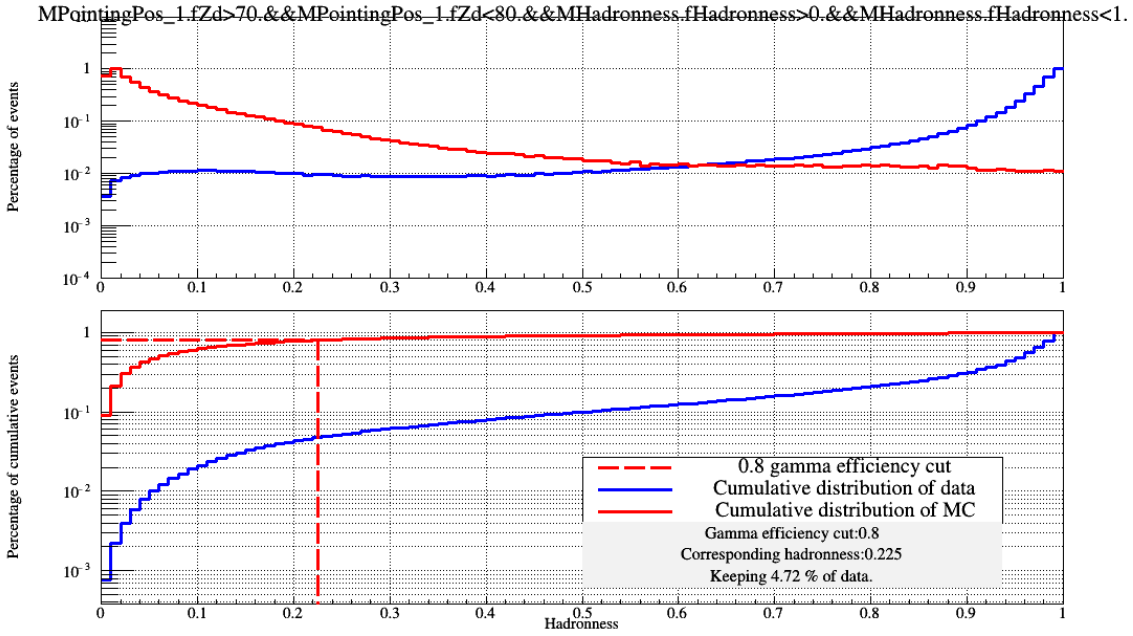

(a) Gamma-hadron performance plot for $70° - 80°$ zenith range for the older dataset.

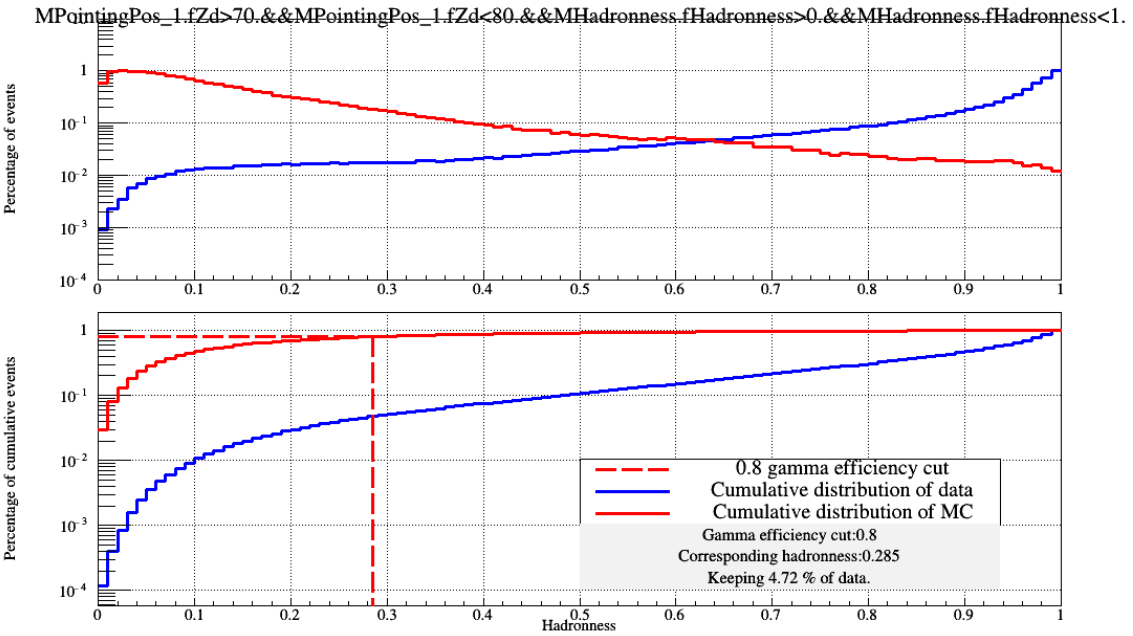

(b) Gamma-hadron performance plot for $70° - 80°$ zenith range for the new dataset.

Figure 3.11: The top plot of individual subplot shows the distribution for the hadronness parameter for the simulated MC events that represent gammas (red) and for the background (blue) which was taken from off observations. The bottom plot shows the cumulative (integral) distribution of the top plot. Both plots are normalized.

between the nominal and reconstructed source coordinates using these maps.

The mispointing data versus time can be found in Figure 3.12, with the breakdown for Right ascension (Ra) and Declination (Dec) shown in Figure 3.14a and Figure 3.14b respectively.

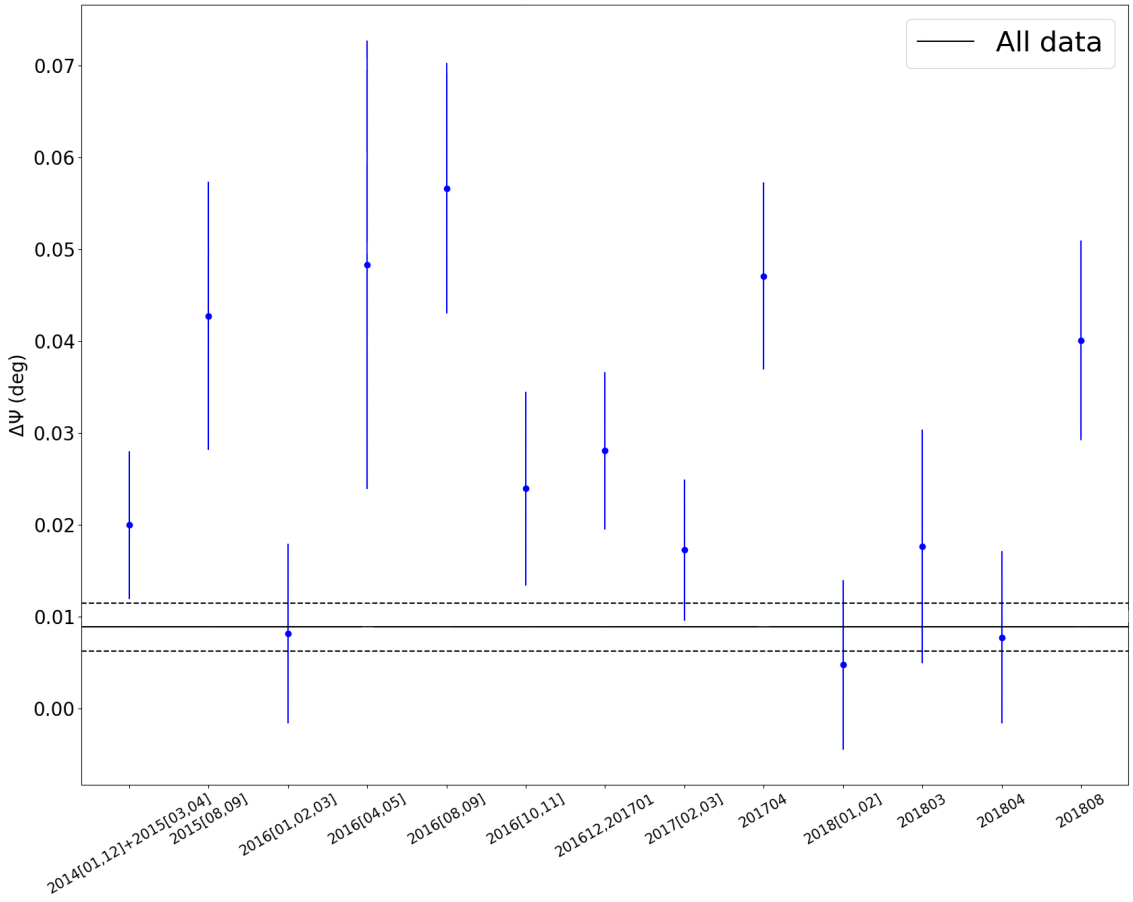

Figure 3.12: Time evolution of mispointing of Crab Nebula using the VLZA method. Each data point represents one or more months of taken data (months shown in the x-axis). The solid line represents the results from the analysis using the complete Crab VLZA data set, and the dashed lines represent the error on that value.

A two-dimensional plot of the mispointings in RA/Dec coordinates can be found in Fig. 3.13. From these results the systematic uncertainty on the reconstructed source position is $\approx 0.04°$. This value is larger than the one reported in [109], which can be explained by the increased mechanical stress on the telescope structure when observing near the horizon in the VLZA regime. Still, this value is ≈ 4 times smaller than the usual MAGIC PSF during such observations.

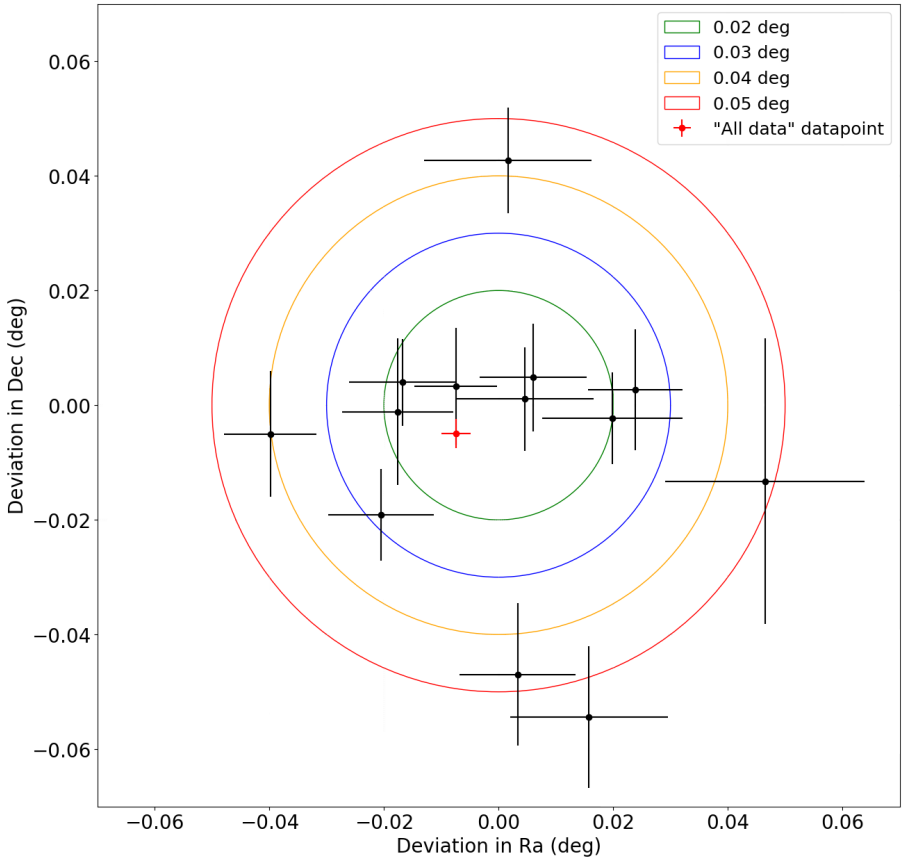

Figure 3.13: Mispointing in RA/Dec of each datapoint, as in Fig. 3.12. The circles represent specific angular distances, as seen in the legend. The data point where all of the Crab VLZA data are analysed is represented in red.

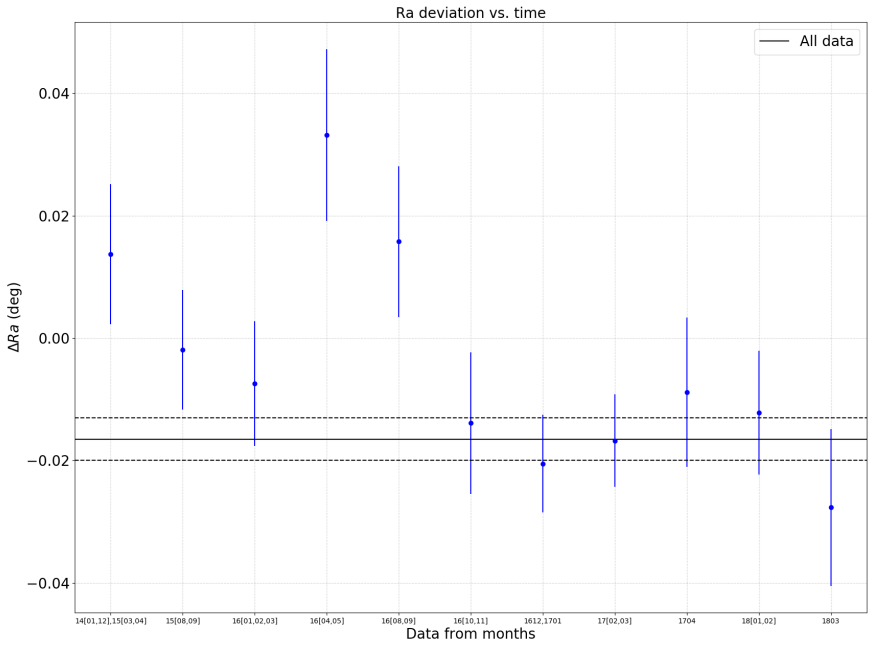

(a) Time evolution of mispointing of Crab Nebula using the VLZA method for the Right ascension sky coordinate.

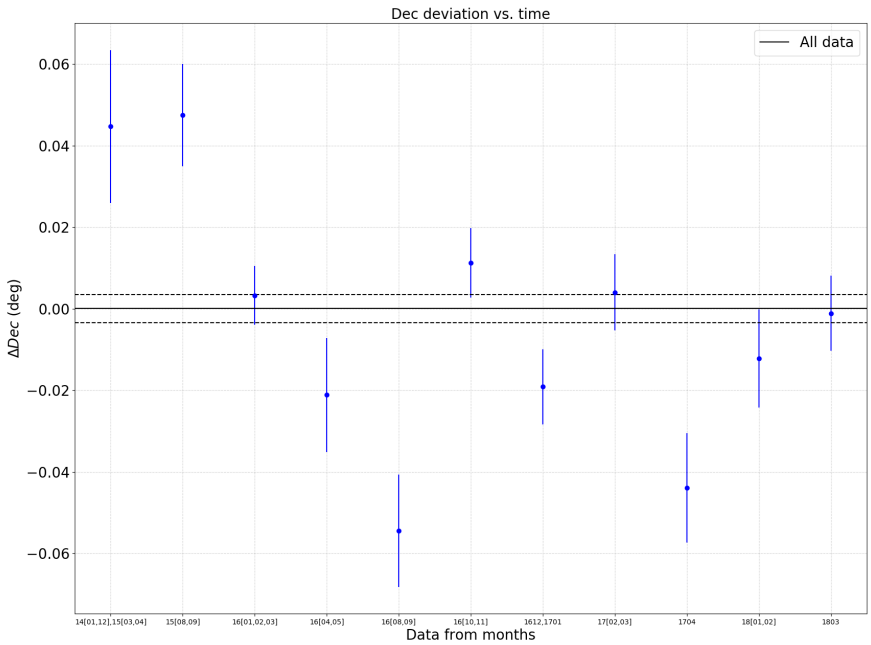

(b) Time evolution of mispointing of Crab Nebula using the VLZA method for the Declination sky coordinate.

Figure 3.14: The dataset and label used is the same as in Figure 3.12.

Additional mispointing results in a larger PSF than estimated by Monte Carlo simulation, influencing true event containment inside a given off-source angle cut. From the Crab Nebula pointing data, one can calculate how it affects the angular containment (so called θ^2, see subsection 2.4.4) on the Monte Carlo data. The Monte Carlo data was divided in 3 datasets by zenith angle: $62° - 70°$, $70° - 75°$, and $75° - 80°$ zenith. The calculations were also done for θ^2 containment efficiency values of 75%, 85%, and 95%. The results of this study are shown in Figure 3.15. The plot represents how the θ^2 changes for certain zenith ranges and efficiencies taking into account the measured mispointing, while the plot in Figure 3.16 show how the containment changes for some defined efficiencies taking into account the measured mispointing.

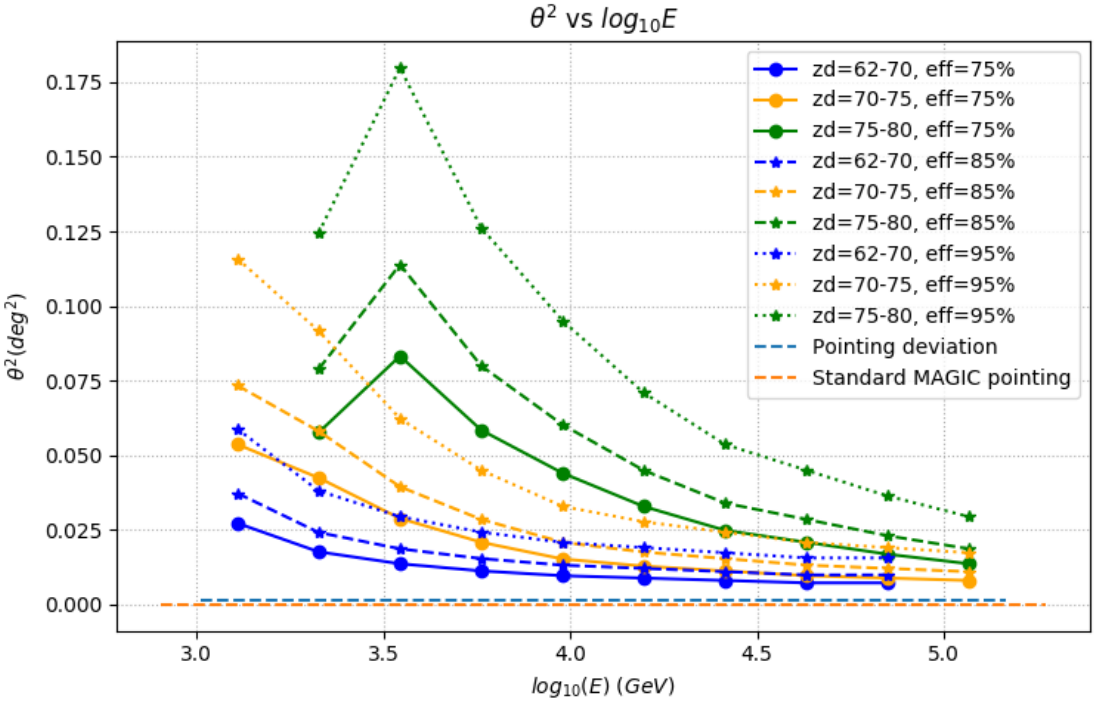

Figure 3.15: θ^2 dependence on the energy of the simulated event, zenith angle and chosen efficiency.

Additional mispointing results in a larger PSF than estimated by Monte Carlo simulation, impacting true event containment inside a given off-source angle cut. The resulting effect is energy dependent and so varies with energy. From this MAGIC VLZA simulation study, the consequence of this mispointing on the PSF is $\lesssim 4\%$ at ~ 3 TeV energies and $\lesssim 8\%$ at ~ 30 TeV energies.

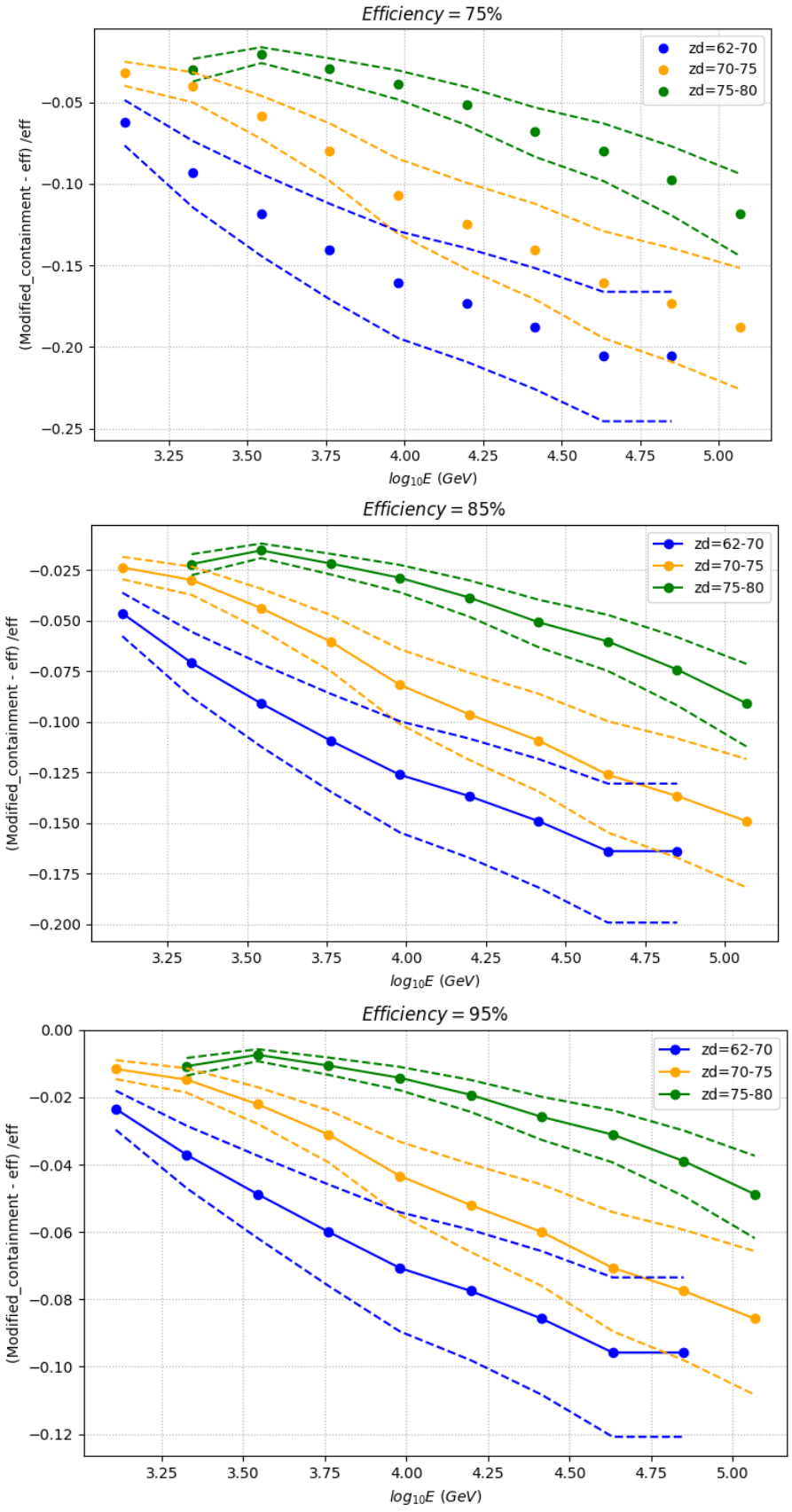

Figure 3.16: The plots represent how the efficiency changes when the mispointing is taken into account for different zenith ranges. The dashed lines represent the errors of the resulting values depicted by solid lines.

3.4.4. Energy bias and resolution

By comparing the true MC simulated event energies to those computed using standard MAGIC energy reconstruction algorithms, the instrument energy resolution and bias can be assessed. The migration matrices for both of the methods are displayed in Figure 3.17. To evaluate the reconstruction's precision, a Gaussian distribution was fit to the scaled $(E_{est} - E_{true})/E_{true}$ distribution of the estimated energies E_{est} in bins of E_{true}. The mean of this distribution is used to quantify bias (Figure 3.18a), whilst its width indicates the energy resolution of the reconstruction method used (Figure 3.18b).

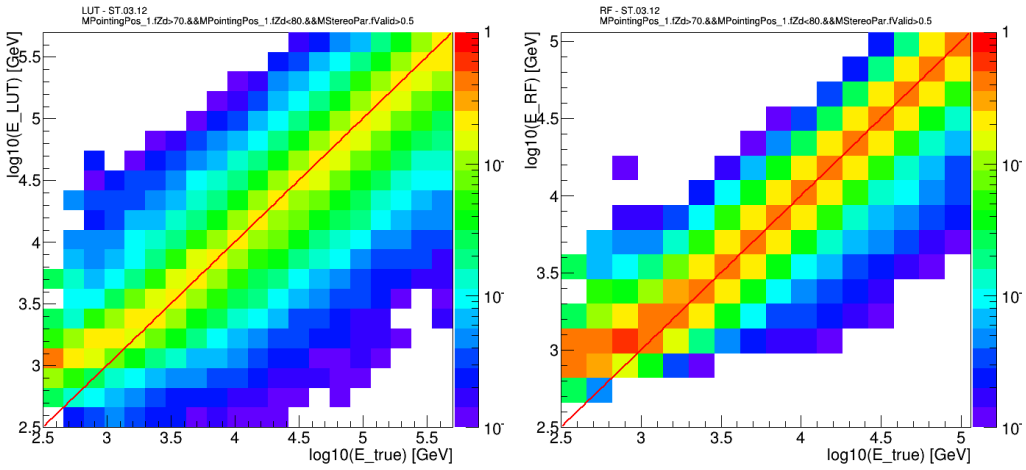

Figure 3.17: The migration matrices for the LUT (left) and for the RF (right) energy reconstruction method for data $70° - 80°$ zenith. The colorbar shows the normalized distribution of the events.

For the case of energy estimation the bias and resolution plots show that the RF method performs better than LUT method. Afterwards the energy unfolding method is applied using the migration matrices to correct the spectrum of the source.

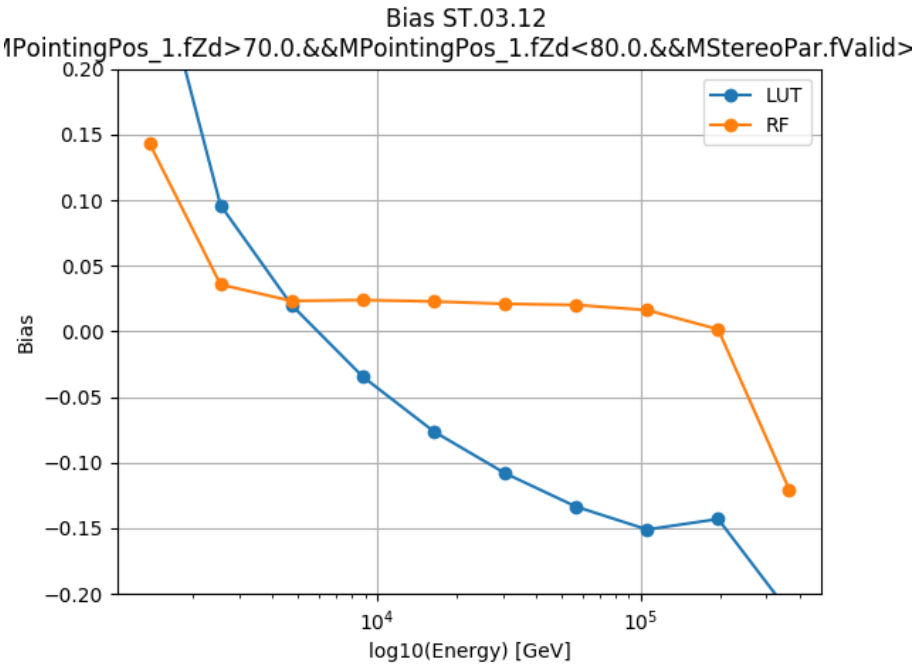

(a) Energy bias comparison for the LUT and RF energy reconstruction method.

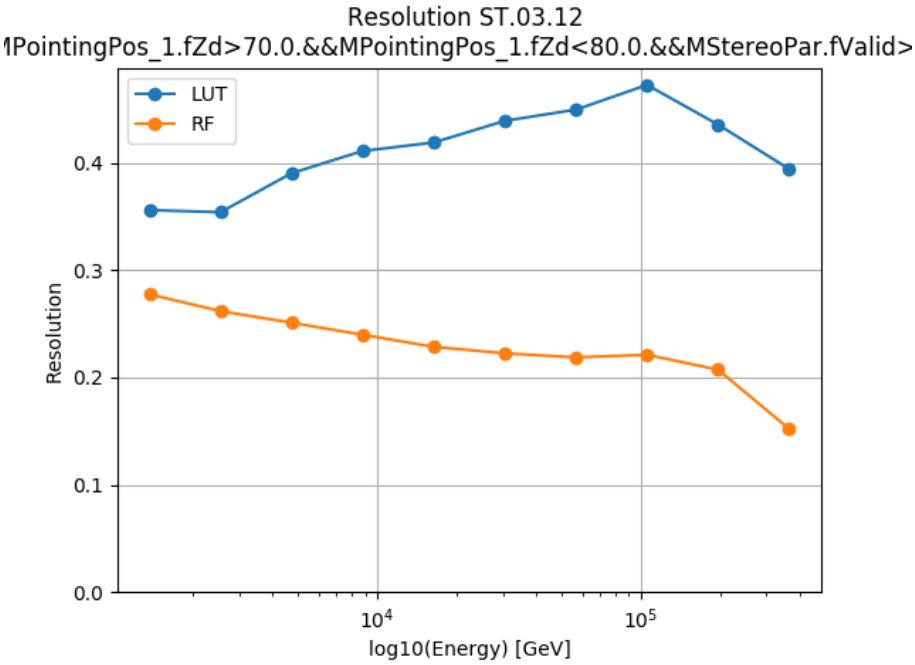

(b) Energy resolution comparison for the LUT and RF energy reconstruction method.

Figure 3.18: LUT and RF energy reconstruction method comparison

3.5. VLZA Crab Nebula results

3.5.1. Crab Nebula significance

For the older VLZA Crab dataset above 70°, the Crab Nebula signal at estimated energies above 30 TeV was detected (see subsection 2.4.5) at a $\approx 6.5\sigma$ significance level (Figure 3.19a). Combining the old and new dataset, and basically doubling the observation time, the significance rises to $\approx 9\ \sigma$ (Figure 3.19b) 30 TeV. And by combining the datasets the significance above 50 TeV was above 5σ. The sensitivity is similar in both cases.

3.5.2. Crab Nebula spectrum

Analysis cuts were used to keep 90% of the Monte Carlo gamma rays for each bin in energy. Despite the increase of the low energy threshold, the spectrum was reconstructed down to the energy of ~ 1 TeV. In Figure 3.20 the results of the 2014-2018 VLZA Crab dataset are compared to the whole VLZA Crab dataset. The results are in good agreement.

The Crab Nebula spectrum up to ~ 100 TeV is shown in Figure 3.21 which demonstrates that the previous HEGRA [74] spectrum, produced using approximately 400 hours of data, is within $\lesssim 20\%$ of the MAGIC results. In Figure 3.22, these data are compared to prior lower energy measurements, including the lower ZA MAGIC observations from [112]. The resulting spectrum does not support the cut-off at ~ 30 TeV previously suggested [95].

The dataset of the Crab Nebula which includes VLZA data and lower zenith data[112]) was fit with the log-parabola function $dN/dE = f_0(E/E_0)^{(\alpha+\beta\log_{10}(E/E_0))}$. The resulting fit produced $\chi^2 \approx 33$ over 14 degrees of freedom, showing that the log-parabola does not adequately describe the Crab Nebula's spectrum over the energy range 60 GeV to 100 TeV. The best-fit parameters are consistent to those in [112]; for $E_0 = 1$ TeV the parameters are: $\alpha = -2.48 \pm 0.03$, $\beta = -0.23 \pm 0.01$, and $f_0 = (2.95 \pm 0.27) \times 10^{-23}$ ph/(cm^2 s eV).

As illustrated in Figure 3.22, the general form of the Crab Nebula's γ-ray emission from GeV to 100 TeV may be reasonably represented using existing theoretical models such as [113], [117], and [114].

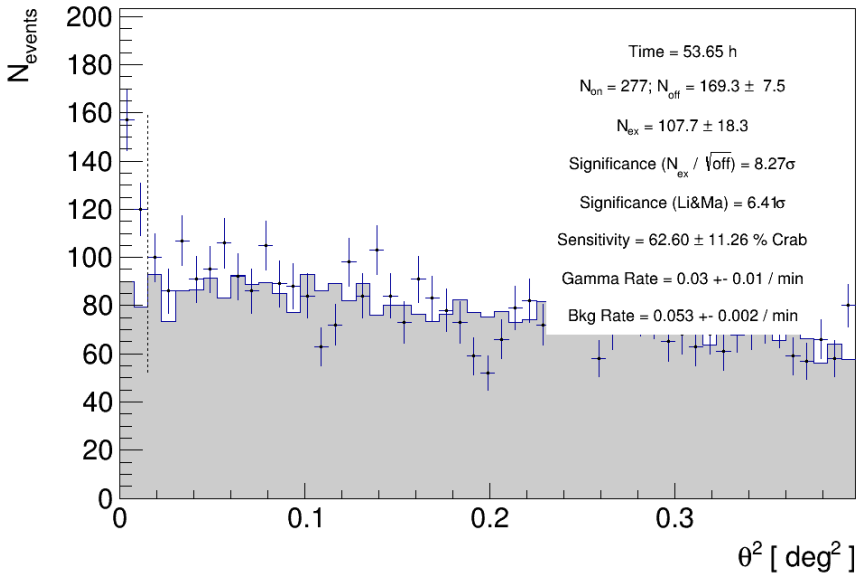

(a) Crab Nebula significance above 30 TeV using old VLZA dateset.

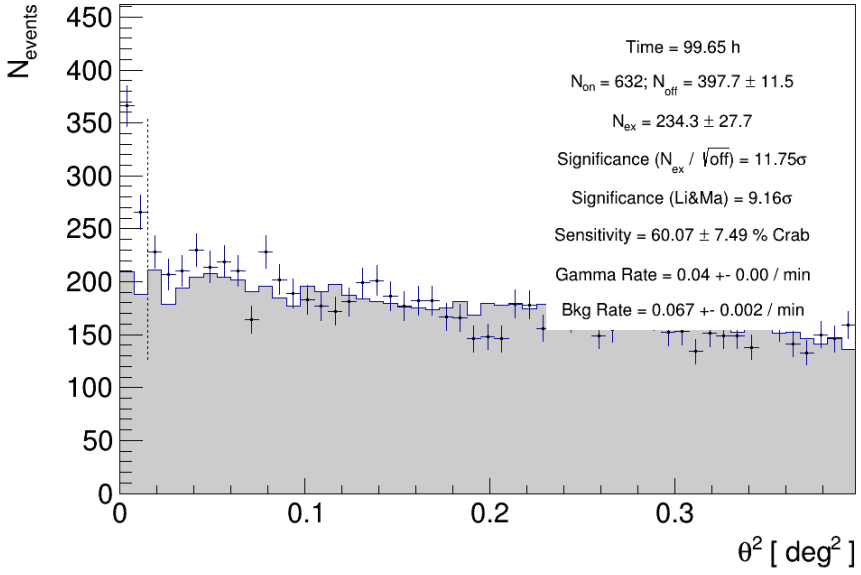

(b) Crab Nebula significance above 30 TeV using old+new VLZA dateset.

Figure 3.19: Crab detection significance results above 30 TeV.

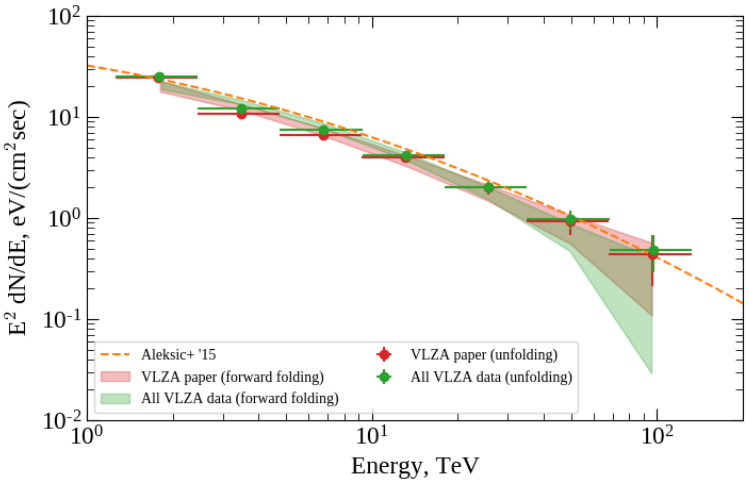

Figure 3.20: Spectral energy distribution of the Crab Nebula, obtained with MAGIC VLZA observations from 2014-2018 (red) [107] and the whole MAGIC VLZA dataset 2014-2021 (green). Results of the spectral unfolding (data points) and of the forward-folding (band) procedures are shown. Dashed orange line denotes the archival best fits to the Crab Nebula spectra [112].

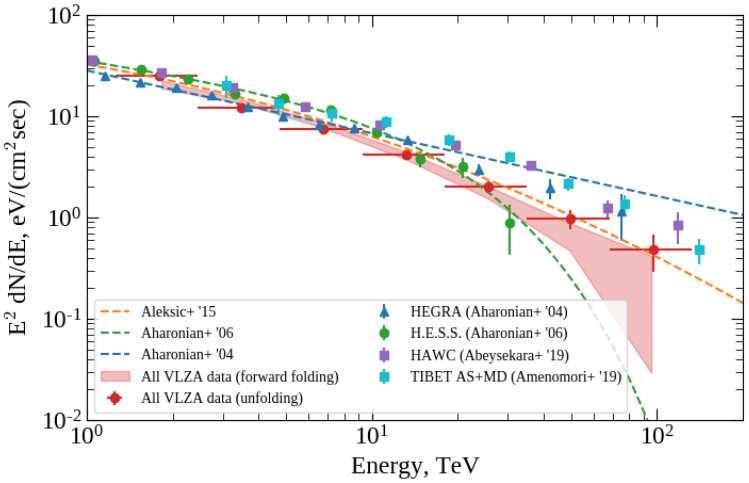

Figure 3.21: Spectral energy distribution of the Crab Nebula, obtained with MAGIC VLZA observations from 2014 to 2021 (red). Results of the spectral unfolding (data points) and of the forward-folding (band) procedures are shown. Dashed colored lines (blue, green, and orange, respectively) denote the archival best fits to the Crab Nebula spectra from [74], [95], and [112]. Data points from [74], [95], [96] and [97] are also shown for comparison.

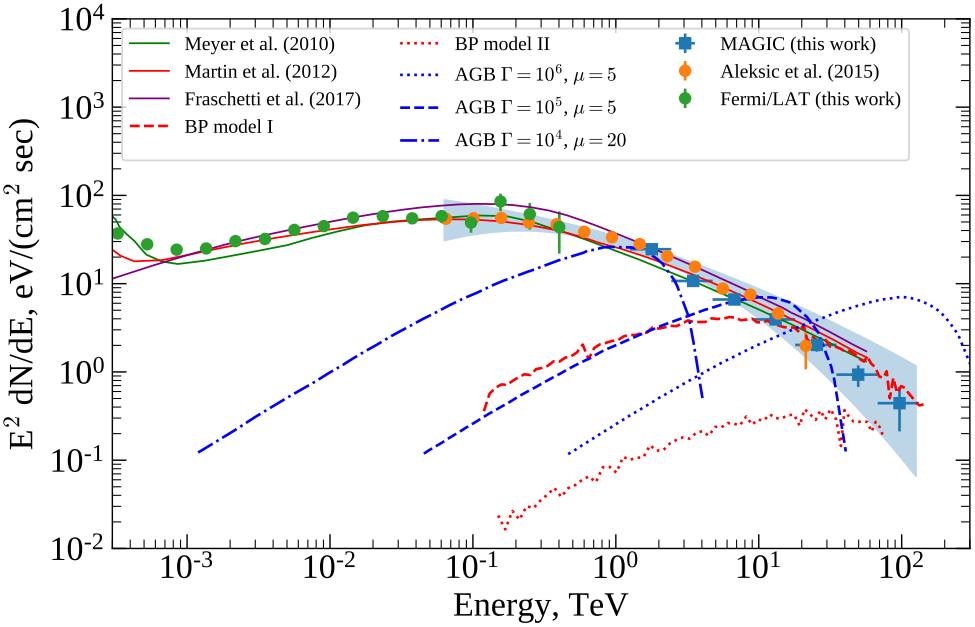

Figure 3.22: Crab Nebula spectrum obtained in [107] compared to the lower energy measurements with MAGIC [112] and *Fermi*/LAT. The blue shaded band denotes the 68% confidence flux range, estimated from the fit with the log-parabola function. Solid lines of different colours show several leptonic models from [113], [112] and [114], previously constructed for the Crab Nebula. Dashed lines denote predictions for hadronic contribution from [115] (BP), and [116] (AGB). Shown is the bulk wind Lorentz factor (Γ), and $\mu = n/\overline{n}$ is the effective target material density increase over its mean value.

3.6. SUMMARY

MAGIC telescopes can detect gamma rays up to $\sim$ 100 TeV in few tens of hours using the technique of VLZA observations.

The increasing distance between the telescope and the showers during VLZA observations effects the instrument's performance, resulting in approximately twofold degradation of the energy and the angular resolution compared to observations at small zenith angles [109]. This has an effect on the capability to infer the highest-energy flux from soft-spectrum sources. Given that this is a novel IACT observations technique, in the future certain improvements can be achieved with a more optimised analysis (like better random forest for gamma-hadron separation). The systematic uncertainties of the MAGIC VLZA observations are similar to those obtained at lower zenith observations [60, 109] in terms of hardware performance. The full report of the VLZA systematic uncertainties can be found in [107].

Nonetheless, the VLZA Crab Nebula data collected at a few tens of TeV match well with earlier, lower zenith angle results reported from HEGRA [74] in observations that were nearly eight times longer. Additionally, the VLZA results provided here indicate the extension of the source spectrum to 100 TeV and beyond. These findings corroborate those recently reported by HAWC [96], Tibet ASγ [97] and LHASSO [118].

While leptonic models may account for the majority of the existing multi-wavelength Crab Nebula flux observations, they do not allow for much flexibility in the spectral shape of the inverse Compton emission part [119]. The flux ratios in energies greater than 0.3 TeV, are generally compatible with the leptonic model expectation, following the argumentation in [119].

Some theories suggest that the Crab Nebula's maximum energy emission may be due in part to the interaction of accelerated particles with the surrounding medium[115, 116, 119, 120]. Extending the synchrotron radiation from the Crab Nebula to $\sim$ 100 MeV indicates the presence of PeV electrons. This implies that hadrons in the Nebula might likewise be accelerated to comparable energies. At TeV energies, protons would contribute to the gamma-ray flux via $p-p$ interactions. In Figure 3.22 projections from such models are shown with dotted and dashed lines.

As illustrated in Figure 3.22, the MAGIC data strongly favor the absence of a large hadronic contribution to the measured TeV flux. This means that the accelerated nuclei contribute a negligible amount to the pulsar wind power and/or do not interact with the dense Nebula filaments in general.

Just recently LHAASO Collaboration reported up to PeV photons coming from the Crab Nebula [118, 121]. But leptonic or hadronic origin of the gamma-ray emission above 60 TeV could not be confirmed with the inadequate statistics at the current moment.

Additionaly, it was previously assumed that gamma-ray emission beyond the Klein-Nishina limit must be hadronic in origin, as electrons incur rapid, severe energy loss during each scattering interaction [122]. However, [123] suggests that in high radiation surroundings, the maximum energy achieved via Inverse Compton scattering may be raised significantly to reach the UHE range. High radiation environments are defined by a balance between the radiation energy density U_{rad} and the magnetic energy density U_B, with $U_{\text{rad}}/U_B = \Xi_{IC} \gg 1$ necessary to accelerate electrons above 100 TeV [123].

An analysis of the available VLZA data above $\sim$ 10 TeV indicated no source variability exceeding a factor of two flux increase so far [124]. Further observations of the Nebula at these energies may allow to improve this constraint - or eventually detect the variability.

Overall, observations at very high zenith angles open a door for a new regime of the very-high energy MAGIC observations. They can increase the number of southern sources, available for the observations with MAGIC via the reduction of the minimal source declination. They can also be used as an efficient way to get measurements of the source spectra at highest energies during the eruptive events like Crab flares.

4. VLZA OBSERVATIONS OF EXTENDED SOURCES

4.1. MOTIVATION

Successful detection of Crab Nebula above ~ 30 TeV indicated that MAGIC could search for potential PeVatrons - at least those comparable in flux with the Crab Nebula in the energy range > 10 TeV. To identify such sources a search was done through the published HAWC/H.E.S.S./VERITAS observations of Galactic sources of > 10TeV emission, for which the reported spectra are hard with $\Gamma \sim 2$ and displayed no evidence for cut-off above several tens of TeV. The recently distributed HAWC detections above 56 TeV [86] were also checked. The list of candidates is shown in Figure 4.1 where their reported spectra is compared with the MAGIC VLZA sensitivity. Based upon this, the source chosen for observations by MAGIC was Dragonfly (MGRO J2019+37) in 2018.

In 2019 a simulation was made to check the excess counts for the candidate sources to be observed that year. This included weighting events by source extension, pointing strategy and spectrum. From Figure 4.2 it can be seen that at ~ 100 TeV HESS J1809-193 had the most excess counts, so that was one of the reason it was chosen for observations.

It is worthy to note, that the target sources are mildly extended beyond the MAGIC VLZA PSF, which allows to study the acceleration as well as diffusion of the PeV energy cosmic rays. The detailed studies like this can not be performed with the lower angular resolution instrument like HAWC and remain only accessible to the IACTs.

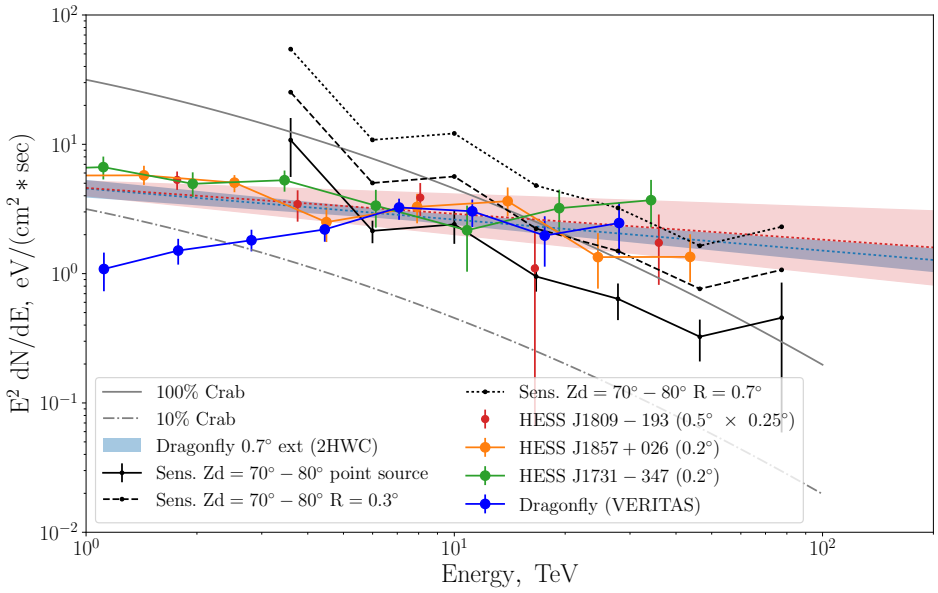

Figure 4.1: Summary of the archival data on the proposed targets, combined with the VLZA sensitivity curves for different sources extensions. For the sources for which the spectral "butterflies" were available (Dragonfly [125] and HESS J1809-193 [126]), they are also shown for comparison.

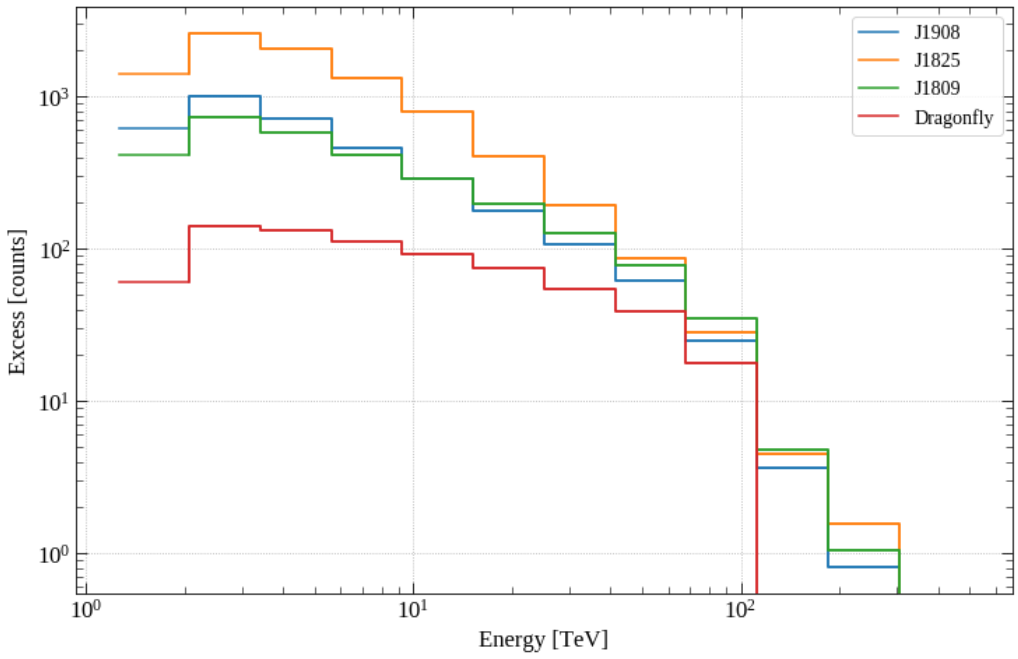

Figure 4.2: Simulated excess counts for candidate sources to be observed for 50 h in the VLZA regime in 2019.

4.2. EXTENDED SOURCES ANALYSIS

4.2.1. Diffuse Monte Carlo data

Instrument response functions (IRFs) of Cherenkov telescopes are usually evaluated by means of MC simulations. For many practical purposes, it is enough to evaluate IRFs for point-like gamma-ray sources. However for the extended sources diffuse Monte Carlo simulations are needed. Diffuse MC data was used to simulate the telescope performance. The MCs had been generated in a way that the events were randomly distributed between 0 and 2.5° from the camera center, thus simulating an extended source. The MCs were simulated with the maximum energy being 500 TeV and processed as as described in subsection 3.3.3.

4.2.2. SkyPrism

The analysis of the extended or off-centred sources starts differing from the standard approach in the higher level of the MARS analysis chain. With the standard MARS tools only sources with an extension smaller than the wobble offset and situated at an camera offset, where the acceptance is flat enough (up to 1 deg), can be analysed.

Recently a novel tool was developed for the use in MAGIC, called SkyPrism [127]. SkyPrism can perform spatial likelihood fitting of the source(s) in the FoV and compute the resulting skymaps and SEDs. It is suited for extended sources, sources far off-centre of the camera, or overlapping sources. The procedure of the spatial likelihood differs significantly from the standard tools which are suitable only for point source analyses. SkyPrism uses a 2D spatial modelling (3D if energy is considered) of the measured sky signal. Applying the instrument response function (IRF) (which is created from the Monte-Carlo simulations and the pointing history of the data) to an assumed source model, it can generate an image of the model as it would be seen by the telescope. This model, along with the estimated background map, is fitted to the measured sky image to estimate the most likely flux of the model sources in the chosen sky region. The SkyPrism chain is depicted in Figure 4.3.

SkyPrism offers 3 background estimation techniques (illustrated in Figure 4.4):

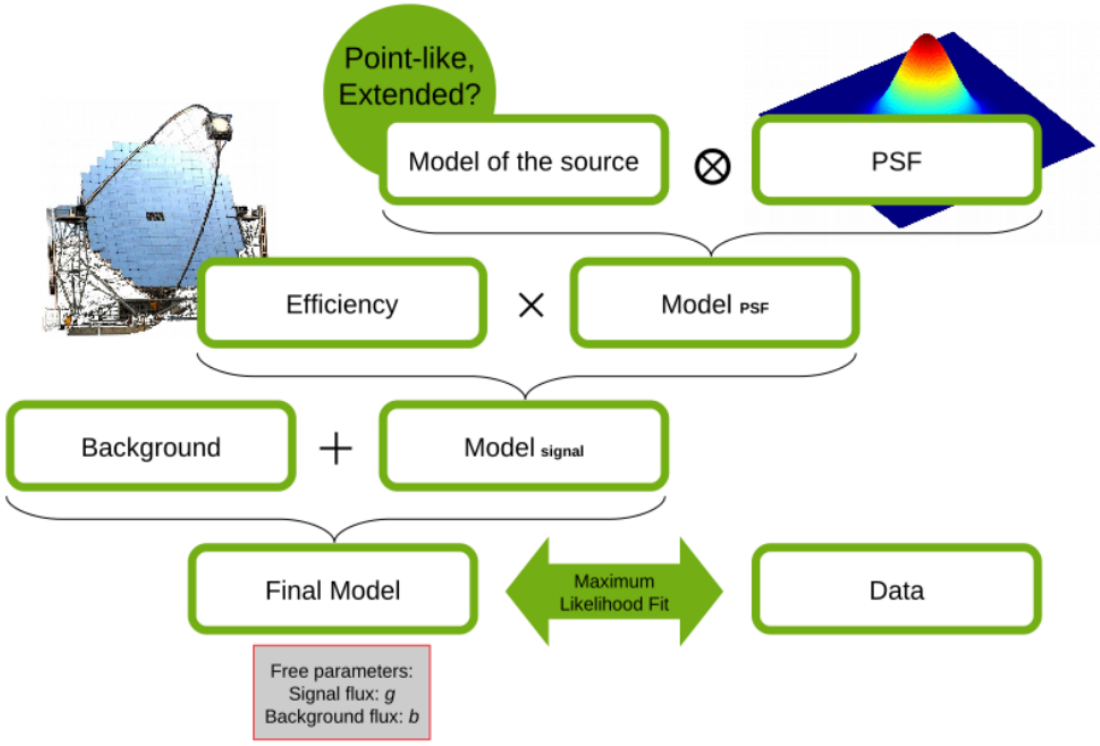

Figure 4.3: SkyPrism chain to obtain and fit the model of the data. Requires knowledge of the instruments IRFs across the field of view.

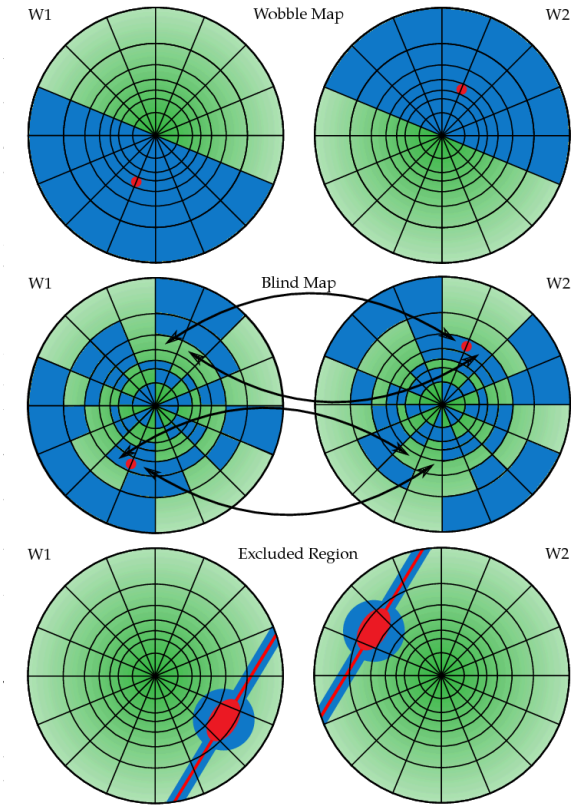

Figure 4.4: Various methods for generating a background camera exposure model from wobble observations. The position and extension of the source are indicated by a red spot, ellipse, or stripe. The blue shading indicates bins that were omitted from the reconstruction of the background map. Adopted from [128], reproduced with permission ©ESO.

- Wobble map:
  Camera FoV in-between the wobbles is split into parts and the one without the source is take as the background.
- Blind map:
  The per-pixel median value in-between the wobbles is taken as the background.
- Exclusion map:
  Certain sky regions are excluded from the background construction; otherwise resembles blind map.

The source fluxes are optimally estimated in each energy bin by maximising the Pois-

sonian likelihood of the observed number of counts given the source model and background:

$$C_{\alpha\beta}^{\mathrm{mod}} = \sum_{p} \left[\left(\mathscr{S}_{ij}^{p} \times \mathscr{E}_{ij} \right) \otimes \mathscr{P}_{\alpha\beta}^{ij} \right] + \mathscr{B}_{\alpha\beta} \tag{4.1}$$

$$\mathscr{L} = \prod_{\alpha\beta} \mathrm{e}^{-C_{\alpha\beta}^{\mathrm{mod}}} \frac{C_{\alpha\beta}^{\mathrm{mod}\, C_{\alpha\beta}^{\mathrm{obs}}}}{C_{\alpha\beta}^{\mathrm{obs}}!} \tag{4.2}$$

where $C_{\alpha\beta}^{\mathrm{obs}}$ are the measured counts in each pixel of the sky map, $\mathscr{S}_{ij}^{p}$ the model source (p denotes the source number in the model), $\mathscr{E}_{ij}$ the exposure maps, and $\mathscr{B}_{\alpha\beta}$ the background maps, while $\mathscr{P}_{\alpha\beta}^{ij}$ is the PSF model, mapping an (i, j) camera pixel to (α, β) sky pixel.

4.3. DRAGONFLY OBSERVATIONS

4.3.1. Introduction

The Cygnus region is a near (1.4 kpc), active star forming region and it is one of the brightest regions in diffuse gamma rays in the northern-hemisphere [129]. The Milagro Collaboration discovered a very extended source MGRO J2019+37 [130], which is the brightest Milagro gamma-ray source in the Cygnus region. The measured flux was about 80% of the Crab Nebula flux above 12 TeV and with no identified counterparts at other wavelengths. Its extent was measured to be about 1° with the most plausible interpretation that is a PWN powered by the young, energetic pulsar PSR J2021+3651 ($\dot{E} = 3.4 \times 10^{36}$ erg/s).

Previous short observations with VERITAS [131] and MAGIC [132] in 2008 led to upper limits consistent with the Milagro source being extended and having a hard spectral energy distribution. The ARGO-YBJ experiment also reported a non-detection of the source [133], with a claim that the source may be variable. However the Tibet Air Shower array has detected an extended VHE source in the same direction [134].

In 2014, the VERITAS collaboration performed a deep observation of this region [125]. VERITAS resolved MGRO J2019+37 into a point source VER J2016+371 and an extended source VER J2019+368, claiming the latter is the cause for the majority of Milagro emission. Its centroid is located at $\alpha_{J2000} = 20^h19^m25^s \pm 72^s_{stat}, \delta_{J2000} = 36^\circ48'14'' \pm 58''$ with an angular extension estimated to be $0.34^\circ \pm 0.03^\circ_{stat}$ along the major axis and $0.13^\circ \pm 0.02^\circ_{stat}$ along the minor axis with the orientation angle 71° east of north as can be seen in Figure 4.5. The energy spectrum of VER J2019+368 was derived from a circular region of 0.5° radius and extends from 1 to 30 TeV where it was fit by a power law model. The spectral index was determined to be $\gamma = 1.75 \pm 0.08_{stat} \pm 0.2_{sys}$ with a differential flux at 5 TeV of $(8.1 \pm 0.7_{stat} \pm 1.6_{sys}) \times 10^{-14}$ TeV^{-1} cm^{-2} s^{-1}.

In the 2017 survey [135] HAWC published the data for 2HWC J2019+367. It has a spectral index of $\gamma = -2.29 \pm 0.06$ with a differential flux at 7 TeV of $30.2 \pm 3.1 \times 10^{-15}$ TeV^{-1} cm^{-2} s^{-1}. The integrated flux obtained by the fit of the HAWC source is more consistent with the Milagro measurement than the VERITAS measurement.

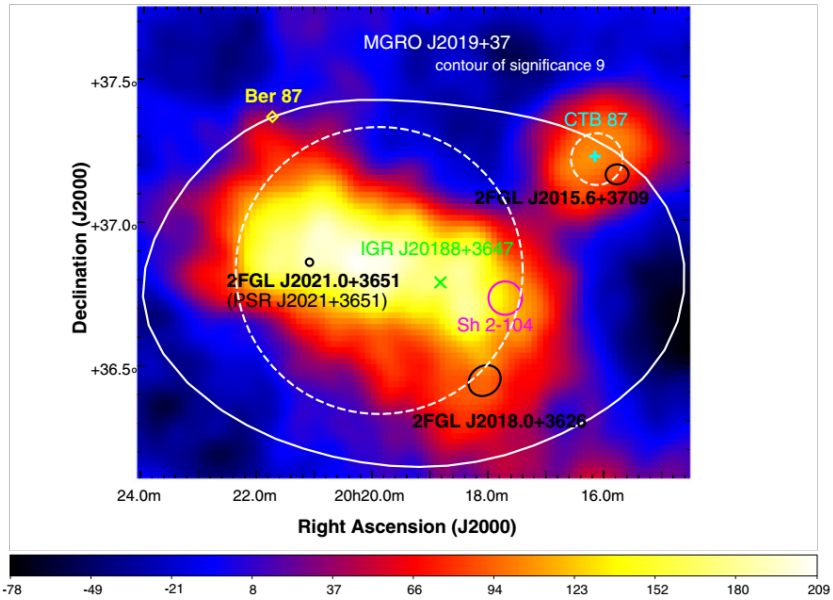

Figure 4.5: VHE gamma-ray excess map of the MGRO J2019+37 region above 600 GeV adopted from [125], reproduced with permission ©AAS.
The color bar indicates the number of excess events within a search radius of 0.23°, which corresponds to the extended source search analysis in [125].

VERITAS again performed a study of this area in 2018 [136]. The source was fit with an asymmetric Gaussian with semi-major axis of $0.34^\circ \pm 0.02^\circ_{stat} \pm 0.01^\circ_{sys}$ and semi-minor axis of $0.14^\circ \pm 0.01^\circ_{stat} \pm 0.02^\circ_{sys}$. However the spectrum has significantly lower flux compared to the previous VERITAS spectrum [125] due to the smaller region used in the recent analysis. Also the spectral index was not as hard as in previous measurements.

The data were fit with a power law (PL) model, as in equation 4.3, where N_0 represents the normalization constant, E_0 the normalization energy and γ represents the spectral index.

$$\frac{dN}{dE} = N_0 \left(\frac{E}{E_0} \right)^{-\gamma} \tag{4.3}$$

The best fit parameters were found to be:
$N_0 = (1.02 \pm 0.11_{stat} \pm 0.20_{svs}) \times 10^{-16}$ GeV^{-1} cm^{-2} s^{-1}, $E_0 = 3110$ GeV, $\gamma = 1.98 \pm 0.09_{stat} \pm 0.20_{sys}$.

4.3.2. MAGIC data taking

The aim of MAGIC observations was to perform measurements in the γ-ray domain above several tens of TeV, which has not been deeply studied so far, expecting to find the hard spectrum extending above tens of TeV. Since PWN are among the possible galactic sources of cosmic rays, it is very interesting to try to measure the maximum energy of the emission particles for this source.

Dragonfly coordinates (Right ascension: 20h 21m 06s, Declination: $+36°51' 05''$) were tracked with both telescopes in stereoscopic mode where only events simultaneously triggering both telescopes are recorded. Data were taken during dark nights without moon, environment humidity below 90%, no rain, with wind speeds below 50km/h and average PMT current below 30 μA. The optical focusing of the telescopes was set to 10 km. The principle of operation of IACT telescope during data taking was previously described in section 2.3 and section 2.4.

The data sample analyzed was accumulated from January 2018 until September 2018 in the zenith angle range 62° - 80° in order to utilize the increase of the collection area when observing with very large zenith angles. The dataset comprises of $\simeq$ 45 hr of good-quality data taken during dark time. The observations were performed in wobble-mode [106] at four symmetrical positions 0.4°away from the desired sky position and with standard angle offsets of 0°, 90°, 180°, 270°which allowed a simultaneous background estimation. The pointing was centered on the PSR J2021+3651 location which is offset from the VER J2019+368 by about 0.3°. Because of this special care has been taken during the analysis as the source was not in the center of the skymaps.

4.3.3. Data analysis

The low level data has been analyzed with standard MARS routines.
Events taken during bad weather conditions were discarded with the procedure described in subsection 3.3.2. Standard MARS routines were used to reconstruct the incoming direction of the gamma rays. A Random Forest (RF) multivariate analysis method was used to reconstruct the energy of the initiating particles of the extended air showers. The cosmic ray background suppression was also based on the RF method.

Skyprism [128] has been used for high-level extended source analysis. The method chosen to reconstruct a background exposure model was the so called "Blind Map" (Figure 4.4). The blind map option calculates the combined background camera exposure using the median value in each pixel of the single wobble pointing normalized exposure times. Typical selection cuts with 90% efficiency, that were based on the MCs, for γ-ray/hadron separation were used. The source was modeled as an extended source with a power law spectrum and the model image was assumed to be an asymmetric 2D Gaussian. The 1σ angular extension was set as 0.34° along the major axis, and 0.14° along the minor axis as reported by [136]. Background was set to be isotropic.

4.3.4. Results and discussion

MAGIC excess map above 1 TeV reveals extended emission in form of an asymmetric 2D Gaussian, as shown in figure 4.6. The MAGIC emission overlaps with the extended emission seen by VERITAS [136]. The low energy threshold of those VERITAS observations was around 400 GeV, while for MAGIC VLZA observation that threshold was $\sim$ 1 TeV. There were no indication of 2 candidate sources comprising VER J2019+368 in this dataset which was hinted in [136].

One issue is that the coordinates observed by MAGIC were pointed to the pulsar PSRJ2021+3651 location. But the emission region of VER J2019+368 is offset by about 0.3° in Right ascension.

The spectrum obtained from the MAGIC observations was fit by a power law model (PL) as in equation 4.3.

The source was detected with a significance exceeding 5σ above 1 TeV as shown in Figure 4.7.

After unfolding, the best fit results are shown in Table 4.1 together with results from other experiments, while the spectrum is shown in Figure 4.8. The integrated flux obtained in the 1-30 TeV range is $(3.9 \pm 0.6) \times 10^{-12}$ cm^{-2} s^{-1}. Result given here provides a higher integrated flux compared to the results published by VERITAS, where it was obtained to be 1.7×10^{-12} cm^{-2} s^{-1} in 2014 and 9.5×10^{-13} cm^{-2} s^{-1} in 2018. This can be explained by the smaller integration region used by VERITAS in 2014 and 2018, where it was set to 0.5° and 0.23° respectively as seen in Figure 4.9. The result obtained here is more in line

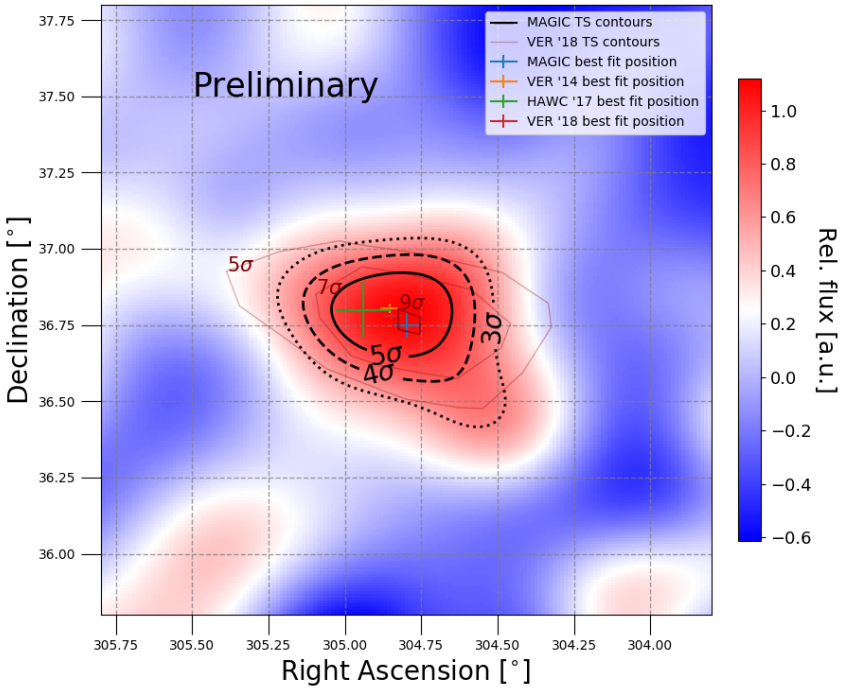

Figure 4.6: Relative flux map measured by MAGIC with the gold contours representing MAGIC significance. The black lines represent contours from VERITAS analysis in 2018 [136].

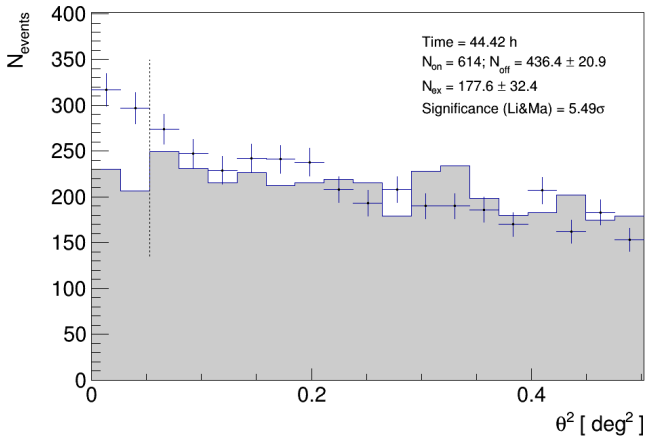

Figure 4.7: Since this is an extended, off centered source the off from wobble partner method was used for estimating detection significance. Position of the source was used from the skymap fit. Signal cut is the same as in VER '14 and VER '18 analysis. PSF had been determined from contemporaneous VLZA Crab data.

with the HAWC result with an extended source assumption (R=0.7°) which amounts to 3.6×10^{-12} cm^{-2} s^{-1}. This is expected as the used integration radius of HAWC contains ∼95% of the events of the 2D Gaussian used in this analysis.

These results present the highest energy emission of this source measured by IACTs. The interpretation of the results is ongoing, but recently even higher γ-ray energies have been detected from this source from particle detector array experiments such as HAWC[137], Tibet ASγ Collaboration[138] and LHAASO [139].

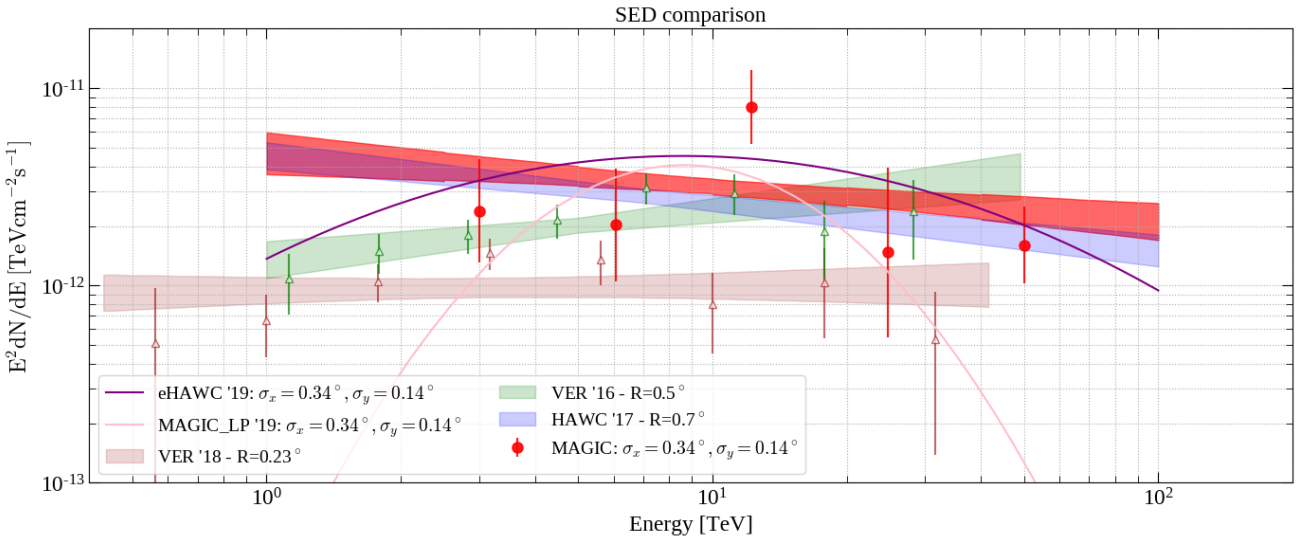

Figure 4.8: Dragonfly SED comparison.

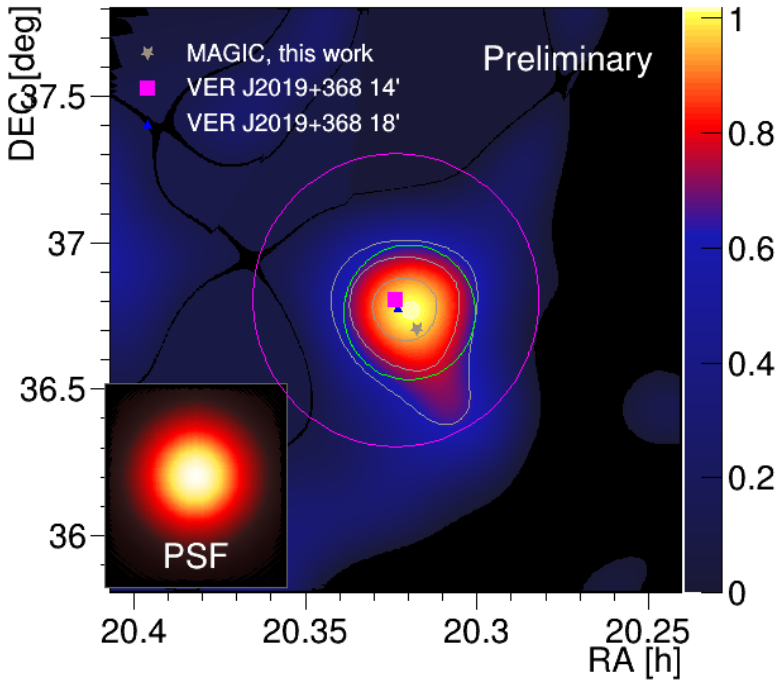

Figure 4.9: MAGIC flux skymap with the marked previous VERITAS best fitted positions. The green circle represents the extraction region used in the VER '18 [136] and in this analysis for significance calculation, radius of that circle is 0.23°. VER '14 [125] also used 0.23°for detection, but used a 0.5°circle for flux estimation, that is represented by the purple circle.

	VERITAS **2014** [125]	HAWC **2017** [135]	VERITAS **2018** [136]	This work
Γ	1.75 ± 0.08	2.24 ± 0.04	1.98 ± 0.09	2.14 ± 0.08
$F_0 \left[\text{TeV}^{-1}\text{cm}^{-2}\text{s}^{-1}\right] \times 10^{-14}$	8.1 ± 0.7	5.8 ± 0.5	10.2 ± 1.1	8.2 ± 0.7
$E_0[\text{TeV}]$	5	7	3.11	7
Integration region	$R = 0.5°$	$R = 0.7°$	$R = 0.23°$	$\sigma_x = 0.34°$ $\sigma_y = 0.14°$

Table 4.1: Comparison of the spectrum measurements from different experiments.

4.4. HESS J1809-193

4.4.1. Introduction

HESS J1809-193 is an unidentified extended Galactic source first discovered by the H.E.S.S. collaboration and classified as a pulsar wind nebula due to its potential association with the young and energetic ($\dot{E} = 1.8 \times 10^{36}$ erg/s) radio pulsar PSR J1809-1917 [140]. The TeV emission of the source was reported to be at a Galactic Longitude and Latitude of $(11.11 \pm 0.08)^\circ$ and $(-0.02 \pm 0.03)^\circ$ with an extension of $(0.40 \pm 0.05)^\circ$ with a majority of the emission emanating from a 0.25° sub region. The peak of the VHE emission lies about $6'$ to the south of PSR J1809-1917. The TeV spectrum of the source was fit by a power-law with a spectral index of 2.2.

A search was later carried for the counterpart of the proposed PWN driven by PSR J1809-1917 using deep radio observations from the Karl G. Jansky Very Large Array[141] (shown in Figure 4.10), but the counterpart was not found. Additionally, their study of the interstellar medium in the direction of the source revealed several molecular clouds at the shock front of the SNR G11.0-0.0, a location that coincides with the brightest peak of the TeV gamma-rays, as well as evidence for interaction between the SNR and the clouds. The distance between the SNR and the clouds is estimated to be 3 kpc by [141]. In view of this, hadronic interactions were proposed[141] to explain the origin of the gamma-ray emission.

Recently, a GeV counterpart to HESS J1809-193 was discovered [142] with a similar spectral index in both the GeV and TeV ranges ($\Gamma \sim 2.2$). This is difficult to explain with only IC emission from high-energy electrons alone and rather indicates a hadronic emission origin. For the case of HESS J1809-193, the hadronic scenario necessitates a proton distribution extending up to 1 PeV. This source is modelled best as a radially symmetric disk with a radius of $0.5^\circ \pm 0.15^\circ$, located at Galactic longitude (l) and latitude (b) of l, b = $11.05^\circ \pm 0.20^\circ$, $-0.12^\circ \pm 0.20^\circ$. This source corresponds to 4FGL J1810.3-1925e in the 4FGL-DR2 catalogue [143, 144]. Modelling the joint spectrum with hadronic emission from *p-p* interactions with a particle population of a power-law with an exponential cutoff at 1 PeV, [142] predicts a total energy of $\sim$6% of the total energy of a typical supernova

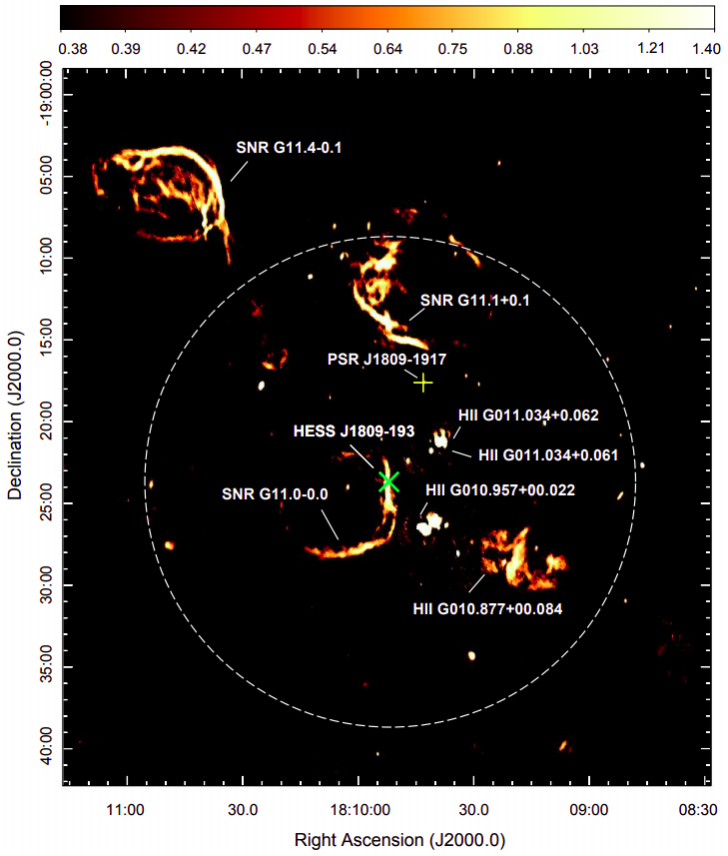

Figure 4.10: Radio continuum image at 1.4 GHz of the region surrounding the pulsar PSR J1809-1917. The location of PSR J1809-1917 is shown with a yellow plus sign, while the best-fit position of the centroid of HESS J1809-193 is indicated with a green cross. The white dashed circle denotes the measured extension of the VHE source in terms of the sigma (rms) of a symmetric 2D Gaussian fit to the TeV data. Image adopted from [141], reproduced with permission ©ESO.

(10^{51} erg) assuming a particle density of 10 cm^{-3} and a distance 3.5 kpc.

HESS J1809-193 is modelled in the H.E.S.S. Galactic Plane Survey (HGPS) with three Gaussian components with their spatial parameters described in Table 4.2 [145]. The total emission is described at l, b = $11.11 \pm 0.08, -0.02 \pm 0.03$ with a R_{68} containment radius of 0.64 ± 0.08 degrees. The TeV spectrum is described as a power-law with a differential flux of $(7.44 \pm 0.53) \times 10^{-12}$ cm^{-2} s^{-1} TeV^{-1} at 1 TeV and an index of -2.38 ± 0.07.

Recently, the HAWC Collaboration reported significant detection (6.97σ) of HESS J1809-193 above 56 TeV [86]. They also reported a consistent extension of $(0.34 \pm 0.13)^{\circ}$

Source Name	RAJ2000 [deg]	DECJ2000 [deg]	l [deg]	b [deg]	R_{68} [deg]	Spatial Model
HESS J1809-193	272.53 ± 0.08	-19.33 ± 0.03	11.11 ± 0.08	-0.02 ± 0.03	0.64 ± 0.07	Gaussian
HGPSC 056	272.16 ± 0.08	-19.45 ± 0.07	10.83 ± 0.08	0.22 ± 0.07	0.58 ± 0.05	Gaussian
HGPSC 058	272.39 ± 0.01	-19.39 ± 0.01	10.99 ± 0.01	0.07 ± 0.01	0.16 ± 0.01	Gaussian
HGPSC 059	272.96 ± 0.03	-19.18 ± 0.03	11.44 ± 0.05	-0.30 ± 0.03	0.45 ± 0.03	Gaussian
4FGL J1810.3-1925e	272.59	-19.43	11.05 ± 0.20	-0.12 ± 0.20	0.41 ± 0.12	Disk
3HWC J1809-190	272.46	-19.04	11.33	0.18	-	Point Source
eHWC J1809-193	272.46 ± 0.13	-19.34 ± 0.14	11.015 ± 0.13	0.00 ± 0.13	0.51 ± 0.19	Gaussian

Table 4.2: The positions and extensions, and reported uncertainties, of GeV and TeV sources associated with HESS J1809-193 [86, 142, 145]

with that of the highest flux sub-region from the HGPS.

Identifying true nature of HESS J1809-193 is difficult as there are a number of known astrophysical sources that are within in the R_{68} radius. Four SNRs are within the R_{68} radius: SNR G011.1+00.1, SNR G011.4-00.1, SNR G011.0-00.0, and SNR G011.2-00.3. SNR G011.2-00.3 and SNR G011.4-00.1 are unlikely to be the origin of the TeV emission as they are too far away from the highest flux component of HESS J1809-193 as can be seen in Figure 4.11. SNR G011.1+00.1 and SNR G011.0-00.0 are closer to the highest flux component of HESS J1809-193 as reported in HGPS.

The hypothesis that HESS J1809-193 is accelerating protons to PeV energy could be important to cosmic ray origin theories. Although the current paradigm for the origin of cosmic rays requires that SNRs act as PeVatrons for at least some time during their evolution, no known SNR shows a gamma-ray spectrum that is compatible with this idea. The confirmation of the acceleration of cosmic rays to PeV energies in the HESS J1809-193/G11.0-0.0 system would be a considerable advancement in the understanding of the origin of cosmic rays, as it would be the first case involving a known SNR.

4.4.2. MAGIC data taking

HESS J1809-193 coordinates (Right ascension: 18h 09m 31s, Declination: -19°25′ 06″) were tracked with both telescopes in stereoscopic mode where only events simultane-

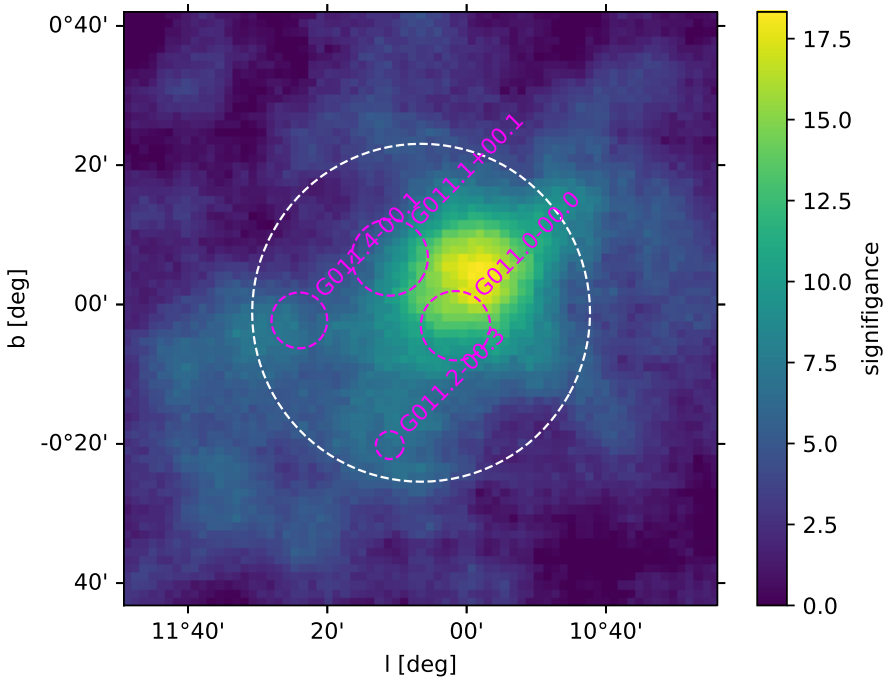

Figure 4.11: The positions of SNRs compared to significance map from HGPS[88]. The white circle radius represents the source size, 1 sigma of a Gaussian being 0.4°, as reported from the HGPS.

ously triggering both telescopes are recorded. Data were taken during dark nights without moon, environment humidity below 90%, no rain, with wind speeds below 50 km/h and average PMT current below 30 μA. The optical focusing of the telescopes was set to 10 km. The principle of operation of IACT telescope during data taking was previously described in section 2.3 and section 2.4.

MAGIC has observed J1809-193 between 2019 and 2021 and has collected $\simeq$ 70 hours after quality cuts excluding times of poor atmospheric transmission and technical problems. The data was taken under dark observational conditions [146] and the observations have been performed in wobble mode[106]. About 43 hours of data has been taken with wobble offset of 0.4° and angle rotations of 30°, 120°, 210° and 300°. While 27 hours of data has been taken with wobble offset of 0.6° and angle rotations of 70°, 160°, 250° and 340°. The wobble offset was increased in order to accommodate for the extension of the source (Figure 4.12). In both cases the angle rotations were chosen to avoid optically bright stars in the field of view of the telescopes. The source has been observed at very large zenith angles, between 60° zenith and 80 °zenith, to increase the effective

area as demonstrated by MAGIC campaign on the Crab Nebula (see chapter 3).

4.4.3. Data analysis

Usually the transparency of the atmosphere during MAGIC observations is monitored using a LIDAR [61]. However, the atmospheric thickness at these zenith angles reaches $\sim$ 100 km whereas the LIDAR system can measure the transmission up to $\sim$20 km. Thus, instead a cut on the number of stars in the field of view (FoV) of the telescope was performed in order to select only data with good atmospheric conditions as explained in subsection 3.3.2. In this case the "starcut" (4.13) value has been increased to 25 (compared to Crab where it was 15) because the average number of stars in the field of view for this source is higher compared to the Crab Nebula because it is located in the Galactic plane.

The low level data has been processed and analysed using the *MARS* [104] software, including calibration, image cleaning, image parameterisation, estimation of the event energy, the arrival direction, and event classification.

The energy threshold of this data sample, taking into account the higher zenith angles, applying the analysis cut and weighting it with the spectrum of the source is $\sim$ 2.5 TeV.

Since there is not a lot of off contemporaneous data available at very large zenith angles, a part of the Crab Nebula dataset has been added to the off data sample used for training the estimators and classifiers. Since the rates are low at VLZA ($\sim$ 100 Hz) the data is dominated by the background so it can be used as off data. Still the amount of added Crab data to the off sample was chosen to be minimal as possible, just enough to have the same (or a bit more) number of events than the Monte Carlo gamma events in the zenith bins (Figure 4.14). Otherwise the excess MC data would be discarded in the training process.

Since this is an extended source the higher level data was further analysed using the SkyPrism tool [127] which is suited for the analysis of extended sources.

The background map has been constructed using the 3° field of view, but excluding the areas containing HESS J1809-193, J1813-178, J1808-204, J1804-216 sources. *ExclusionMap* method was used and 4 exclusion regions were specified around known TeV source HESS J1809-193, HESS J1813-178, HESS J1808-204, and HESS J1804-216 with

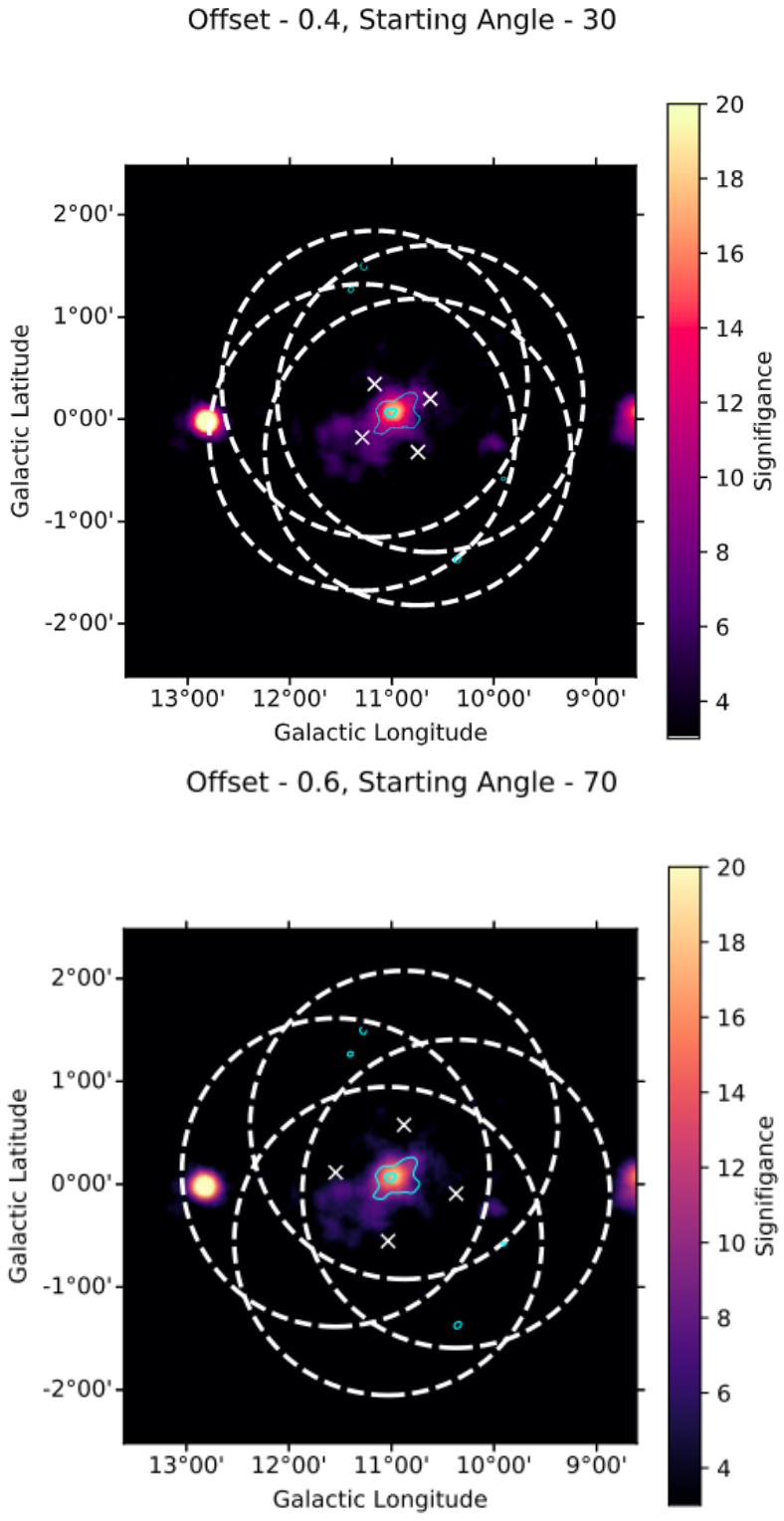

Figure 4.12: Plots show the significance map from the HGPS survey [88]. White crosses depict the wobble pointing positions and the dashed lines the MAGIC FoV. In the first cycle of observations 0.4° wobble offeset was used, while in the later cycles 0.6° wobble offset was used due to source extension.

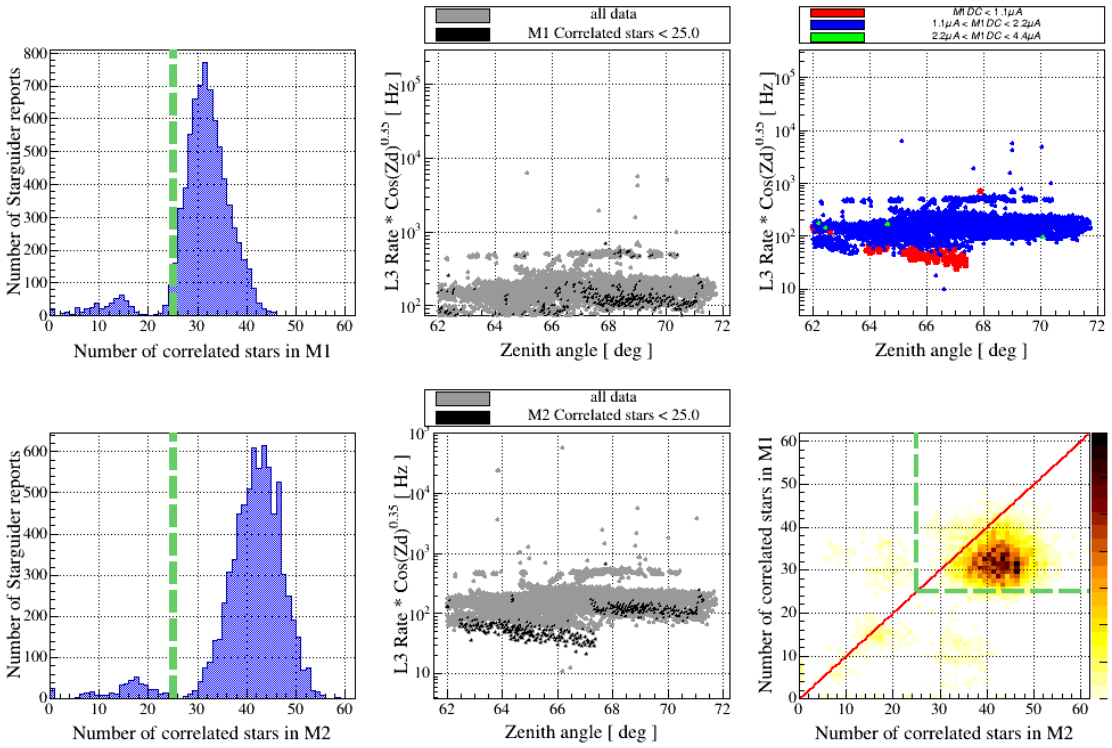

Figure 4.13: Data quality selection plot example for HESS J1809 data. The star-cut value has been increased to 25 due to denser Galactic background with respect to the Crab Nebula background.

a radius corresponding to the HGPS R_{70} value for each source. This ensured that the background calculation is not contaminated by signal from these 4 sources. The skymap was constructed to span 3° in each axis with 60 bins each resulting in 0.05° span per bin.

The best cut values were optimized using simulated MC data and separate off data sample. The source was simulated using the values from HGPS [88] for the spectrum and the extension. Based on the source spectrum, extension and pointing directions the MC and off data events were weighted accordingly. Then the size and hadronness cuts were optimized in order to produce the maximum significance as shown in Figure 4.15. No HESS J1809 data was used in this simulation, so there were no trials involved. For the analysis on the real data the size cut was lowered to 300 photoelectrons in order not to discard too much events at ∼TeV energies. As there was no big dependence on hadronness, typical selection cuts with 80 % efficiency, based on the MCs, for gamma-ray/hadron separation were used. Analysis was performed above ∼ 3 TeV to ensure the

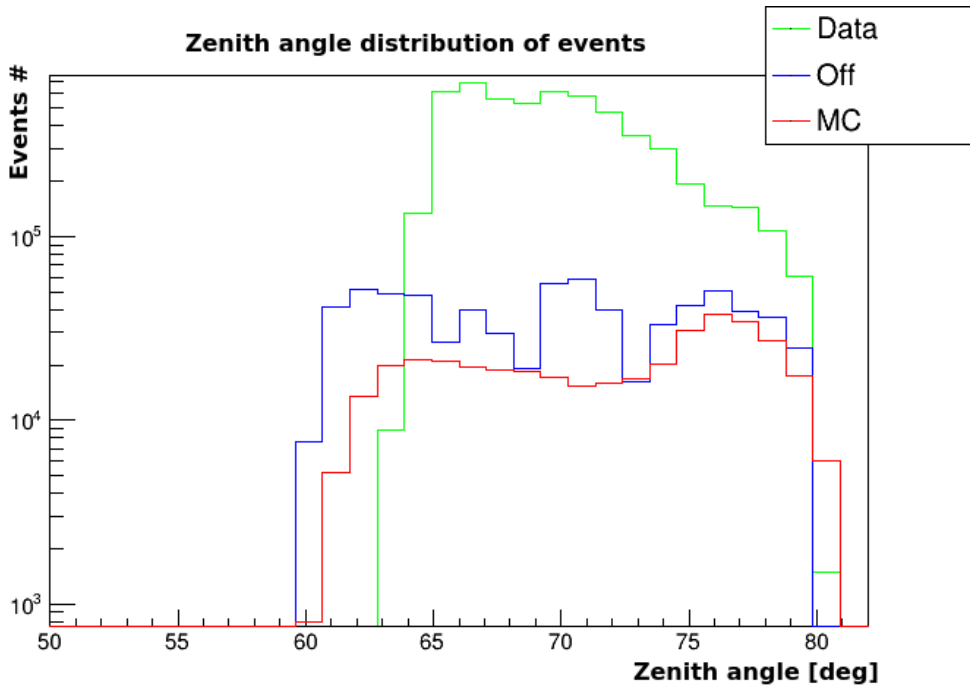

Figure 4.14: Distribution for HESS J1809-193 data, off and MC events in zenith bins. Some Crab data was added to the off data sample so that there is just enough off events to cover the MC events in each zenith bin.

best sensitivity from the VLZA technique as the threshold was around $\sim$ 2.5 TeV.

4.4.4. Morphology

To parameterise the morphology of HESS J1809-193, a spatial grid scan was performed using a maximum likelihood fit where each parameter is divided into a step size of 0.04 degrees. The grid scan is over a single energy bin assuming a spectral model of a power-law and spectral index of 2.5 and a morphology that does not evolve with energy.

Three models were tested to parameterise the morphology of HESS J1809-193 as measured by MAGIC: a Point Source, a radially symmetric disk, and a radially symmetric 2D Gaussian distribution. For the point source model the flux normalisation and the localisation are free parameters, whereas for the latter two the extension is an additional one. Figure 4.16 shows the parameter distribution for the localisation and extension tests. The results indicate that the extension of the source decreases with the increasing energy. The results of the likelihood scan can be seen in Table 4.3. The best result is the radially

Significance as a function of hadronness (rows) and size (columns).

	30	50	100	150	200	250	300	400	500	600	700
0.1	3.5	3.5	3.8	3.8	3.7	4.2	4	4.2	4.6	4.3	4
0.2	4.2	4.2	4.4	4.3	4.5	4.7	4.7	5.1	5.3	4.8	4.5
0.3	4.2	4.2	4.4	4.3	4.7	4.8	4.8	5	4.9	4.5	4.5
0.4	4.2	4.2	4.5	4.4	4.7	4.8	4.8	5	4.9	4.5	4.4
0.5	4.1	4.1	4.4	4.3	4.6	4.7	4.6	4.8	4.6	4.6	4.5
0.6	4	4	4.2	4.1	4.4	4.4	4.4	4.7	4.5	4.5	4.6
0.7	3.5	3.5	3.6	3.6	3.7	3.7	3.6	4	3.7	3.8	3.8

Figure 4.15: Significance as a function of hadronness (rows) and size in photoelectron counts (columns).

Model	l [°]	b [°]	R_{68} [°]	TS	TS_{ext}
Point Source	11.07 ±0.05	0.10 ±0.05	-	25.07	-
Disk	10.99±0.05	-0.03±0.05	0.30±0.07	48.58	23.51
Gaussian	10.95±0.05	0.03±0.05	0.44±0.07	51.86	26.79

Table 4.3: Results of the grid scan for HESS J1809-193 obtained by MAGIC. All sizes correspond to the R_{68} confidence interval. The errors are 1σ confidence level and are estimated by interpolating the grid points in each parameter space.

Spectral model	f_0 [cm^{-2} s^{-1} TeV^{-1}]	Γ/α	E_{cut} [TeV]/β	TS
PL	$(6.36 \pm 0.51) \times 10^{-14}$	2.37 ± 0.05	-	191.9
ECPL	$(9.39 \pm 0.45) \times 10^{-14}$	1.46 ± 0.41	33.90 ± 2.41	204.8
LP	$(7.43 \pm 0.89) \times 10^{-14}$	1.71 ± 0.08	0.80 ± 0.10	208.6

Table 4.4: The results of the MAGIC forward folding fit. The parameters are described in 4.4, 4.5, and 4.6. The errors represent the combined statistical and systematic uncertainties. The spectral models are normalised at $E_0 = 10$ TeV.

symmetric 2D Gaussian with a Test Statistic (TS) $TS_{ext} = 26.79$ when compared to the Point Source. This shows that HESS J1809-193 as seen by MAGIC is a significantly extended source and was therefore modelled as one for the spectral analysis study.

4.4.5. Spectrum

For the flux estimation, diffuse MCs were used to take into account the source's morphology to compute the IRFs. Following the study of systematic uncertainty on [105] and [109], there is a 15% systematic uncertainty on the energy scale, 11-18% for the flux normalisation, and 0.04 degrees for pointing accuracy for the VLZA case [107].

For the spectral analysis the best spatial model (radially symmetric 2D Gaussian) was used for estimating the spectral parameters. For the spectral analysis the estimated energy events were binned in five logarithmic energy bins from 3 to 400 TeV and four energy bins in true energy are binned logarithmically from 1.5 TeV to 200 TeV. Background was chosen to be isotropic with a log parabola cutoff spectrum. The forward folding results are shown in Table 4.4 and the best result for the MAGIC data the LogParabola over a power-law with 4.1σ obtained via a square root of difference of the TS values. The unfolded data points are shown in Figure 4.19 in comparison to *Fermi*-LAT, H.E.S.S., and HAWC.

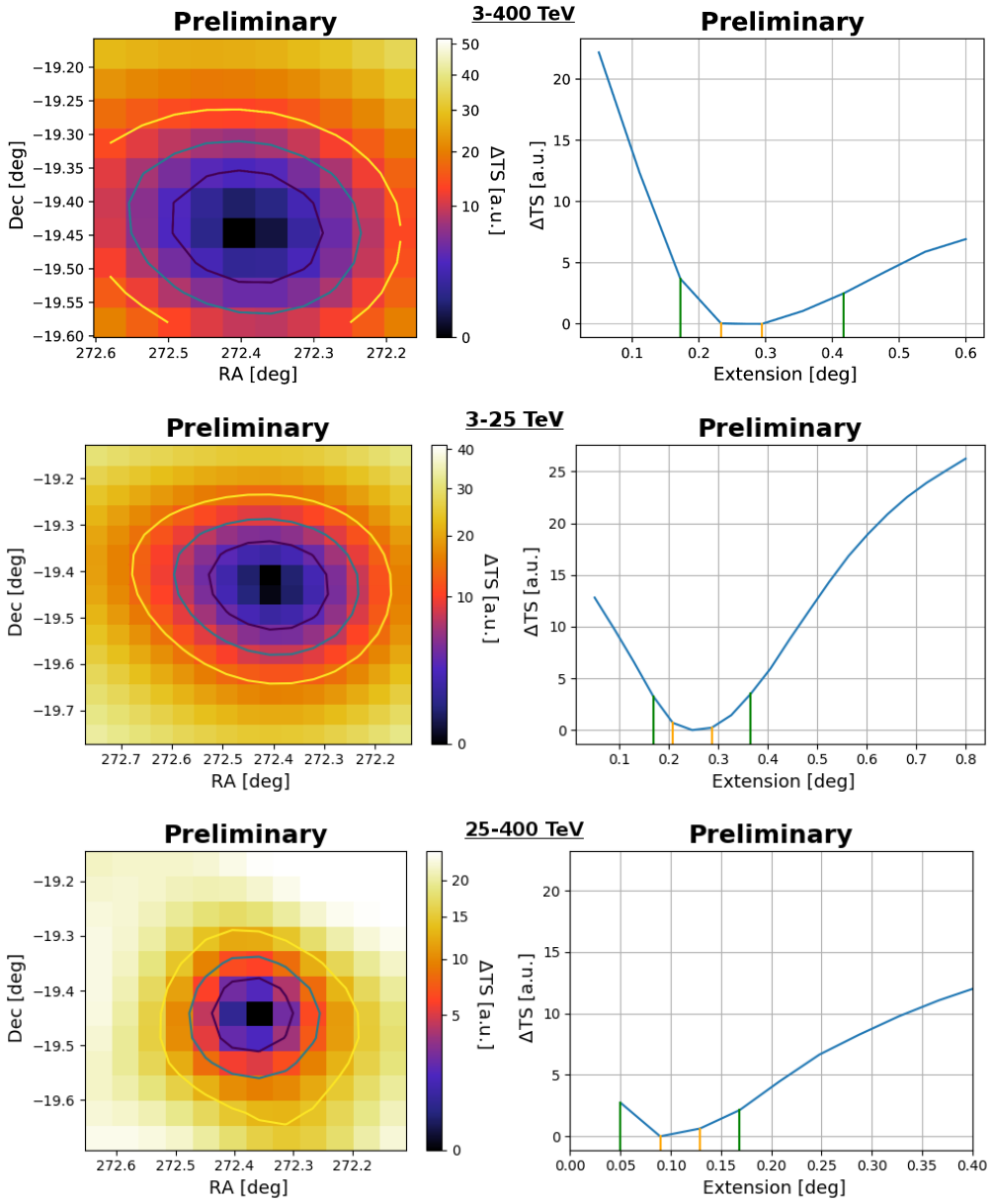

Figure 4.16: The plots display the results of the TS map scan for the best value for the Ra, Dec and extension using the MAGIC data based on the radially symmetric Gaussian source model. The contours for the 2D plots represent the 1σ (purple), 2σ (blue), 3σ (yellow) errors from this this scan, while for the 1D plots the vertical lines represent the 1σ (yellow) and 2σ (green) errors from this scan. Each subplot displays the results for the corresponding energy range.

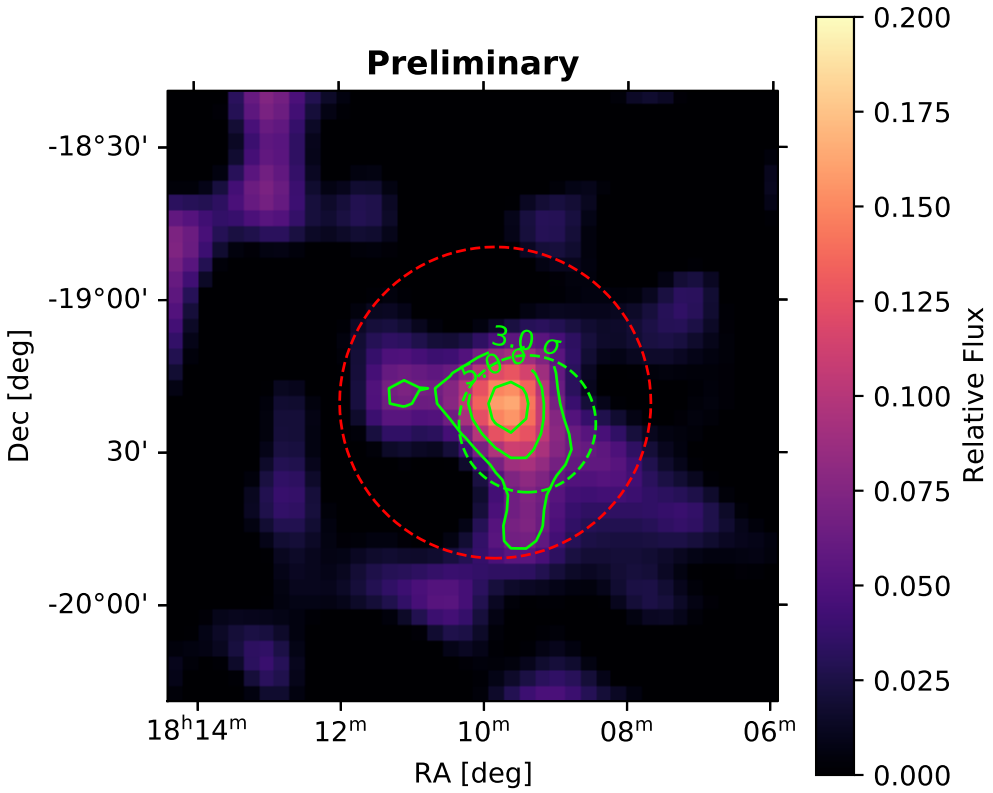

Figure 4.17: The relative flux skymap of HESS J1809-193 as seen by MAGIC. The skymap covers 3 TeV to 400 TeV in estimated energy. The green dotted circle represents the R_{68} from the morphology study. The green solid lines represent the 3σ, 4σ, and 5σ contours. The red dashed line is the R_{68} of eHWC J1809-193 [86].

4.4.6. Discussion

Figure 4.17 shows the relative flux map measured by MAGIC compared to recent HAWC measurements [86]. eHWC J1809-193 has similar position and flux to that of the measured MAGIC results. eHWC J1809-193 has measured extension of $R_{68} = 0.51^\circ \pm 0.19^\circ$ and position within the uncertainty of MAGIC extension of $R_{68} = 0.23^\circ \pm 0.07^\circ$. Position and morphology do not clearly match known multiwavelength sources which can be seen in radio and X-ray data maps in Figure 4.18.

The MAGIC spatial parameters are more inline with HGPSC 058 component, with only a 0.05° separation, but with a larger extension. The extension of 4FGL J1810.3-1925e measured by Fermi-LAT is much closer to that of the measured MAGIC extension but additionally implies morphology changes from a disk to a Gaussian.

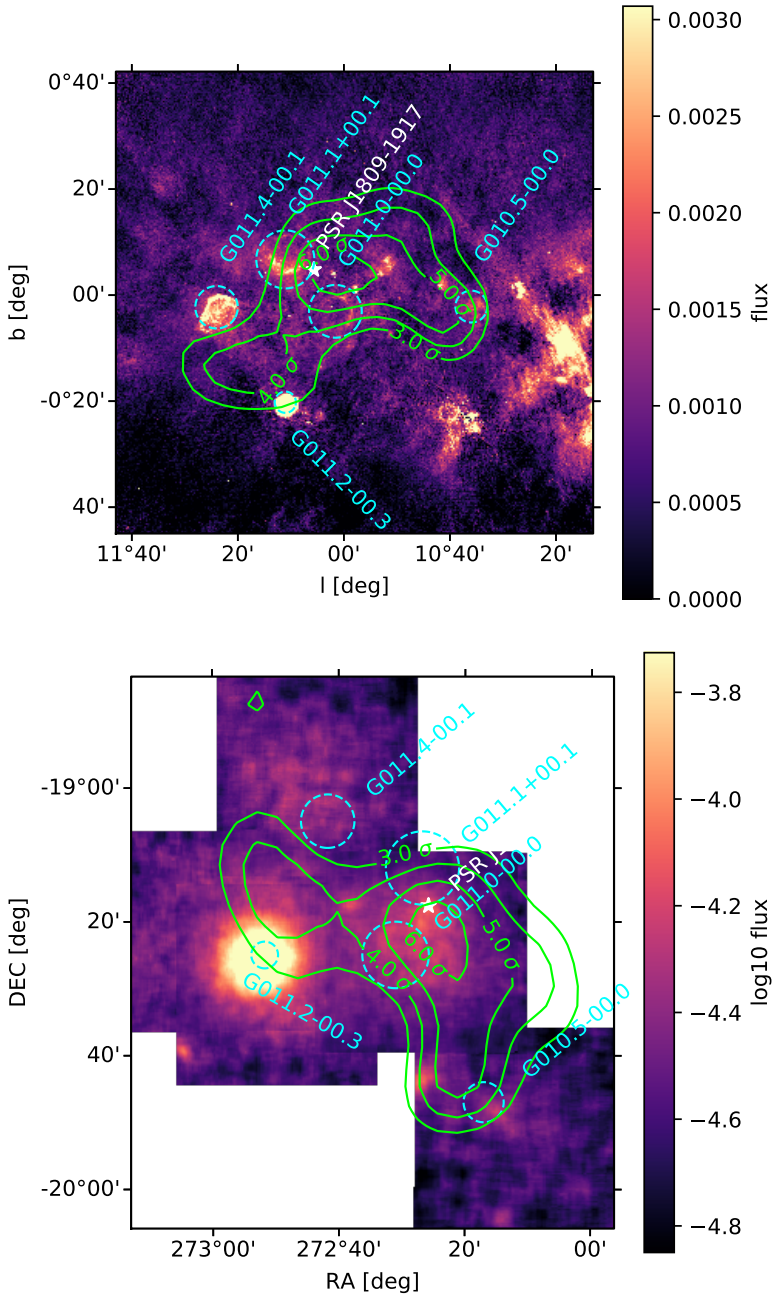

Figure 4.18: *Top* : The MAGPIS 20 cm radio emission with MAGIC TS contours overlaid and relevant sources marked. *Bottom* : The ASCA x-ray (0.4 keV - 10 keV) map with MAGIC TS contours overlaid and relevant sources marked.

Spectral model	f_0 [cm^{-2} s^{-1} TeV^{-1}]	Γ/α	E_{cut} [TeV]/β	LogLikelihood
PL	$(3.49^{+0.51}_{-0.67}) \times 10^{-12}$	$2.00^{+0.03}_{-0.03}$	-	-9.46
ECPL	$(4.80^{+0.07}_{-0.09}) \times 10^{-12}$	$1.90^{+0.07}_{-0.07}$	$103.18^{+182.13}_{-38.35}$	-4.94
LP	$(3.80^{+0.67}_{-1.30}) \times 10^{-12}$	$2.0^{+0.04}_{-0.04}$	$(1.03^{+1.4}_{-1.1}) \times 10^{-2}$	-8.18

Table 4.5: The results of the joint-forward folding fit. The parameters are described in 4.4, 4.5, and 4.6. The errors represent the combined statistical and systematic uncertainties. The spectral models are normalised at $E_0 = 1\,\text{TeV}$.

Joint fit to the *Fermi*-LAT and MAGIC spectrum was performed using Markov Chain Monte Carlo (MCMC) to minimise the LogLikelihood and to extract spectral parameters. Three spectral functions were tested:

- a single PL function

$$\text{PL}: \frac{\mathrm{d}F}{\mathrm{d}E} = f_0 \left(\frac{E}{E_0}\right)^{-\Gamma}, \tag{4.4}$$

- an exponential cutoff power-law (ECPL) function

$$\text{ECPL}: \frac{\mathrm{d}F}{\mathrm{d}E} = f_0 \left(\frac{E}{E_0}\right)^{-\Gamma} \exp\left(-\frac{E}{E_{\text{cut}}}\right), \tag{4.5}$$

- and a LogParabola

$$\text{LP}: \frac{\mathrm{d}F}{\mathrm{d}E} = f_0 \left(\frac{E}{E_0}\right)^{-\alpha-\beta\log\left(\frac{E}{E_0}\right)}. \tag{4.6}$$

The results of the joint-forward folding fit are summarised in Table 4.5. All three functions are able to describe the joint spectrum but the joint spectrum is best fit with ECPL function probability of $3.0\,\sigma$ preferred over the PL. The resultant cutoff is measured to be $103.18^{+182.13}_{-38.35}$ TeV with a spectral index of 1.90 ± 0.07. The results of the joint fit can be see in Figure 4.19, it should be noted that the H.E.S.S. and HAWC data points are not used in the fit. Although the uncertainties on the cutoff are large, they are consistent with the expectations of gamma-ray emission from hadronic interactions of a PeVatron with a spectral index of 2 and a cutoff near 100 TeV.

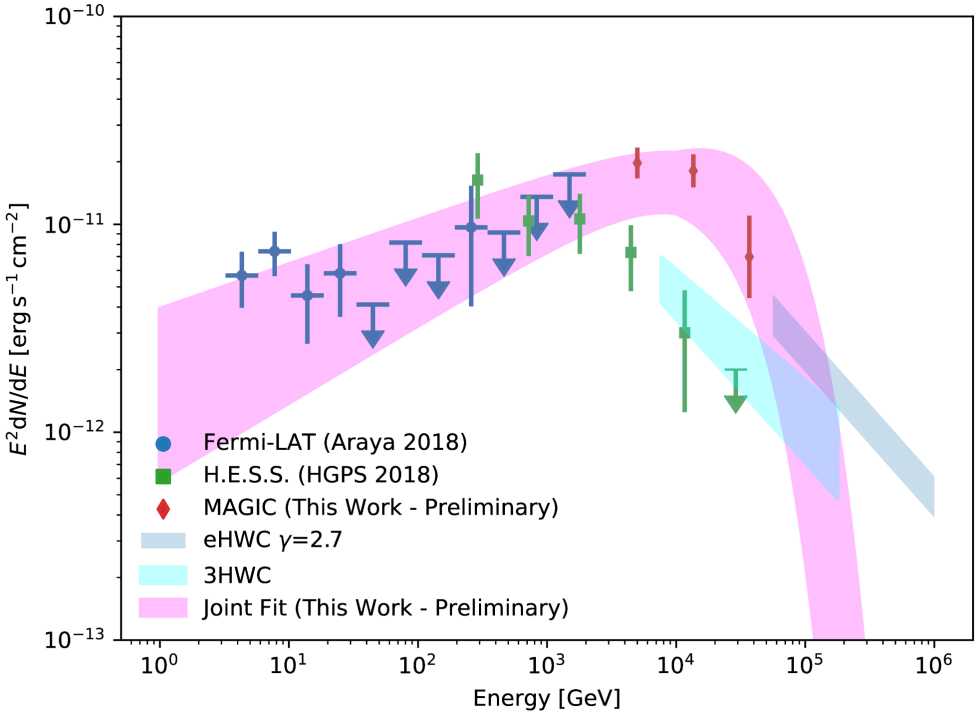

Figure 4.19: Joint Fermi-LAT and MAGIC fit using an ECPL described in equation 4.5. The blue points from Fermi-LAT [142], the green data points are from HGPS [145], the cyan shaded region are from 3HWC [147], the gray shaded region is the eHWC flux with an index of 2.7 [86], and the red data points are MAGIC. The pink shaded region is the joint fit results with propagated uncertainties. The H.E.S.S. and HAWC data are not used in the fit.

The MAGIC spectral results agree well with the reported HAWC results [86] as seen in Figure 4.19, which is expected considering the similar extraction region and energy range. The difference in flux from [147] could easily be due to 3HWC J1809-190 being modelled as point source and therefore not accounting for the flux from the extended emission. The *Fermi*-LAT spectrum connects to the MAGIC spectrum and can be easily fit with a ECPL as shown in Table 4.5.

As shown in Figure 4.19 there is an energy turnover in the TeV energy range showing that further observations by IACTs are crucial in understanding the nature of this source.

Interpretation is ongoing, but the two most likely scenarios are being explored. One is the TeV PWN scenario of the PSR escaping it's SNR and free electrons diffusing into

surroundings. The other one is the SNR scenario/cloud interaction. There are several clouds of enough mass and density near the two SNRs that could create enough target material for substantial hadronic emission.

5. Camera Displacement Monitor for LST-1

5.1. Large Size Telescope

The prototype of the Large Size Telescope (LST-1) of the CTA was installed in 2018 at the north CTA site located at the Roque de los Muchachos Observatory on La Palma in the Canary Island and it is now in commissioning phase.

Telescope pointing precision refers to the accuracy with which a Cherenkov camera coordinate in the focal plane of the CTA telescopes can be transformed to a celestial coordinate. To meet the performance requirements of CTA [37], it is necessary to know the Cherenkov camera position very precisely during favorable observation conditions. The root-mean-square (RMS) systematic error on the localization of a point-like source of gamma rays less than 100 GeV must be $< 10''$ per axis under favorable observing conditions. To accomplish this, the LST telescopes' RMS space-angle post-calibration pointing precision must be $< 14''$.

The LST design aims to provide a large photon collection area sensitive enough to operate with a low energy threshold of 20 GeV, while maintaining a light structure that enables swift response to transient events. To fulfill these two goals, a large collection area necessitates a large (i.e. heavy) mechanical construction, whereas fast repositioning necessitates a light structure, which results in a deformable structure degrading the telescope's pointing precision.

Based on the previous experiences with the existing IACTs it is known that a completely rigid and light telescope cannot be built. So, the acquired science data must be

corrected for the telescope deformations. On the telescope, different forms of deformations can occur, including those caused by gravity, temperature changes, stable wind, or a wind gust. In the case of MAGIC telescopes only gravity [110, 111] is considered in the correction procedures, while the remaining deformations are corrected online using the "drive bending model" and offline using a precise correction by a Starguider system.

5.1.1. Deformations of the LST

The bending model alone is insufficient to account for deformations caused by temperature changes, static and dynamic winds, since these three factors are difficult to reproduce in advance. A gust, or the dynamic component of a continuous wind, can change dramatically in a matter of seconds. Due to the fact that the Starguider (SG) system is capable of providing corrections at a rate of one Hz, another system is needed to account for these deformations. To disentangle the camera displacement from the dish structure deflection, Optical Axis Reference Laser (OARL) spots are used as a reference, and then the camera positions are determined using reference light-emitting diodes (LEDs). To account for the effect of a gust with oscillations of $\sim$2 Hz, a dedicated 10 Hz Camera Displacement Monitor (CDM) is installed [148]. This means that OARL serves as a reference to the dish structure, inclinometers relate it to the drive system and CDM relates it to the PMT camera [149]. The LST-1 structure and the pointing componens are shown in Figure 5.1.

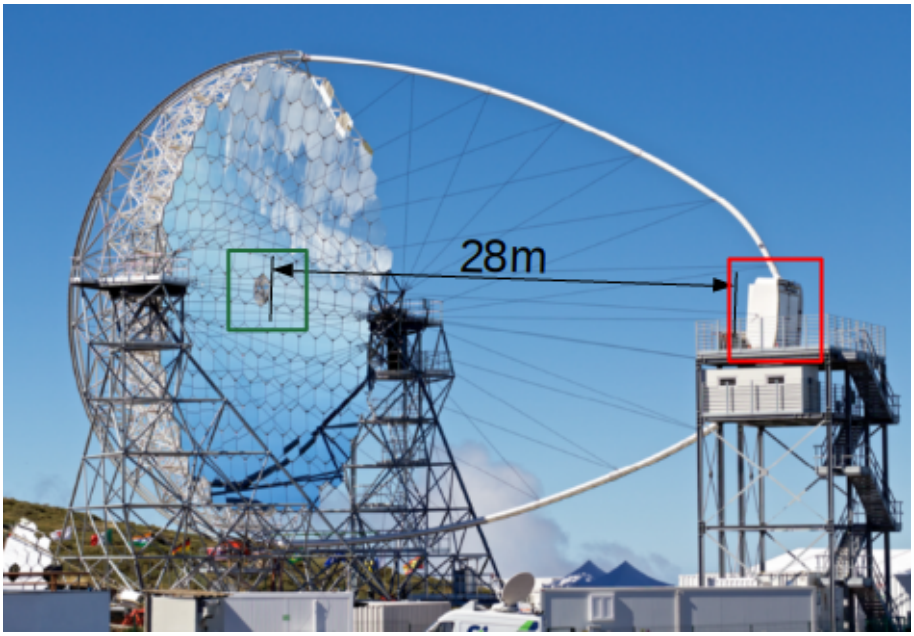

(a) LST-1

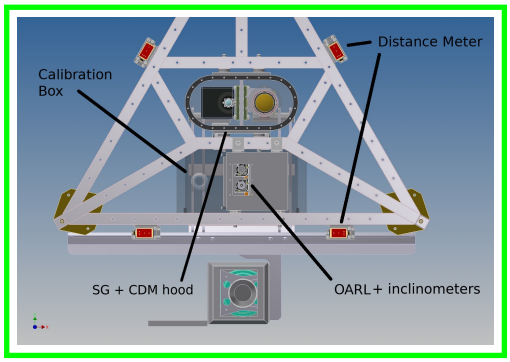

(b) Devices in the dish center

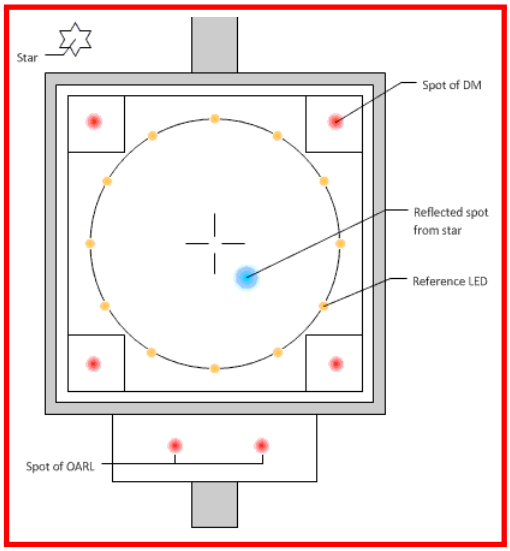

(c) PMT camera front

Figure 5.1: LST-1 telescope structure. CDM is located in the center of the dish, while the LEDs and OARL spots are located at the front of the PMT camera. The distance between them is 28 m.

It is essential to identify and disentangle all structural deformations that contribute to telescope mispointing using a variety of monitoring systems. Apart from global misalignment of the azimuth and elevation axes of the telescope, pointing deviations are expected as a result of structural deformations of the telescope, such as:

(a) a rotation or twist of the telescope structure in azimuth direction (not taken account for by the drive assembly)

(b) a twist of the elevation towers

(c) a twist between the elevation structure (dish and arc) and the elevation motor sitting in the lower telescope structure

(d) a deformation of the mirror dish

These cases are depicted in Figure 5.2. For (a) this deformation is expected to make only a slow common deflection to the dish and the arch, thus it can be corrected for with the Starguider.
For (c) inclinometers are installed in the dish center and are firmly attached to the OARL, directly measuring the dish's inclination angle. Active Mirror Control (AMC) can compensate for deformations (d) caused by static forces (gravity, temperature, and static wind).

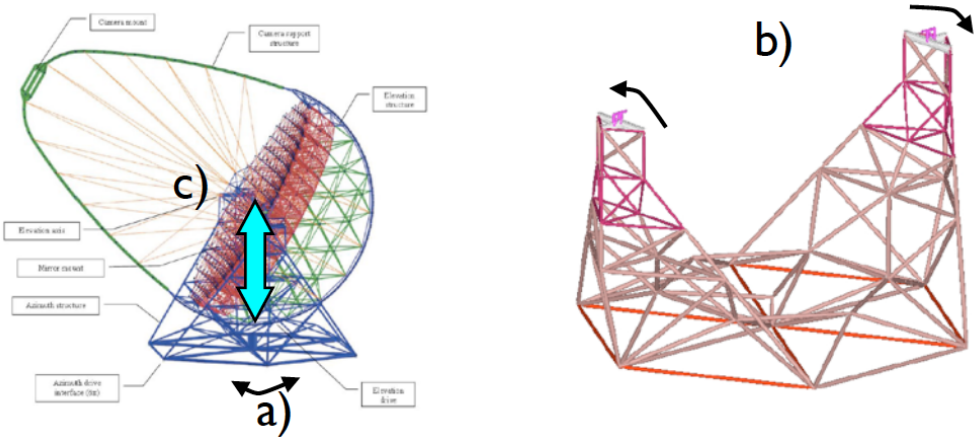

Figure 5.2: Deformations in the lower structure.
A rotation of the azimuthal structure (a) and a twist of the elevation angle (b). A deflection between the elevation motor and the dish center (c).

Additionally, as illustrated in 5.3, deformation of the arc structure may affect the relative orientation of the PMT camera with respect to the telescope's optical axis, such as:

(i) a vertical or horizontal shift of the focal plane

(ii) a rotation of the focal plane around the optical axis

(iii) tilts of the focal plane w.r.t. the optical axis

(iv) a shift along the optical axis.

For item (iii) and (iv) four distance-meters are installed at the dish centre, to measure the distance to the camera plane, and also its tilting angle.

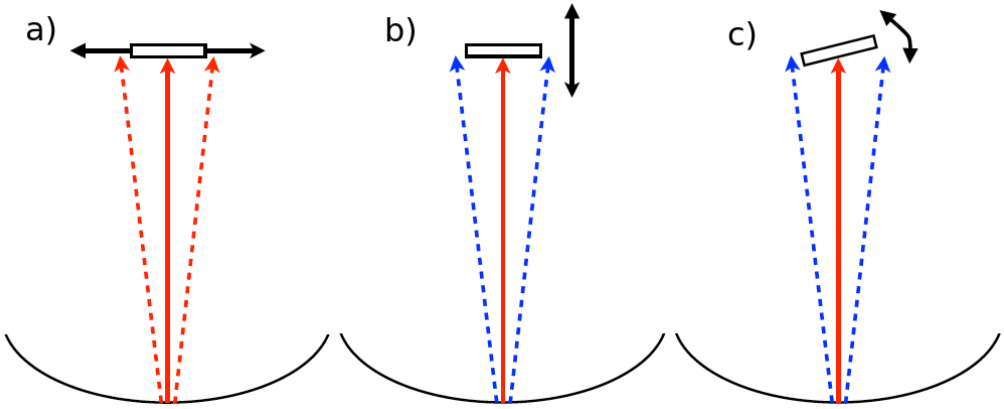

Figure 5.3: Deformation between the dish and the camera. a) Displacement on the focal surface for x- and y-axes (and rotation around z-axis. b) Change of the focal length along z-axis, and c) Tilting of the focal surface, rotations around x- and y-axes

In order to achieve the final pointing precision less than 14 arc-seconds, corrections coming from the Starguider, which uses the sky field as a reference, need to be applied at the end.

Elastic deformations can be well parametrised by a bending model prepared in advance (using special calibration observations where the telescope is pointed at several bright stars uniformly distributed in the azimuth-elevation plane). Such bending model, however, cannot correct for inelastic deformations of the telescope structure (e.g. due to temperature changes, constant or gusty wind loads). To take these effects into account in the pointing calibration, deformations have to be recorded as much as possible during science data taking. For the LST dedicated monitoring devices are installed.

5.2. POINTING HARDWARE COMPONENTS

5.2.1. Reference LEDs

Reference LEDS are installed around the PMT camera and are used as a reference to determine the PMT camera centre, even during data acquisition (DAQ). There are 12 LEDs mounted in a circle around the PMTs, and 3 more are located in each corner of the PMT camera hood as seen in Figure 5.4. The LEDs are ROHM SLI-343V8R3F with a dominant wavelength of 630 nm and on each LED there is a cap with a collimated hole with a size of 1 mm.

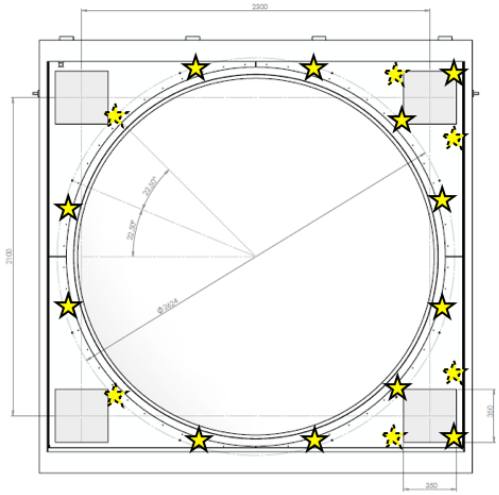

Figure 5.4: Position of the LEDs on the lid of the PMT camera.

5.2.2. Starguider camera

This camera corrects for the telescope pointing with a high precision, using known stars in the star catalogues. It sees a star field, and also a part of reference LEDs. Since the Starguider camera is located in the dish centre, its line of sight is inclined by a few degrees w.r.t. the telescopes optical axis. The Starguider knows only the relative position of the camera in the sky field, which does not necessarily correspond to the pointing direction of the telescope dish. In fact, a Finite Element Analysis (FEA) for the LST structure [150] shows that, the dish and the arch deform differently, strongly dependent on the direction

of the wind. For that reason CDM is used.

While the LST drive system tracks the source, every few seconds the SG camera takes the images of stars in its field of view close to the tracking source. Images of stars taken by SG camera are analyzed to identify the star and their relative position using the star catalogue to provide mapping of the SG pixels to sky coordinates and the number of correlated stars. Since the SG camera also measures the center of the PMT camera (part of the LEDs mounted on circle around the PMT camera are also in the SG camera field of view) and the mapping between the SG camera pixels and the sky coordinates is known, the sky coordinates of the PMT camera are also known. The Starguider correction is then later applied offline.

For the SG a Peltier cooled low-noise camera from Allied vision was chosen. Bigeye G-283 Cool has resolution of 1928 (H) $\times$ 1452 (V) with pixel size 4.54 microns x 4.54 microns. The Kowa LM50HC lens of 50 mm focal lens gives the field of view (FoV) of 9.938 deg (horizontal) x 7.485 deg (vertical), which results with a resolution of 18.56 arcsec/pix. At 28 m the FoV measures 4.90 m x 3.66 m. The software to control SG camera manages image taking, control of camera settings and sending images over the Ethernet link to the defined IP address.

5.2.3. Optical Axis Reference Laser (OARL)

OARL defines the optical axis of the LST during science observations. Two OARLs are installed in order to provide 2 dimensional information. They are installed at the dish centre, pointing towards screen targets at the edges of the PMT camera. When observed by the CDM, the two reference spots can be compared to the reference LEDs, providing a correction for the PMT camera displacement. A stiff unit is built, in which the inclinometer is sandwiched by the two OARLs, to represent the dish structure. The unit is installed at the center of the dish with a dummy facet in order to avoid any additional systematic deformation at the central hub. Two focusable, 3 mW lasers chosen as the OARL are made by ProPhotonix. Their wavelength is in infrared (780 nm) in order to not affect the blue Cherenkov light.

5.2.4. Inclinometers

The inclinometers are used to measure dish deformations during data taking. Finite element analysis of the LST structure has confirmed that the inclination at the dish center is closely representing that of the whole dish structure. Therefore, it is planned to measure directly the inclination angle at the dish center, by inclinometers firmly attached to OARL. The inclinometer are combined with OARL in the hardware level. There are two inclinometers ("Tuff Tilt Digital" by Jewell Instruments), one for the elevation angle (parallel to the optical axis) and one parallel to the elevation axis. The former one has a wide range of ± 50 deg with 14 arsec of precision, while the latter one has more narrow range ± 3 deg, but with a higher precision of 1 arsec.

5.2.5. Distancemeter

Distancemeters (DMs) measure the distance and tilting of the focal plane w.r.t. the dish centre. In general measurements for a 28 m distance utilize a time-of-flight sensor with a laser. There are 4 DMs (model DL35 made by SICK) that use infrared lasers (laser class 1) in order not to affect the DAQ by PMTs. They each point in the corner of the PMT camera lid and they each have ± 15 mm of accuracy.

5.2.6. Camera Displacement Monitor

CDM is located in the central hole of the dish (Figure 5.1b) and during science observations measures the horizontal and vertical displacement of the PMT camera relative to the optical axis defined by the OARL. Its FoV contains OARL spots and reference LEDs (Figure 5.1c). It uses a frame rate of 10 Hz and it separates the camera displacement from the dish deformation. The CDM correction can then be applied offline.

The CDM system is built of: camera, lens, processing unit and a sensor for measuring temperature, pressure and humidity. Processing unit is Intel NUC Mini PC NUC5i7RYH running CentOS. It was chosen due to its small dimensions ($115 \times 111 \times 49$ mm), so it can fit inside the custom made water-tight hood. The devices comprising the CDM system are displayed in Figure 5.5 Camera is produced by Imaging Development Systems (IDS), and the model is UI-3590CP Rev. 2, which is a Complementary metal-oxide-

semiconductor (CMOS) camera connected with USB 3.0 to the processing unit. The specifications are listed in Table 5.1. It can achieve 21 frames per secons (FPS) and its maximum resolution is 4912 $\times$ 3684 which amount to 18.10 MPix. It was chosen due to its high frame rate and number of pixels. Because of that it can detect small movements of the PMT camera with high frequencies. The infrared (IR) filter has been removed from the camera so it can be sensitive to the OARL spots. It is equipped with Edmund Optics 35 mm lens. Having focal length of 35 mm provides the horizontal FoV of 7 deg and vertical of 9 deg and a sampling of 7.35 arcsec/pixel.

IDS UI-3590CP Rev. 2

Interface	USB3
Sensor type	CMOS Color
Max framerate	21 fps
Resolution	4912×3684 px
Optical area	6.140 mm $\times$ 4.605 mm
Shutter	Rolling shutter
Optical class	$1/2.3$”
Resolution	18.10 Mpix
Pixel size	1.25 μm
IP code	IP30
ADC	10 bit
Color depth	12 bit
Exposure time	$0.013 - 998$ ms
Power consumption	$1.5 - 3.3$ W

Table 5.1: CDM camera specifications.

(a) Camera: IDS UI-3590CP Rev. 2.

(b) Camera lens: Edmund Optics 35mm.

(c) Environmental sensor: Yoctopuce Yocto-Meteo-V2.

(d) Processing unit: Intel NUC Mini PC NUC5i7RYH.

Figure 5.5: CDM devices.

5.2.6.1 Bending model

The CDM camera is also used for taking images used for generating the bending models. During the pointing calibration observations it observes the reference LEDs around the PMT camera and the image of the bright star projected on a reflective screen in front of the PMT camera. The only difference is that in this mode the camera takes images with longer exposition times so that the projected star spot is bright enough to be seen by the camera.

During the pointing calibration a star is tracked. Its direction (Zd, Az) is calculated from (Ra, Dec) of the tracked star, and (Zd, Az) is converted to the motor steps with the encoders. The star spot is visible on the central screen with a shift with respect to the optical axis (defined by the OARL spots). The shift values taken with all the tracked stars in a large range of (Zd, Az) are stored with the encoder data and inclinometer measurements.

Then a bending model, a relation from the encoders and inclinometers to the optical axis, can be generated. The correction is used online during DAQ.

The parameters used in the bending model are:

- offsets between the axes and encoders
- azimuth axis misalignment
- non-perpendicularity of the azimuth and elevation axes
- non-perpendicularity of the elevation and optical axis
- small non-centricity of the axes
- a zenith-angle dependent deflection of the optical axis

5.3. CDM SOFTWARE

CDM program is written in C++ programming language and it controls the camera and the environment sensor, it performs image analysis, data storage and communication with other subsystems. The data results are later stored in a database so they can be later easily used reanalyzed. The whole program is controlled and monitored by Open Platform Communications United Architecture (OPCUA) [151] protocol. Briefly, the OPCUA, is an abstract software-hardware layer allowing the interfacing between a device and software components. The OPCUA standard has been chosen by CTA as the communication standard to connect the framework components of ALMA Common Software (ACS) and the different devices composing the telescopes and auxiliary systems in order to homogenize the monitoring and control of devices. In particular it is Multipurpose OPCUA Server (MOS) implementation of the OPCUA protocol that is used in LST. The main input of the OPCUA server creation is the Interface Control Document (ICD) which defines the interface of the program and it contains the exposed device data points and methods.

The program can take images in two ways: offline and online mode. In the offline mode each image is taken and converted to FITS[1] format. In the header of each image additional information is stored such as right ascension and declination coordinates of tracked source, zenith and azimuth position from the drive subsystem, camera settings, LED and OARL settings and other auxiliary information. Each image is then saved to a shared file system where they can be later analysed. Even compressed the images size is about 15 MB and usually one image is taken each second. This mode is needed for taking the bending model images of the telescope which are analyzed offline. But this is also useful for offline analysis of images for the purpose of settings and analysis optimisation.

In the online mode the images are not saved to disk but are continuously analyzed in memory and only the results of the analysis are saved. Typically the images are taken and processed with a frequency of 10 Hz.

[1] https://fits.gsfc.nasa.gov

5.3.1. Image analysis

CDM program heavily uses the OpenCV [152] library to efficiently perform image analysis. In particular after each image is taken the algorithm finds the centers of 12 LEDs and the centers of 2 OARL spots. This is done by calculating the image moments of the predefined regions around the LED and OARL position, where the image moment is a weighted average (moment) of the image pixels' intensities. The centers of integrating regions of the LED and OARL spots are found from the previously stored offline images and are fixed in the program. Similarly the size of the integrating regions in set to 40 pixels for LEDs and 60 pixels for OARL spots as the OARL spots are larger where the number of pixels represents the side of the square of the integrating region. This was also determined from the optimizations on the stored images.

In case of an 2D image having pixel intensities stored as $I(x,y)$ where x,y are coordinates of the pixels the spatial moments m_{ji} are computed as:

$$m_{ji} = \sum_{x,y} (I(x,y) \cdot x^j \cdot y^i), \tag{5.1}$$

and the central moment mu_{ji} are computed as:

$$mu_{ji} = \sum_{x,y} (I(x,y) \cdot (x-\bar{x})^j \cdot (y-\bar{y})^i), \tag{5.2}$$

where the mass center $((\bar{x},\bar{y}))$ being:

$$\bar{x} = \frac{m_{10}}{m_{00}}, \bar{y} = \frac{m_{01}}{m_{00}}. \tag{5.3}$$

Using Equation 5.3 the centers of each LED are determined $((\vec{\bar{x}},\vec{\bar{y}}))$. Then those LED centers are fit with a circle using the "Hyper" fit algorithm [153]. It is an algebraic circle fit with with zero essential bias. From that the circle radius (r), center coordinates $((a,b))$ and the root mean square error are computed (RMS).

The RMS is computes as:

$$RMS = \sqrt{\frac{\sum_i^n (\sqrt{(x_i-a)^2+(y_i-b)^2}-r)^2}{n}} \tag{5.4}$$

where n is the number of LEDs, in this case 12.

Also using Equation 5.3 the centers of each OARL spot is determined. After that the mean OARL position is just taken as the average of the both OARL spot coordinates.

Finally the distance between the circle center and the OARL mean value is calculated which is the displacement of the PMT camera centre with respect to the optical axis of the telescope.

A Graphical User Interface (GUI) was made for the shifters to use during observations. The interface is shown in Figure 5.6a and it allows for camera control and online viewing of images that are being taken. The Finite State Machine (FSM) state and methods of the CDM are displayed in Figure 5.6a.

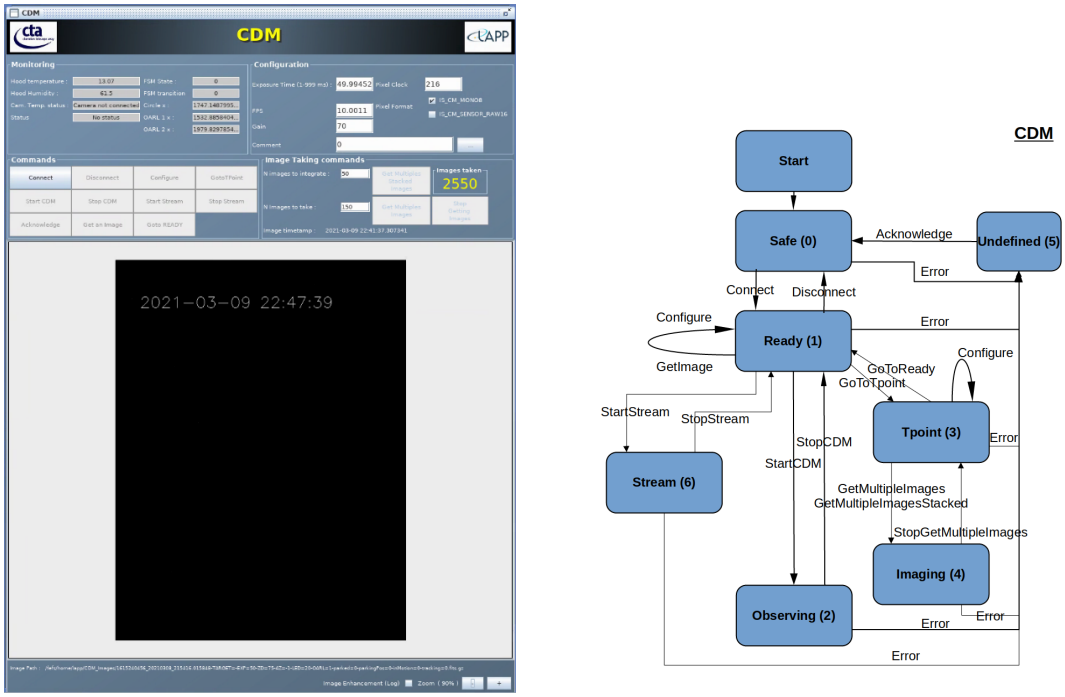

(a) GUI for CDM made by the Annecy LAPP team. Contains control and monitoring sections.

(b) Finite State Machine and methods of the CDM.

Figure 5.6: GUI and FSM for CDM.

5.3.2. CDM FSM states

The FSM states and transitions are shown in Figure 5.6b. The description of the FSM states are listed below:

- In the $Safe$ state the camera is disconnected from the program. This is the default state during the day when there is no observations.
- The program can connect to the camera and then the system is in *Ready* state. In *Ready* state various camera settings can be adjusted; such as exposure, gain, pixel format, frames per second etc. Also individual camera images can be taken and stored.
- In the *Observing* state the camera images are continuously analyzed in memory with 10 Hz and the outputs of the analysis updated continuously. This is the usual mode of observation during the night. It is used to check for any oscillations of the PMT camera.
- In the $Stream$ state the program just streams the video of the camera and no analysis is performed. This is usually used just to check if there any visual issues with the PMT camera.
- In $Tpoint$ and *Imaging* states a batch of images is taken and stored for later offline analysis. This is always done while taking the bending model images. The images can be taken one by one, or the batch of images can be stacked and saved as only one image.

5.4. LABORATORY MEASUREMENTS

5.4.1. LED measurements

In the laboratory, located in Split, a setup has been designed to replicate the CDM setup at LST. The laboratory setup is displayed in Figure 5.7. On the one side of the laboratory a board with the LEDs was mounted on a supporting plate which could be moved, while the CDM camera was on the other side of the laboratory. It was not possible to put the LEDs and the CDM at a distance of 28 m (which is the distance between CDM and the LEDs at LST) in the lab due to lack of space, so the whole setup was scaled to 20 m.

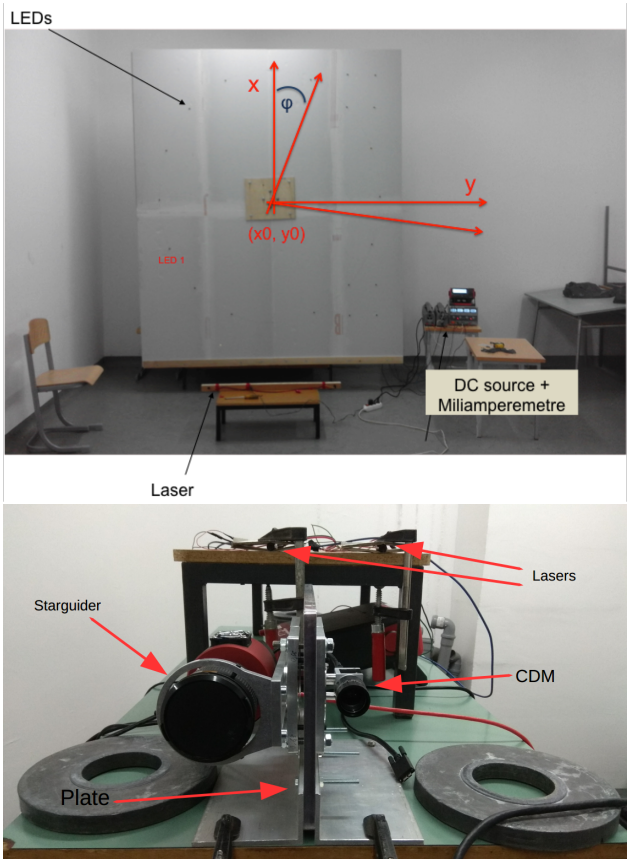

Figure 5.7: Setup in the laboratory. *Top*: 12 LEDs mounted on a circle of 2m diameter with the collimator holes of 1 mm. The whole board is mounted on a supporting plate which could be moved in steps of 0.02 mm and rotated in steps of 0.033°. *Bottom*: Devices were setup on the other side of the lab, 20 m away, which included the CDM camera, SG camera and the reference lasers.

To fulfill the LST requirement the CDM needs to have a precision of 5″ which corresponds to 0.7 mm at 28 m distance or 0.5 mm at 20 m. When everything has been set up the CDM took 6000 images of the circle centers and analyzed them. After that board containing the LEDs has been shifted by 0.5 mm in the direction perpendicular to the angle of viewing of CDM in the horizontal direction. Then CDM took another 6000 images. The results are displayed in Figure 5.8. For the horizontal direction (Figure 5.8a) an expected distribution shift of 0.5 mm is seen. Also the width of the distributions is narrow and there is no overlap. In the vertical coordinate the there was no shift in the distribution, which is expected with the only horizontal movement.

5.4.2. OARL measurements

For the OARL measurements the CDM was left running for 14 hours during the night taking 10 images per second. The results are shown in Figure 5.9. It can be seen that there are some drifts of the measurements with respect to time showing some erratic behavior. This is due to the projected OARL spot changing shape over time causing this drift in the results. Because of this the OARL measurements are not as stable as the LED measurement.

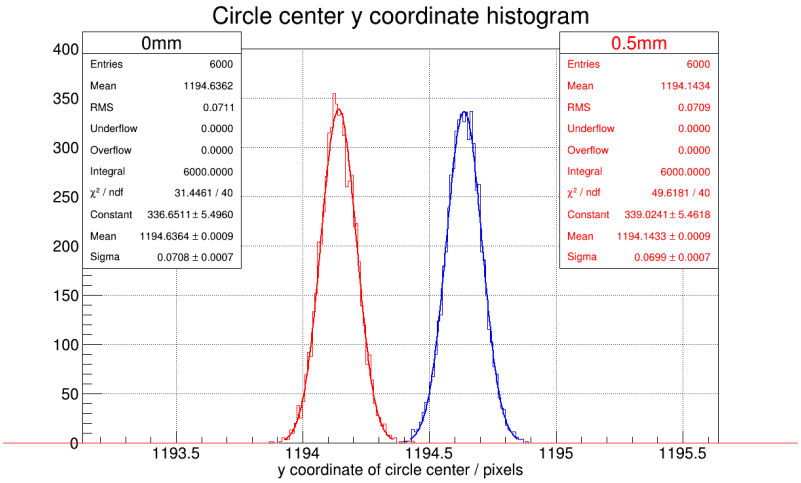

(a) Horizontal coordinate of the camera circle center. An expected shift is seen.

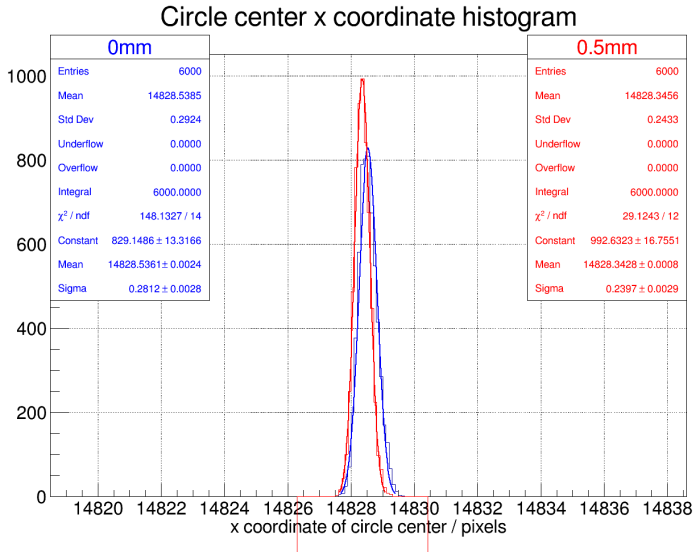

(b) Vertical coordinate of the camera circle center. The CDM vertical coordinate is unchanged with the horizontal shift.

Figure 5.8: Laboratory results for the circle center. The first set of images is displayed in blue, while the second set of images is displayed in red. The second set of images is taken after the LEDs have been shifted by 0.5 mm (5″) in the horizontal direction.

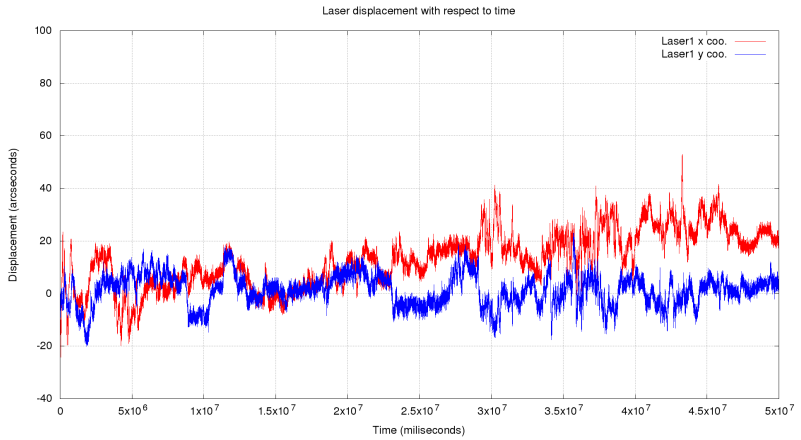

(a) Results for the OARL-1.

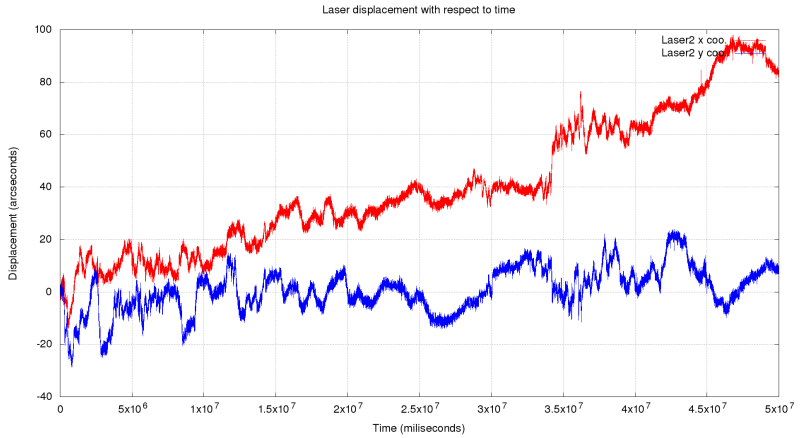

(b) Results for the OARL-2.

Figure 5.9: Laboratory results for the OARL spots. The CDM was left running for 14 hours during the night taking 10 images per second. Results for the OARL horizontal and vertical coordinate. The displacement is relative to the results of the first taken image.

5.5. INSTALLATION AT LST-1

To minimize systematic error between SG and CDM, both cameras are housed in a single hood. The hood is a custom water tight container containing the processing unit , environmental sensor and the CDM/SG cameras as shown in Figure 5.10. In August of 2019 the CDM, located inside the hood, was installed in LST-1. The monitoring devices are located in the center of the dish which can be seen in Figure 5.1a marked with green square and in Figure 5.1b. The hood mounted in LST-1 can be seen in Figure 5.11.

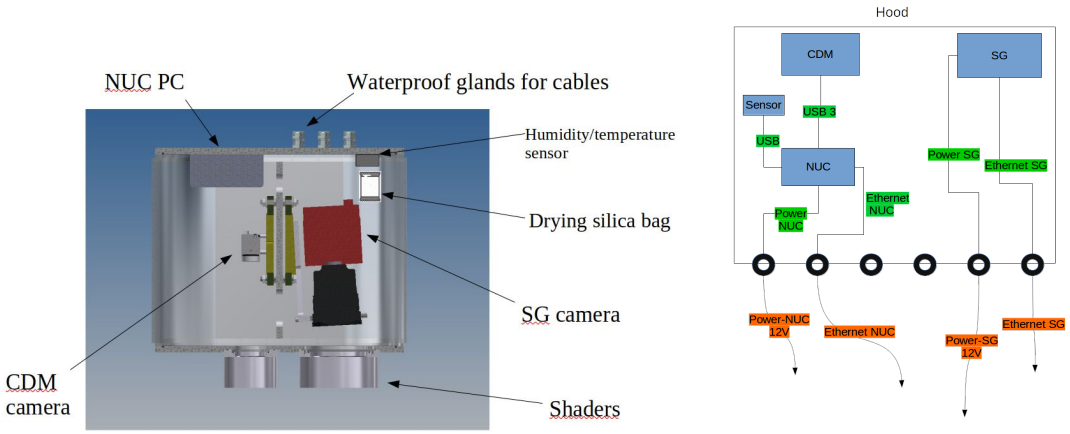

(a) Hood top view

(b) Cable scheme of the hood

Figure 5.10: Schematic view of the CDM/SG hood.

Typical images taken by CDM are shown in Figure 5.12. Figure 5.12b shows a typical image containing LEDs and OARL spots that the CDM is analyzing.

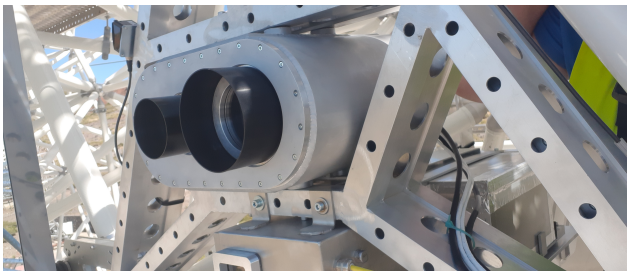

(a) Front view of the hood. The left window opening is for the CDM, the right is for the SG.

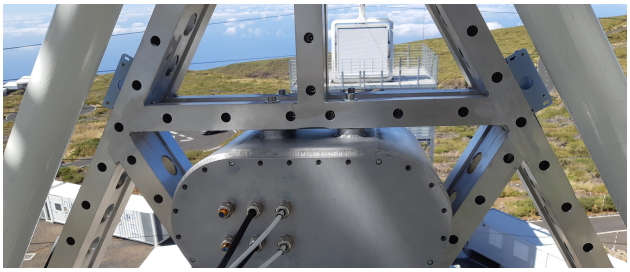

(b) Back view of the hood. The PMT camera, with the shutters being closed, can be seen in the background.

Figure 5.11: Hood housing the CDM/SG cameras mounted in the LST-1 dish center.

(a) Image of the PMT camera taken by CDM during the day. The shutter is closed to protect the PMTs.

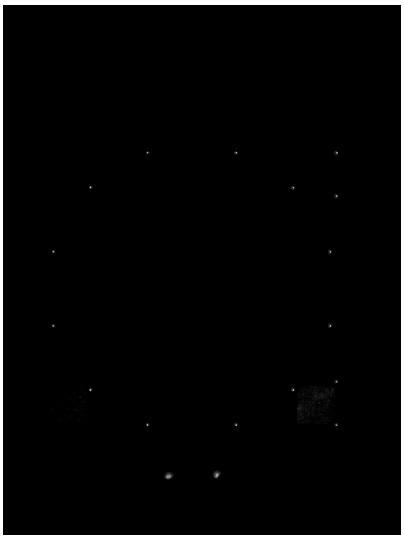

(b) Image of the PMT camera taken by CDM during the night with the shutter open, LEDs and OARL on.

Figure 5.12: CDM images of the PMT camera during the day and night.

5.6. CALIBRATION AT LST-1

5.6.1. Tuning of the settings

After the CDM was installed in LST-1 technical data was taken during some of the nights to find the best combination of setting for the CDM. It included tuning the LED intensities and camera exposure settings since OARL spot brightness cannot be adjusted and has a fixed value. So, CDM images were taken with different level of exposure times in order to find which exposure produces the brightest OARL spots in the image, but without them being over saturated. The best value for exposure was found to be 50 ms. Then the CDM images were taken with 50 ms exposure and different LED intensity settings to find the brightest LED intensity not over saturating the CDM camera pixels. The best value for LED intensity was 20 in an internal scale ranging from 0-255.

5.6.2. Parked dataset

To verify the performance of the CDM data was taken while the telescope was parked. The data was taken during the night, with the LEDs and OARL turned on. The key assumption being that when the telescope is parked then the PMT camera will not move. Then any dispersion of the circle center results comes just from the CDM resolution of estimating the circle center. While parked about 1000 CDM images were taken. For reference, the LST parked position is at 95°zenith.

The result of this measurements for individual LED coordinate is shown in Figure 5.13. There the plots are displayed for 6 LEDs. The coordinates are relative to the CDM camera image frame, the top left corner being the origin of the coordinate system. In the subplots the mean values and standard deviations of the histograms are displayed, but only the resolutions are important here. It can be seen that each distribution is approximately Gaussian and the standard deviations are $\sim$0.5 arcsec for each of them. Based on this, the individual LED positions are reconstructed nicely.

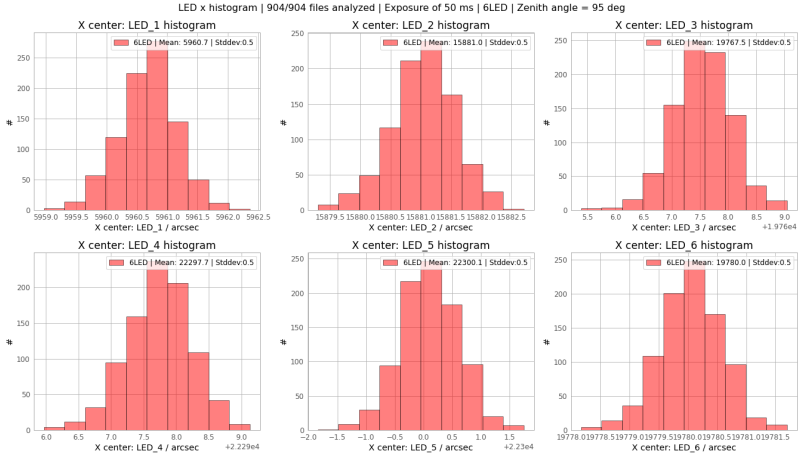

(a) Distribution of results for horizontal coordinate of the center for individual LED.

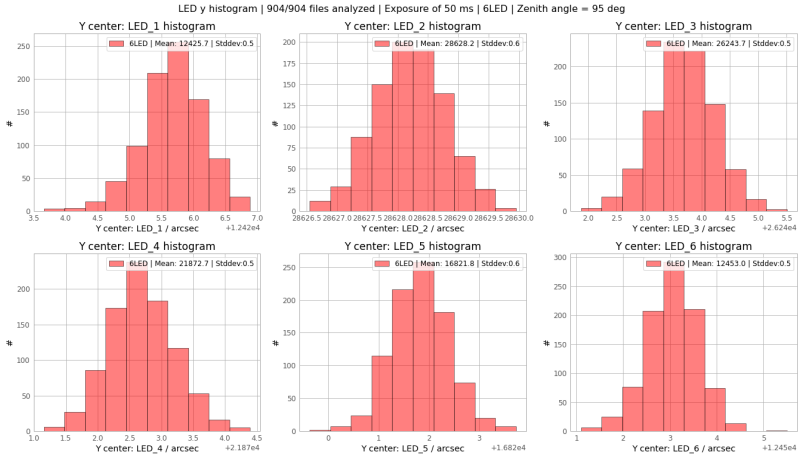

(b) Distribution of results for vertical coordinate of the center for individual LED.

Figure 5.13: Distribution of individual LED results when the camera is parked. The standard deviation gives the resolution of the measurements.

After the positions of the LED centers have been determined, the circle can be fit through them. These results are displayed in Figure 5.14. The top subplots show the result for the circle center fitted horizontal and vertical coordinate together with the radius. The bottom subplots represent how good the results of the fits are. The left bottom subplot shows the distribution of the standard deviations of the distance of each LED (R_i) to the fitted circle center. The center bottom subplot show the $\sum_i (R_i - R_c)^2$ distribution, where R_c is the fitted radius. And the right bottom subplot shows the $\sum_i (R_i^2 - R_c^2)^2$ distribution. Again all the results in Figure 5.14 have nice distributions with the standard deviations

being the same in vertical and horizontal coordinates.

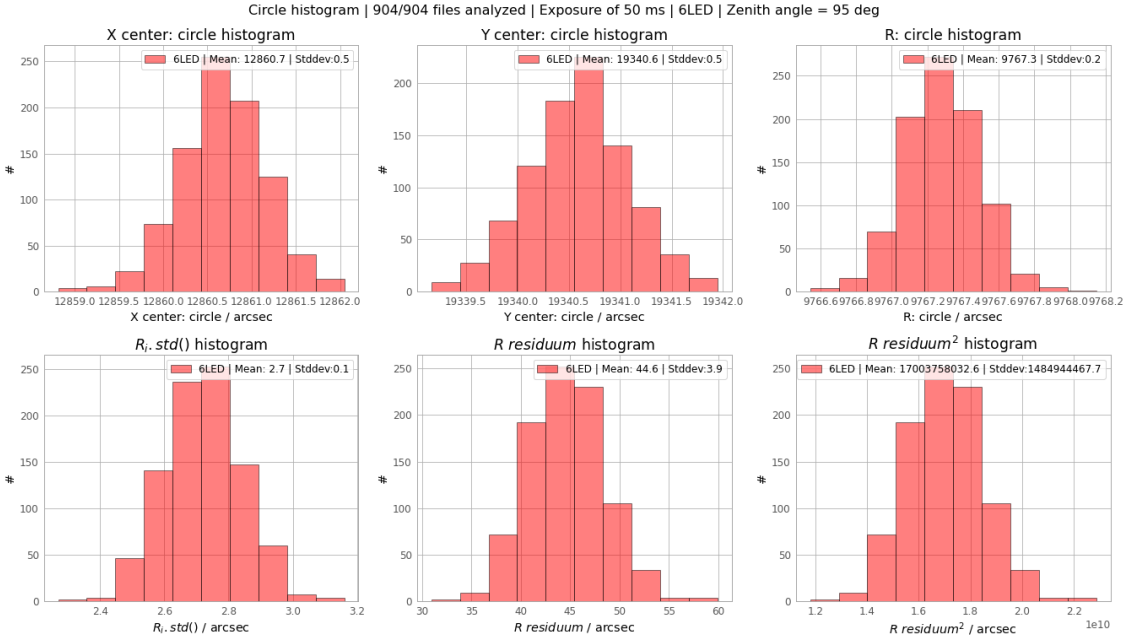

Figure 5.14: Distribution of circle center results when the PMT camera is parked. The standard deviation gives the resolution of the measurements.

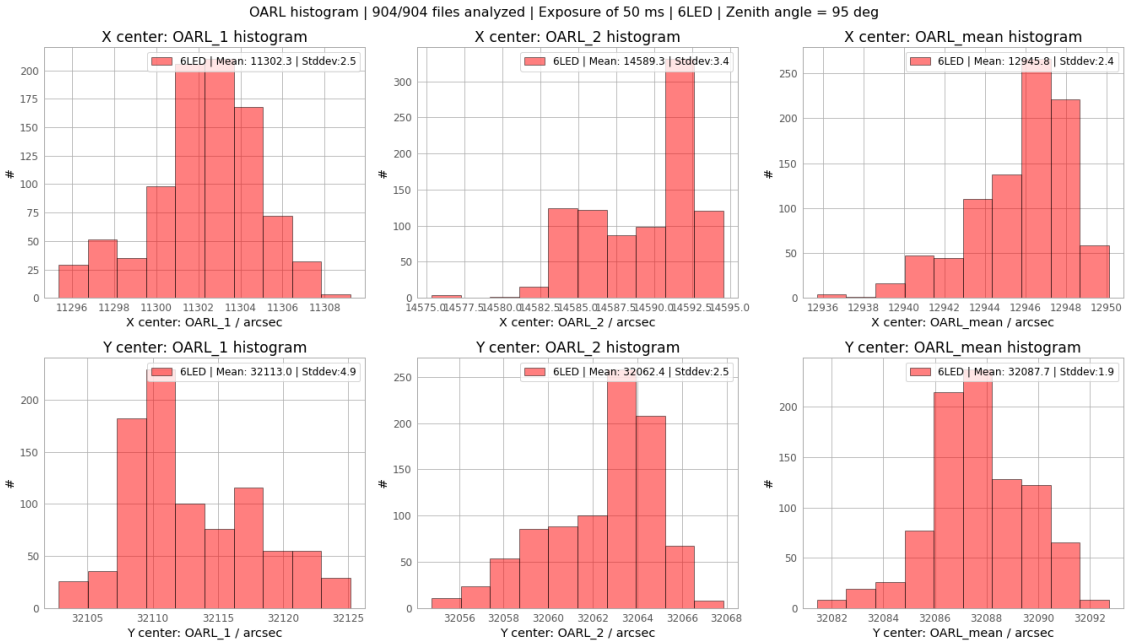

Figure 5.15: Distribution of OARL center results when the PMT camera is parked. The standard deviation gives the resolution of the measurements.

The OARL results are shown in Figure 5.15. There the results are shown for each laser and the mean value of each laser for vertical and horizontal coordinates. Here the distributions are not as good compared to the LED results, which can also be seen in the larger standard deviations of the distributions.

In particular for the CDM we are interested in the results of the displacement of the PMT camera relative to the OARL. Displacement is the distance between the fitted circle center and the OARL center mean. This is shown in Figure 5.16. The first two columns of subplots are the same as in the Figure 5.14 and Figure 5.15, while the third column represents the displacement measurements for each axis.

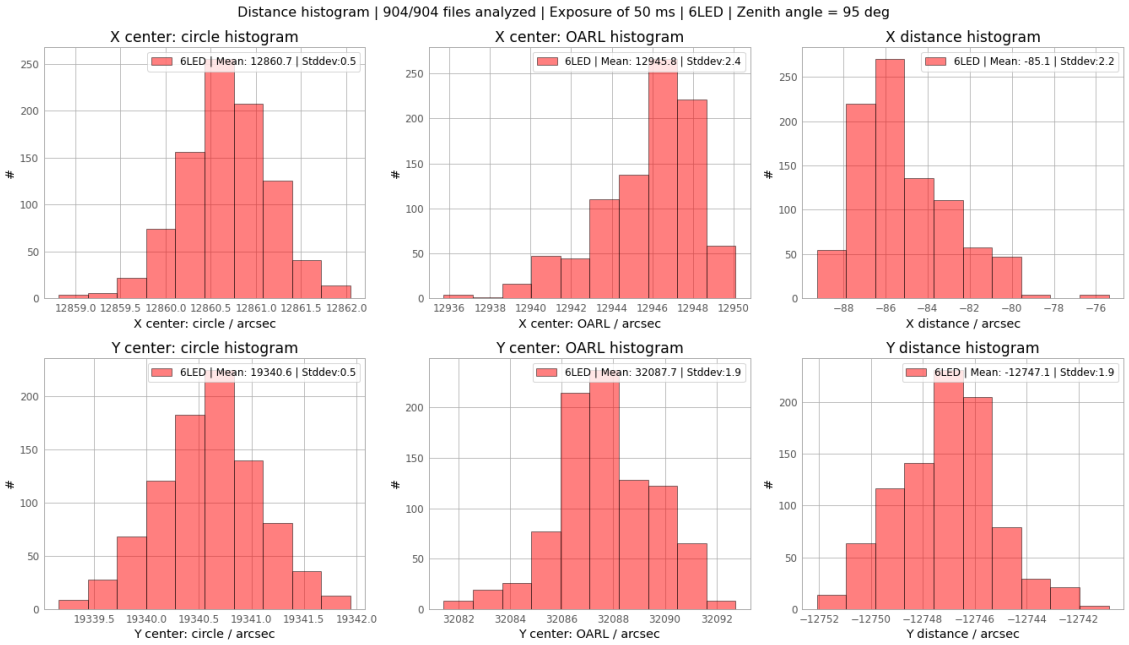

Figure 5.16: Distribution of displacement results when the camera is parked. Displacement is the distance between the fitted circle center and the OARL center mean. The standard deviation gives the resolution of the measurements.

Figure 5.17 shows the total displacement results. There the standard deviations of the displacement is $\sim$2 arcsec, which is below the required resolution of $\sim$ 5 arcsec. So even when the results are degraded due to the worse OARL resolution, the end result is still within the requirements.

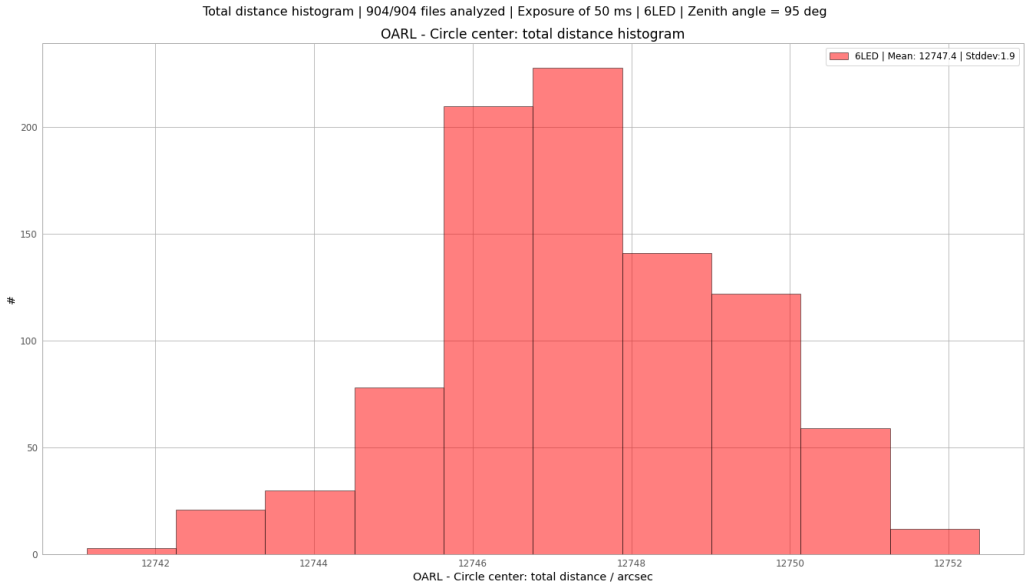

Figure 5.17: Histogram of total displacement results when the camera is parked. Displacement is the distance between the circle center and the OARL center mean. The standard deviation gives the resolution of the measurements.

In the Figure 5.18 the previous results are shown, but with respect to time. For the circle center the results display no pattern. But for the OARL result there are some drift and even some erratic jumps of the result. The subplot scales are not the same, the range of the OARL vertical axis is larger by approximately an order of magnitude.

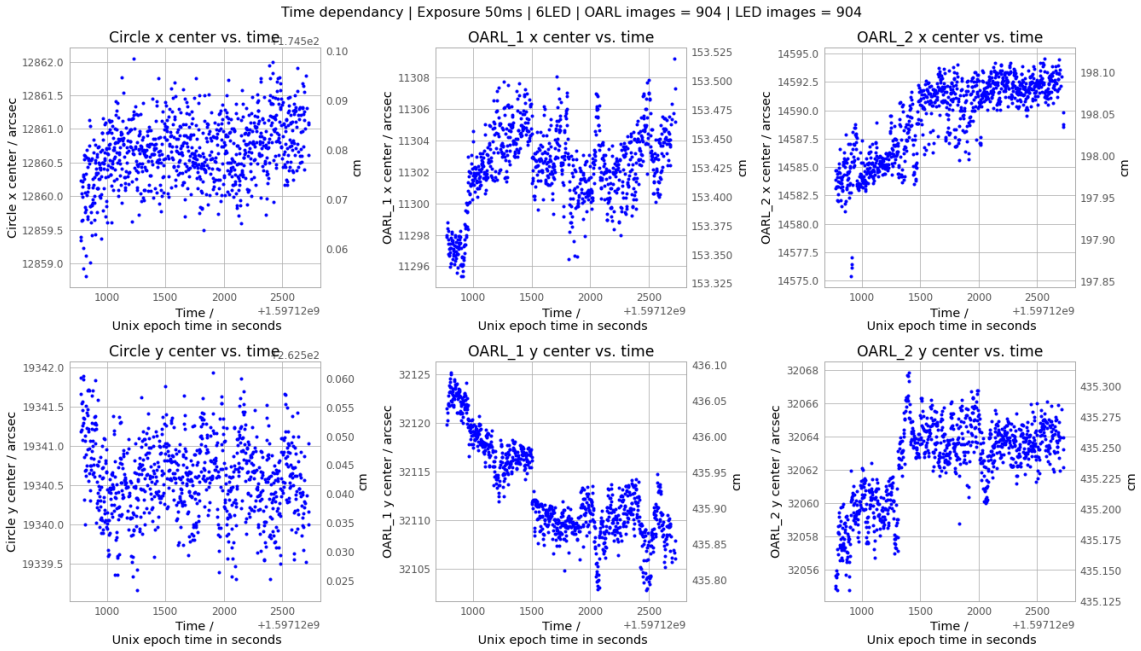

Figure 5.18: Circle center and OARL center results with respect to time. The left vertical axis is given in arcseconds, while the right vertical axis given in cm. Mind the scales in each individual subplot, they are not the same.

Multiple parked datasets during different nights have been taken. The results are shown in Table 5.2. The total displacement results are ∼2.5 arcseconds, which is within the requirement of 5 arcseconds. From the table is clear that the final results are limited by OARL resolution.

Dataset #	Circle center: X	Circle center: Y	OARL center: X	OARL center: Y	Displacement X	Displacement Y	Total displacement
1	0.4	0.4	1.5	2.7	1.6	2.6	2.6
2	0.5	0.7	2.0	1.2	2.0	1.3	1.3
3	0.5	0.5	4.2	2.9	4.1	2.9	2.8
4	0.7	0.7	4.6	1.8	4.1	1.7	1.7
5	0.4	0.4	1.8	1.2	1.8	1.2	1.2
6	0.5	0.5	3.8	3.3	3.8	3.4	3.4
7	0.5	0.4	2.1	1.9	2.2	1.8	1.8
8	0.5	0.5	1.8	1.3	1.8	1.4	1.4
9	0.5	0.5	5.0	2.2	4.9	2.1	2.0
10	0.4	0.4	2.6	5.4	3.7	1.4	1.3
11	0.6	0.6	2.3	2.2	2.5	2.4	2.4
12	0.4	0.4	1.2	0.7	1.2	0.8	0.8
13	0.4	0.4	2.0	2.8	2.0	2.3	2.3
14	0.5	0.5	2.4	1.9	2.2	1.9	1.9

Table 5.2: Resolution results of parked datasets. Units are in arcseconds.

5.6.2.1 Validation of the results - circle radius

From the taken data the radius of the LED circle was determined. From the CDM data it was determined to be 1323 ± 1 mm, while from the camera design it was 1322 mm which was in a good agreement.

5.6.3. Zenith scan dataset

For the zenith scan dataset the telescope was pointed to azimuth = 0°and different zenith angles. The zenith angle positions were from 0° to 75° in steps of 5°. Then for each zenith angle ∼500 CDM images were taken. This way the effect of zenith angles on the CDM results could be checked.

The results of the zenith scan for the circle fit are shown in Figure 5.19. For the circle center vertical coordinate (top center subplot) there is a clear correlation with the zenith angle. This is due to the camera of mass ∼2 tons located at the end of a support structure of ∼28 m. With the increasing zenith angle the load on the structure increases causing the camera to sag. In total there is a shift when moving from $0° - 75°$ zenith the shift is a bit less than 2 cm.

In Figure 5.19 the top right subplot shows that there is also an effect of reconstructed circle radius with respect to the zenith angle. This is again due to camera sag which causes the center of the PMT camera to be a bit below the CDM line of sight. Because of this the CDM sees the PMT camera at a slight angle which changes the reconstructed radius a bit. It can be seen that the effect on the reconstructed radius is ∼0.3 mm when the telescope zenith angle is changed by 75°.

There is also a minor effect on the horizontal position of the camera with respect to the zenith angle, about 0.3 mm in the full zenith range.

But the results of the fit are all consistent at all zenith angles, as seen in the bottom subplots of Figure 5.19.

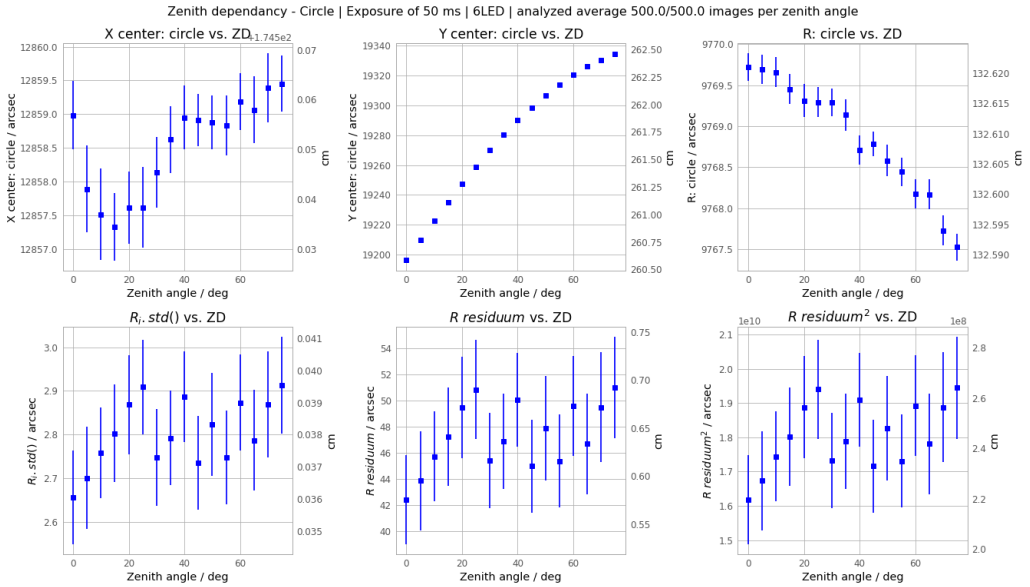

Figure 5.19: CDM circle fit results for the zenith scan dataset.

Figure 5.20 shows the result of a zenith scan for the fitted circle center. It shows that there is some azimuthal effect on the camera center with respect to the zenith angle.

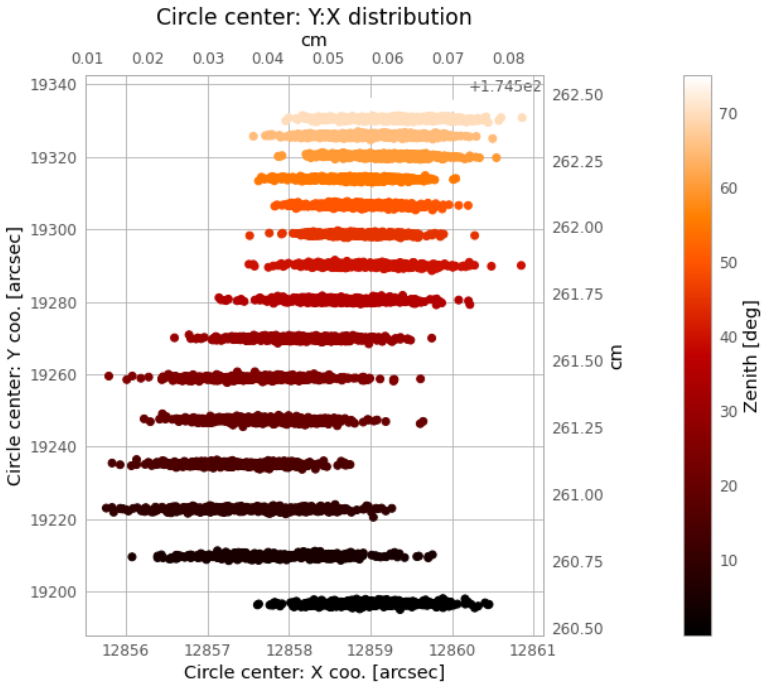

Figure 5.20: Results of the zenith scan for the fitted circle center coordinates. Color represent the zenith angle at which the data was taken. A shift in the azimuthal direction with respect to the zenith angle can be seen.

The OARL results for the zenith scan are shown in Figure 5.21. There there is some effect of the zenith angle on the OARL vertical position but much less than the camera sag effect.

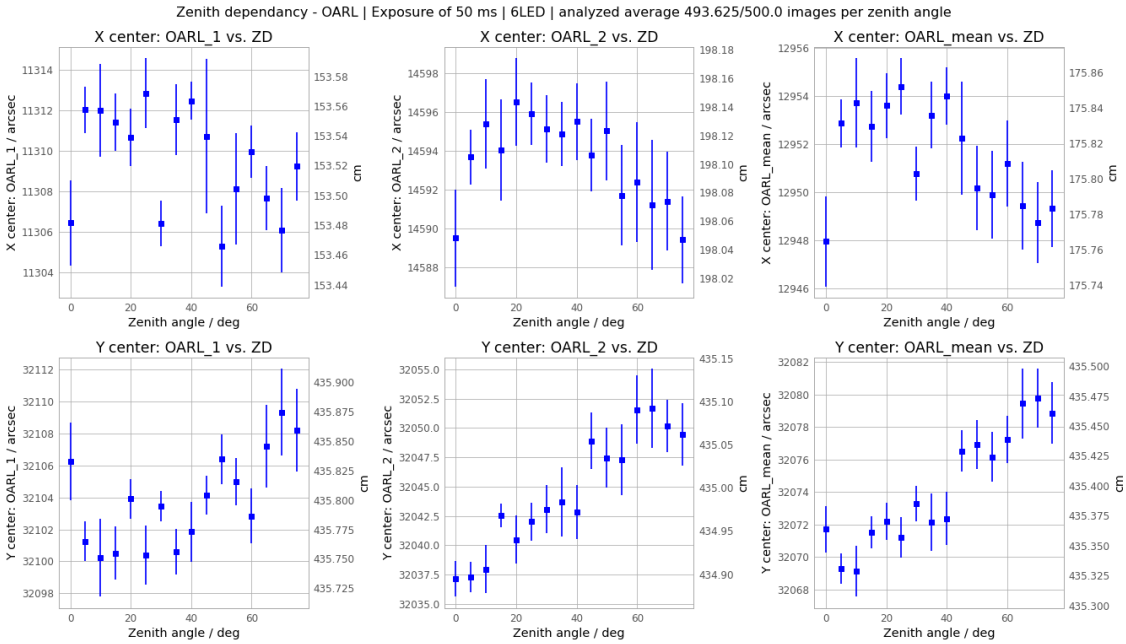

Figure 5.21: CDM OARL results for the zenith scan dataset.

The displacement results can be seen in the last column of Figure 5.22.

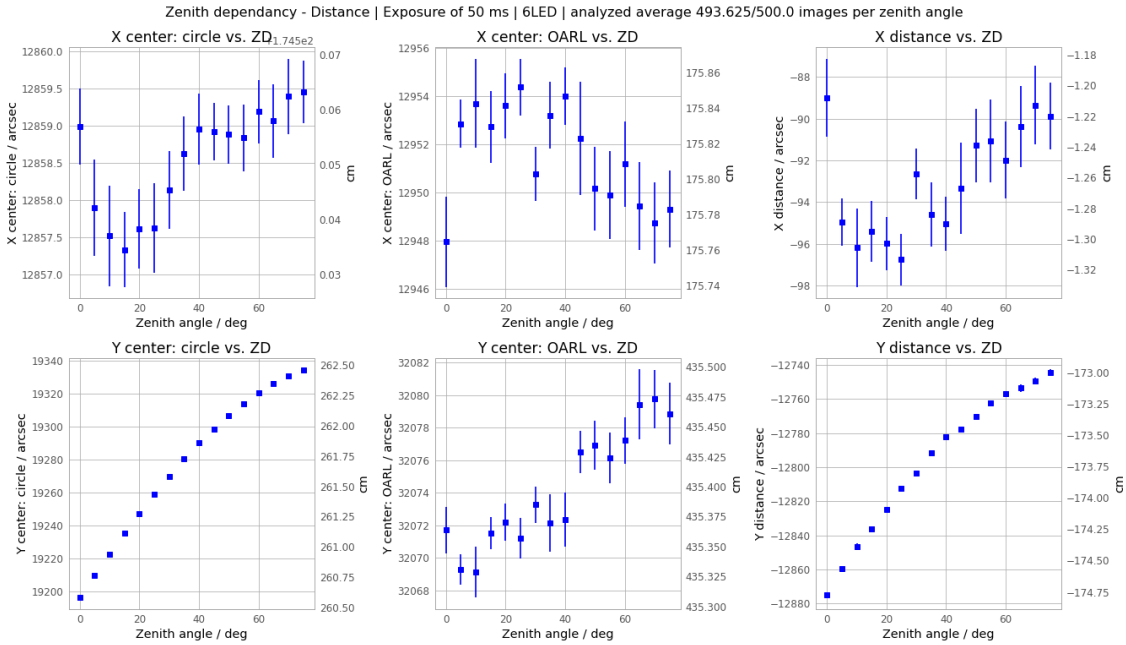

Figure 5.22: CDM displacement results for the zenith scan dataset.

The total displacement with respect to the zenith angle is shown in Figure 5.23. The bottom subplot shows the error bars of the top subplot.

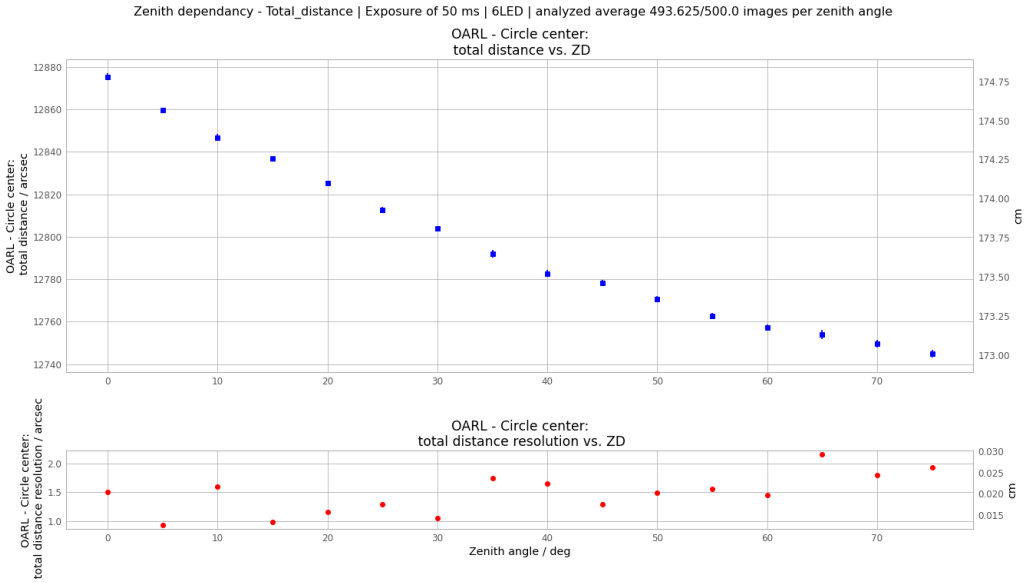

Figure 5.23: CDM total displacement results for the zenith scan dataset.

Some more technical data was taken in which the telescope zenith position changed from 0° to 75° zenith angle. The measurements plots are shown in Table 5.3. CDM measured the sag of the camera and it was around 1.9 cm, which was in accordance with the simulations [154].

Dataset #	**Sag / arcsec**	**Sag resolution / arcsec**	**Sag / cm**	**Sag resolution / cm**
1	139.5	0.35	1.898	0.005
2	139.9	0.3	1.899	0.004
3	137.7	0.4	1.869	0.005
4	137.1	0.35	1.861	0.005

Table 5.3: CDM camera sag results for several taken datasets.

5.6.3.1 Azimuthal dependency

A zenith scan was performed in two different pointing direction. One pointing at azimuth angle of 0° and another pointing at azimuth angle of 180°. The result is shown in Fig-

ure 5.24. For the position of the camera horizontal coordinate a shift of about 0.5 mm is seen.

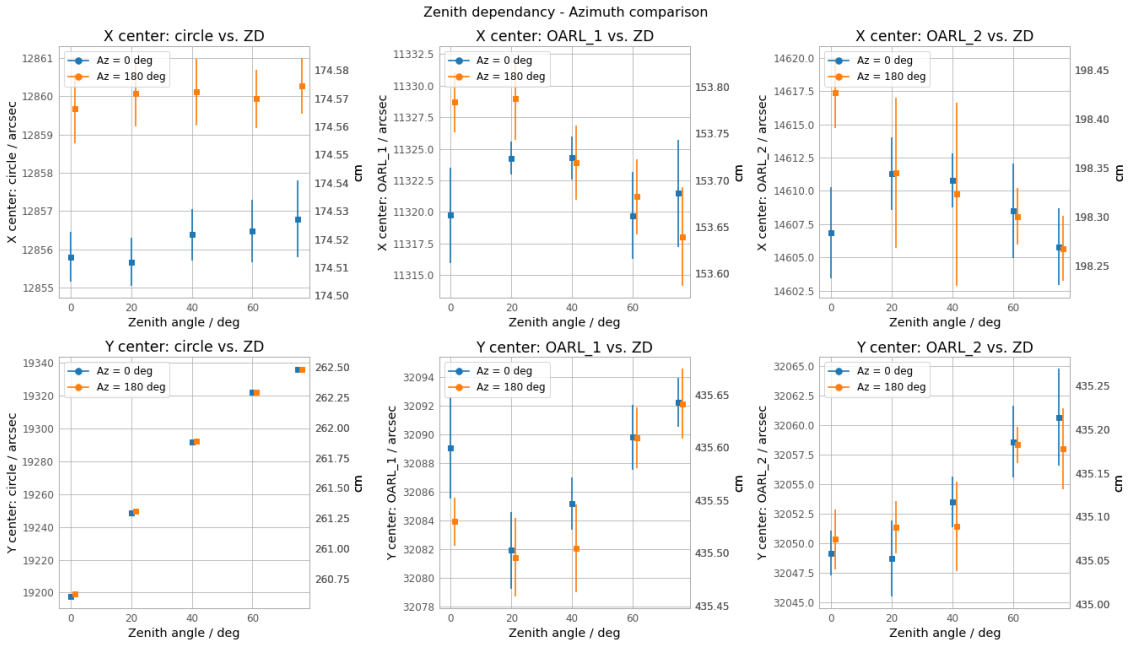

Figure 5.24: Results of the CDM zenith scan for 2 different azimuth angles differing by 180°.

5.6.4. LED fit tests

The reference LEDs are seen by both CDM and SG camera. The SG camera is more sensitive because it has bigger pixel size so more light falls on each pixel and it is Peltier cooled. For the SG camera the LEDs are too bright and they are saturate parts of the SG images and this can cause less precision from SG. One of the ideas to resolve this was to put light attenuation filters on top of LEDs.

Filters were put on some of the LEDs and CDM images were taken to assess the result:

- without a filter the CDM could operate with the LED intensity being 1-50, but best at 20.
- 20% attenuation filter would still be OK for the CDM with the LED intensity being increased to 50-100.
- 1% and 0.2% filters attenuate too much for CDM and the LEDs are not visible enough.

The CDM sees all the LEDs in it's field of view but the SG sees only half of the reference LEDs, in particular it only sees the left part of the PMT camera. So the idea was to put the filters on only the LEDs of the left side of the PMT camera and to leave the rest of the LEDs unchanged. Then the CDM would use only the LEDs without the filters to fit the circle.

For this test zenith scan data was taken from 0° to 75° zenith angle in steps of 5° with the azimuth being fixed at 0°. For each of the zenith angle positions 60 CDM images were taken and analysed.

At the time of these tests an older shutter for the PMT camera was installed. This shutter obstructed the 2 top LEDs from being seen by the CDM camera so the maximum number of LED that coud be used to fit the circle was 10, instead of 12. Later the shutter was replaced with a new one and currently 12 LEDs can be used to fit the circle.

Five methods of LED fit were tested:

- Fit with 10 LEDs (labeled "10LED").
- Fit with 5 right LEDs (labeled "5rLED").
- Fit with fixed radius (labeled "fixR") using 5 LEDs on the right.
- Fit with 5 LEDs on the opposite (left) side (labeled "5lLED")
- Fit with 5 right LEDs + 1 left LED (labeled "6LED")

The comparison of these methods is shown in Figure 5.25. From these plots it can be seen that (5rLED) method produces bigger error bars due to unstable fit. Also (5lLED) and (5rLED) methods predict wrong circle center and radius result. This is because the lack of LEDs on the other side of the circle make the radius of the fitting procedure too small, causing a bias. The (fixR) method overestimates the circle center horizontal and vertical positions. The (10LED) and (6LED) methods match very good. So the presence of a LED on the other side of the circle improves the fit significantly. Comparison of just these 2 methods is shown in Figure 5.26. This can be seen in the bottom plots which show that these two methods have the best fit results, while the (fixR) method performs worst.

In the end it was decided that the SG won't be using the filters on top of LEDs. So in the CDM analysis 10 LED method was used with the old shutter, and 12 LEDs were used when the new shutter was installed.

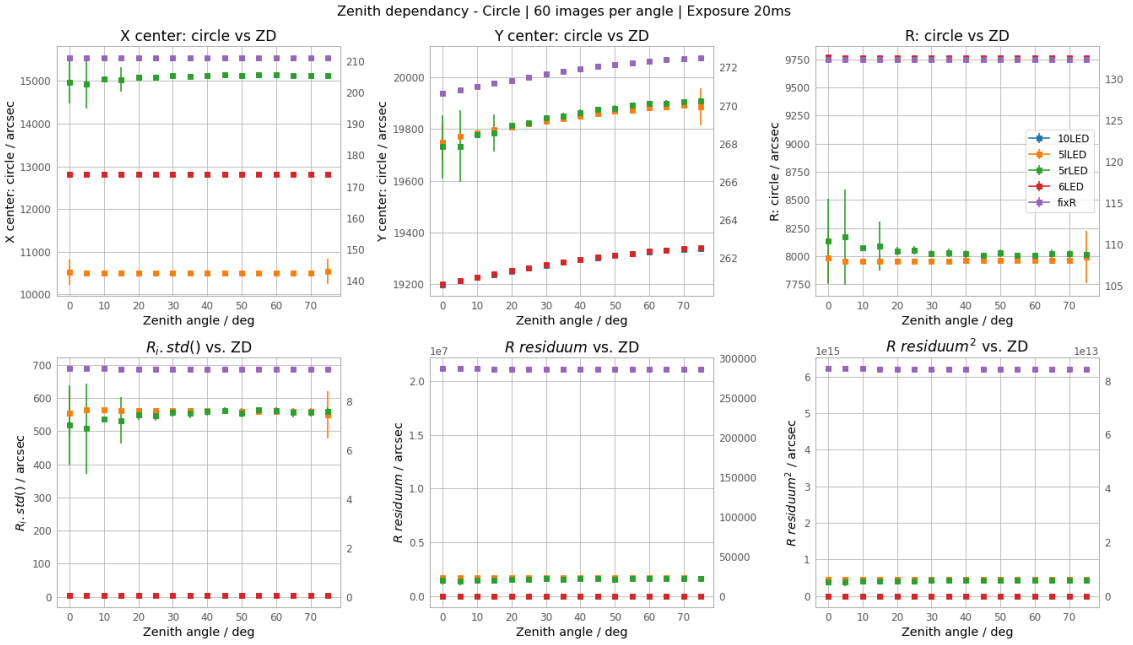

Figure 5.25: Comparison of different LED fitting methods for CDM.

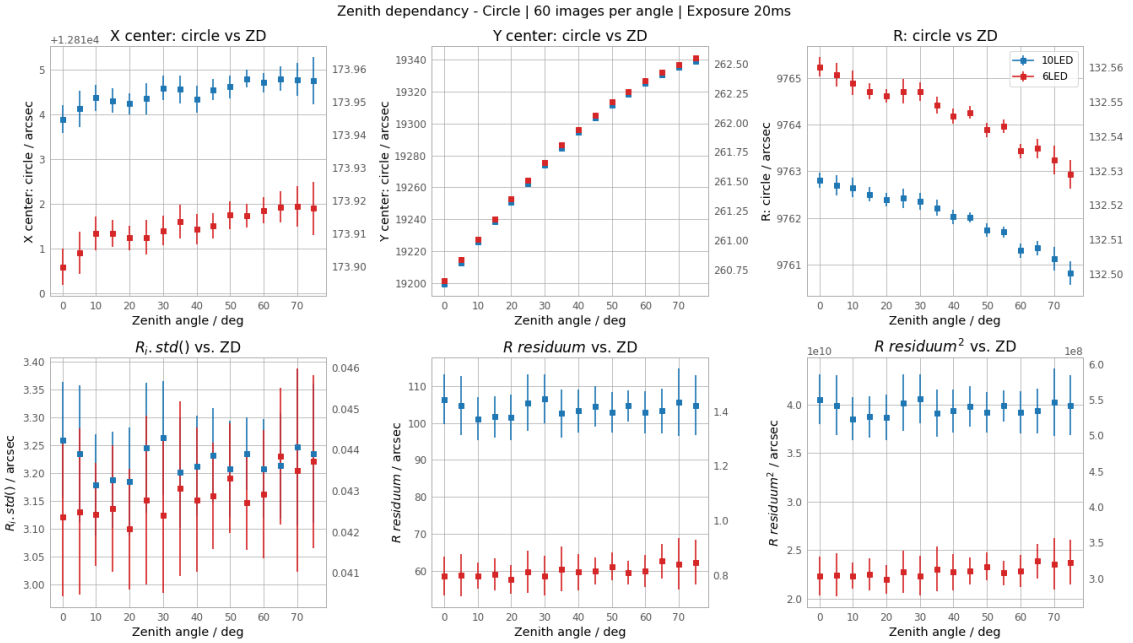

Figure 5.26: Comparison of (10LED) and (6LED) fitting methods for CDM.

5.6.5. Test of OARL influence on circle reconstruction

From some of CDM datasets it was seen that the OARL spots were not always present. This was investigated and was found out that there was some cabling issue which caused the OARL to frequently turn off and on. This was a good opportunity to test if there is any dependence of the circle center results with respect to the OARL state. This can happen if the light from the OARL is too bright and would affect the LED spots and their center reconstructions. For example, such effect is affecting the SG position reconstruction.

CDM images were taken while the telescope was parked. Out of 1000 images, 319 of them was when the OARL was off. The two distributions are compared in Figure 5.27. From there it is clear there is no effect of OARL on circle center results as the means and standard deviations of the distributions match.

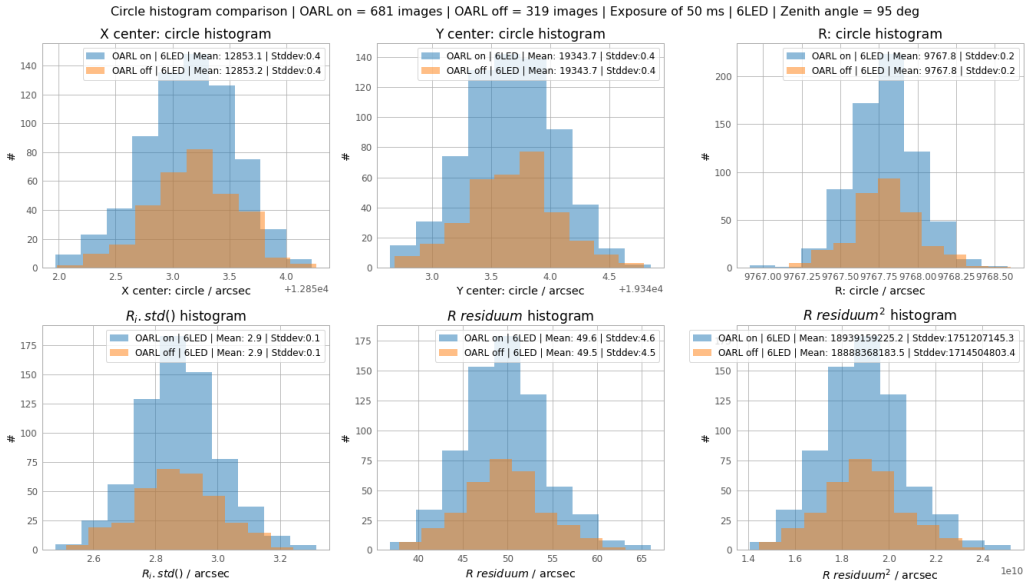

Figure 5.27: CDM parked distributions when the OARL was on (blue) and off (orange) are the same.

Then the CDM images were taken in zenith scan mode with 500 images per zenith angle taken. About half of them had OARL off. Result are shown in Figure 5.28 and there both distributions match, further confirming that there is no effect of OARL on circle reconstruction.

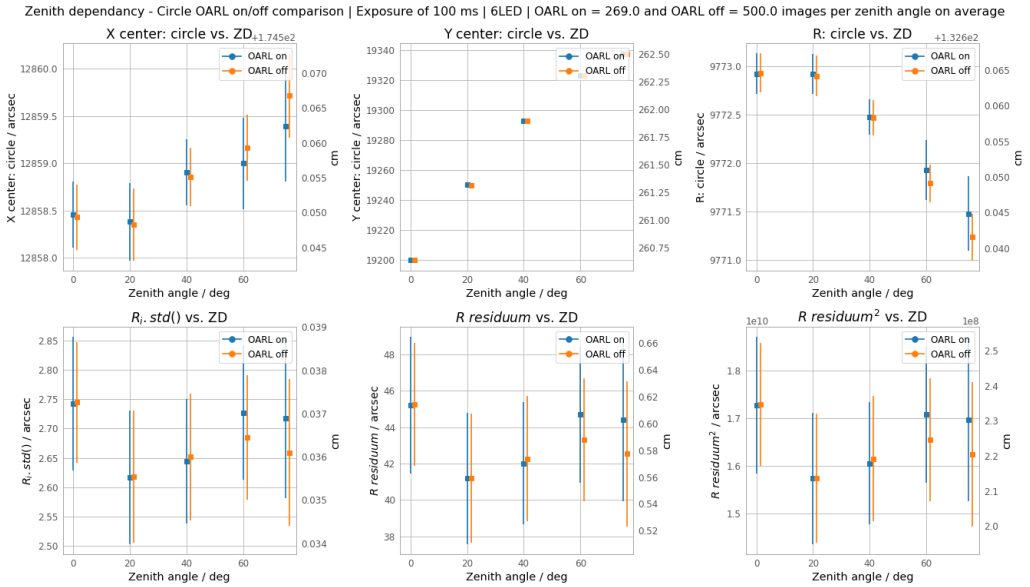

Figure 5.28: CDM zenith scan distributions when the OARL was on (blue) and off (orange) are the same.

5.6.6. CDM-SG comparison

During the zenith scan technical observations the CDM and SG data was taken at the same time so the results could be compared directly. The comparison can be seen in Figure 5.29. The results match and are within errorbars proving the validity of CDM and SG reconstruction methods. The SG results have larger errrorbars because the SG has bigger pixels and it is not optimized for the camera displacement monitoring.

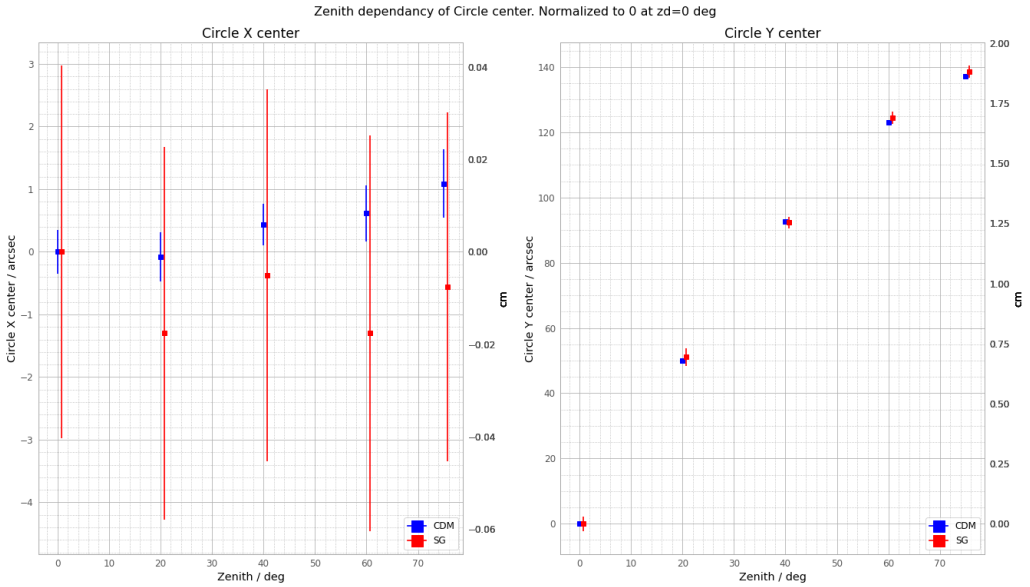

Figure 5.29: Comparison of CDM and SG zenith scan results.

5.6.7. OARL image stacking

As it can be seen from the previous results the displacement results are limited by the OARL measurements. One idea to improve the OARL measurements is not to use the OARL information from each individual image, but to stack several images to extract a more stable OARL center measurement. The LED and fitted circle results would still be updated based on each taken image, only the OARL information would be updated after several analysed images. Using this method the OARL information would no longer be updated with a frequency of 10 Hz, but that is acceptable as from the FEM studies the deformations of the dish should not have a high oscillation frequency.

For this purpose CDM data was taken while the telescope was parked. First CDM images were taken where from each image the OARL data was extracted. Then the data was taken where the OARL measurements were extracted from 10 stacked images. Finally the data was taken where the OARL measurements were extracted from 30 stacked images. Proportionally more images were taken for the stacked result with respect to the no stack option in order to get a comparable number of OARL measurements. The results are shown in Figure 5.30 and Figure 5.31. The results are not conclusive and another set of data needs to be taken for a better analysis method. With these measurements there are 3 independent datasets which are compared to one another. For a better comparison

different stack settings should be done on the same dataset so the result can be directly compared. This test will be done in the future.

OARL stacking

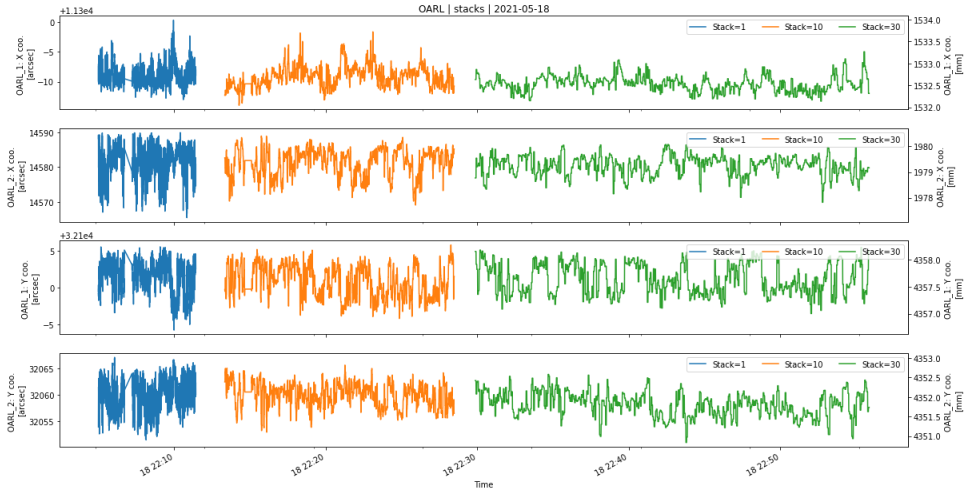

Figure 5.30: OARL results w.r.t. time. It shows 3 different results with different number of images stacked. The blue data is analyzed from 1 image, orange from 10 images, green from 30 images.

OARL stacking histograms

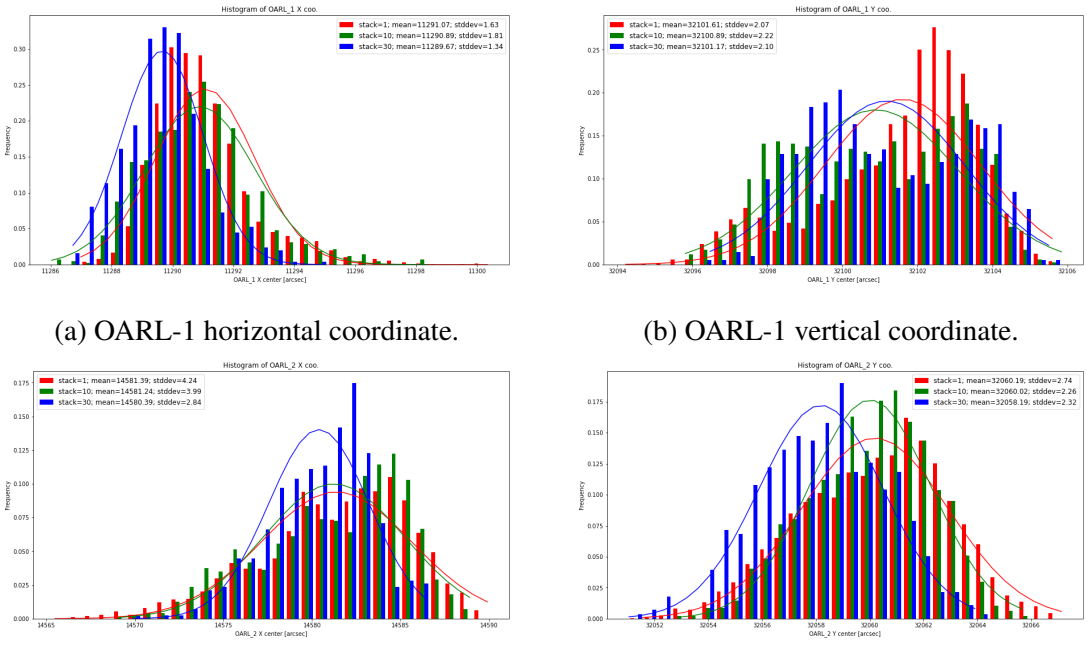

(a) OARL-1 horizontal coordinate.

(b) OARL-1 vertical coordinate.

(c) OARL-2 horizontal coordinate.

(d) OARL-2 vertical coordinate.

Figure 5.31: OARL stacking histograms for both OARL spots and for both coordinates.

5.7. TRACKING RESULTS - OFFLINE ANALYSIS

To check the CDM tracking performance data was taken while the telescope was tracking and CDM images were saved for offline analysis. As the images are ∼15 Mb in size the CDM was saving images approximately once every second.

5.7.1. Mothallah dataset

On 2020/11/08 about 6 hours of technical data was taken consisting out of continuous tracking taken on the Mothallah (Caput Trianguli) star. It was chosen as is traversed the zenith range from 0° to about 65° while the telescope was tracking it.

The timeline of the events from the reports of the shifters and drive experts is listed here:

- 23:30 h - Data taking started
- 23:49 h - Tracking stopped (drive subsystem low zenith angle limit)
- 01:51 h - Telescope stopped tracking (maximum tracking time reached)
- 01:53-01:57 h - Telescope hit the azimuth limit, so it rotated itself 360° to continue tracking
- 03:52 h - Drive stopped tracking (time limit)
- 04:21 h - Drive tracking stopped on its own

5.7.1.1 All night results

The results for the circle center horizontal coordinate and the horizontal displacement are shown in Figure 5.32. From Figure 5.32a the times when the telescope stopped tracking can be clearly identified. In Figure 5.32b those events are harder to distinguish due to the PMT camera centre results being smeared with OARL measurements which have not as good resolution.

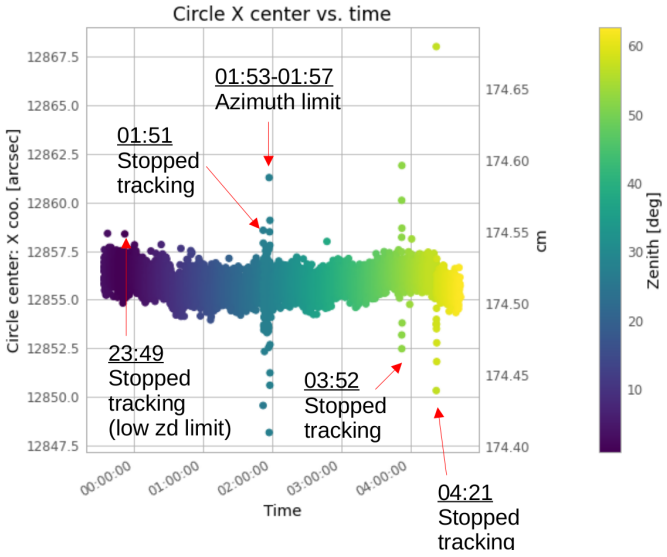

(a) Circle center horizontal coordinate.

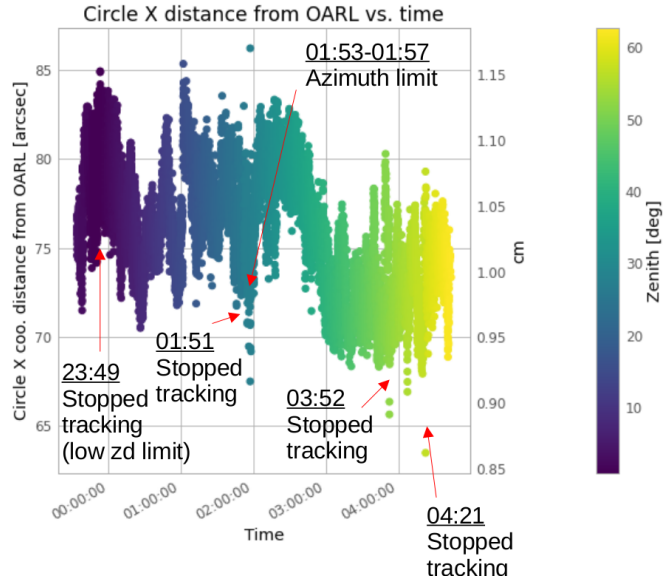

(b) Horizontal camera displacement.

Figure 5.32: Results for the horizontal components while tracking Mothallah. Each dot represents one CDM image analysed. The color bar represents the zenith angle of the telescope and was taken from the drive subsystem.

Similarly the results for the circle center vertical coordinate and the vertical displacement are shown in Figure 5.33. From Figure 5.33a the times when the telescope stopped tracking can be clearly identified. Also, the shape of the overall curve shows the camera sag effect. Again in Figure 5.33b those events are harder to distinguish due to worse OARL resolution.

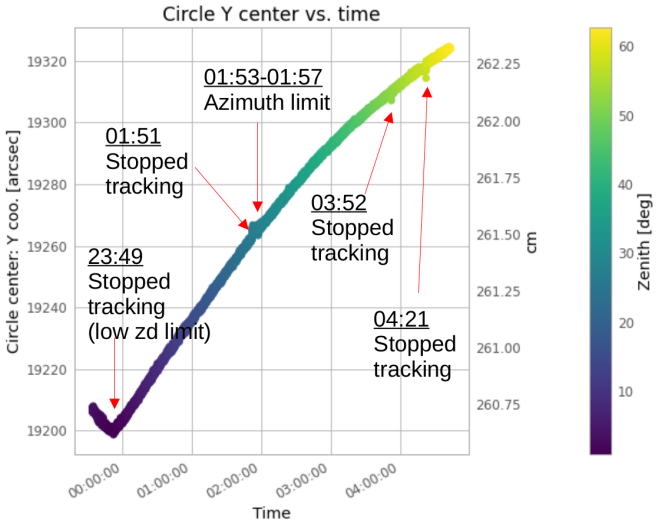

(a) Circle center vertical coordinate.

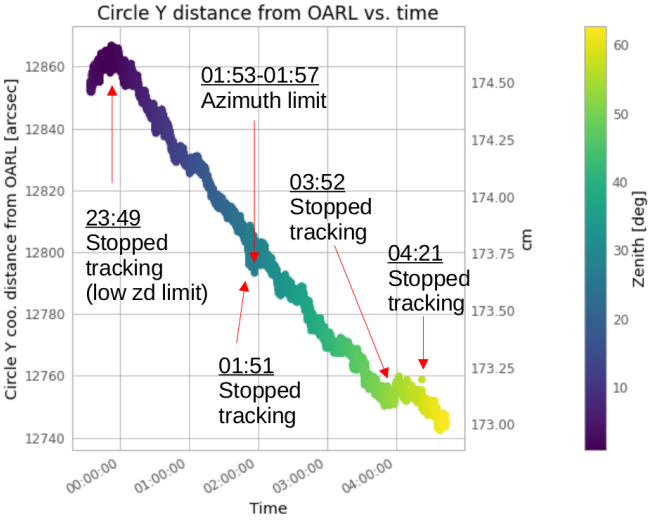

(b) Horizontal camera displacement.

Figure 5.33: Results for the vertical components while tracking Mothallah. Each dot represents one CDM image analysed. The color bar represents the zenith angle of the telescope and was taken from the drive subsystem.

The results for the circle radius are shown in Figure 5.34. From Figure 5.34a the times when the telescope stopped tracking can be clearly identified. The overall shape of the curve shows the radius dependence on zenith angle. This is due to the changing angle between the CDM and the PMT camera caused by the camera sag. Figure 5.34b shows the standard deviation for the radius result and again the times when drive stopped tracking can be seen.

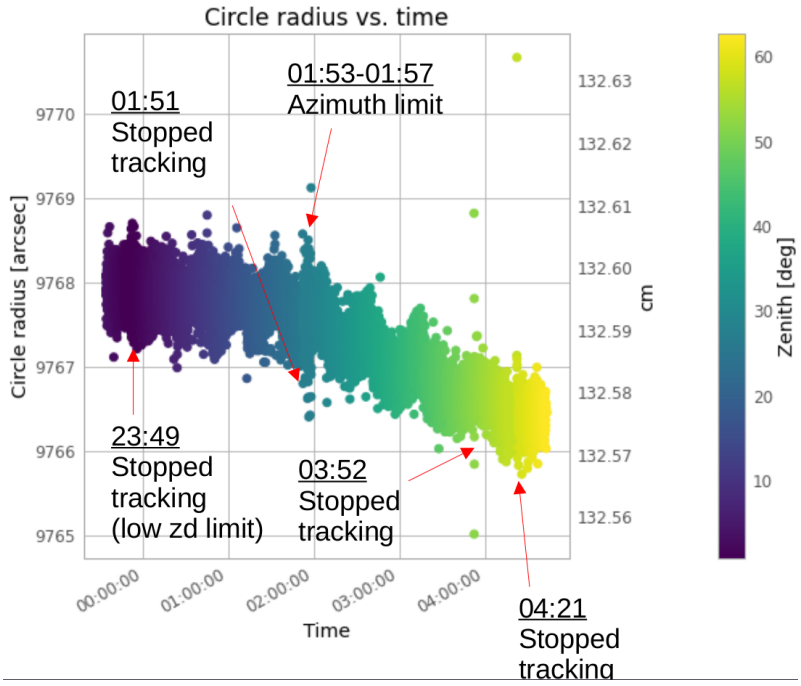

(a) Circle radius while tracking Mothallah. Here the radius dependence on zenith angle can be seen.

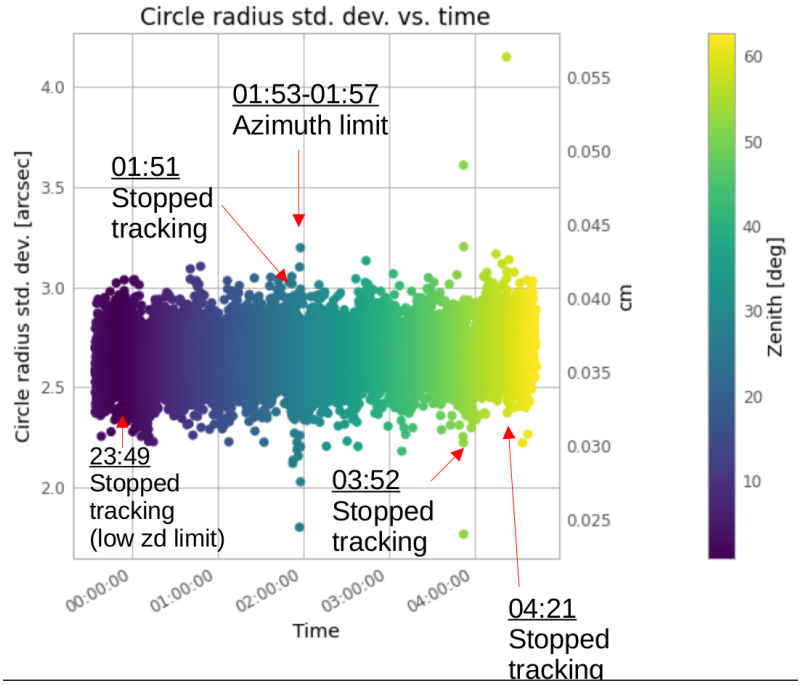

(b) Circle radius standard deviation while tracking Mothallah.

Figure 5.34: Results for the circle radius and it's standard deviation while tracking Mothallah. Each dot represents one CDM image analysed. The color bar represents the zenith angle of the telescope and was taken from the drive subsystem.

5.7.1.2 Correlation with the drive subsystem

To better inspect the time correlation of the CDM and the drive subsystem the plots were zoomed in around the times when the drive stopped.

Figure 5.35 shows the plot for CDM circle center results when the drive was stopped because it reached the low zenith angle limit. The correlation is especially seen in Figure 5.35b which makes sense as the telescope hitting the zenith angle limit should primarily affect the vertical coordinate of the PMT camera.

Clear correlation of drive and CDM data can be seen in the rest of the plots Figure 5.36, Figure 5.37, Figure 5.38.

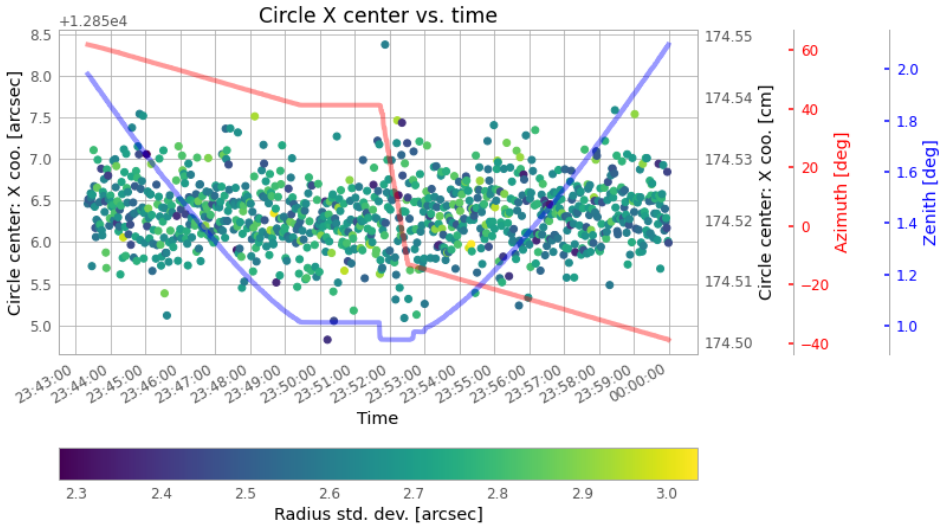

(a) Circle center horizontal coordinate.

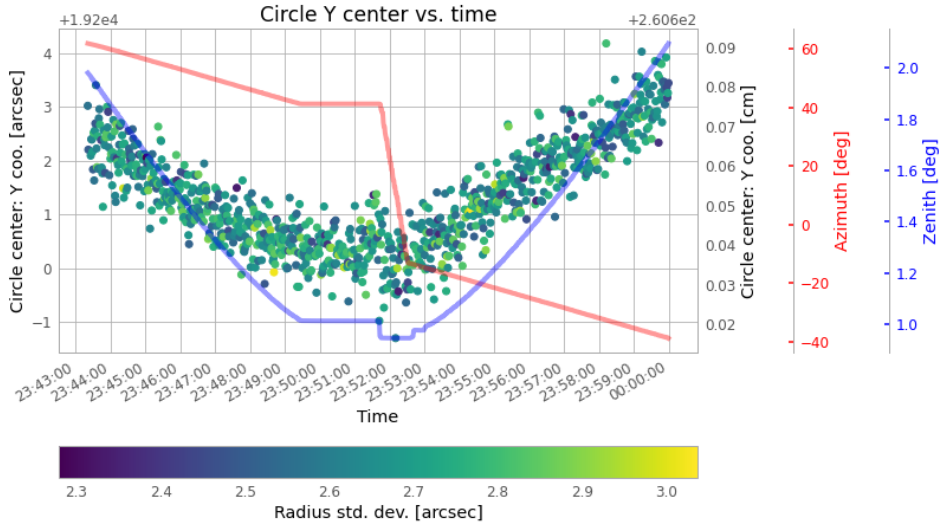

(b) Circle center vertical coordinate.

Figure 5.35: CDM results while tracking Mothallah at 23:51 h when tracking stopped due to low zenith limit. Each dot represents one CDM image analysed. The color bar represents the radius standard deviation value. The two rightmost secondary vertical axes represent the zenith (blue) and azimuth (red) angle of the telescope taken from the drive subsystem.

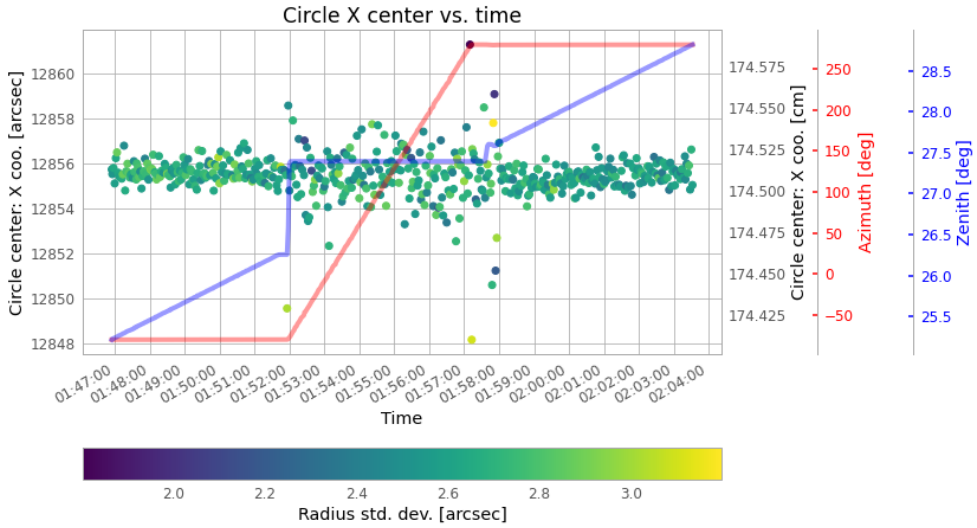

(a) Circle center horizontal coordinate.

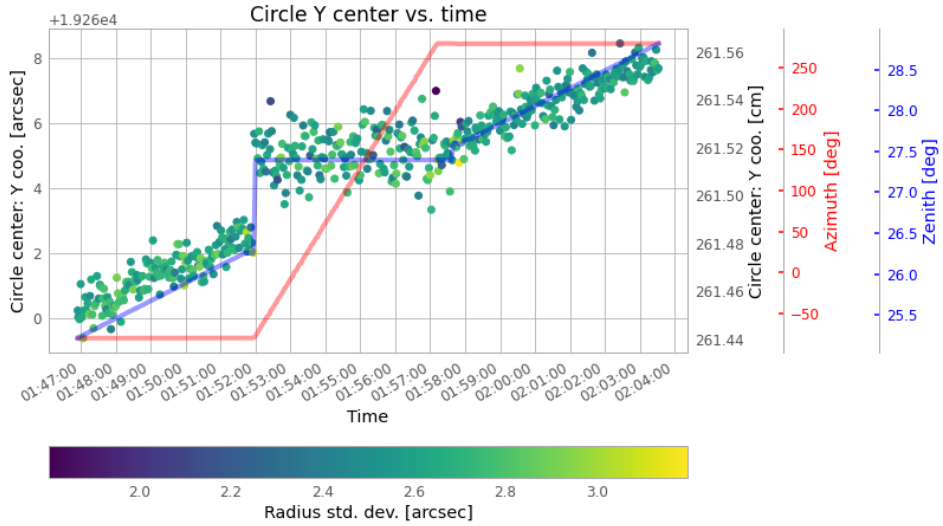

(b) Circle center vertical coordinate.

Figure 5.36: CDM results while tracking Mothallah at 01:51 h when tracking was stopped due to time limit. The color bar represents the radius standard deviation value. The two rightmost secondary vertical axes represent the zenith (blue) and azimuth (red) angle of the telescope taken from the drive subsystem.

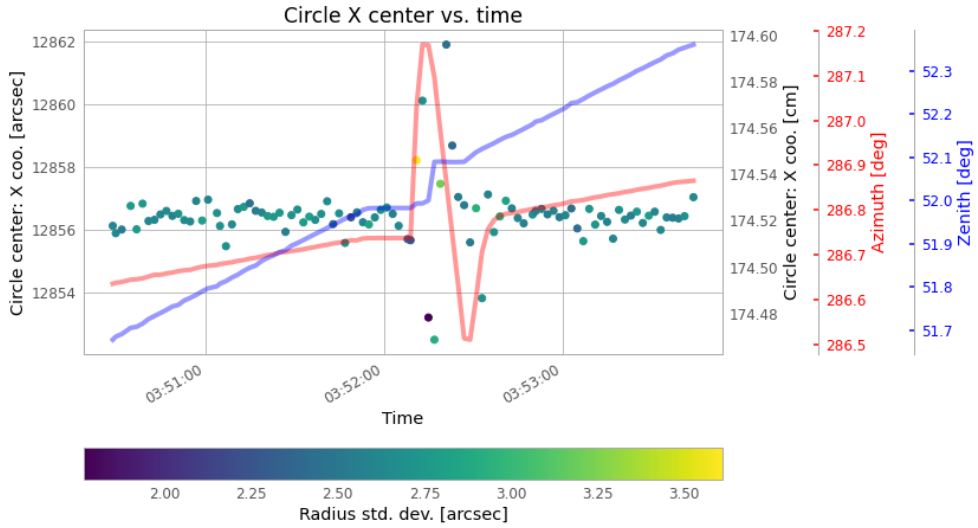

(a) Circle center horizontal coordinate.

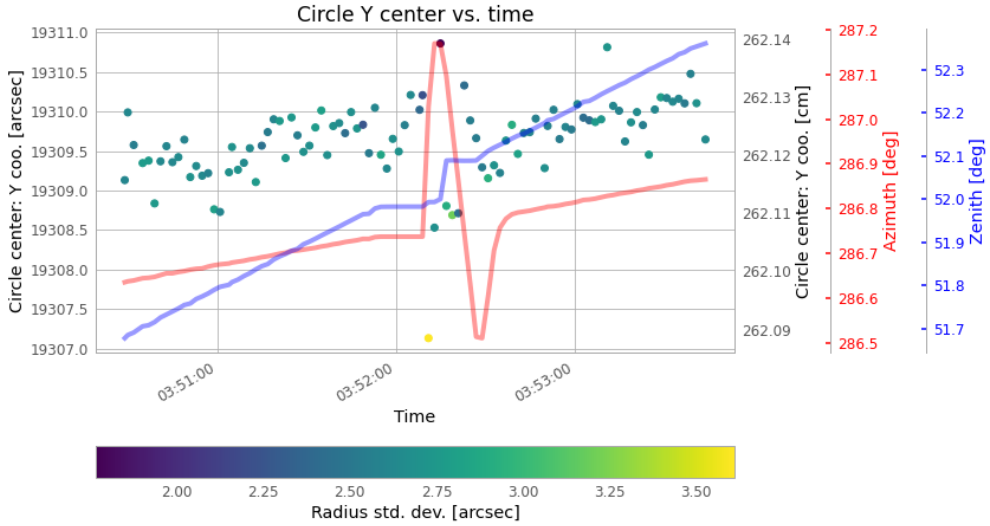

(b) Circle center vertical coordinate.

Figure 5.37: CDM results while tracking Mothallah at 03:52 h when tracking stopped due to time limit. The color bar represents the radius standard deviation value. The two rightmost secondary vertical axes represent the zenith (blue) and azimuth (red) angle of the telescope taken from the drive subsystem.

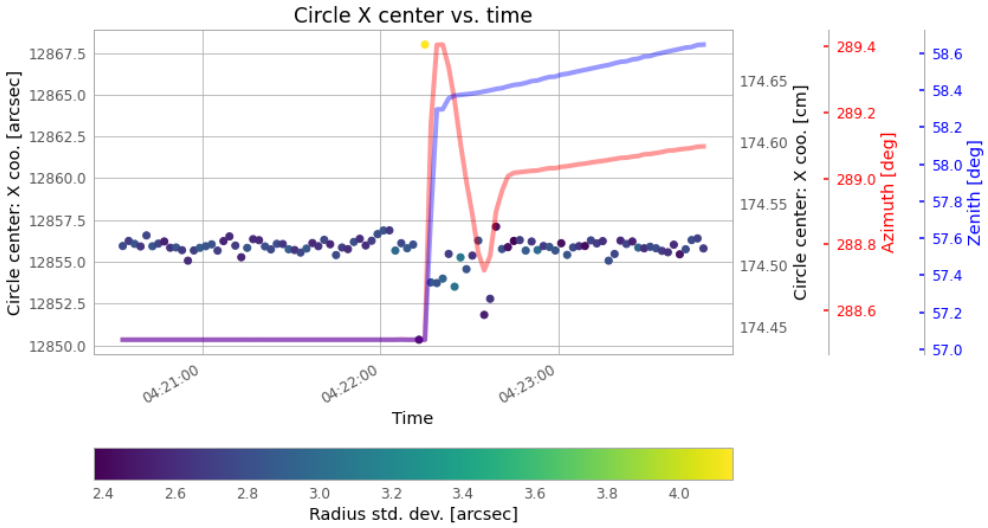

(a) Circle center horizontal coordinate.

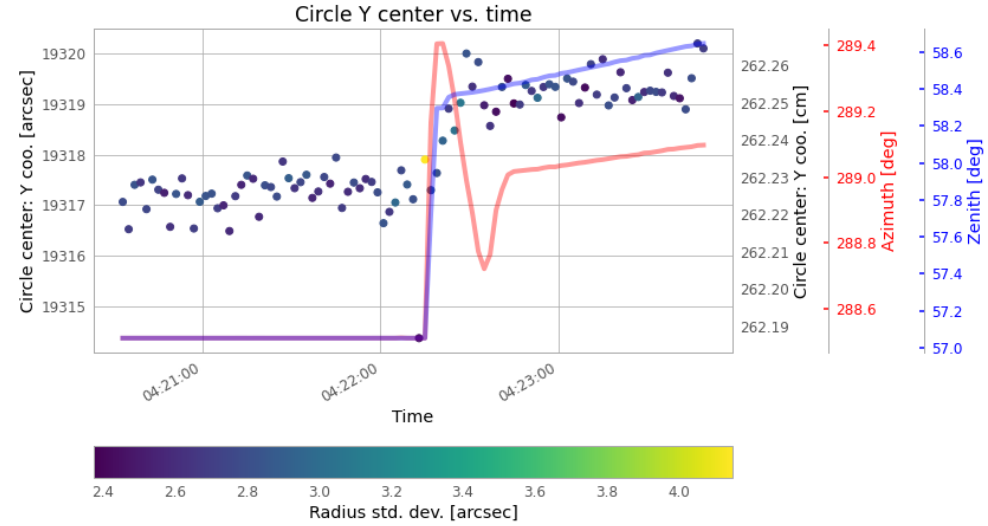

(b) Circle center vertical coordinate.

Figure 5.38: CDM results while tracking Mothallah at 04:22 h when tracking stopped on its own. The color bar represents the radius standard deviation value. The two rightmost secondary vertical axes represent the zenith (blue) and azimuth (red) angle of the telescope taken from the drive subsystem.

5.8. TRACKING RESULTS - ONLINE ANALYSIS

CDM is currently working in fully online mode which means that is taking data all the time while the telescope is tracking and the results are analysed on the fly. As opposed to the offline analysis mode, there the images are never stored to disk.

5.8.1. Timing

During normal observations the images need to be analyzed with the frequency of 10 Hz due to the requirement from the CTA. The CDM program was optimized to analyze the images quickly, in particular with the use of efficient OpenCV methods. The distribution of time differences of consecutive images taken in online mode is shown in Figure 5.39. The resulting value is 100 ms which is 10 Hz as set by the program and satisfies the requirements.

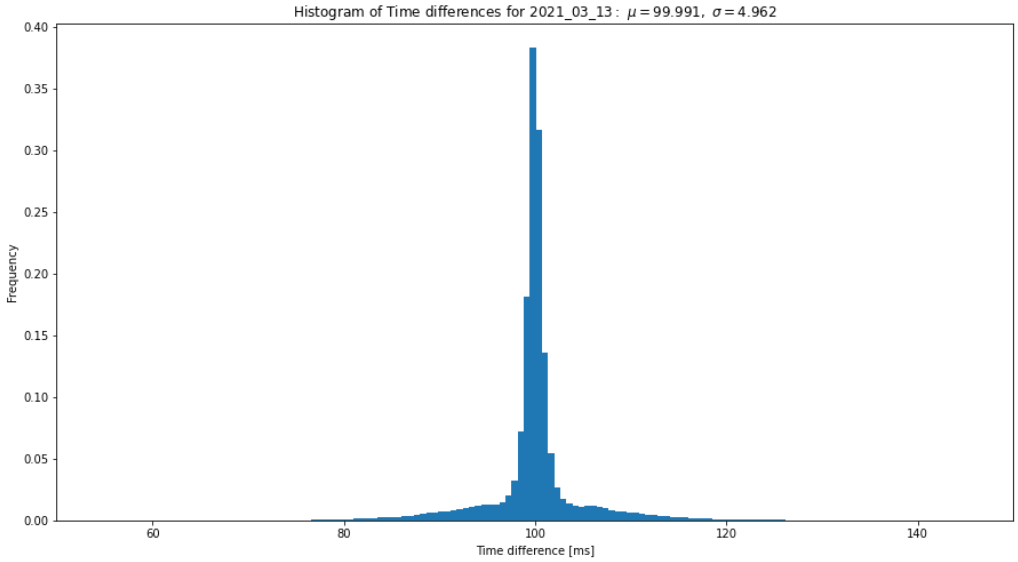

Figure 5.39: Distribution of time differences between each subsequent taken image int eh CDM online mode.

5.8.2. Drive commands correlation

Figure 5.40 shows the CDM circle fit (top four subplots) and drive (bottom two subplots) results. The vertical dashed lines represent times when the drive system received some commands such as: start tracking, stop tracking, park etc. Again, it can be seen that the CDM can measure each moment when Drive subsystem receives such commands.

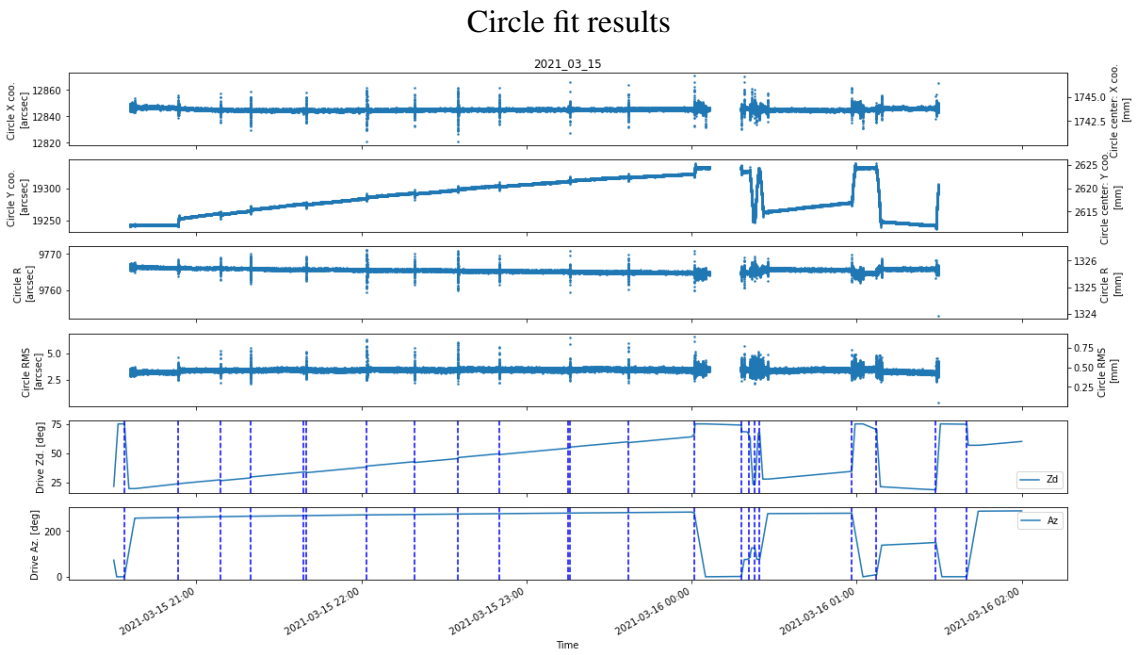

Figure 5.40: Top four subplots show different CDM circle fit result. The two bottom subplots represent information coming from the drive system (zenith and azimuth angle). In particular the vertical dashed lines represent the times when Drive system received different commands such as track or stop tracking. Around midnight there was no CDM data because the CDM was turned off by the shifters for some other tests.

Figure 5.41 shows the CDM OARL (top four subplots) and drive (bottom two subplots) results. Again, the OARL resolution is larger than the circle fit resolution.

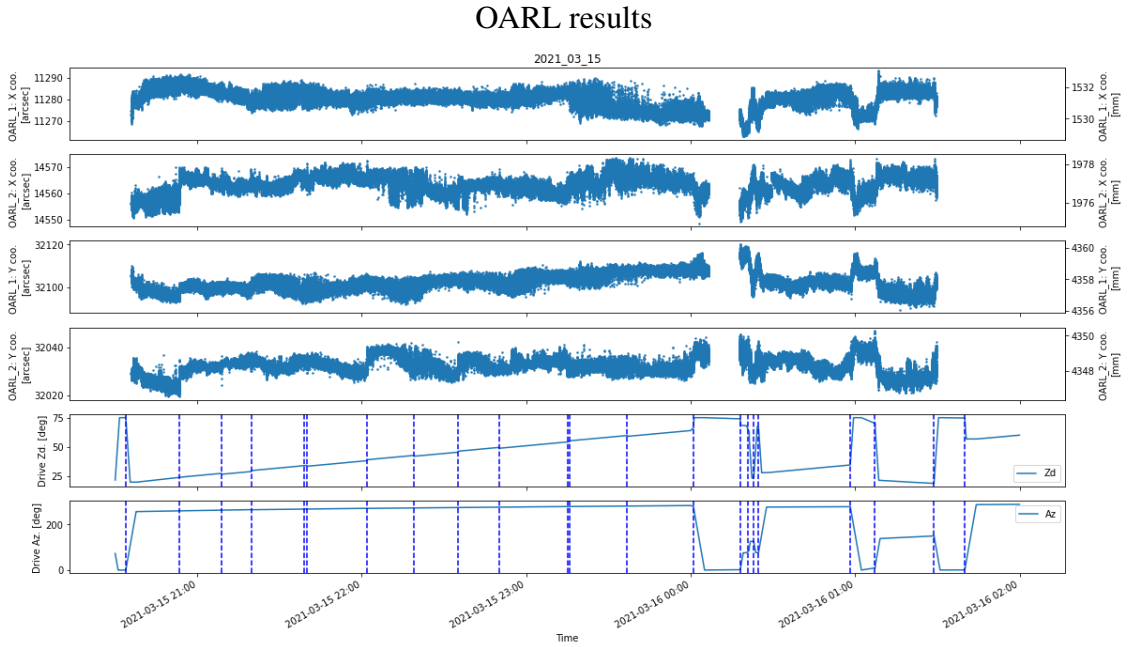

Figure 5.41: Top four subplots show different CDM OARL result. The two bottom subplots represent information coming from the drive system (zenith and azimuth angle). In particular the vertical dashed lines represent the times when Drive system received different commands such as track or stop tracking. Around midnight there was no CDM data because the CDM was turned off by the shifters for some other tests.

Displacement results are shown in Figure 5.42. Still the CDM-drive correlation is seen.

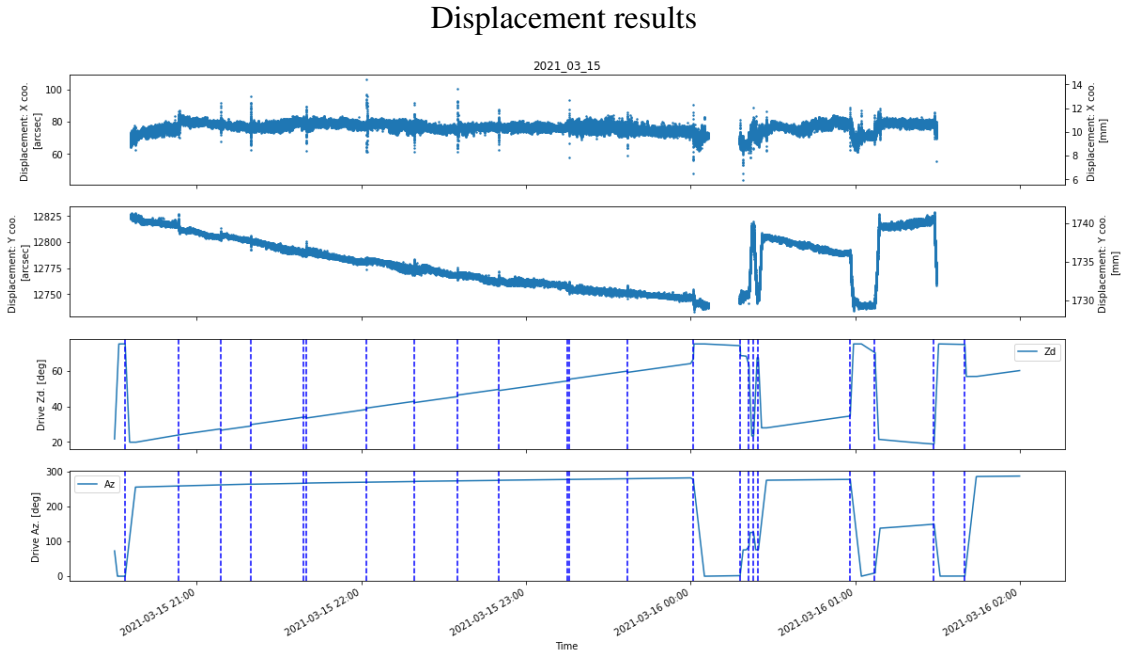

Figure 5.42: Top two subplots show CDM displacement result. The two bottom subplots represent information coming from the drive system (zenith and azimuth angle). In particular the vertical dashed lines represent the times when Drive system received different commands such as track or stop tracking. Around midnight there was no CDM data because the CDM was turned off by the shifters for some other tests.

In LST the load pins measure the tension of the ropes that are attached to the PMT camera. The comparison of CDM and load pin results is shown in Figure 5.43. The CDM and load pin results are in excellent agreement, especially the vertical component of the CDM. This is because the tension of the ropes mostly depends on the zenith angle of the telescope.

Load pin comparison

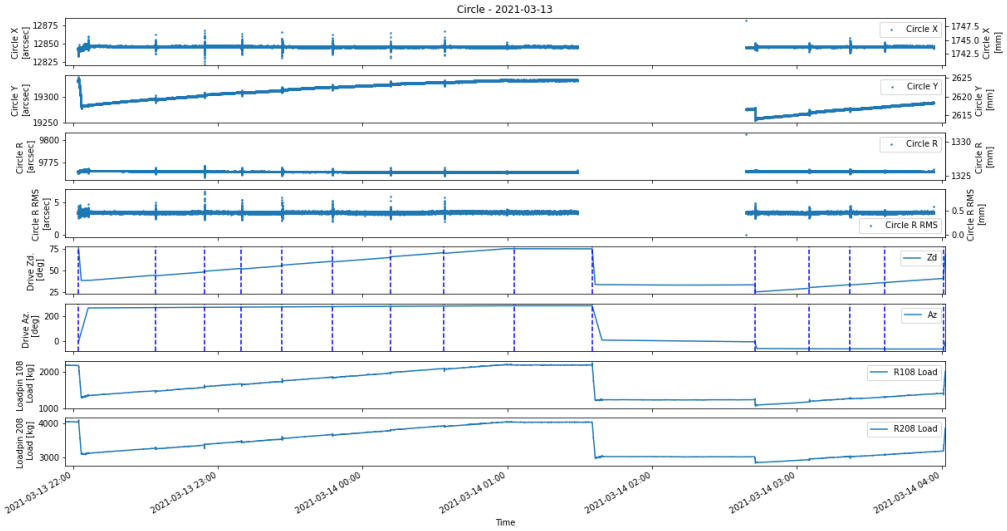

Figure 5.43: Top four subplots represent different CDM circle fit result. The two middle subplots represent information coming from the drive system (zenith and azimuth angle). In particular the vertical dashed lines represent the times when Drive system received different commands such as track or stop tracking. The bottom two subplots show the load pin results. Around midnight there was no CDM data because the CDM was turned off by the shifters for some other tests.

5.8.3. PMT Camera Oscillations

Measuring displacement of the PMT camera at a rate of 10 Hz allows to study the oscillations of the telescope. An example is shown in Figure 5.44, there the oscillations of the telescopes can be clearly seen for both horizontal and vertical component. In general the tails of oscillations last longer for vertical oscillations. There is about $\sim$2 s difference

between the measured CDM start of oscillation time and the reported time of issued drive commands which needs more investigation.

Oscillations. After Drive Start Tracking command

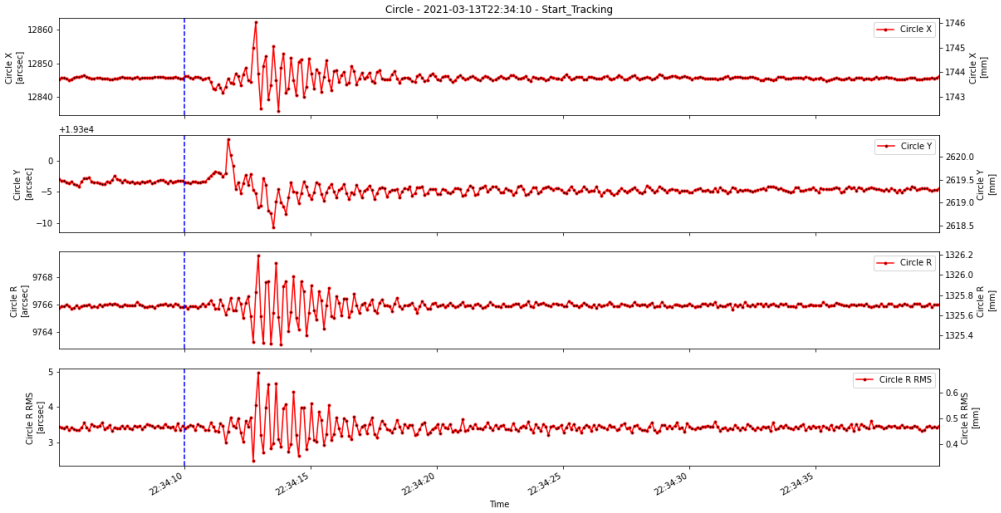

Figure 5.44: CDM results for the circle fit. Vertical dashed lines represent the time of issued drive command. The oscillations of the telescope can be seen.

The measured oscillation data are fit with a damped harmonic oscillator function:

$$x(t) = Asin(2\pi f(t-t_0))e^{\frac{-t}{\tau}} + B \tag{5.5}$$

where x is the vertical or horizontal CDM measured coordinate, A is the amplitude, f is the frequency of the oscillations, t time, t_0 the time offset, τ is the damping factor and B is the constant offset.

The fits are shown in Figure 5.45 and Figure 5.46. For the horizontal oscillation of the PMT camera the frequency is $\sim$3 Hz, while for the vertical oscillations the frequency is frequency is $\sim$2 Hz, which is consistent with the FEM simulations [154].

Oscillations. After Drive Start Tracking command

Circle horizontal coordinate. Fit as damped oscillations.

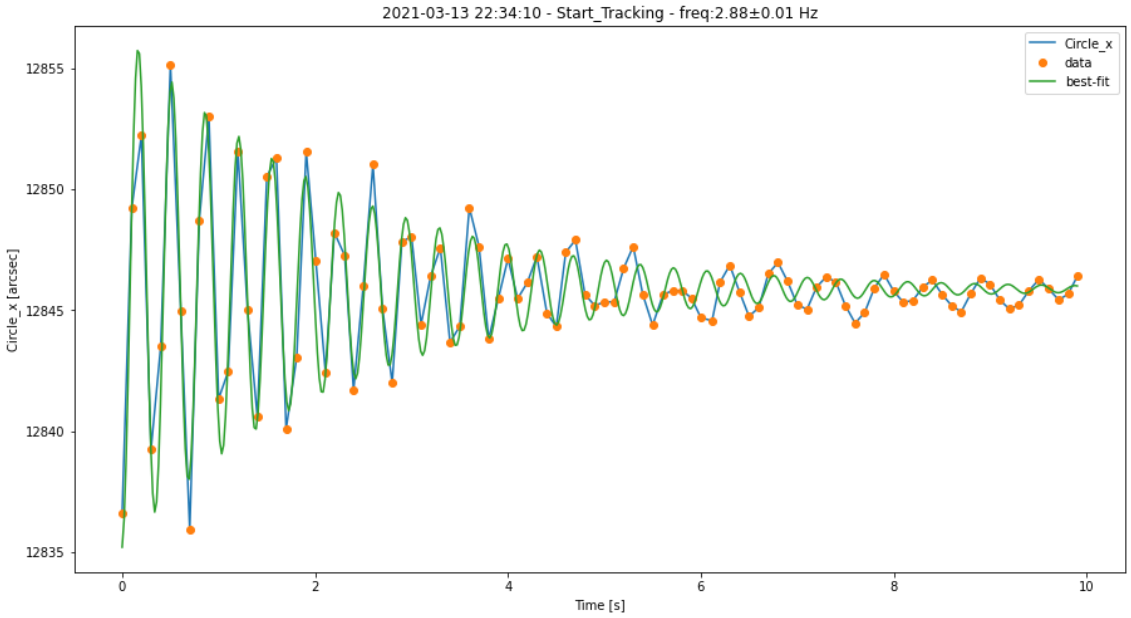

Figure 5.45: Fitted oscillation for the horizontal coordinate of the PMT camera circle fit.

Oscillations. After Drive Start Tracking command

Circle vertical coordinate. Fit as damped oscillations.

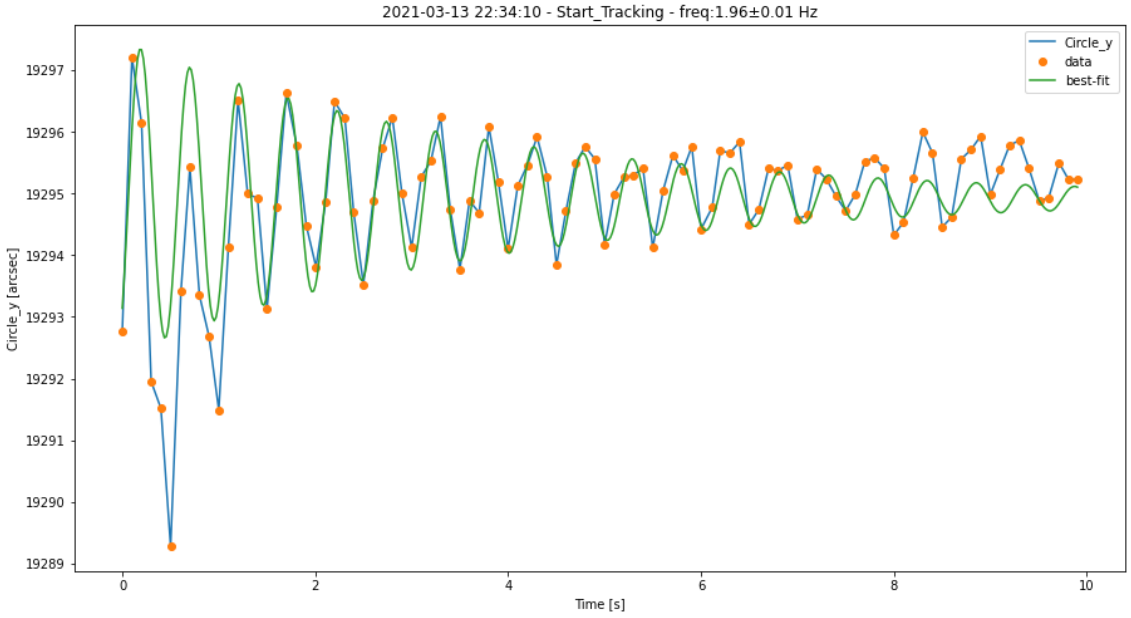

Figure 5.46: Fitted oscillation for the vertical coordinate of the PMT camera circle fit.

5.9. SUMMARY

In this chapter the components of the auxiliary pointing devices for LST-1 were described and the CDM software implementation was explained. First the results of the laboratory measurements with the CDM were given and then the results of the calibration at LST-1 were shown. The results show that the CDM satisfies the CTA requirements on the displacement resolution of $5''$ and timing of 10 Hz. However the OARL resolution is still a limiting factor for further improving the results. Results also show clear time correlation with the drive commands, which confirm the validity of results. The measured LST oscillation frequencies are 3 Hz for horizontal oscillations and 2 Hz for vertical oscillations, as expected from the FEA studies.

For the LST2-4 telescopes a new version of the CDM camera will be used, based on the experience during the LST-1 commissioning. In particular the current camera is not suitable for the bending model data taking because the exposure time of the current camera is limited to 1 s. List of specifications for the next version of CDM camera is given in Appendix A.

CONCLUSION

The search for cosmic particle accelerators capable of reaching the PeV range, PeVatrons, is a key science objective for VHE gamma-ray community. As the PeV particles are accelerated, gamma rays in the ∼100 TeV range should be produced. Thus, investigations into this energy domain are necessary in the search for PeVatrons. In order to perform these measurements a novel observation method for observing at very large zenith angles is introduced in the first part of the thesis. This observational strategy allows current IACTs to reach $\sim$ km^2 collection areas without using large size telescope arrays. The Crab Nebula was the first source observed with VLZA and it demonstrated that MAGIC telescopes can detect gamma rays up to $\sim$ 100 TeV in few tens of hours using the this technique. Performance of the VLZA method has been investigated and approximately twofold degradation of the energy and the angular resolution compared to observations at small zenith angles. Still, the VLZA Crab Nebula data collected at a few tens of TeV match well with earlier, lower zenith angle results reported from HEGRA in observations that were nearly eight times longer. Also, the results are in good agreement with the recent results from particle detector arrays. The data strongly favor the absence of a large hadronic contribution to the measured TeV flux. This means that the accelerated nuclei contribute a negligible amount to the pulsar wind power or do not interact with the dense Nebula filaments in general.

Extended sources Dragonfly and HESSJ 1809-193 were observed with VLZA in order to investigate the spectrum at the highest part of the TeV energies. Due to their extension spatial likelihood methods were used for the analysis of these sources. For Dragonfly the spectrum has been measured up to $\sim$ 50 TeV, which are the highest IACT measurements for this source. For HESS J1809-193 morphology and spectrum results are in line with the recent results from HAWC. This area of research is interesting, particularly with re-

cent particle detector array results at $\sim$ 100 TeV that show that the PeVatron search is a currently a very active field.

Overall, observations at very high zenith angles allow for a new regime of the very-high energy observations. It can also increase the number of southern sources, available for the observations with in the northern hemisphere via the reduction of the minimal source declination. Also it can be used as an efficient way to get measurements of the source spectra at highest energies during the eruptive events like Crab flares.

In the last part of the thesis the technical contribution to the LST-1 pointing precision monitoring was presented. For LST-1 in order to achieve the total post-calibration pointing precision of $< 14''$ the CDM system was designed, developed and implemented. The system was installed on site and then calibrated and validated. Technical data was taken and results show that the CDM fulfills the requirements of the CTA, namely the resolution of measuring the displacement of the PMT camera with $5''$ and timing requirement of 10 Hz. However the OARL resolution is still a limiting factor for further improving the results. From the datasets a good agreement with the drive system data is seen. The PMT camera sag has been determined and it in agreement with the FEA study predictions. The measured LST oscillation frequencies are 3 Hz for horizontal oscillations and 2 Hz for vertical oscillations, as expected from the FEA studies.

From the lessons learned at LST-1, a new CDM camera will be installed for the LST2-4 telescopes. In particular the current CDM camera is not suitable for bending model image taking, so the next camera will address those issues.

Appendices

A. SPECIFICATIONS FOR THE NEXT CDM CAMERA

A document was made with the required specifications needed for the Camera Displacement Monitor (CDM) and bending model camera for the LST2-4 telescopes. The specifications based on the LST requirements are here revised to include learned lesson during the operations of the existing camera on LST-1 prototype. Since CDM and bending model camera are to be considered as a single device with dual purpose, the specifications capture the requirements of both systems.

A.1. CURRENT CAMERA

The camera currently being used in the LST-1 prototype is UI-3590CP Rev. 2 by the IDS, where the IR filter has been removed and a 35 mm fixed focal length lens is installed. Some of the characteristics are displayed in Table 5.1

A.2. PROPOSED SPECIFICATIONS

To improve the performance of the CDM and bending model procedures, next camera should have characteristics listed below.

A.2.1. High resolution

The camera should have high pixel resolution of at least 18 Mpix so the CDM can be sensitive to small movements. With high number of pixels, the sensitivity of pixels will likely drop off due to small size of each pixel as the amount of light impinging each pixel decreases. This is not a problem for CDM as the LEDs are bright but could be an issue while taking images for the bending models as the reflected images of the stars are dim. A bigger sensor can compensate for this drop in sensitivity, so the minimum pixel size should be 1.25 μm. Possibly, the camera should have an integration time large enough to compensate for the reduced pixel sensitivity due to the size.

A.2.2. High framerate

It should be at least 10 frames per second to conform to CTA requirements.

A.2.3. Long exposure time

It should have long exposure time ($\gg$1 s) so the images of the reflected stars can be discriminated from the background.

A.2.4. Controllable shutter

A controllable shutter would be good for taking bending model images so that the dark frame image can be subtracted from the actual image. The shutter would allow to disentangle the sensor noise.

A.2.5. Camera Bit depth

The camera has to have a bit depth of at least 12 bits.

A.2.6. Field of View

Sensor dimensions combined with the camera lens should provide a FoV greater than 4.5°, in order to contain the whole LST camera frame inside the camera image. At the same time, the FoV should not be too big, as to not have too many pixels with no useful information.

A.2.7. Wavelength response

Color information is not important, a grayscale sensor is preferable. Without color filters, each pixel will have a wider spectral integration range and so a better sensitivity to the dim light of stars which is important for the bending models. It should be sensitive in the red color range because of LEDs and OARLs. Therefore the camera should not have any infrared (IR) filters inside or should be removed by the manufacturer.

A.2.8. Interface

The camera should be equipped with USB3 interface to transfer the images to the NUC PC with a reasonable rate. Ethernet is not recommended as it could be too slow. The camera should be powered from NUC via USB to simplify the system. The use of an external power supply has drawback. The supply has to work with the 12V available from the dish center. The power cable shall go through the hood gland, and therefore has to be cut and reconnected.

A.2.9. Size

Camera size and shape, together with accompanying lens, should fit inside the metal hood that contains the current CDM and Starguider cameras.

A.2.10. Lens

The current camera uses C type mount, but this is not mandatory. Depending on the lens size, the lens holder has to be considered to ensure that the assembly stays in position in any observing condition. The lens should have aperture of at least f/1.65.

A.2.11. Fixation

Camera body shall have well defined screw slots or similar way of attaching it to the central plate of the hood.

A.2.12. Cooling

For the bending models images, in order to reduce the noise an active cooling of the camera shall be considered. A cooling solution using fans is not preferred as the fans may stop working after years of use. Active cooling can be considered, but has to be compatible with power currently available.

A.2.13. Control and Configuration Software

The control software has to be supported under Linux and shall have C++ libraries to allow to develop the needed MOS plugin. Python support is welcome but not mandatory.

A.2.14. Documentation

The camera shall have a complete accompanying documentation (Users Manual, Maintenance Manual, CE certification).

A.2.15. Maintenance

The camera should not require preventive maintenance.

A.2.16. Price

The cost of camera and lens should be around 1000 EUR, as the current one (Camera 600 EUR plus lens which is 350 EUR).

A.2.17. Ambient conditions

The camera should work under these ambient conditions.

Temperature during storage	$-5\ ^{\circ}\mathrm{C} - 40\ ^{\circ}\mathrm{C}$
Temperature during operation	$0\ ^{\circ}\mathrm{C} - 35\ ^{\circ}\mathrm{C}$
Humidity (relative, non condensing)	$20\ \% - 80\ \%$

Table A.1: CDM camera ambient conditions requirement.

A.2.18. Output format

The camera shall be able to output the taken images in raw format. In that case no software postprocessing of the image shall be applied by the camera manufacturers software before the image is delivered to the developer from the camera side. In that case averaging, smearing, demosaicing or compression shall not be applied to the image.

ACRONYMS

a.s.l Above sea level

ACD Anti Coincedence Detector

ACS ALMA Common Software

ACTL Array Control and Data Acquisition System

AGN Active Galactic Nuclei

CCD Charged Coupled Device

CDM Camera Displacement Monitor

CMB Cosmic Microwave Background

CMOS Complementary metaloxidesemiconductor

CR Cosmic Rays

CTA Cherenkov Telescope Array

DAQ Data Acquisition

DM Dark Matter

DMs Distancemeters

EAS Extended Air Showers

EBL Extragalactic Background Light

ESO European Southern Observatory

FACT First G-APD Cherenkov Telescope

FEA Finite Element Analysis

FoV Field of View

FSM Finite State Machine

GBM Gamma Burst Monitor

GC Galactic Center

GRB Gamma Ray Burst

GUI Graphical User Interface

GW Gravitational Waves

GZK Greisen-Zatsepin-Kuzmin

HAWC High Altitude Water Cherenkov

HE High Energy

HESS High Energy Stereoscopic System

IACT Imaging Atmospheric Cherenkov Telescope

IC Inverse Compton

IR Infrared

IRF Instrument Response Function

KM2A Square Kilometer Array

LAT Large Area Telescope

LED Light-emitting diode

LHAASO Large High Altitude Air Shower Observatory

LHC Large Hadron Collider

LIDAR Light detection and ranging

LST Large Size Telescope

LUT Look Up Table

MAGIC Major Atmospheric Gamma Imaging Cherenkov Telescopes

MARS MAGIC Analysis and Reconstruction Software

MC Monte Carlo

MST Medium Size Telescope

MWL Multiwavelength

OARL Optical Axis Reference Lasers

OPCUA Open Platform Communications United Architecture

PMT Photomulitplier tube

PWN Pulsae Wind Nebula

RF Random Forest

RMS Root Mean Square

SED Spectral Energy Distribution

SG Starguider

SMBH Super Massive Black Hole

SNR Super Nova Remnant

SSC Synchrotron Self Compton

SST Small Size Telescope

TS Test Statistic

UHE Ultra High Energy

UHECR Ultra-High-Energyy Cosmic Ray

UV Ultraviolet

VHE Very High Energy

VLZA Very Large Zenith Angles

WCDA Water Cherenkov Detector Array

WFCTA Wide-Field Air Cherenkov Telescope Array

WIMP Weakly Interacting Massice Particle

ZA Zenith Angles

BIBLIOGRAPHY

[1] V. F. Hess, "Über Beobachtungen der durchdringenden Strahlung bei sieben Freiballonfahrten," en, *Phys.Z.*, vol. 13, pp. 1084–1091, 1912. [Online]. Available: https://inspirehep.net/literature/1623161 (cit. on p. 1).

[2] L. A. Anchordoqui, "Ultra-High-Energy Cosmic Rays," en, *Physics Reports*, vol. 801, pp. 1–93, Apr. 2019, arXiv: 1807.09645, ISSN: 03701573. DOI: 10.1016/j.physrep.2019.01.002. [Online]. Available: http://arxiv.org/abs/1807.09645 (cit. on pp. 1, 6, 8).

[3] M. Dova, "Ultra-High-Energy Cosmic Rays," en, 2015, Publisher: CERN. DOI: 10.5170/CERN-2015-001.169. [Online]. Available: https://cds.cern.ch/record/2019742 (cit. on p. 1).

[4] P. Auger, R. Maze, and T. Grivet-Mayer, "Grandes gerbes cosmiques atmospheriques contenant des corpuscules ultrapenetrants," en, *Compt.Rend.Hebd.Seances Acad.Sci.*, vol. 206, no. 23, pp. 1721–1723, 1938. [Online]. Available: https://inspirehep.net/literature/42721 (cit. on p. 2).

[5] P. Auger *et al.*, "Extensive Cosmic-Ray Showers," *Reviews of Modern Physics*, vol. 11, no. 3-4, pp. 288–291, Jul. 1939, Publisher: American Physical Society. DOI: 10.1103/RevModPhys.11.288. [Online]. Available: https://link.aps.org/doi/10.1103/RevModPhys.11.288 (cit. on p. 2).

[6] L. Anchordoqui *et al.*, "Ultrahigh energy cosmic rays: The state of the art before the auger observatory," *International Journal of Modern Physics A*, vol. 18, no. 13, pp. 2229–2366, May 2003, Publisher: World Scientific Publishing Co., ISSN: 0217-751X. DOI: 10.1142/S0217751X03013879. [Online]. Available:

https://www.worldscientific.com/doi/abs/10.1142/S0217751X03013879 (cit. on p. 2).

[7] Particle Data Group *et al.*, "Review of Particle Physics," en, *Progress of Theoretical and Experimental Physics*, vol. 2020, no. 8, p. 083C01, Aug. 2020, ISSN: 2050-3911. DOI: 10.1093/ptep/ptaa104. [Online]. Available: https://academic.oup.com/ptep/article/doi/10.1093/ptep/ptaa104/5891211 (cit. on p. 3).

[8] M. Aglietta *et al.*, "The cosmic ray primary composition in the knee region through the EAS electromagnetic and muon measurements at EAS-TOP," en, *Astroparticle Physics*, vol. 21, no. 6, pp. 583–596, Sep. 2004, ISSN: 0927-6505. DOI: 10.1016/j.astropartphys.2004.04.005. [Online]. Available: https://www.sciencedirect.com/science/article/pii/S092765050400074X (cit. on p. 4).

[9] T. Antoni *et al.*, "KASCADE measurements of energy spectra for elemental groups of cosmic rays: Results and open problems," en, *Astroparticle Physics*, vol. 24, no. 1, pp. 1–25, Sep. 2005, ISSN: 0927-6505. DOI: 10.1016/j.astropartphys.2005.04.001. [Online]. Available: https://www.sciencedirect.com/science/article/pii/S0927650505000691 (cit. on p. 4).

[10] W. D. Apel *et al.*, "Energy spectra of elemental groups of cosmic rays: Update on the KASCADE unfolding analysis," en, *Astroparticle Physics*, vol. 31, no. 2, pp. 86–91, Mar. 2009, ISSN: 0927-6505. DOI: 10.1016/j.astropartphys.2008.11.008. [Online]. Available: https://www.sciencedirect.com/science/article/pii/S0927650508001783 (cit. on p. 4).

[11] J. Bluemer, R. Engel, and J. R. Hoerandel, "Cosmic Rays from the Knee to the Highest Energies," *Progress in Particle and Nuclear Physics*, vol. 63, no. 2, pp. 293–338, Oct. 2009, arXiv: 0904.0725, ISSN: 01466410. DOI: 10.1016/j.ppnp.2009.05.002. [Online]. Available: http://arxiv.org/abs/0904.0725 (cit. on p. 4).

[12] M. E. Bertaina, "Cosmic rays from the knee to the ankle," en, *Comptes Rendus Physique*, Ultra-high-energy cosmic rays: From the ankle to the tip of the spec-

trum, vol. 15, no. 4, pp. 300–308, Apr. 2014, ISSN: 1631-0705. DOI: 10.1016/j.crhy.2014.03.001. [Online]. Available: https://www.sciencedirect.com/science/article/pii/S1631070514000449 (cit. on p. 4).

[13] A. M. Hillas, "The energy spectrum of cosmic rays in an evolving universe," en, *Physics Letters A*, vol. 24, no. 12, pp. 677–678, Jun. 1967, ISSN: 0375-9601. DOI: 10.1016/0375-9601(67)91023-7. [Online]. Available: https://www.sciencedirect.com/science/article/pii/0375960167910237 (cit. on p. 4).

[14] V. Berezinsky, A. Gazizov, and S. Grigorieva, "On astrophysical solution to ultrahigh energy cosmic rays," *Physical Review D*, vol. 74, no. 4, p. 043 005, Aug. 2006, Publisher: American Physical Society. DOI: 10.1103/PhysRevD.74.043005. [Online]. Available: https://link.aps.org/doi/10.1103/PhysRevD.74.043005 (cit. on p. 4).

[15] R. Aloisio *et al.*, "A dip in the UHECR spectrum and the transition from galactic to extragalactic cosmic rays," en, *Astroparticle Physics*, vol. 27, no. 1, pp. 76–91, Feb. 2007, ISSN: 0927-6505. DOI: 10.1016/j.astropartphys.2006.09.004. [Online]. Available: https://www.sciencedirect.com/science/article/pii/S0927650506001368 (cit. on p. 4).

[16] G. Cocconi, "About the most energetic cosmic rays," en, *Astroparticle Physics*, vol. 4, no. 3, pp. 281–283, Feb. 1996, ISSN: 0927-6505. DOI: 10.1016/0927-6505(95)00040-2. [Online]. Available: https://www.sciencedirect.com/science/article/pii/0927650595000402 (cit. on p. 5).

[17] High Resolution Flys Eye Collaboration *et al.*, "First Observation of the Greisen-Zatsepin-Kuzmin Suppression," *Physical Review Letters*, vol. 100, no. 10, p. 101 101, Mar. 2008, Publisher: American Physical Society. DOI: 10.1103/PhysRevLett.100.101101. [Online]. Available: https://link.aps.org/doi/10.1103/PhysRevLett.100.101101 (cit. on p. 5).

[18] The Pierre Auger Collaboration *et al.*, "Observation of the Suppression of the Flux of Cosmic Rays above 40 EeV," *Physical Review Letters*, vol. 101, no. 6, p. 061 101, Aug. 2008, Publisher: American Physical Society. DOI: 10.1103/

PhysRevLett.101.061101. [Online]. Available: https://link.aps.org/doi/10.1103/PhysRevLett.101.061101 (cit. on p. 5).

[19] K. Greisen, "End to the Cosmic-Ray Spectrum?" *Physical Review Letters*, vol. 16, no. 17, pp. 748–750, Apr. 1966, Publisher: American Physical Society. DOI: 10.1103/PhysRevLett.16.748. [Online]. Available: https://link.aps.org/doi/10.1103/PhysRevLett.16.748 (cit. on p. 5).

[20] G. T. Zatsepin and V. A. Kuz'min, "Upper Limit of the Spectrum of Cosmic Rays," *Soviet Journal of Experimental and Theoretical Physics Letters*, vol. 4, p. 78, Aug. 1966, ISSN: 0021-3640. [Online]. Available: https://ui.adsabs.harvard.edu/abs/1966JETPL...4...78Z (cit. on p. 5).

[21] A. M. Hillas, "The Origin of Ultra-High-Energy Cosmic Rays," *Annual Review of Astronomy and Astrophysics*, vol. 22, no. 1, pp. 425–444, 1984. DOI: 10.1146/annurev.aa.22.090184.002233. [Online]. Available: https://doi.org/10.1146/annurev.aa.22.090184.002233 (cit. on pp. 5, 7).

[22] P. Blasi, R. I. Epstein, and A. V. Olinto, "UltraHigh-Energy Cosmic Rays from Young Neutron Star Winds," en, *The Astrophysical Journal*, vol. 533, no. 2, pp. L123–L126, Apr. 2000, Publisher: American Astronomical Society, ISSN: 0004-637X. DOI: 10.1086/312626. [Online]. Available: https://doi.org/10.1086/312626 (cit. on p. 5).

[23] E. Fermi, "On the Origin of the Cosmic Radiation," *Physical Review*, vol. 75, no. 8, pp. 1169–1174, Apr. 1949, Publisher: American Physical Society. DOI: 10.1103/PhysRev.75.1169. [Online]. Available: https://link.aps.org/doi/10.1103/PhysRev.75.1169 (cit. on p. 5).

[24] R. D. Blandford and J. P. Ostriker, "Particle acceleration by astrophysical shocks," en, *The Astrophysical Journal*, vol. 221, p. L29, Apr. 1978, ISSN: 0004-637X, 1538-4357. DOI: 10.1086/182658. [Online]. Available: http://adsabs.harvard.edu/doi/10.1086/182658 (cit. on p. 5).

[25] T. K. Gaisser, R. Engel, and E. Resconi, *Cosmic Rays and Particle Physics*, 2nd ed. Cambridge: Cambridge University Press, 2016, ISBN: 978-0-521-01646-9. DOI: 10.1017/CBO9781139192194. [Online]. Available: https://www.

cambridge.org/core/books/cosmic-rays-and-particle-physics/C81BA71195ADFC89EFCC2C565B617702 (cit. on p. 6).

[26] A. De Angelis and M. Mallamaci, "Gamma-Ray Astrophysics," *The European Physical Journal Plus*, vol. 133, no. 8, p. 324, Aug. 2018, arXiv: 1805.05642, ISSN: 2190-5444. DOI: 10.1140/epjp/i2018-12181-0. [Online]. Available: http://arxiv.org/abs/1805.05642 (cit. on pp. 9, 12, 18).

[27] W. Baade and F. Zwicky, "Cosmic Rays from Super-Novae," en, *Proceedings of the National Academy of Sciences*, vol. 20, no. 5, pp. 259–263, May 1934, Publisher: National Academy of Sciences Section: Astronomy, ISSN: 0027-8424, 1091-6490. DOI: 10.1073/pnas.20.5.259. [Online]. Available: https://www.pnas.org/content/20/5/259 (cit. on p. 10).

[28] A. Abramowski *et al.*, "Acceleration of petaelectronvolt protons in the Galactic Centre," en, *Nature*, vol. 531, no. 7595, pp. 476–479, Mar. 2016, ISSN: 1476-4687. DOI: 10.1038/nature17147. [Online]. Available: https://www.nature.com/articles/nature17147 (cit. on pp. 10, 51).

[29] A. De Angelis, M. Roncadelli, and O. Mansutti, "Evidence for a new light spin-zero boson from cosmological gamma-ray propagation?" *Physical Review D*, vol. 76, no. 12, p. 121 301, Dec. 2007, Publisher: American Physical Society. DOI: 10.1103/PhysRevD.76.121301. [Online]. Available: https://link.aps.org/doi/10.1103/PhysRevD.76.121301 (cit. on p. 11).

[30] A. De Angelis and M. Pimenta, *Introduction to Particle and Astroparticle Physics*, en, ser. Undergraduate Lecture Notes in Physics. Cham: Springer International Publishing, 2018, ISBN: 978-3-319-78180-8 978-3-319-78181-5. DOI: 10.1007/978-3-319-78181-5. [Online]. Available: http://link.springer.com/10.1007/978-3-319-78181-5 (cit. on pp. 11, 14, 15).

[31] E. Fermi, "Galactic Magnetic Fields and the Origin of Cosmic Radiation.," *The Astrophysical Journal*, vol. 119, p. 1, Jan. 1954, ISSN: 0004-637X. DOI: 10.1086/145789. [Online]. Available: https://ui.adsabs.harvard.edu/abs/1954ApJ...119....1F (cit. on p. 12).

[32] A. M. Hillas, "Cosmic Rays: Recent Progress and some Current Questions," *arXiv:astro-ph/0607109*, Sep. 2006, arXiv: astro-ph/0607109. [Online]. Available: http://arxiv.org/abs/astro-ph/0607109 (cit. on p. 12).

[33] F. A. Aharonian, A. M. Atoyan, and T. Kifune, "Inverse Compton gamma radiation of faint synchrotron X-ray nebulae around pulsars," *Monthly Notices of the Royal Astronomical Society*, vol. 291, no. 1, pp. 162–176, Oct. 1997, ISSN: 0035-8711. DOI: 10.1093/mnras/291.1.162. [Online]. Available: https://doi.org/10.1093/mnras/291.1.162 (cit. on p. 13).

[34] T. IceCube *et al.*, "Multi-messenger observations of a flaring blazar coincident with high-energy neutrino IceCube-170922A," *Science*, vol. 361, no. 6398, eaat1378, Jul. 2018, arXiv: 1807.08816, ISSN: 0036-8075, 1095-9203. DOI: 10.1126/science.aat1378. [Online]. Available: http://arxiv.org/abs/1807.08816 (cit. on p. 15).

[35] G. Breit and J. A. Wheeler, "Collision of Two Light Quanta," *Physical Review*, vol. 46, no. 12, pp. 1087–1091, Dec. 1934, Publisher: American Physical Society. DOI: 10.1103/PhysRev.46.1087. [Online]. Available: https://link.aps.org/doi/10.1103/PhysRev.46.1087 (cit. on p. 17).

[36] R. J. Protheroe and P. L. Biermann, "A new estimate of the extragalactic radio background and implications for ultra-high-energy -ray propagation," en, *Astroparticle Physics*, vol. 6, no. 1, pp. 45–54, Dec. 1996, ISSN: 0927-6505. DOI: 10.1016/S0927-6505(96)00041-2. [Online]. Available: https://www.sciencedirect.com/science/article/pii/S0927650596000412 (cit. on p. 17).

[37] *CTA Technology*, en-US. [Online]. Available: https://www.cta-observatory.org/project/technology/ (cit. on pp. 19, 64, 109).

[38] *The Fermi Gamma-ray Space Telescope*. [Online]. Available: https://fermi.gsfc.nasa.gov/ (cit. on p. 20).

[39] W. Galbraith and J. V. Jelley, "Light Pulses from the Night Sky associated with Cosmic Rays," en, *Nature*, vol. 171, no. 4347, pp. 349–350, Feb. 1953, ISSN:

1476-4687. DOI: 10.1038/171349a0. [Online]. Available: https://www.nature.com/articles/171349a0 (cit. on pp. 21, 23).

[40] A. M. Hillas, "Cerenkov Light Images of EAS Produced by Primary Gamma Rays and by Nuclei," vol. 3, p. 445, Aug. 1985, Conference Name: 19th International Cosmic Ray Conference (ICRC19), Volume 3. [Online]. Available: https://ui.adsabs.harvard.edu/abs/1985ICRC....3..445H (cit. on pp. 21, 38, 40).

[41] T. C. Weekes *et al.*, "Observation of TeV Gamma-rays from the Crab Nebula using the Atmospheric Cherenkov Imaging Technique," en, *Astrophysical Journal*, vol. 342, pp. 379–395, Jul. 1989, Publisher: American Astronomical Society, ISSN: 0004-637X. [Online]. Available: http://mural.maynoothuniversity.ie/12618/ (cit. on pp. 21, 23, 25).

[42] *The HEGRA Atmospheric Cherenkov Telescope System*. [Online]. Available: https://www.mpi-hd.mpg.de/hfm/CT/CT.html (cit. on p. 21).

[43] *CANGAROO Experiment*. [Online]. Available: http://icrhp9.icrr.u-tokyo.ac.jp/ (cit. on p. 21).

[44] *H.E.S.S. - The High Energy Stereoscopic System*. [Online]. Available: https://www.mpi-hd.mpg.de/hfm/HESS/ (cit. on p. 21).

[45] *MAGIC*. [Online]. Available: https://magic.mpp.mpg.de/ (cit. on p. 21).

[46] *First G-APD Cherenkov Telescope*. [Online]. Available: https://www.isdc.unige.ch/fact/ (cit. on p. 21).

[47] *VERITAS*. [Online]. Available: https://veritas.sao.arizona.edu/ (cit. on p. 21).

[48] *LST1 - the Large Size Telescope prototype website in La Palma*. [Online]. Available: https://lst1.iac.es/ (cit. on p. 21).

[49] *Cherenkov Telescope Array (CTA)*, en-US. [Online]. Available: https://www.cta-observatory.org/ (cit. on p. 21).

[50] *HAWC: The High-Altitude Water Cherenkov Observatory*. [Online]. Available: https://www.hawc-observatory.org/ (cit. on p. 22).

[51] S. P. Wakely and D. Horan, "TeVCat: An online catalog for Very High Energy Gamma-Ray Astronomy," vol. 3, pp. 1341–1344, Jan. 2008, Conference Name: International Cosmic Ray Conference ADS Bibcode: 2008ICRC....3.1341W. [Online]. Available: https://ui.adsabs.harvard.edu/abs/2008ICRC....3.1341W (cit. on p. 23).

[52] *Welcome to TeVCat, an Online Gamma-Ray Catalog!* [Online]. Available: http://tevcat.uchicago.edu/ (cit. on pp. 23, 24).

[53] M. de Naurois and D. Mazin, "Ground-based detectors in very-high-energy gamma-ray astronomy," en, *Comptes Rendus Physique*, vol. 16, no. 6-7, pp. 610–627, Aug. 2015, ISSN: 16310705. DOI: 10.1016/j.crhy.2015.08.011. [Online]. Available: https://linkinghub.elsevier.com/retrieve/pii/S1631070515001462 (cit. on p. 23).

[54] J. Holder, "Atmospheric Cherenkov Gamma-ray Telescopes," *arXiv:1510.05675 [astro-ph]*, Oct. 2015, arXiv: 1510.05675. [Online]. Available: http://arxiv.org/abs/1510.05675 (cit. on p. 23).

[55] J. V. Jelley and W. Galbraith, "Light pulses from the night sky and erenkov radiation part II," en, *Journal of Atmospheric and Terrestrial Physics*, vol. 6, no. 1, pp. 304–312, Jan. 1955, ISSN: 0021-9169. DOI: 10.1016/0021-9169(55)90047-7. [Online]. Available: https://www.sciencedirect.com/science/article/pii/0021916955900477 (cit. on p. 25).

[56] W. Heitler, *Quantum theory of radiation*. Jan. 1954, Publication Title: International Series of Monographs on Physics. [Online]. Available: https://ui.adsabs.harvard.edu/abs/1954qtr..book.....H (cit. on p. 26).

[57] J. Matthews, "A Heitler model of extensive air showers," en, *Astroparticle Physics*, vol. 22, no. 5, pp. 387–397, Jan. 2005, ISSN: 0927-6505. DOI: 10.1016/j.astropartphys.2004.09.003. [Online]. Available: https://www.sciencedirect.com/science/article/pii/S0927650504001598 (cit. on p. 27).

[58] F. Schmidt and J. Knapp, *CORSIKA Shower Images*, 2005. [Online]. Available: https://www-zeuthen.desy.de/~jknapp/fs/showerimages.html (cit. on p. 30).

[59] *ASTRI-Horn is first Cherenkov telescope in dual-mirror configuration to detect the Crab Nebula at TeV energies*, en-US, Section: Press Releases, May 2019. [Online]. Available: https://www.cta-observatory.org/astri-detects-crab-at-tev-energies/ (cit. on p. 32).

[60] J. Aleksic *et al.*, "The major upgrade of the MAGIC telescopes, Part I: The hardware improvements and the commissioning of the system," en, *Astroparticle Physics*, vol. 72, pp. 61–75, Jan. 2016, ISSN: 09276505. DOI: 10.1016/j.astropartphys.2015.04.004. [Online]. Available: https://linkinghub.elsevier.com/retrieve/pii/S0927650515000663 (cit. on pp. 36, 65, 78).

[61] C. Fruck *et al.*, "A novel LIDAR-based Atmospheric Calibration Method for Improving the Data Analysis of MAGIC," *arXiv:1403.3591 [astro-ph]*, Mar. 2014, arXiv: 1403.3591. [Online]. Available: http://arxiv.org/abs/1403.3591 (cit. on pp. 36, 55, 97).

[62] W. Hofmann *et al.*, "On the optimum spacing of stereoscopic imaging atmospheric Cherenkov telescopes," en, *Astroparticle Physics*, vol. 13, no. 4, pp. 253–258, Jul. 2000, ISSN: 0927-6505. DOI: 10.1016/S0927-6505(99)00126-7. [Online]. Available: https://www.sciencedirect.com/science/article/pii/S0927650599001267 (cit. on p. 37).

[63] P. Colin and S. LeBohec, "Optimization of large homogeneous air Cherenkov arrays and application to the design of a 1100 TeV gamma-ray observatory," en, *Astroparticle Physics*, vol. 32, no. 5, pp. 221–230, Dec. 2009, ISSN: 0927-6505. DOI: 10.1016/j.astropartphys.2009.09.002. [Online]. Available: https://www.sciencedirect.com/science/article/pii/S0927650509001376 (cit. on p. 37).

[64] K. Bernlöhr *et al.*, "Monte Carlo design studies for the Cherenkov Telescope Array," en, *Astroparticle Physics*, Seeing the High-Energy Universe with the Cherenkov Telescope Array - The Science Explored with the CTA, vol. 43, pp. 171–188, Mar. 2013, ISSN: 0927-6505. DOI: 10.1016/j.astropartphys.2012.10.002. [Online]. Available: https://www.sciencedirect.com/science/article/pii/S0927650512001867 (cit. on p. 37).

[65] S. J. Fegan and V. V. Vassiliev, "The performance of an idealized large-area array of moderate-sized IACTs," *arXiv:0708.2716 [astro-ph]*, Aug. 2007, arXiv: 0708.2716. [Online]. Available: http://arxiv.org/abs/0708.2716 (cit. on p. 37).

[66] D. Carreto Fidalgo, "Cherenkov Telescopes and MAGIC," en, in *Revealing the Most Energetic Light from Pulsars and Their Nebulae*, ser. Springer Theses, D. Carreto Fidalgo, Ed., Cham: Springer International Publishing, 2019, pp. 49–81, ISBN: 978-3-030-24194-0. DOI: 10.1007/978-3-030-24194-0_3. [Online]. Available: https://doi.org/10.1007/978-3-030-24194-0_3 (cit. on p. 39).

[67] R. D. Wills and B. Battrick, "Recent advances in gamma-ray astronomy," *Recent Advances in Gamma-Ray Astronomy*, vol. 124, Jan. 1977, ISSN: 1609-042X. [Online]. Available: https://ui.adsabs.harvard.edu/abs/1977ESASP.124...W (cit. on p. 40).

[68] A. Daum *et al.*, "First results on the performance of the HEGRA IACT array," en, *Astroparticle Physics*, vol. 8, no. 1, pp. 1–11, Dec. 1997, ISSN: 0927-6505. DOI: 10.1016/S0927-6505(97)00031-5. [Online]. Available: https://www.sciencedirect.com/science/article/pii/S0927650597000315 (cit. on p. 40).

[69] M. Peresano, "MAGIC telescopes observations at Very Large Zenith angles and the first neutrino-gamma association," Ph.D. dissertation, University of Udine, 2018 (cit. on p. 41).

[70] J. Albert *et al.*, "Implementation of the Random Forest method for the Imaging Atmospheric Cherenkov Telescope MAGIC," en, *Nuclear Instruments and Methods in Physics Research Section A: Accelerators, Spectrometers, Detectors and Associated Equipment*, vol. 588, no. 3, pp. 424–432, Apr. 2008, ISSN: 0168-9002. DOI: 10.1016/j.nima.2007.11.068. [Online]. Available: https://www.sciencedirect.com/science/article/pii/S0168900207024059 (cit. on pp. 41, 58).

[71] W. Hofmann *et al.*, "Comparison of techniques to reconstruct VHE gamma-ray showers from multiple stereoscopic Cherenkov images," en, *Astroparticle Physics*,

vol. 12, no. 3, pp. 135–143, Nov. 1999, ISSN: 0927-6505. DOI: 10.1016/S0927-6505(99)00084-5. [Online]. Available: https://www.sciencedirect.com/science/article/pii/S0927650599000845 (cit. on p. 42).

[72] T.-P. Li and Y.-Q. Ma, "Analysis methods for results in gamma-ray astronomy," en, *The Astrophysical Journal*, vol. 272, p. 317, Sep. 1983, ISSN: 0004-637X, 1538-4357. DOI: 10.1086/161295. [Online]. Available: http://adsabs.harvard.edu/doi/10.1086/161295 (cit. on p. 43).

[73] G. Mohanty *et al.*, "Measurement of TeV gamma-ray spectra with the Cherenkov imaging technique," en, *Astroparticle Physics*, vol. 9, no. 1, pp. 15–43, Jun. 1998, ISSN: 0927-6505. DOI: 10.1016/S0927-6505(98)00005-X. [Online]. Available: https://www.sciencedirect.com/science/article/pii/S092765059800005X (cit. on p. 44).

[74] F. Aharonian *et al.*, "The Crab Nebula and Pulsar between 500 GeV and 80 TeV: Observations with the HEGRA Stereoscopic Air Cerenkov Telescopes," en, *The Astrophysical Journal*, vol. 614, no. 2, pp. 897–913, Oct. 2004, Publisher: American Astronomical Society, ISSN: 0004-637X. DOI: 10.1086/423931. [Online]. Available: https://doi.org/10.1086/423931 (cit. on pp. 44, 52, 74, 76, 78).

[75] J. Albert *et al.*, "Unfolding of differential energy spectra in the MAGIC experiment," en, *Nuclear Instruments and Methods in Physics Research Section A: Accelerators, Spectrometers, Detectors and Associated Equipment*, vol. 583, no. 2, pp. 494–506, Dec. 2007, ISSN: 0168-9002. DOI: 10.1016/j.nima.2007.09.048. [Online]. Available: https://www.sciencedirect.com/science/article/pii/S0168900207020840 (cit. on p. 46).

[76] T. C. T. A. Consortium *et al.*, "Science with the Cherenkov Telescope Array," *arXiv:1709.07997 [astro-ph, physics:hep-ex]*, Mar. 2019, arXiv: 1709.07997. DOI: 10.1142/10986. [Online]. Available: http://arxiv.org/abs/1709.07997 (cit. on p. 48).

[77] R. Atkins *et al.*, "Observation of TeV Gamma Rays from the Crab Nebula with Milagro Using a New Background Rejection Technique," en, *The Astrophysical Journal*, vol. 595, no. 2, pp. 803–811, Oct. 2003, ISSN: 0004-637X, 1538-4357.

DOI: 10.1086/377498. [Online]. Available: https://iopscience.iop.org/article/10.1086/377498 (cit. on p. 50).

[78] J. A. Goodman, "Recent Results from the Milagro Gamma Ray Observatory," en, *Nuclear Physics B - Proceedings Supplements*, VERY HIGH ENERGY COSMIC RAY INTERACTIONS, vol. 151, no. 1, pp. 101–107, Jan. 2006, ISSN: 0920-5632. DOI: 10.1016/j.nuclphysbps.2005.07.018. [Online]. Available: https://www.sciencedirect.com/science/article/pii/S0920563205009096 (cit. on p. 50).

[79] F. Aharonian *et al.*, "Cosmic Rays in Galactic and Extragalactic Magnetic Fields," en, *Space Science Reviews*, vol. 166, no. 1-4, pp. 97–132, May 2012, ISSN: 0038-6308, 1572-9672. DOI: 10.1007/s11214-011-9770-3. [Online]. Available: http://link.springer.com/10.1007/s11214-011-9770-3 (cit. on p. 50).

[80] "THE ORIGIN OF COSMIC RAYS," en, in *The Origin of Cosmic Rays*, V. L. Ginzburg and S. I. Syrovatskii, Eds., Pergamon, Jan. 1964, VIIIa, ISBN: 978-0-08-013526-7. DOI: 10.1016/B978-0-08-013526-7.50003-7. [Online]. Available: https://www.sciencedirect.com/science/article/pii/B9780080135267500037 (cit. on p. 50).

[81] A. M. Hillas, "Can diffusive shock acceleration in supernova remnants account for high-energy galactic cosmic rays?" en, *Journal of Physics G: Nuclear and Particle Physics*, vol. 31, no. 5, R95–R131, Apr. 2005, Publisher: IOP Publishing, ISSN: 0954-3899. DOI: 10.1088/0954-3899/31/5/R02. [Online]. Available: https://doi.org/10.1088/0954-3899/31/5/r02 (cit. on p. 50).

[82] A. Neronov and D. V. Semikoz, "Origin of TeV Galactic cosmic rays," *Physical Review D*, vol. 85, no. 8, p. 083 008, Apr. 2012, Publisher: American Physical Society. DOI: 10.1103/PhysRevD.85.083008. [Online]. Available: https://link.aps.org/doi/10.1103/PhysRevD.85.083008 (cit. on p. 50).

[83] A. M. Bykov and G. D. Fleishman, "On non-thermal particle generation in superbubbles," *Monthly Notices of the Royal Astronomical Society*, vol. 255, no. 2, pp. 269–275, Mar. 1992, ISSN: 0035-8711. DOI: 10.1093/mnras/255.2.269.

[Online]. Available: https://doi.org/10.1093/mnras/255.2.269 (cit. on p. 51).

[84] E. O. Angüner *et al.*, "Very high energy emission from the hard spectrum sources HESS J1641-463, HESS J1741-302 and HESS J1826-130," *arXiv:1708.04844 [astro-ph]*, Aug. 2017, arXiv: 1708.04844. [Online]. Available: http://arxiv.org/abs/1708.04844 (cit. on p. 51).

[85] A. M. W. Mitchell *et al.*, "Observations of the Pulsar Wind Nebula HESS J1825-137 with H.E.S.S. II," *arXiv:1708.03126 [astro-ph]*, Aug. 2017, arXiv: 1708.03126. [Online]. Available: http://arxiv.org/abs/1708.03126 (cit. on p. 51).

[86] HAWC Collaboration *et al.*, "Multiple Galactic Sources with Emission Above 56 TeV Detected by HAWC," *Physical Review Letters*, vol. 124, no. 2, p. 021 102, Jan. 2020, Publisher: American Physical Society. DOI: 10.1103/PhysRevLett.124.021102. [Online]. Available: https://link.aps.org/doi/10.1103/PhysRevLett.124.021102 (cit. on pp. 51, 80, 94, 95, 104, 107).

[87] A. M. W. Mitchell, "Status of Ground-based and Galactic Gamma-ray Astronomy," en, p. 24, (cit. on p. 51).

[88] H. Abdalla *et al.*, "The H.E.S.S. Galactic plane survey," en, *Astronomy & Astrophysics*, vol. 612, A1, Apr. 2018, Publisher: EDP Sciences, ISSN: 0004-6361, 1432-0746. DOI: 10.1051/0004-6361/201732098. [Online]. Available: https://www.aanda.org/articles/aa/abs/2018/04/aa32098-17/aa32098-17.html (cit. on pp. 51, 96, 98, 99).

[89] A. Albert *et al.*, "3HWC: The Third HAWC Catalog of Very-high-energy Gamma-Ray Sources," en, *The Astrophysical Journal*, vol. 905, no. 1, p. 76, Dec. 2020, Publisher: American Astronomical Society, ISSN: 0004-637X. DOI: 10.3847/1538-4357/abc2d8. [Online]. Available: https://doi.org/10.3847/1538-4357/abc2d8 (cit. on p. 51).

[90] B. M. Gaensler and P. O. Slane, "The Evolution and Structure of Pulsar Wind Nebulae," *Annual Review of Astronomy and Astrophysics*, vol. 44, no. 1, pp. 17–47, 2006, _eprint: https://doi.org/10.1146/annurev.astro.44.051905.092528. DOI:

10.1146/annurev.astro.44.051905.092528. [Online]. Available: https://doi.org/10.1146/annurev.astro.44.051905.092528 (cit. on p. 51).

[91] D. Horns *et al.*, "Nucleonic gamma-ray production in Vela X," en, *Astronomy & Astrophysics*, vol. 451, no. 3, pp. L51–L54, Jun. 2006, Number: 3 Publisher: EDP Sciences, ISSN: 0004-6361, 1432-0746. DOI: 10.1051/0004-6361:20065116. [Online]. Available: https://www.aanda.org/articles/aa/abs/2006/21/aa5116-06/aa5116-06.html (cit. on p. 52).

[92] A. M. Hillas *et al.*, "The Spectrum of TeV Gamma Rays from the Crab Nebula," en, *The Astrophysical Journal*, vol. 503, no. 2, pp. 744–759, Aug. 1998, Publisher: American Astronomical Society, ISSN: 0004-637X. DOI: 10.1086/306005. [Online]. Available: https://doi.org/10.1086/306005 (cit. on p. 52).

[93] T. Tanimori *et al.*, "Detection of Gamma Rays of up to 50 T[CLC]e[/CLC]V from the Crab Nebula," en, *The Astrophysical Journal*, vol. 492, no. 1, pp. L33–L36, Jan. 1998, Publisher: American Astronomical Society, ISSN: 0004-637X. DOI: 10.1086/311077. [Online]. Available: https://doi.org/10.1086/311077 (cit. on p. 52).

[94] A. A. Abdo *et al.*, "OBSERVATION AND SPECTRAL MEASUREMENTS OF THE CRAB NEBULA WITH MILAGRO," en, *The Astrophysical Journal*, vol. 750, no. 1, p. 63, Apr. 2012, Publisher: American Astronomical Society, ISSN: 0004-637X. DOI: 10.1088/0004-637X/750/1/63. [Online]. Available: https://doi.org/10.1088/0004-637x/750/1/63 (cit. on p. 52).

[95] F. Aharonian *et al.*, "Observations of the Crab nebula with HESS," en, *Astronomy & Astrophysics*, vol. 457, no. 3, pp. 899–915, Oct. 2006, Number: 3 Publisher: EDP Sciences, ISSN: 0004-6361, 1432-0746. DOI: 10.1051/0004-6361:20065351. [Online]. Available: https://www.aanda.org/articles/aa/abs/2006/39/aa5351-06/aa5351-06.html (cit. on pp. 52, 74, 76).

[96] A. U. Abeysekara *et al.*, "Measurement of the Crab Nebula Spectrum Past 100 TeV with HAWC," en, *The Astrophysical Journal*, vol. 881, no. 2, p. 134, Aug. 2019, Publisher: American Astronomical Society, ISSN: 0004-637X. DOI: 10.

3847/1538-4357/ab2f7d. [Online]. Available: https://doi.org/10.3847/1538-4357/ab2f7d (cit. on pp. 52, 76, 78).

[97] Tibet AS Collaboration *et al.*, "First Detection of Photons with Energy beyond 100 TeV from an Astrophysical Source," *Physical Review Letters*, vol. 123, no. 5, p. 051 101, Jul. 2019, Publisher: American Physical Society. DOI: 10.1103/PhysRevLett.123.051101. [Online]. Available: https://link.aps.org/doi/10.1103/PhysRevLett.123.051101 (cit. on pp. 52, 76, 78).

[98] A. A. Abdo *et al.*, "Gamma-Ray Flares from the Crab Nebula," en, *Science*, vol. 331, no. 6018, pp. 739–742, Feb. 2011, Publisher: American Association for the Advancement of Science Section: Report, ISSN: 0036-8075, 1095-9203. DOI: 10.1126/science.1199705. [Online]. Available: https://science.sciencemag.org/content/331/6018/739 (cit. on p. 52).

[99] R. Buehler *et al.*, "GAMMA-RAY ACTIVITY IN THE CRAB NEBULA: THE EXCEPTIONAL FLARE OF 2011 APRIL," en, *The Astrophysical Journal*, vol. 749, no. 1, p. 26, Mar. 2012, Publisher: American Astronomical Society, ISSN: 0004-637X. DOI: 10.1088/0004-637X/749/1/26. [Online]. Available: https://doi.org/10.1088/0004-637x/749/1/26 (cit. on p. 52).

[100] R. Mirzoyan *et al.*, "Extending the observation limits of Imaging Air Cherenkov Telescopes toward horizon," en, *Nuclear Instruments and Methods in Physics Research Section A: Accelerators, Spectrometers, Detectors and Associated Equipment*, vol. 952, p. 161 587, Feb. 2020, ISSN: 01689002. DOI: 10.1016/j.nima.2018.11.046. [Online]. Available: https://linkinghub.elsevier.com/retrieve/pii/S0168900218316218 (cit. on pp. 54, 55, 64, 200).

[101] P. Sommers and J. W. Elbert, "Ultra-high-energy gamma-ray astronomy using atmospheric Cerenkov detectors at large zenith angles," en, *Journal of Physics G: Nuclear Physics*, vol. 13, no. 4, pp. 553–566, Apr. 1987, Publisher: IOP Publishing, ISSN: 0305-4616. DOI: 10.1088/0305-4616/13/4/019. [Online]. Available: https://doi.org/10.1088/0305-4616/13/4/019 (cit. on p. 54).

[102] A. Konopelko *et al.*, "Effectiveness of TeV gamma-ray observations at large zenith angles with a stereoscopic system of imaging atmospheric Cerenkov telescopes,"

en, *Journal of Physics G: Nuclear and Particle Physics*, vol. 25, no. 9, pp. 1989–2000, Sep. 1999, Publisher: IOP Publishing, ISSN: 0954-3899. DOI: 10.1088/0954-3899/25/9/316. [Online]. Available: https://doi.org/10.1088/0954-3899/25/9/316 (cit. on p. 54).

[103] M. L. Ahnen *et al.*, "Observations of Sagittarius A* during the pericenter passage of the G2 object with MAGIC," en, *Astronomy & Astrophysics*, vol. 601, A33, May 2017, Publisher: EDP Sciences, ISSN: 0004-6361, 1432-0746. DOI: 10.1051/0004-6361/201629355. [Online]. Available: https://www.aanda.org/articles/aa/abs/2017/05/aa29355-16/aa29355-16.html (cit. on p. 54).

[104] R. Zanin *et al.*, "MARS, the MAGIC analysis and reconstruction software," in *Proc. of the 33st International Cosmic Ray Conference, Rio de Janeiro, Brasil*, 2013 (cit. on pp. 58, 97).

[105] J. Aleksi *et al.*, "Performance of the MAGIC stereo system obtained with Crab Nebula data," en, *Astroparticle Physics*, vol. 35, no. 7, pp. 435–448, Feb. 2012, ISSN: 0927-6505. DOI: 10.1016/j.astropartphys.2011.11.007. [Online]. Available: https://www.sciencedirect.com/science/article/pii/S0927650511002064 (cit. on pp. 58, 102).

[106] V. Fomin *et al.*, "New methods of atmospheric Cherenkov imaging for gamma-ray astronomy. I. The false source method," en, *Astroparticle Physics*, vol. 2, no. 2, pp. 137–150, May 1994, ISSN: 09276505. DOI: 10.1016/0927-6505(94)90036-1. [Online]. Available: https://linkinghub.elsevier.com/retrieve/pii/0927650594900361 (cit. on pp. 58, 88, 96).

[107] MAGIC Collaboration *et al.*, "MAGIC very large zenith angle observations of the Crab Nebula up to 100 TeV," en, *Astronomy & Astrophysics*, vol. 635, A158, Mar. 2020, ISSN: 0004-6361, 1432-0746. DOI: 10.1051/0004-6361/201936899. [Online]. Available: https://www.aanda.org/10.1051/0004-6361/201936899 (cit. on pp. 58, 64, 76–78, 102, 200).

[108] D. Heck *et al.*, *CORSIKA: a Monte Carlo code to simulate extensive air showers*. Feb. 1998, Publication Title: CORSIKA: a Monte Carlo code to simulate

extensive air showers ADS Bibcode: 1998cmcc.book.....H. [Online]. Available: https://ui.adsabs.harvard.edu/abs/1998cmcc.book.....H (cit. on p. 63).

[109] J. Aleksic *et al.*, "The major upgrade of the MAGIC telescopes, Part II: A performance study using observations of the Crab Nebula," en, *Astroparticle Physics*, vol. 72, pp. 76–94, Jan. 2016, ISSN: 09276505. DOI: 10.1016/j.astropartphys.2015.02.005. [Online]. Available: https://linkinghub.elsevier.com/retrieve/pii/S0927650515000316 (cit. on pp. 63–65, 68, 78, 102).

[110] T. Bretz *et al.*, "The drive system of the Major Atmospheric Gamma-ray Imaging Cherenkov Telescope," en, *Astroparticle Physics*, vol. 31, no. 2, pp. 92–101, Mar. 2009, arXiv: 0810.4593, ISSN: 09276505. DOI: 10.1016/j.astropartphys.2008.12.001. [Online]. Available: http://arxiv.org/abs/0810.4593 (cit. on pp. 65, 110).

[111] P. T. Wallace, "TPOINT – Telescope Pointing Analysis System," *Starlink User Note*, vol. 100, Jan. 1994, ADS Bibcode: 1994StaUN.100.....W. [Online]. Available: https://ui.adsabs.harvard.edu/abs/1994StaUN.100.....W (cit. on pp. 65, 110).

[112] J. Aleksi *et al.*, "Measurement of the Crab Nebula spectrum over three decades in energy with the MAGIC telescopes," en, *Journal of High Energy Astrophysics*, vol. 5-6, pp. 30–38, Mar. 2015, ISSN: 2214-4048. DOI: 10.1016/j.jheap.2015.01.002. [Online]. Available: https://www.sciencedirect.com/science/article/pii/S2214404815000038 (cit. on pp. 74, 76, 77).

[113] M. Meyer, D. Horns, and H.-S. Zechlin, "The Crab Nebula as a standard candle in very high-energy astrophysics," en, *Astronomy & Astrophysics*, vol. 523, A2, Nov. 2010, ISSN: 0004-6361, 1432-0746. DOI: 10.1051/0004-6361/201014108. [Online]. Available: http://www.aanda.org/10.1051/0004-6361/201014108 (cit. on pp. 74, 77).

[114] F. Fraschetti and M. Pohl, "Particle acceleration model for the broad-band baseline spectrum of the Crab nebula," *Monthly Notices of the Royal Astronomical Society*, vol. 471, pp. 4856–4864, Nov. 2017, ISSN: 0035-8711. DOI: 10.1093/

mnras/stx1833. [Online]. Available: https://ui.adsabs.harvard.edu/abs/2017MNRAS.471.4856F (cit. on pp. 74, 77).

[115] W. Bednarek and R. J. Protheroe, "Gamma Rays and Neutrinos from the Crab Nebula Produced by Pulsar Accelerated Nuclei," *Physical Review Letters*, vol. 79, pp. 2616–2619, Oct. 1997, ISSN: 0031-9007. DOI: 10.1103/PhysRevLett.79.2616. [Online]. Available: https://ui.adsabs.harvard.edu/abs/1997PhRvL..79.2616B (cit. on pp. 77, 78).

[116] E. Amato, D. Guetta, and P. Blasi, "Signatures of high energy protons in pulsar winds," en, *Astronomy & Astrophysics*, vol. 402, no. 3, pp. 827–836, May 2003, ISSN: 0004-6361, 1432-0746. DOI: 10.1051/0004-6361:20030279. [Online]. Available: http://www.aanda.org/10.1051/0004-6361:20030279 (cit. on pp. 77, 78).

[117] J. Martín, D. F. Torres, and N. Rea, "Time-dependent modelling of pulsar wind nebulae: Study on the impact of the diffusion-loss approximations: Time-dependent modelling of PWNe," en, *Monthly Notices of the Royal Astronomical Society*, vol. 427, no. 1, pp. 415–427, Nov. 2012, ISSN: 00358711, 13652966. DOI: 10.1111/j.1365-2966.2012.22014.x. [Online]. Available: https://academic.oup.com/mnras/article-lookup/doi/10.1111/j.1365-2966.2012.22014.x (cit. on p. 74).

[118] T. L. Collaboration* *et al.*, "Petaelectron volt gamma-ray emission from the Crab Nebula," en, *Science*, vol. 373, no. 6553, pp. 425–430, Jul. 2021, Publisher: American Association for the Advancement of Science Section: Research Article, ISSN: 0036-8075, 1095-9203. DOI: 10.1126/science.abg5137. [Online]. Available: https://science.sciencemag.org/content/373/6553/425 (cit. on pp. 78, 79).

[119] A. M. Atoyan and F. A. Aharonian, "On the mechanisms of gamma radiation in the Crab Nebula," *Monthly Notices of the Royal Astronomical Society*, vol. 278, no. 2, pp. 525–541, Jan. 1996, ISSN: 0035-8711. DOI: 10.1093/mnras/278.2.525. [Online]. Available: https://doi.org/10.1093/mnras/278.2.525 (cit. on p. 78).

[120] W. Bednarek and M. Bartosik, "Gamma-rays from the pulsar wind nebulae," en, *Astronomy & Astrophysics*, vol. 405, no. 2, pp. 689–702, Jul. 2003, Number: 2 Publisher: EDP Sciences, ISSN: 0004-6361, 1432-0746. DOI: 10.1051/0004-6361:20030593. [Online]. Available: https://www.aanda.org/articles/aa/abs/2003/26/aa3605/aa3605.html (cit. on p. 78).

[121] L. Wang *et al.*, "The Crab Nebula: Observations and a search for UHE -ray ares with LHAASO," en, *The Crab Nebula*, p. 10, (cit. on p. 79).

[122] G. R. BLUMENTHAL and R. J. GOULD, "Bremsstrahlung, Synchrotron Radiation, and Compton Scattering of High-Energy Electrons Traversing Dilute Gases," *Reviews of Modern Physics*, vol. 42, no. 2, pp. 237–270, Apr. 1970, Publisher: American Physical Society. DOI: 10.1103/RevModPhys.42.237. [Online]. Available: https://link.aps.org/doi/10.1103/RevModPhys.42.237 (cit. on p. 79).

[123] M. Breuhaus *et al.*, "Ultra-high Energy Inverse Compton Emission from Galactic Electron Accelerators," en, *The Astrophysical Journal*, vol. 908, no. 2, p. L49, Feb. 2021, Publisher: American Astronomical Society, ISSN: 2041-8205. DOI: 10.3847/2041-8213/abe41a. [Online]. Available: https://doi.org/10.3847/2041-8213/abe41a (cit. on p. 79).

[124] J. van Scherpenberg *et al.*, "Searching for Variability of the Crab Nebula Flux at TeV Energies using MAGIC Very Large Zenith Angle Observations," en, in *Proceedings of 36th International Cosmic Ray Conference — PoS(ICRC2019)*, Madison, WI, U.S.A.: Sissa Medialab, Jul. 2019, p. 812. DOI: 10.22323/1.358.0812. [Online]. Available: https://pos.sissa.it/358/812 (cit. on p. 79).

[125] E. Aliu *et al.*, "SPATIALLY RESOLVING THE VERY HIGH ENERGY EMISSION FROM MGRO J2019+37 WITH VERITAS," *The Astrophysical Journal*, vol. 788, no. 1, p. 78, May 2014, ISSN: 0004-637X, 1538-4357. DOI: 10.1088/0004-637X/788/1/78. [Online]. Available: http://stacks.iop.org/0004-637X/788/i=1/a=78?key=crossref.df4c101cc786f6ea03aef1d81214e9ea (cit. on pp. 81, 86, 87, 92).

[126] F. Aharonian *et al.*, "Discovery of two candidate pulsar wind nebulae in very-high-energy gamma rays," en, *Astronomy & Astrophysics*, vol. 472, no. 2, pp. 489–495, Sep. 2007, ISSN: 0004-6361, 1432-0746. DOI: 10.1051/0004-6361:20077280. [Online]. Available: http://www.aanda.org/10.1051/0004-6361:20077280 (cit. on p. 81).

[127] I. Vovk *et al.*, "Novel Very Large Zenith Angle Observation Technique Performed by the MAGIC Telescopes," en, in *Proceedings of 36th International Cosmic Ray Conference — PoS(ICRC2019)*, Madison, WI, U.S.A.: Sissa Medialab, Jul. 2019, p. 828. DOI: 10.22323/1.358.0828. [Online]. Available: https://pos.sissa.it/358/828 (cit. on pp. 82, 97).

[128] I. Vovk, M. Strzys, and C. Fruck, "Spatial likelihood analysis for MAGIC telescope data: From instrument response modelling to spectral extraction," *Astronomy & Astrophysics*, vol. 619, A7, Nov. 2018, ISSN: 0004-6361, 1432-0746. DOI: 10.1051/0004-6361/201833139. [Online]. Available: https://www.aanda.org/10.1051/0004-6361/201833139 (cit. on pp. 84, 89).

[129] S. D. Hunter *et al.*, "EGRET Observations of the Diffuse GammaRay Emission from the Galactic Plane," en, *The Astrophysical Journal*, vol. 481, no. 1, pp. 205–240, May 1997, ISSN: 0004-637X, 1538-4357. DOI: 10.1086/304012. [Online]. Available: http://stacks.iop.org/0004-637X/481/i=1/a=205 (cit. on p. 86).

[130] A. A. Abdo *et al.*, "Discovery of TeV Gamma-Ray Emission from the Cygnus Region of the Galaxy," en, *The Astrophysical Journal*, vol. 658, no. 1, pp. L33–L36, Mar. 2007, ISSN: 0004-637X, 1538-4357. DOI: 10.1086/513696. [Online]. Available: https://iopscience.iop.org/article/10.1086/513696 (cit. on p. 86).

[131] D. B. Kieda, "A VERITAS Search for VHE -Ray Point Sources Near Selected MILAGRO Tar- get Regions," en, p. 4, (cit. on p. 86).

[132] H. Bartko *et al.*, "Search for gamma-ray emission from Unidentified EGRET sources Located in the Cygnus Region with the MAGIC Telescope," *International Cosmic Ray Conference*, vol. 2, pp. 649–652, 2008 (cit. on p. 86).

[133] B. Bartoli *et al.*, "OBSERVATION OF TeV GAMMA RAYS FROM THE CYGNUS REGION WITH THE ARGO-YBJ EXPERIMENT," en, *The Astrophysical Journal*, vol. 745, no. 2, p. L22, Jan. 2012, Publisher: American Astronomical Society, ISSN: 2041-8205. DOI: 10.1088/2041-8205/745/2/L22. [Online]. Available: https://doi.org/10.1088/2041-8205/745/2/l22 (cit. on p. 86).

[134] Y. Wang, "Study on TeV Ray Emission from Cygnus Region Using the Tibet Air Shower Array," in *Proceedings, 30th International Cosmic Ray Conference (ICRC 2007): Merida, Yucatan, Mexico, July 3-11, 2007*, bibtex*[collaboration=TIBET AS], vol. 2, 2007, pp. 695–698. [Online]. Available: http://indico.nucleares.unam.mx/contributionDisplay.py?contribId=548&confId=4 (cit. on p. 86).

[135] A. U. Abeysekara *et al.*, "The 2HWC HAWC Observatory Gamma-Ray Catalog," en, *The Astrophysical Journal*, vol. 843, no. 1, p. 40, Jun. 2017, ISSN: 1538-4357. DOI: 10.3847/1538-4357/aa7556. [Online]. Available: https://iopscience.iop.org/article/10.3847/1538-4357/aa7556 (cit. on pp. 86, 92).

[136] A. U. Abeysekara *et al.*, "A Very High Energy -Ray Survey toward the Cygnus Region of the Galaxy," *The Astrophysical Journal*, vol. 861, no. 2, p. 134, Jul. 2018, ISSN: 1538-4357. DOI: 10.3847/1538-4357/aac4a2. [Online]. Available: http://stacks.iop.org/0004-637X/861/i=2/a=134?key=crossref.96d29316fced9322e829519e3bbf1081 (cit. on pp. 87, 89, 90, 92).

[137] H. Collaboration *et al.*, "Spectrum and Morphology of the Very-High-Energy Source HAWC J2019+368," *arXiv:2101.01649 [astro-ph]*, Jan. 2021, arXiv: 2101.01649. [Online]. Available: http://arxiv.org/abs/2101.01649 (cit. on p. 91).

[138] M. Amenomori *et al.*, "Gamma-ray Observation of the Cygnus Region in the 100 TeV Energy Region," *Physical Review Letters*, vol. 127, no. 3, p. 031 102, Jul. 2021, arXiv: 2107.01064, ISSN: 0031-9007, 1079-7114. DOI: 10.1103/PhysRevLett.127.031102. [Online]. Available: http://arxiv.org/abs/2107.01064 (cit. on p. 91).

[139] Z. Cao *et al.*, "Ultrahigh-energy photons up to 1.4 petaelectronvolts from 12 -ray Galactic sources," en, *Nature*, vol. 594, no. 7861, pp. 33–36, Jun. 2021, ISSN: 0028-0836, 1476-4687. DOI: 10.1038/s41586-021-03498-z. [Online]. Available: http://www.nature.com/articles/s41586-021-03498-z (cit. on p. 91).

[140] F. Aharonian *et al.*, "Discovery of two candidate pulsar wind nebulae in very-high-energy gamma rays," en, *Astronomy and Astrophysics*, vol. 472, no. 2, pp. 489–495, Sep. 2007, ISSN: 0004-6361. DOI: 10.1051/0004-6361:20077280. [Online]. Available: https://ui.adsabs.harvard.edu/abs/2007A&A...472..489A/abstract (cit. on p. 93).

[141] G. Castelletti, E. Giacani, and A. Petriella, "Unveiling the origin of HESS J1809193," en, *Astronomy & Astrophysics*, vol. 587, A71, Mar. 2016, ISSN: 0004-6361, 1432-0746. DOI: 10.1051/0004-6361/201527578. [Online]. Available: http://www.aanda.org/10.1051/0004-6361/201527578 (cit. on pp. 93, 94).

[142] M. Araya, "GeV Emission in the Region of HESS J1809193 and HESS J1813178: Is HESS J1809193 a Proton Pevatron?" en, *The Astrophysical Journal*, vol. 859, no. 1, p. 69, May 2018, ISSN: 1538-4357. DOI: 10.3847/1538-4357/aabd7e. [Online]. Available: https://iopscience.iop.org/article/10.3847/1538-4357/aabd7e (cit. on pp. 93, 95, 107).

[143] J. Ballet *et al.*, "Fermi Large Area Telescope Fourth Source Catalog Data Release 2," Tech. Rep., May 2020, Publication Title: arXiv e-prints ADS Bibcode: 2020arXiv200511208B Type: article. [Online]. Available: https://ui.adsabs.harvard.edu/abs/2020arXiv200511208B (cit. on p. 93).

[144] S. Abdollahi *et al.*, "Fermi Large Area Telescope Fourth Source Catalog," *The Astrophysical Journal Supplement Series*, vol. 247, p. 33, Mar. 2020, ADS Bibcode: 2020ApJS..247...33A, ISSN: 0067-0049. DOI: 10.3847/1538-4365/ab6bcb. [Online]. Available: https://ui.adsabs.harvard.edu/abs/2020ApJS..247...33A (cit. on p. 93).

[145] H. E. S. S. Collaboration *et al.*, "The H.E.S.S. Galactic plane survey," en, *Astronomy and Astrophysics*, vol. 612, A1, Apr. 2018, ISSN: 0004-6361. DOI: 10.1051/

0004-6361/201732098. [Online]. Available: https://ui.adsabs.harvard.edu/abs/2018A&A...612A...1H/abstract (cit. on pp. 94, 95, 107).

[146] M. L. Ahnen *et al.*, "Performance of the MAGIC telescopes under moonlight," en, *Astroparticle Physics*, vol. 94, pp. 29–41, Sep. 2017, ISSN: 0927-6505. DOI: 10.1016/j.astropartphys.2017.08.001. [Online]. Available: https://www.sciencedirect.com/science/article/pii/S092765051730110X (cit. on p. 96).

[147] A. Albert *et al.*, "3HWC: The Third HAWC Catalog of Very-high-energy Gamma-Ray Sources," *The Astrophysical Journal*, vol. 905, p. 76, Dec. 2020, ADS Bibcode: 2020ApJ...905...76A, ISSN: 0004-637X. DOI: 10.3847/1538-4357/abc2d8. [Online]. Available: https://ui.adsabs.harvard.edu/abs/2020ApJ...905...76A (cit. on p. 107).

[148] D. Zaric *et al.*, "Pointing System for the Large Size Telescopes Prototype of the Cherenkov Telescope Array," en, in *Proceedings of 36th International Cosmic Ray Conference — PoS(ICRC2019)*, Madison, WI, U.S.A.: Sissa Medialab, Jul. 2019, p. 829. DOI: 10.22323/1.358.0829. [Online]. Available: https://pos.sissa.it/358/829 (cit. on pp. 110, 202).

[149] K. Noda, *Alignment and pointing corrections and procedures | Document 2354702 (v.1)*. [Online]. Available: https://edms.cern.ch/ui/#!master/navigator/document?D:100604911:100604911:subDocs (cit. on p. 110).

[150] *LST pointing and alignment performance with the finite element analysis*. [Online]. Available: https://edms.cern.ch/document/2354699 (cit. on p. 114).

[151] *Unified Architecture*, en-US. [Online]. Available: https://opcfoundation.org/about/opc-technologies/opc-ua/ (cit. on p. 120).

[152] G. Bradski, "The OpenCV library," *Dr. Dobb's Journal of Software Tools*, 2000. [Online]. Available: https://opencv.org/ (cit. on p. 121).

[153] A. Al-Sharadqah and N. Chernov, "Error analysis for circle fitting algorithms," *Electronic Journal of Statistics*, vol. 3, no. none, pp. 886–911, Jan. 2009, Publisher: Institute of Mathematical Statistics and Bernoulli Society, ISSN: 1935-

7524, 1935-7524. DOI: 10.1214/09-EJS419. [Online]. Available: https://projecteuclid.org/journals/electronic-journal-of-statistics/volume-3/issue-none/Error-analysis-for-circle-fitting-algorithms/10.1214/09-EJS419.full (cit. on p. 121).

[154] J. Eder, E. Sambenedetto, and A. Targusi, *LST1 structure analysis*. [Online]. Available: https://edms.cern.ch/document/2403334 (cit. on pp. 139, 161).

[155] D. Zaric *et al.*, "MAGIC observations of Dragonfly Nebula at TeV Energies using the Very Large Zenith Angle Technique," en, in *Proceedings of 36th International Cosmic Ray Conference PoS(ICRC2019)*, Madison, WI, U.S.A.: Sissa Medialab, Jul. 2019, p. 827. DOI: 10.22323/1.358.0827. [Online]. Available: https://pos.sissa.it/358/827 (cit. on p. 201).

[156] D. Zaric *et al.*, "MAGIC observations of HESS J1809-193 using the Very Large Zenith Angle technique at energies above TeV," en, in *Proceedings of 37th International Cosmic Ray Conference PoS(ICRC2021)*, Berlin, Germany - Online: Sissa Medialab, Jul. 2021, p. 818. DOI: 10.22323/1.395.0818. [Online]. Available: https://pos.sissa.it/395/818 (cit. on p. 201).

AUTHOR'S CONTRIBUTIONS

CHAPTER 3: VLZA OBSERVATIONS

The author conducted a performance study of the pointing accuracy for the first Crab VLZA dataset (2014-2018). For the second Crab VLZA dataset (2018-2021) the author was the main MAGIC data analyzer and has led the analysis to assess the VLZA performance and the Crab Nebula results. He then led the study of the combined datasets to assess the overall VLZA performance and the overall Crab Nebula results.

Results from this chapter are published in [100] and [107] papers. Here the author performed MAGIC data analysis, participated in the interpretation of the results, prepared part of the plots and wrote parts of the text.

CHAPTER 4: VLZA OBSERVATIONS OF EXTENDED SOURCES

The author performed a search for the best observable PeVatron candidates for MAGIC. From that study Dragonfly and HESS J1809 were chosen for VLZA observations. The author was the main analyzer for the MAGIC analysis of Dragonfly and HESS J1809 sources. Spatial likelihood analysis was here applied for the first time to VLZA sources.

The results of this chapter were presented at two ICRC conferences for which the author is the leading author of the proceedings: [155] and [156]. He performed all of the analysis, prepared all of the plots, made presented presentations and wrote all of the proceedings.

The paper containing results for HESS J1809 is in preparation. Here the author lead MAGIC data analysis, participated in the interpretation of the results, prepared most of the plots and wrote parts of the text.

CHAPTER 5: CAMERA DISPLACEMENT MONITOR FOR LST-1

The author alone designed, developed, tested and implemented a system to monitor the oscillations of the LST Cherenkov camera. Author developed the whole software to control the system, analyze the data, store the results and communicate with other subsystems. Author performed tests in laboratory in FESB-Split and performed tests on-site. He alone produced all of the data and all of the plots.

Results from this chapter were presented at ICRC conference for which the author is the leading author of the proceedings: [148]. Here the author made a poster and wrote the proceedings.

CURRICULUM VITAE

Darko Zarić was born in Split, Croatia in 1990, where he completed primary and secondary education. In 2015 he graduated from the Faculty of Science, University of Split with the thesis title "Osnovno stanje He-He-Na trimera" ("Ground state of He-He-Na trimer") under the supervision of prof. dr. sc. Leandra Vranješ Markić. During his studies he was awarded with Dean's and Rector's awards.

After graduation he started working at the Faculty of Electrical Engineering, Mechanical Engineering and Naval Architecture, University of Split as a teaching assistant by joining the project "Very high energy gamma ray astronomy with the MAGIC and CTA telescopes" led by prof. dr. sc. Nikola Godinović and funded by the Croatian Science Foundation (HRZZ). At the same time he enrolled in the physics doctoral program at the Faculty of Science, University of Zagreb. Simultaneously he joined the MAGIC, LST and CTA Collaborations as a member of the Croatian Consortium and started with his research and contributions.

In 2018-2019 period he visited the Max Planck Institute for Physics (Werner-Heisenberg-Institut) in Munich, Germany three times and spent in total 11 months doing research specialization. This research stay was mostly funded with the DAAD scholarship grants for which he applied and was awarded for. As an active member of the MAGIC Collaboration Darko's research work is concerned with Galactic physics, particularly the investigation of the origin of cosmic rays. For the LST Collaboration Darko has contributed to the technical development of the pointing system of the telescope in which he designed, implemented and tested a system for monitoring the camera oscillations.

He is the author of 49 scientific articles, and attended 2 scientific conferences and 6 schools.

List of publications

Refereed published articles

[1] H. Abdalla *et al.*, "H.E.S.S. and MAGIC observations of a sudden cessation of a very-high-energy gamma-ray flare in PKS 1510089 in May 2016," *Astronomy and astrophysics (Berlin)*, vol. 648, p. 22, 2021. DOI: 10.1051/0004-6361/202038949.

[2] H. Abdalla *et al.*, "Sensitivity of the Cherenkov Telescope Array for probing cosmology and fundamental physics with gamma-ray propagation," *Journal of cosmology and astroparticle physics*, vol. 2021, no. 2, p. 66, 2021. DOI: 10.1088/1475-7516/2021/02/048.

[3] A. Acharyya *et al.*, "Sensitivity of the Cherenkov Telescope Array to a dark matter signal from the Galactic centre," *Journal of cosmology and astroparticle physics*, vol. 2021, no. 1, p. 64, 2021. DOI: 10.1088/1475-7516/2021/01/057.

[4] V. A. Acciari *et al.*, "Testing two-component models on very high-energy gamma-ray-emitting BL Lac objects," *Astronomy and Astrophysics*, vol. 640, p. 29, 2020. DOI: 10.1051/0004-6361/202037811.

[5] V. A. Acciari *et al.*, "MAGIC observations of the diffuse gamma-ray emission in the vicinity of the Galactic center," *Astronomy and Astrophysics*, vol. 642, p. 9, 2020. DOI: 10.1051/0004-6361/201936896.

[6] V. A. Acciari *et al.*, "Detection of the Geminga pulsar with MAGIC hints at a power-law tail emission beyond 15 GeV," *Astronomy and astrophysics (Berlin)*, vol. 643, p. 6, 2020. DOI: 10.1051/0004-6361/202039131.

[7] V. A. Acciari *et al.*, "Multiwavelength variability and correlation studies of Mrk 421 during historically low X-ray and gamma-ray activity in 2015-2016," *Monthly notices of the Royal Astronomical Society*, vol. 504, pp. 1427–1451, 2020. DOI: 10.1093/mnras/staa3727.

[8] V. A. Acciari *et al.*, "An intermittent extreme BL Lac: MWL study of 1ES2344+514 in an enhanced state," *Monthly notices of the Royal Astronomical Society*, vol. 496, no. 3, pp. 3912–3928, 2020. DOI: 10.1093/mnras/staa1702.

[9] V. A. Acciari *et al.*, "Broadband characterisation of the very intense TeV flares of the blazar 1ES 1959+650 in 2016," *Astronomy and astrophysics (Berlin)*, vol. 638, p. 16, 2020. DOI: 10.1051/0004-6361/201935450.

[10] V. A. Acciari *et al.*, "Bounds on Lorentz invariance violation from MAGIC observation of GRB 190114C," *Physical review letters*, vol. 125, no. 2, p. 7, 2020. DOI: 10.1103/PhysRevLett.125.021301.

[11] V. A. Acciari *et al.*, "Study of the variable broadband emission of Markarian 501 during the most extreme Swift X-ray activity," *Astronomy and astrophysics (Berlin)*, vol. 637, p. 27, 2020. DOI: 10.1051/0004-6361/201834603.

[12] V. A. Acciari *et al.*, "Unravelling the complex behavior of Mrk 421 with simultaneous X-ray and VHE observations during an extreme flaring activity in 2013 April," *The Astrophysical journal. Supplement series*, vol. 248, no. 2, pp. 29–65, 2020. DOI: 10.3847/1538-4365/ab89b5.

[13] A. U. Abeysekara *et al.*, "The Great Markarian 421 Flare of 2010 February: Multiwavelength Variability and Correlation Studies," *The Astrophysical journal*, vol. 890, no. 2, p. 41, 2020. DOI: 10.3847/1538-4357/ab6612.

[14] V. A. Acciari *et al.*, "New Hard-TeV Extreme Blazars Detected with the MAGIC Telescopes," *The Astrophysical journal. Supplement series*, vol. 247, no. 1, p. 30, 2020. DOI: 10.3847/1538-4365/ab5b98.

[15] V. Acciari *et al.*, "A search for dark matter in TriangulumII with the MAGIC telescopes," *Physics of the Dark Universe*, vol. 28, p. 14, 2020. DOI: 10.1016/j.dark.2020.100529.

[16] V. A. Acciari *et al.*, "Monitoring of the radio galaxy M87 during a low- emission state from 2012 to 2015 with MAGIC," *Monthly Notices of the Royal Astronomical Society*, vol. 492, no. 4, pp. 5354–5365, 2020. DOI: 10.1093/mnras/staa014.

[17] V. A. Acciari *et al.*, "MAGIC very large zenith angle observations of the Crab Nebula up to 100 TeV," *Astronomy and Astrophysics*, vol. 635, p. 10, 2020. DOI: 10.1051/0004-6361/201936899.

[18] M. L. Ahnen *et al.*, "Statistics of VHE gamma-rays in temporal association with radio giant pulses from the Crab pulsar," *Astronomy and Astrophysics*, vol. 634, p. 14, 2020. DOI: 10.1051/0004-6361/201833555.

[19] V. A. Acciari *et al.*, "Testing emission models on the extreme blazar 2WHSPJ073326.7+515354 detected at very high energies with the MAGIC telescopes," *Monthly Notices of the Royal Astronomical Society*, vol. 490, no. 2, pp. 2284–2299, 2019. DOI: 10.1093/mnras/stz2725.

[20] V. A. Acciari *et al.*, "Observation of inverse Compton emission from a long gamma-ray burst," *Nature*, vol. 575, no. 7783, pp. 459–463, 2019. DOI: 10.1038/s41586-019-1754-6.

[21] V. A. Acciari *et al.*, "Teraelectronvolt emission from the gamma-ray burst GRB 190114C," *Nature*, vol. 575, no. 7783, pp. 455–458, 2019. DOI: 10.1038/s41586-019-1750-x.

[22] V. A. Acciari *et al.*, "Constraints on Gamma-Ray and Neutrino Emission from NGC 1068 with the MAGIC Telescopes," *The Astrophysical Journal*, vol. 883, no. 2, p. 11, 2019. DOI: 10.3847/1538-4357/ab3a51.

[23] V. A. Acciari *et al.*, "Measurement of the extragalactic background light using MAGIC and Fermi-LAT gamma-ray observations of blazars up to z = 1," *Monthly notices of the Royal Astronomical Society*, vol. 486, no. 3, pp. 4233–4251, 2019. DOI: 10.1093/mnras/stz943.

[24] V. A. Acciari *et al.*, "A fast, very-high-energy gamma-ray flare from BL Lacertae during a period of multi-wavelength activity in June 2015," *Astronomy and astrophysics (Berlin)*, vol. 623, no. A175, pp. 1–14, 2019. DOI: 10.1051/0004-6361/201834010.

[25] V. A. Acciari *et al.*, "Deep observations of the globular cluster M15 with the MAGIC telescopes," *Monthly notices of the Royal Astronomical Society*, vol. 484, no. 2, pp. 2876–2885, 2019. DOI: 10.1093/mnras/stz179.

[26] M. L. Ahnen *et al.*, "MAGIC and Fermi-LAT gamma-ray results on unassociated HAWC sources," *Monthly notices of the Royal Astronomical Society*, vol. 485, no. 1, pp. 356–366, 2019. DOI: 10.1093/mnras/stz089.

[27] V. A. Acciari *et al.*, "Discovery of TeV gamma-ray emission from the neighbourhood of the supernova remnant G24.7+0.6 by MAGIC," *Monthly notices of the Royal Astronomical Society*, vol. 483, no. 4, pp. 4578–4585, 2019. DOI: 10.1093/mnras/sty3387.

[28] A. U. Abeysekara *et al.*, "Periastron Observations of TeV Gamma-Ray Emission from a Binary System with a 50-year Period," *The Astrophysical Journal Letters*, vol. 867, no. 1, p. 8, 2018. DOI: 10.3847/2041-8213/aae70e.

[29] V. A. Acciari *et al.*, "Detection of persistent VHE gamma-ray emission from PKS 1510089 by the MAGIC telescopes during low states between 2012 and 2017.," *Astronomy and astrophysics (Berlin)*, vol. 619, no. A159, pp. 1–11, 2018. DOI: 10.1051/0004-6361/201833618.

[30] M. L. Ahnen *et al.*, "Multi-wavelength characterization of the blazar S5 0716+714 during an unprecedented outburst phase," *Astronomy and astrophysics (Berlin)*, vol. 619, no. A45, pp. 1–18, 2018. DOI: 10.1051/0004-6361/201832677.

[31] M. L. Ahnen *et al.*, "Extreme HBL behavior of Markarian 501 during 2012," *Astronomy and astrophysics (Berlin)*, vol. 620, no. A181, pp. 1–23, 2018. DOI: 10.1051/0004-6361/201833704.

[32] V. A. Acciari *et al.*, "Constraining very-high-energy and optical emission from FRB 121102 with the MAGIC telescopes," *Monthly Notices of the Royal Astronomical Society*, vol. 481, no. 2, pp. 2479–2486, 2018. DOI: 10.1093/mnras/sty2422.

[33] S. Ansoldi *et al.*, "Gamma-ray flaring activity of NGC1275 in 20162017 measured by MAGIC," *Astronomy and astrophysics (Berlin)*, vol. 617, p. 9, 2018. DOI: 10.1051/0004-6361/201832895.

[34] S. Ansoldi *et al.*, "The Blazar TXS 0506+056 Associated with a High-energy Neutrino: Insights into Extragalactic Jets and Cosmic-Ray Acceleration," *The Astrophysical journal*, vol. 863, no. 1, p. 10, 2018. DOI: 10.3847/2041-8213/aad083.

[35] A. Babic *et al.*, "Multimessenger observations of a flaring blazar coincident with high-energy neutrino IceCube-170922A," *Science*, vol. 361, no. 6398, p. 8, 2018. DOI: 10.1126/science.aat1378.

[36] S. Ansoldi *et al.*, "The broad-band properties of the intermediate synchrotron peaked BL Lac S2 0109+22 from radio to VHE gamma-rays," *Monthly notices of the Royal Astronomical Society*, vol. 480, no. 1, pp. 879–892, 2018. DOI: 10.1093/mnras/sty1753.

[37] V. Acciari *et al.*, "Constraining dark matter lifetime with a deep gamma-ray survey of the Perseus galaxy cluster with MAGIC," *Physics of the Dark Universe*, vol. 22, pp. 38–47, 2018. DOI: 10.1016/j.dark.2018.08.002.

[38] M. L. Ahnen *et al.*, "The detection of the blazar S4 0954+65 at very-high-energy with the MAGIC telescopes during an exceptionally high optical state," *Astronomy and astrophysics (Berlin)*, vol. 617, no. A30, pp. 1–15, 2018. DOI: 10.1051/0004-6361/201832624.

[39] M. Ahnen *et al.*, "Limits on the flux of tau neutrinos from 1 PeV to 3 EeV with the MAGIC telescopes," *Astroparticle physics*, vol. 102, no. 1, pp. 77–78, 2018. DOI: 10.1016/j.astropartphys.2018.05.002.

[40] M. Ahnen *et al.*, "Indirect dark matter searches in the dwarf satellite galaxy Ursa Major II with the MAGIC telescopes," *Journal of cosmology and astroparticle physics*, vol. 2018, no. 03, pp. 009–009, 2018. DOI: 10.1088/1475-7516/2018/03/009.

[41] A. Babic *et al.*, "Constraints on particle acceleration in SS433/W50 from MAGIC and H.E.S.S. observations," *Astronomy and astrophysics (Berlin)*, vol. 612, no. A14, p. 8, 2018. DOI: 10.1051/0004-6361/201731169.

[42] M. Ahnen *et al.*, "Constraining Lorentz Invariance Violation Using the Crab Pulsar Emission Observed up to TeV Energies by MAGIC," *The Astrophysical journal. Supplement series*, vol. 232, no. 1, p. 26, 2017. DOI: 10.3847/1538-4365/aa8404.

[43] M. L. Ahnen *et al.*, "Search for very high-energy gamma-ray emission from the microquasar Cygnus X-1 with the MAGIC telescopes," *Monthly notices of the Royal Astronomical Society*, vol. 472, no. 3, pp. 3474–3485, 2017. DOI: 10.1093/mnras/stx2087.

[44] M. L. Ahnen *et al.*, "Performance of the MAGIC telescopes under moonlight," *Astroparticle physics*, vol. 94, no. 1, pp. 29–41, 2017. DOI: 10.1016/j.astropartphys.2017.08.001.

[45] M. L. Ahnen *et al.*, "A cut-off in the TeV gamma-ray spectrum of the SNR Cassiopeia A," *Monthly notices of the Royal Astronomical Society*, vol. 472, no. 3, pp. 2956–2962, 2017. DOI: 10.1093/mnras/stx2079.

[46] M. L. Ahnen *et al.*, "MAGIC observations of the microquasar V404 Cygni during the 2015 outburst," *Monthly notices of the Royal Astronomical Society*, vol. 471, no. 2, pp. 1688–1693, 2017. DOI: 10.1093/mnras/stx1690.

[47] M. L. Ahnen *et al.*, "Observation of the Black Widow B1957+20 millisecond pulsar binary system with the MAGIC telescopes," *Monthly notices of the Royal Astronomical Society*, vol. 470, no. 4, pp. 4608–4617, 2017. DOI: 10.1093/mnras/stx1405.

[48] P. Stipanovic *et al.*, "Ground-state properties of weakly bound helium-alkali trimers," *The Journal of chemical physics*, vol. 146, no. 1, p. 7, 2017. DOI: 10.1063/1.4973381.

[49] M. Ahnen *et al.*, "Multiwavelength observations of a VHE gamma-ray flare from PKS 1510089 in 2015," *Astronomy and astrophysics (Berlin)*, vol. 603, p. 12, 2017. DOI: 10.1051/0004-6361/201629960.

ARTICLES IN PREPARATION

[1] V. A. Acciari *et al.*, "Observations of the PeVatron candidate J1809-193 with MAGIC at VLZA," 2022.

CONFERENCE CONTRIBUTIONS

[1] D. Zaric *et al.*, "Pointing System for the Large Size Telescopes Prototype of the Cherenkov Telescope Array," en, in *Proceedings of 36th International Cosmic Ray Conference — PoS(ICRC2019)*, Madison, WI, U.S.A.: Sissa Medialab, Jul. 2019, p. 829. DOI: 10.22323/1.358.0829. [Online]. Available: https://pos.sissa.it/358/829.

[2] D. Zaric *et al.*, "MAGIC observations of Dragonfly Nebula at TeV Energies using the Very Large Zenith Angle Technique," en, in *Proceedings of 36th International Cosmic Ray Conference — PoS(ICRC2019)*, Madison, WI, U.S.A.: Sissa Medialab, Jul. 2019, p. 827. DOI: 10.22323/1.358.0827. [Online]. Available: https://pos.sissa.it/358/827.

[3] D. Zaric *et al.*, "MAGIC observations of HESS J1809-193 using the Very Large Zenith Angle technique at energies above TeV," en, in *Proceedings of 37th International Cosmic Ray Conference PoS(ICRC2021)*, Berlin, Germany - Online: Sissa Medialab, Jul. 2021, p. 818. DOI: 10.22323/1.395.0818. [Online]. Available: https://pos.sissa.it/395/818.

[4] M. Peresano *et al.*, "The Crab Nebula Spectrum at $\sim$100 TeV Measured With MAGIC Under Very Large Zenith Angles," en, in *Proceedings of 36th International Cosmic Ray Conference PoS(ICRC2019)*, vol. 358, SISSA Medialab, Jul. 2021, p. 759. DOI: 10.22323/1.358.0759. [Online]. Available: https://pos.sissa.it/358/759/.

[5] J. van Scherpenberg *et al.*, "Searching for Variability of the Crab Nebula Flux at TeV Energies using MAGIC Very Large Zenith Angle Observations," en, in *Proceedings of 36th International Cosmic Ray Conference PoS(ICRC2019)*, Madison, WI, U.S.A.: Sissa Medialab, Jul. 2019, p. 812. DOI: 10.22323/1.358.0812. [Online]. Available: https://pos.sissa.it/358/812.

[6] I. Vovk *et al.*, "Novel Very Large Zenith Angle Observation Technique Performed by the MAGIC Telescopes," en, in *Proceedings of 36th International Cosmic Ray Conference PoS(ICRC2019)*, Madison, WI, U.S.A.: Sissa Medialab, Jul. 2019, p. 828. DOI: 10.22323/1.358.0828. [Online]. Available: https://pos.sissa.it/358/828.

OTHER PUBLICATIONS

[1] R. Mirzoyan *et al.* (2019). "MAGIC detection of an increased activity from BL Lacertae at very-high-energy gamma rays."

[2] R. Mirzoyan *et al.* (2019). "Detection of sub-TeV gamma-ray emission from the flaring blazar TXS 1515-273 with the MAGIC telescopes."

[3] R. Mirzoyan *et al.* (2019). “First time detection of a GRB at sub-TeV energies ; MAGIC detects the GRB 190114C.”

[4] R. Mirzoyan *et al.* (2019). “MAGIC detects an unprecedented activity from the blazar 1ES 1218+304 at very high energy gamma rays.”

[5] R. Mirzoyan *et al.* (2018). “MAGIC detects enhanced flux of VHE gamma rays from TXS 0506+056.”